Intraseasonal variability of currents along east coast of India

Arnab Mukherjee

531.2
MUK/Int

Thesis

submitted to Goa University

for the degree of

Doctor of Philosophy

in

Physics

GOA UNIVERSITY LIBRARY GOA

Goa University

July 2017

Examined. All the suggestions of the referees have been incorporated.

Guide Examiner Chairman BoE

T-811 811

To my parents

and grandmother

Declaration

As required under the University ordinance OB 9.9(vi), I state that this thesis entitled *Intraseasonal variability of currents along east coast of India* is my original contribution and it has not been submitted on any previous occasion. The literature related to the problem investigated has been cited. Due acknowledgements have been made wherever facilities and suggestions have been availed of.

Arnab Mukherjee

CSIR- National Institute of Oceanography

July, 2017

Certificate

This is to certify that the thesis entitled *Intraseasonal variability of currents along east coast of India*, submitted by Arnab Mukherjee to Goa University for the degree of Doctor of Philosophy, is based on his original studies carried out under my supervision. The thesis or any part thereof has not been previously submitted for any other degree or diploma in any university or institution.

Shankar Doraiswamy

CSIR- National Institute of Oceanography

July, 2017

Acknowledgement

The successful completion of this thesis is due to support and guidance of a lot of people. I would like to thank all the people who have helped me during this journey.

I am most indebted to my advisor, Dr. D. Shankar, National Institute of Oceanography, Goa, India. Without his help, it would have been impossible for me to make the thesis as it is. Shankar Sir has taught me to be more careful and precise with my research. His scientific temperament, innovative approach, dedication towards research, and modest yet straightforward nature has inspired me the most.

I express special thanks to Dr. S. R. Shetye, former Director of National Institute of Oceanography, Goa for his support, encouragement, and guidance in the development of my Ph.D work.

I would like to express my sincere gratitude to Prof. Julian McCreary for expanding my knowledge on ocean dynamics. I was fortunate to work under him during his visits in India. His ability to solve complex oceanographic problems using a linear process was a great learning experience for me. I am also thankful to Prof. Vinayachandran for his useful insights on ocean dynamics.

I am particularly grateful to Dr. S. G. Aparna, G. S. Michael and D. Sundar for their invaluable help during my Ph.D, and for sharing their scientific and technical ideas at every stage of my Ph.D. I express my special thanks to Dr. Unnikrishnan, Group leader and a member of my FRC committee, for his keen interest in my work and constant encouragement and support.

I express my sincere gratitude to Prof. Ramesh Pai, Head, Department of Physics, Prof. Alfred Desa and Prof. R. Tangsali, Goa University, for their kind advice, encouragement and help.

My sincere thanks goes to entire mooring group, without them this work was not possible. I would like to show my greatest appreciation to Mr. Fernando and his team members Yogesh, Khalap, Narayan, Prakash, Mithun and Siddharth. I also thank the officers, crew and seamen on the mooring cruises for providing the necessary support for deploying the ADCPs. Special thanks goes to INCOIS (Ministry of Earth Science) and CSIR-aided

projects for providing financial support to the mooring cruises. I thank Ministry of Earth Science for providing my Ph.D fellowship.

This thesis would not be possible without the friendly environment of my lab. My sincere thanks to my senior, Abhisek Chatterjee, for introducing me to Ferret and fortran programming during my initial days and later to ocean modeling. A special thanks to my senior Amol Prakash, who introduced me to ADCP data processing and analysis. I have benefited a lot from many discussions with my lab seniors Suprit and Manoj. Working with my friends Kankan, Soumya, Vineet and Anil was always a pleasure. I am thankful to our system administrators Ashok, Sarvesh, and Mahesh for taking care of the technical problems. My colleagues in the physical oceanography division deserve a special word of thanks for creating a friendly and comfortable working atmosphere. I especially thank Vijith, Nidheesh, Charls, Subeesh, Vipin, Ronnie, Remya and many others. My deepest appreciation goes to my following friends for their continued support and encouragement: Suchandan, Priyanka, Rakesh, Kalyan, Pabitra, Pratirupa, Swetha, Simontini and Ingita.

I would like to thank my seniors and friends Rajdeep da, Amit da, Sabya da, Pranab da, Anindya da, Partho da for their wonderful company. Also, it was my great fortune to be associated with "Music Club" and its cultural programs during foundation day and Independence day at National Institute of Oceanography.

I would like to express my deep sense of gratitude and sincere thanks to Dr. S. S. Shenoi, Director, Indian National Centre For Ocean Information Services (INCOIS), Hyderabad and Dr. Balakrishna Nair, Group Head for providing their constant support and encouragement at INCOIS. I have received immense help and support from my INCOIS colleagues namely, Francis, Kunal da, Arya da, Sourav da, Deepsankar and Prerna.

Lastly, and most importantly, I wish to thank world of Internet. Without freely available open source softwares like Ferret, Wavelet and coherence, my Ph.D was not possible. A special thanks also goes to freely available MOM4p1 model source codes and their discussion forums.

I would like to pay my highest regards to my parents, my sister and grandmom. Without their blessings, this thesis would not have materialized. The thesis is dedicated to them.

Arnab Mukherjee

CSIR- National Institute of Oceanography

July, 2017

List of Publications

1. P. Amol, D. Shankar, S. G. Aparna, S. S. C. Shenoi, V. Fernando, S. R. Shetye, **A. Mukherjee**, Y. Agarvadekar, S. Khalap, and N. P. Satelkar. Observational evidence from direct current measurements for propagation of remotely forced waves on the shelf off the west coast of India. *Journal of Geophysical Research.*, 117:C05017, doi:10.1029/2011JC007606, 2012.

2. **A. Mukherjee**, D. Shankar, S. G Aparna, P. Amol, V. Fernando, R. Fernandes, S. Khalap, S. Narayan, Y. Agarvadekar, M. Gaonkar, P. Tari, A. Kankonkar, and S. Vernekar. Near-inertial currents off the east coast of India. *Continental Shelf Research.*, 55: 29-39, 2013.

3. Meenakshi Chatterjee, D. Shankar, G.K. Sen, P. Sanyal , D. Sundar, G.S. Michael, Abhisek Chatterjee, P. Amol, Debabrata Mukherjee, K. Suprit, **A. Mukherjee**, V. Vijith, Siddhartha Chatterjee, Anwesha Basu, Madhumita Das, Sharanya Chakraborti, Arvind Kalla, Surya Kanta Mishra, Soumya Mukhopadhyay, Gopal Mandal, Kankan Sarkar, Tidal variations in the Sundarbans Estuarine systems, India., *Journal of Earth System Science*. 122(4):899—933, 2013.

4. P. Amol, D. Shankar, V. Fernando, **A. Mukherjee**, S. G. Aparna, R. Fernandes, G. S. Michael, S. T. Khalap, N. P. Satelkar, Y. Agarvadekar, M. G. Gaonkar, A. P. Tari, A. Kankonkar, and S. P. Vernekar. Observed intraseasonal and seasonal variability of the West India Coastal Current on the continental slope. *Journal of Earth System Science*. 123 (5), 1045–1074, 2014.

5. **A. Mukherjee**, D. Shankar, V. Fernando, P. Amol, S. G. Aparna, R. Fernandes, G. S. Michael, S. T. Khalap, N. P. Satelkar, Y. Agarvadekar, M. G. Gaonkar, A. P. Tari, A. Kankonkar, and S. P. Vernekar. Observed seasonal and intraseasonal variability of the East

India Coastal Current on the continental slope. *Journal of Earth System Science*. 123 (6), 1197–1232, 2014.

6. V. Jain, D. Shankar, P. N. Vinayachandran, A. Kankonkar, A. Chatterjee, P. Amol, A. M. Almeida, G. S. Michael, **A. Mukherjee**, Meenakshi Chatterjee, R. Fernandes, R. Luis, Amol Kamble, A. K. Hegde, Siddhartha Chatterjee, Umasankar Das and C. P. Neema. Evidence for the existence of Persian Gulf Water and Red Sea Water in the Bay of Bengal. *Climate Dynamics*, doi:10.1007/s00382-016-3259-4, 1–20, 2016.

7. A. Chatterjee, D. Shankar, J. P. McCreary, P. N. Vinayachandran and **A. Mukherjee**. Role of the Andaman Sea in the dynamical connection between the Equatorial Indian Ocean and the Bay of Bengal. *Journal of Geophysical Research*, doi:10.1002/2016JC012300, 122, 1–19, 2017.

8. **A. Mukherjee**, D. Shankar, A. Chatterjee, P. N. Vinayachandran. Numerical simulation of the observed near-surface East India Coastal Current on the continental slope. *Re-revised version communicated to Climate Dynamics.*, 2017.

Synopsis

The circulation of the ocean, as manifested in the horizontal and vertical velocity field, has implications for our climate and weather, our fisheries, navigation, etc. This importance of the circulation extends to the North Indian Ocean (NIO), which is split by the Indian peninsula into two parts, the Bay of Bengal (BoB) to the east and the Arabian Sea (AS) to the west. The BoB is a semi-enclosed basin lying south of 22°N and has a zonal extent of ~1200 km. Through the BoB and AS lie in the same latitude band, they are strikingly different as freshwater inflow from rainfall and rivers exceeds evaporation in the former, but evaporation is grater over the latter. Studies have shown that the relatively sluggish circulation of the BoB and low-salinity surface mixed layer play a role in keeping it warmer than the AS during the summer monsoon (June–September), leading to more low-pressure systems forming over the BoB. One component of this circulation of the BoB is the current along its western boundary, marked by the east coasts of India and Sri Lanka.

The dynamics of this boundary current, which has been called the East India Coastal Current (EICC), has been shown to be intimately connected to that of the equatorial Indian Ocean (EIO) and the boundary current along the eastern boundary of the AS, the West India Coastal Current (WICC).

As is also true of the rest of the NIO, the EICC reverses seasonally owing to the forcing by the seasonally reversing monsoon winds. Initial descriptions of the EICC were due to hydrographic and ship-drift data and were complemented later by geostrophic estimates of the surface EICC from satellite-borne altimeters. These data show that the EICC flows poleward during February– September and equatorward during November–January. The data show that the poleward EICC is strongest during March–April, when the winds over the BoB are weak, and weakens when the winds strengthen with the onset of the summer monsoon. Model studies have shown that the seasonal cycle of the EICC is forced not only by the winds local to the western boundary of the basin, but also from the eastern boundary, the interior of the BoB, and the EIO. Connection between these regimes is via equatorial and coastal Kelvin waves and Rossby waves. In turn, these coastal Kelvin waves generated

off the Indian east coast have been shown to play a significant role in forcing the WICC.

While the hydrographic and ship-drift data provided essentially a climatological perspective of the EICC, the altimeter data permitted an analysis of the intraseasonal variability. The altimeter data cannot, however, resolve satisfactorily periods shorter than a fortnight and are also restricted to providing estimates of the surface current. Direct current measurements of the WICC and EICC were few and restricted to short-term projects, prompting the CSIR-National Institute of Oceanography to launch a program for measuring currents in the Indian Exclusive Economic Zone (EEZ) using acoustic Doppler current profilers (ADCPs) deployed on moorings on the continental shelf and slope off the Indian west and east coasts. In the BoB, seven moorings were deployed on the continental shelf (water column depth 100 m or 180 m and ADCP located just above the acoustic releases; sampling at interval of 15 or 30 minutes) and continental slope (water column depth$\sim$ 1100 m and ADCP typically deployed at 300–350 m; sampling interval of one hour). These pairs were located roughly off Gopalpur (northern end of east coast of India), Kakinada (central east coast of India), and Cuddalore (southern east coast of India). An additional ADCP mooring was deployed at (89°E, 19°N), which is located at a depth of$\sim$2000 m on the continental slope off the northern boundary of the BoB. Since this mooring is located at roughly the latitude of the port of Paradip on the Indian east coast, we refer to it by this name.

These ADCP moorings have provided an unprecedented view of the variability of the EICC over four years. In this thesis, we use these data to describe the variability of the EICC and use a suit of models to simulate the observations. Our focus is on the data from the continental slope because these data are more continuous; the shelf ADCPs exhibit more data gaps and are used only in one chapter. The data are detided and we analyze only the non-tidal current in this thesis, which begins with a brief introduction (Chapter 1) that provides an outline of the thesis and presents its objective. Background information from the literature is presented in Chapter 2. This background includes both observational (hydrography, ship drifts, drifters, and altimeter-derived currents) and model studies and includes a list of available direct current measurements, which were typically restricted to less than a fortnight in most cases.

The high-frequency end of the spectrum descried in this thesis is around the inertial period. Currents in this near-inertial frequency band are called near-inertial currents (NICs) and Chapter 3 describes their observed variability on the slope as well as the shelf. One key result is that the NICs are weak on the east-coast shelf and the likely reason is that the shelf width is less than the local Rossby radius of deformation at all locations. The NICs are stronger on the slope makes them relevant to the thesis. We have found strong

intraseasonal, seasonal and interannual variability of the observed NICs. The NICs are not seen largely during January–April at all moorings locations. They are prominent at the northern locations during May-September, when the strong winds associated with the summer monsoon depressions and cyclones are observed in the region. The storms shift southward following the summer monsoon, and so do the NICs, which are generated off Cuddalore during October–December. In the central part of the coast, the NICs are weak, but exist during both summer and winter monsoon owing to the effect of storms over the northern and southern bay. A histogram of the ratio of the NICs to the total current shows that the NICs is comparable to the residual current, i.e., non-tidal and sub-inertial current, on more than nine days in a year off Paradip and Cuddalore; the magnitude of the NICs exceeds half that of the residual current on more than 16 days. The rest of the thesis deals with EICC on the slope. The NICs were discussed here because it is stronger on the slope compared to the shelf.

A detail description of the variability of the detided, sub-inertial EICC forms the subject of Chapter 4. The seasonal cycle is defined to cover the 100–400 day band and intraseasonal variability is split into two parts, 30–90 days, which is the more conventional intraseasonal band, and 4–25 days, which represents the high-frequency part of the intraseasonal spectrum. The ADCP data show that the seasonal cycle, which includes the annual cycle, the semi-annual cycle and a peak around ~120 days, dominates the observed variability of the EICC. Spectral analysis suggests that the 120-day peak dominates the seasonal variability at Paradip and is strong at Gopalpur and Kakinada. The annual cycle of the EICC is coherent along the east coast of India, but with significant phase differences between moorings. At the semi-annual and 120-day periods, the alongshore coherence is weaker. Intraseasonal variability is weaker than the seasonal cycle, particularly at Cuddalore and Paradip, and it exhibits seasonality: the strongest intraseasonal variation is observed at Gopalpur and Kakinada during spring (February–April). High-frequency variability with peaks around 12 and ~20–22 days are also seen at Gopalpur, Kakinada, and Cuddalore. The observations show evidence of upward phase propagation, which indicates downward propagation of energy and leads to a distinct coastal undercurrent at Cuddalore (particularly) during winter. At the other three locations, however, the vertical phase speed is much higher compared to Cuddalore in the top 100 m, making the sub-surface EICC mostly unidirectional, except on a few occasions. During spring, however, the EICC tends to flow poleward (eastward) at Cuddalore, Kakinada and Gopalpur (Paradip) over the top ~ 300 m, which is the maximum depth to which observations were made. The cross-shore component of the EICC is much weaker than the alongshore component at Cuddalore and except, for a few bursts during

spring, at Kakinada and Gopalpur. It is only at Paradip that significant cross-shore flows are seen during spring and the summer monsoon (June–August) and these flows are seen to be associated with eddy-like circulations in the altimeter data. In summary, the seasonal cycle dominates over intraseasonal variability for the EICC, unlike for the WICC, for which it has been shown using ADCP data that intraseasonal variability dominates over the seasonal cycle.

In order to validate freely available ocean-current data products with these direct measurements of the EICC, we used three popular data products and the validation results are described in Chapter 5. One data product we validate is the Ocean Surface Current Analysis-Real Time (OSCAR) current, which is based on geostrophic estimates based on altimeter sea level and the wind-driven Ekman current. The two other data products, ECCO2 (Estimating the Circulation and Climate of the Ocean, Phase II) and GODAS (Global Ocean Data Assimilation System), are data-assimilated model outputs. The OSCAR currents at Paradip match the observed currents well, but the correlation is much weaker at the other three locations. The OSCAR currents are able to capture only the seasonal variability; the match at intraseasonal periods is weak and one possible reason is that the ADCP current is at 40 m and the latter represents the current in the 0-30 m depth range. Another possible reason is upward phase propagation. The variability simulated by GODAS is very weak; ECCO2 fares better at the three locations off the Indian east coast, particularly at the annual period, but shows significantly bad performance at Paradip. A key reason for the poor match between these data products and direct current measurements is likely to be the coarse model horizontal resolution. The horizontal resolution of GODAS (ECCO2) is 1° x 0.33° (0.25° x 0.25°) in the x–y direction.

To simulate the variability observed in these ADCP data, we use two models in Chapter 6. The simpler of these models is a linear, continuously stratified (LCS) model that has been used extensively in earlier model studies of the NIO circulation. The other model is an ocean general circulation model (OGCM) called the Modular Ocean Model (MOM); we use version MOM4p1 at a horizontal resolution of 0.1° x 0.1°. Validation with data from the EIO and the eastern BoB shows that both models are capable of simulating the intraseasonal variability at the equator even at the coarser resolution of 0.25°. The performance degrades away from the equator in the eastern BoB. Nevertheless, in spite of the known influence of the equatorial winds on the EICC, both models simulate the annual EICC at the three western-boundary locations fairly well; they are not as good, however, at simulating the observed intra-annual (semi-annual and 120-day) variability. MOM simulates more intraseasonal events compared to the LCS model. Since the LCS model studies for the In-

dian Ocean have traditionally used a density profile from the western EIO for decomposing into vertical normal modes and this profile is significantly different from the density profile in the BoB owing to the much shallower surface mixed layer there, we experimented with different density profiles to test the sensitivity of the LCS model to the density profile. The BoB profiles show a dominant first baroclinic mode compared to a dominant second mode for the western EIO profile; in addition, the contribution of higher-order modes was higher for the BoB profiles. The simulations show that BoB profiles has an impact on the surface current, with the LCS model performing better when the more local profile is used. This impact is significant for the locally forced EICC because the high-order modes tend to be more important for this component; the remotely forced component is not affected as much. The performance of both models is not as good at below ~100 m of Cuddalore, where a strong presence of undercurrent is observed. At Paradip, the magnitude of the LCS model current is negligible, but the high- resolution (0.1°) MOM simulation shows an improvement during spring compared to the low-resolution (0.25°), suggesting that nonlinearity may be important. Eddy-mean energy computations show that nonlinearity is indeed important in the northern BoB: this improvement at Paradip is mostly due to formation of eddy kinetic energy by barotropic instability.

The major conclusions of the thesis are summarized in Chapter 7. In this thesis, we first present a detailed description of the EICC variability over the depth range of 40–300 m from the inertial to the annual time scale, something not possible earlier, and evaluate the performance of an OGCM in simulating the observed variability. The OGCM performs fairly well at seasonal periods, but not as well at intraseasonal periods. Furthermore, we show that local stratification, horizontal resolution, and nonlinear dynamics play a major role in determining the observed variability of the EICC.

The observations are continuing and a long time series of direct current measurements will allow an evaluation of the impact on the EICC of the major climate modes like ENSO (El Niño and Southern Oscillation) and IOD (Indian Ocean Dipole) or the minima of interannual variability that have been reported using altimeter sea-level data.

Contents

List of Publications vii

Synopsis ix

Contents xiv

List of Figures xvii

List of Tables xx

1 Introduction 1

1.1 Objectives and strategy 5

2 Observational and Theoretical Background 7

2.1 Climatological seasonal cycle 7

2.2 Theoretical studies 10

2.3 Satellite altimetry 12

2.4 Direct current measurements 14

2.5 Summary 15

3 Near-Inertial currents 16

3.1 Introduction 16

3.2 Data 18

3.3 NICs on the continental shelf and slope 19

3.4 Impact of storms on the NICs 23

3.5 NICs in a simple slab model 31

3.6 Summary and discussion 33

4 Observed seasonal and intraseasonal variability of the sub-inertial EICC 38
4.1 Alongshore current 38
4.1.1 Seasonal cycle 46
4.1.2 Intraseasonal variability 51
4.1.3 Undercurrents 57
4.2 Crossshore current 57
4.3 Discussion 59

5 Validation of Data Products 68
5.1 Data Products 68
5.2 Validation of OSCAR 70
5.3 Validation of ECCO2 and GODAS 71
5.4 Discussion 75

6 Numerical simulation of the EICC 81
6.1 Ocean models 82
6.2 Numerical experiments 83
6.3 The control runs 84
6.3.1 Current simulations in the EEIO and EBoB 84
6.3.2 Current simulations in the WBoB 89
6.4 Forcing mechanisms 95
6.5 Importance of high-order vertical modes 100
6.6 Impact of stratification 106
6.7 Role of nonlinear dynamics 113
6.8 Summary 117

7 Summary 139

Appendix A MOM4p1 Model configuration 145
A.1 Equation of motion and coordinate systems 145
A.2 Model physics parametrization 148
A.2.1 Advection 148
A.2.2 Horizontal mixing 148
A.2.3 Vertical mixing 149
A.2.4 Neutral Physics 149
A.2.5 Shortwave Radiation 150

A.2.6 Tidal dissipation 150
A.2.7 Boundary condition 150
A.3 Forcing 152

Appendix B LCS model configuration **153**
B.1 Equations of motion 153
B.2 Computation of the vertical mode structure in the LCS model 155
B.3 Model grid, domain and forcing 157

References **159**

List of Figures

1.1 Major currents in the NIO 2
1.2 ADCP location along Indian Coast 5

2.1 Climatological EICC 8

3.1 Clockwise and anticlockwise rotary spectra 20
3.2 Clockwise rotary spectra at slope with respect to depth and time 22
3.3 high frequency wind and clockwise rotary spectra 24
3.4 Formation of cyclonic storms 28
3.5 Upward phase propagation of NIC 30
3.6 NIC using simple slab model 32
3.7 Importance of inertial current over subinertial current 36

4.1 2.5 day low-pass-filtered detided, residual alongshore currents 40
4.2 Histogram and cumulative curve for both alongshore and cross-shore currents 42
4.3 Variance preserving spectra for the raw alongshore and cross-shore currents 43
4.4 Morlet wavelet power spectra of alongshore current at 40 m 45
4.5 Annual variability of EICC 48
4.6 Intra-annual variability of EICC 49
4.7 Vertical section of wavelet at annual period 50
4.8 Wavelet coherence between ADCP mooring pairs 52
4.9 30–90 day band pass filtered alongshore current 54
4.10 4–25 day band pass filtered alongshore current 55
4.11 4–25 day band average wavelet of alongshore current 56
4.12 Vertically averaged, over 40–200 m, wavelet power for the 1–32-day band. . 58
4.13 Sub-inertial Cross-shore current 60
4.14 Comaprison between alongshore and cross-shore current 61
4.15 Morlet wavelet of cross-shore current 62

4.16 Wavelet coherence of cross-shore currents between ADCP moorings 63
4.17 Oscar current and sea level anomalies from altimeter 67

5.1 Comparison between ADCPs and data products at 40 m 72
5.2 Wavelet coherence between ADCP and OSCAR alongshore current 73
5.3 Wavelet coherence between ADCP and ECCO2 alongshore current 74
5.4 Correlation between ADCP and model products (ECCO2 and GODAS) . . 75
5.5 Morlet wavelet of OSCAR alongshore current at ADCP locations 77
5.6 Wavelet coherence for the OSCAR alongshore currents at ADCP locations . 78
5.7 Climatology of mixed layer at ADCP locations 79
5.8 30 day low pass filtered alongshore current at Gopalpur 79

6.1 Models and RAMA current comparion (part 1) 86
6.2 Models and RAMA current comparison (part 2) 88
6.3 RAMA and models simulated wavelet power spectra of zonal current 90
6.4 RAMA and models simulated wavelet power spectra of meridional current . 91
6.5 Comparison of zonal current wavelet coherence between RAMA and models 92
6.6 Comparison of meridional current wavelet coherence between RAMA and models 93
6.7 Comparison between WBoB ADCPs and model simulated alongshore currents 94
6.8 Comparion of wavelet power spectra and coherence between WBoB ADCPs and models 96
6.9 Domain of stratification, boundary points for LCS experiments 121
6.10 Local and remote forcing response on seasonal EICC 122
6.11 Local and remote forcing response on intraseasonal EICC 123
6.12 Remote forcing response from EIO to WBoB 124
6.13 Contribution of different modes on current and sea level 125
6.14 Remote EIO response for ideal experiments 126
6.15 The contribution of different modes for ideal experiments 127
6.16 Density and Brünt-Vaïsala-frequency for the LCS models 128
6.17 EICC simulation using LCS stratification experiments at surface 129
6.18 EICC simulation using LCS stratification experiments at 40 m 130
6.19 Change of local and remote forcing response on EICC due to stratification . 131
6.20 Role of vertical modes on local andremote forcing response on EICC . . . 132
6.21 Mode coupling coefficient using observed and MOMCR model simulated climatology 133

6.22 Eddy and nolinearity at BoB 134
6.23 Comparison of current wavelet at Paradip between models and ADCPs . . . 135
6.24 Coherence of current between ADCPs and models at Paradip 136
6.25 Eddy energy estimation during March–April 2010 and 2011 by models at BoB 137
6.26 Eddy energy estimation during March–April 2012 by models 138

A.1 0.1 degree MOM model grid 147

B.1 0.1 degree LCS model grid land mask 158

List of Tables

1.1 Details of ADCP moorings 6

2.1 Transport estimation using hydrography data 10
2.2 Direct current measurement prior to 2009 14

3.1 Angle of rotation for observed current 19
3.2 Magnitude of clockwise and anticlockwise rotary spectra 21
3.3 Details of wind-data sources. 25
3.4 Details of low pressure system 26
3.5 IMD classification of storms 27
3.6 Shelf width and Rossby radius 33

5.1 Correlation between currents from ADCP measurements and data products for both alongshore and cross-shore components of the current 71

6.1 MOM4p1 model parametrization 83
6.2 Correlation between models and RAMA zonal currents (part 1) 85
6.3 Correlation between models and RAMA Meridional currents (part 1) 87
6.4 Correlation between models and RAMA currents (part 2) 87
6.5 Correlation between WBoB ADCPs and models 95
6.6 List of experiments related to local and remote forcing response 97
6.7 List of LCS model ideal experiments related to vertical modes 103
6.8 Values of LCS mode parameters 107
6.9 List of LCS model stratification experiments 108
6.10 Correlation between RAMA zonal currents and LCS model stratification experiments 109
6.11 Correlation between RAMA meridional currents and LCS model stratification experiments 109

6.12 Correlation between alongshore currents from WBoB and LCS model stratification experiments at 40 m 110
6.13 Correlation of EICC between observations and LCS model stratification experiments at surface 110

A.1 Forcing in the MOM model 152

Chapter 1

Introduction

The Indian Ocean (IO) is the third largest ocean and holds almost 20% percent of the water on the earth's surface. We divide the IO into two parts; the region north of 10°S (North Indian Ocean (NIO)), which is our region of interest and South of 10°S (South Indian Ocean (SIO)). The spatial domain of the NIO mostly covers the tropical region (Figure 1.1). It is bounded by the Asian continent in the north and east and by Africa in the west. The NIO can be divided into three different regions by their distinctive features: Equatorial Indian Ocean (EIO), the Arabian Sea (AS) and the Bay of Bengal (BoB).

The first comprehensive international Indian Ocean expedition (IIOE) were conducted between 1959–1965. IIOE was a collaborative research project by countries surrounding the Indian Ocean and around the world. This expedition change forever the face of Indian Ocean oceanography. There are many publication using IIOE data which was measured north of 40°S. For example, Rochford (1964) identified water masses in the IO and studied salinity distribution in the AS, Warren et al. (1966) studied water masses of the Somali current region during summer monsoon, Wyrtki (1971) produced a hydrographic atlas of the Indian Ocean. After IIOE, there was several observational programs conducted in the IO. These included the summer monsoon experiments such as Indo-Soviet Monsoon experiment (ISMEX-73), the MONSOON-77 and MONEX-73, ISMEX-73 meteorological and oceanographic data over AS, BoB, EIO and SIO.

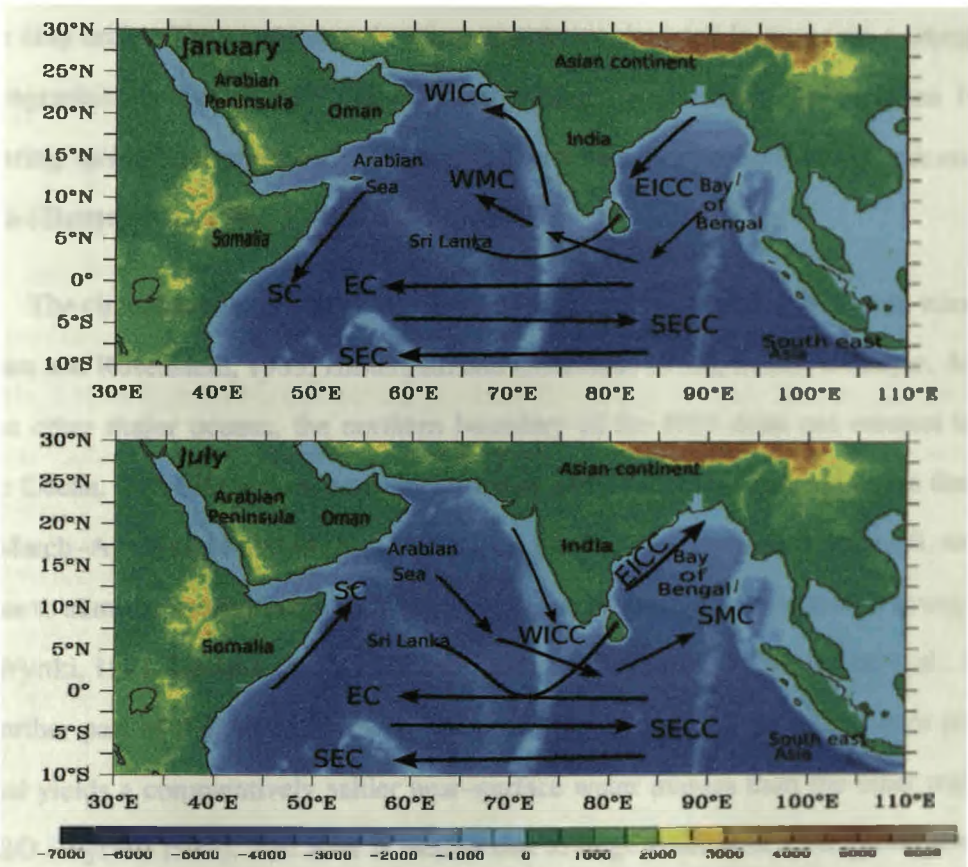

Figure 1.1: Schematic representation of the NIO circulation, as described in the literature, in the Indian Ocean during January (winter monsoon) and July (summer monsoon). The abbreviations are as follows: SC, Somali Current; EC, Equatorial Current; SMC, Summer Monsoon Current; WMC, Winter Monsoon Current; EICC, East India Coastal Current; WICC, West India Coastal Current; SEC, South Equatorial Current, SECC, South Equatorial Counter Current.

All these above hydrographic surveys were useful to map a rough picture of NIO circulation, but not sufficient to map seasonal pattern of the boundary currents along the east and west coasts of India. In order to map the seasonal circulation of the NIO, Cutler and Swallow (1984) and Mariano et al. (1995) used coarse resolution current observations based on ship drifts. The seasonal and surface circulation depicted in these are confirmed by hydrographic surveys by the CSIR-National Institute of Oceanography between 1987–1994 during spring intermonsoon, summer and winter monsoon periods along both coasts of India (Shetye et al., 1990, 1991b,c, 1993, 1996).

The circulation in the NIO is dominated by seasonally reversing monsoon winds (Hellerman and Rosenstein, 1983; Hastenrath and Greischar, 1986), makes it unique. Also, unlike the other major oceans, the northern boundary of the NIO does not connect to the Arctic Ocean. The EIO is dominated by strong semiannual eastward wind bursts during spring (March–April) and fall (October–November) intermonsoon periods. In the AS, strong winds due to summer monsoon blow among Somali and Oman coasts give rise to strong upwelling (Wyrtki, 1971; Leetma, 1972, 1973; Hurburt and Thompson, 1976; Schott et al., 1990). The norther part of the AS is also well known for its excess of evaporation over precipitation and yields a comparatively saltier near–surface water masses than the other regions of the NIO (Wyrtki, 1971). The BoB is fresher due to large amount of river runoff and excess of precipitation over evaporation. Also, high sea surface temperature (SST) in the BoB leads to formation of more low pressure systems over BoB compared to AS (Krishnamurti, 1971; Mooley and Shukla, 1989). Due to close proximity at the EIO, the circulation in both BoB and AS effected by the equatorial winds via remotely forced planetary waves (Yu et al., 1991; Potemra et al., 1991; McCreary et al., 1993; Shankar et al., 1996; McCreary et al., 1996). Due to interconnections among EIO, AS and BoB, they form a single dynamical system, known as NIO.

In 1980s, additional tools such as expendable bathythermograph (XBT), surface drifters

and satellite based sensors became available. The satellite based sensor provides significant near–surface data. Based on these data, it became possible to describe the seasonal circulation off the boundary currents off the Indian coasts. The current off the Indian east coast was named as East India Coastal Current (EICC) (Shetye et al., 1996; Shankar et al., 1996; McCreary et al., 1996) and off the Indian west coast was named as West India Coastal Current (WICC) (Shankar and Shetye, 1997) (Figure 1.1)..

While the hydrographic data provided essentially a climatological perspective of the EICC and WICC, the satellite altimeter permitted an analysis of surface currents from intraseasonal to seasonal time scale. The altimeter data cannot, however, resolve satisfactorily periods shorter than a fortnight and are also restricted to providing estimates of the surface current. Direct current measurements of the WICC and EICC were few and restricted to short-term projects, prompting the CSIR-National Institute of Oceanography to launch a program for measuring currents in the Indian Exclusive Economic Zone (EEZ) using acoustic Doppler current profilers (ADCPs) deployed on moorings on the continental shelf and slope off the Indian west and east coasts (Figure 1.2). Details of observed WICC variability at both continental shelf and slope are discussed by Amol (2014). Our thesis objective is based on ADCPs observed current along western boundary of BoB (WBoB). In the WBoB, total nine moorings are deployed on the continental shelf (water column depth 100 m or 180 m and ADCPs located just above the acoustic releases; sampling at interval of 15 or 30 minutes) and continental slope (water column depth$\sim$ 1100 m and ADCPs typically deployed at 300–350 m; sampling interval of one hour) locations. These pairs were located roughly off Gopalpur (northern end of east coast of India), Kakinada (central east coast of India), Ramyapatnam (central east coast of India) and Cuddalore (southern east coast of India). An additional ADCP mooring was deployed at (89°E, 19°N), which is located at a depth of$\sim$2000 m on the continental slope off the northern boundary of the BoB. Since this mooring is located at roughly the latitude of the port of Paradip on the Indian east coast, we

refer to it by this name. The mooring details are given in Table 1.1.

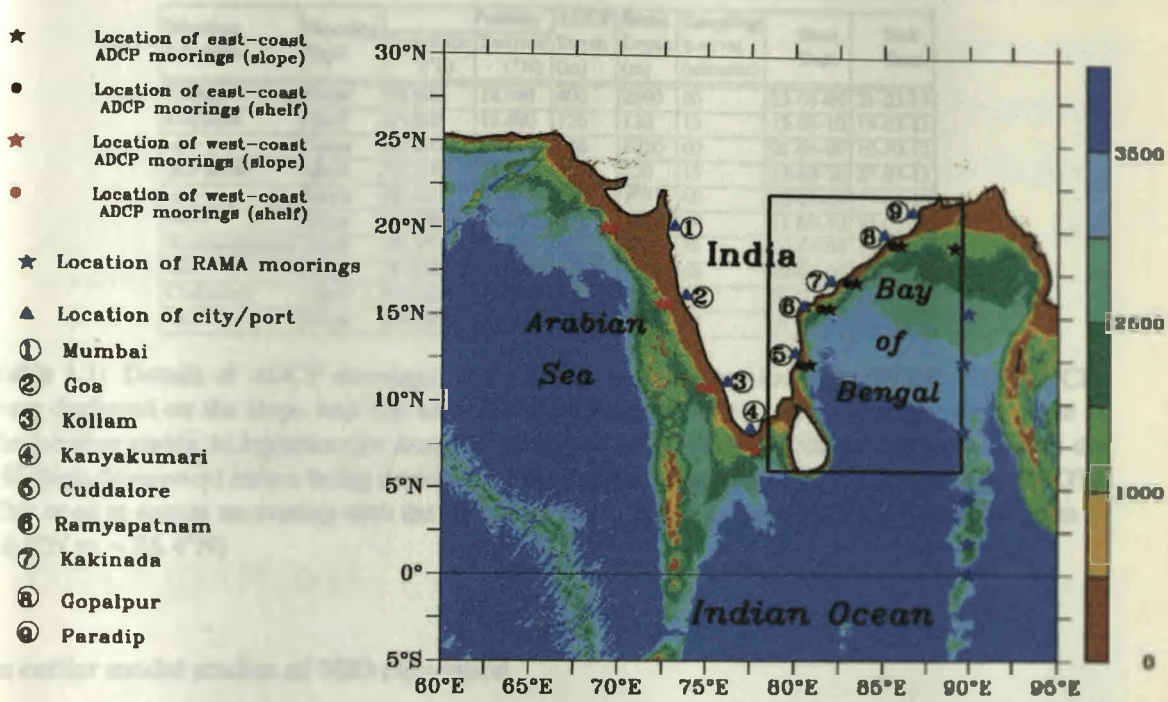

Figure 1.2: The ADCP moorings along the coast of India are shown here. the color shading shows the bathymetry (m). Star (dot) symbol denotes slope (shelf) ADCPs. Moorings along the west coast of India (red symbol) were used by Amol (2014). Moorings along the east coast (black symbol) of India are discussed in this thesis. The box marked by solid lines is the western-bay region, which is our region of interest. Blue star symbol represents RAMA (Research Moored Array for African-Asian-Australian Monsoon Analysis and Prediction) current observations (McPhaden et al., 2009).

1.1 Objectives and strategy

The first objective of the thesis is to quantify the intraseasonal variability of the EICC using moored ADCPs observed current profiles. Our focus is on the data from the continental slope because these data are continuous for a period of ~ four years (Table 1.1).

The second objective of the thesis is to simulate the variability observed in these ADCP data. We have used a linear, continuously stratified model abbreviated as LCS (McCreary, 1980) and a nonlinear Ocean General Circulation Model (OGCM) called the Modular Ocean Model (MOM) (Griffies et al., 2004; Griffies, 2009). These two models are used extensively

Mooring Location	Mooring Type	Position Longitude (°E)	Position Latitude (°N)	ADCP Depth (m)	Water Depth (m)	Sampling interval (minutes)	Start Date	End Date
Paradip	Slope	88.500	18.998	400	2500	60	23-04-09	21-03-13
Gopalpur	Shelf	85.600	19.400	120	130	15	13-05-10	19-03-11
-do-	Slope	85.430	18.850	340	1020	60	01-05-09	10-10-12
Kakinada	Shelf	82.170	16.300	95	120	15	13-05-10	27-03-11
-do-	Slope	82.980	16.837	330	1031	60	20-04-09	13-05-10
-do-	Slope	82.500	16.400	320	1000	60	11-05-10	15-03-13
Ramayapatnam	Shelf	80.336	15.000	92	100	30	19-04-09	28-04-10
-do-	Slope	80.550	14.997	310	1013	60	19-04-09	08-05-10
Cuddalore	Shelf	80.100	12.010	140	150	15	01-05-10	24-03-11
-do-	Slope	80.205	12.016	320	1080	60	01-05-10	12-03-13

Table 1.1: Details of ADCP moorings. All ADCPs were upward-looking. 75 kHz RDI ADCPs were deployed on the slope and 300 kHz RDI ADCPs on the shelf. Some changes were made in the location owing to logistics (for example, restricted areas) and to facilitate comparison with the HF (high-frequency) radars being deployed by the National Institute of Ocean Technology (NIOT). This need to ensure an overlap with the HF radars led to a shift in the ADCPs at Kakinada (from ~ 16.8°N to ~ 16.4°N)

in earlier model studies of NIO circulation.

Thesis is organized as follows. Details of theoretical and observational studies related to EICC from the literature are presented in Chapter 2. Due to availability of the ADCP data at hourly interval, we can estimate observed inertial period, which will be near the high frequency end of the spectrum described in this thesis (intraseasonal). Currents in the inertial frequency band are known as near-Inertial current (NICs) which are discussed in Chapter 3. We have defined seasonal cycle to cover the 100–400 day band and intraseasonal variability is split into two parts: 30–90 day known as MJO (Madden-Julian Oscillations (Madden and Julian, 1971, 1972, 1993; Han et al., 2001a; Vialard et al., 2009)) and is the more conventional intraseasonal band. The other band is 4–25 day, which represents the high-frequency part of the intraseasonal spectrum. Detailed analysis of observed seasonal, intraseasonal and high frequency variability are discussed in Chapter 4. In order to validate freely available ocean-current data products with these direct measurements of the EICC, we have used three popular data products and the validation results are described in Chapter 5. Chapter 6 is devoted to numerical simulation of the EICC.

Chapter 2

Observational and Theoretical Background

Details of observational and theoretical studies related to EICC are discussed here. This discussion is limited to studies prior to the ADCP observations and includes ship drifts, hydrography, Lagrangian drifters, altimeter sea level and few short term direct current measurement measurement off the east coast of India.

2.1 Climatological seasonal cycle

The monthly climatology of ship drifts (Mariano et al., 1995) shows that, poleward of 10°N, the EICC flows poleward (upwelling favourable) during February–August; it flows equatorward during October–December, with the direction in January and September changing along the coast (Figure 2.1a,b). Equatorward of 10°N, the EICC is mostly equatorward over the entire year; this difference in the EICC direction across 10°N (McCreary et al., 1993; Shankar et al., 1996) appears to be consistent in the ship-drift data sets (Cutler and Swallow, 1984; Rao et al., 1991; Mariano et al., 1995). The data from Lagrangian drifers (Shenoi et al., 1999) are inconclusive owing to the gaps in data coverage, but a weekly climatology

of geostrophic currents estimated from satellite altimetry (Figure 2.1c) suggests that seasonality of the EICC extends equatorward of 10°N as well. The climatological seasonal cycle of the EICC inferred by Durand et al. (2009) from the MAP (Margins Altimetry Project) data set (Birol et al., 2006), which provides a superior resolution of the cross-shore structure of the EICC (Durand et al., 2008), also suggests a seasonal change in the direction of the EICC south of 10°N, including the east coast of Sri Lanka. A similar change in direction is seen in the north: during the summer monsoon, when the EICC flows poleward along the Indian east coast, its direction is equatorward north of ~ 18°N (Figure 2.1) (Shetye et al., 1991c; Shankar et al., 2002; Vinayachandran and Kurian, 2007).

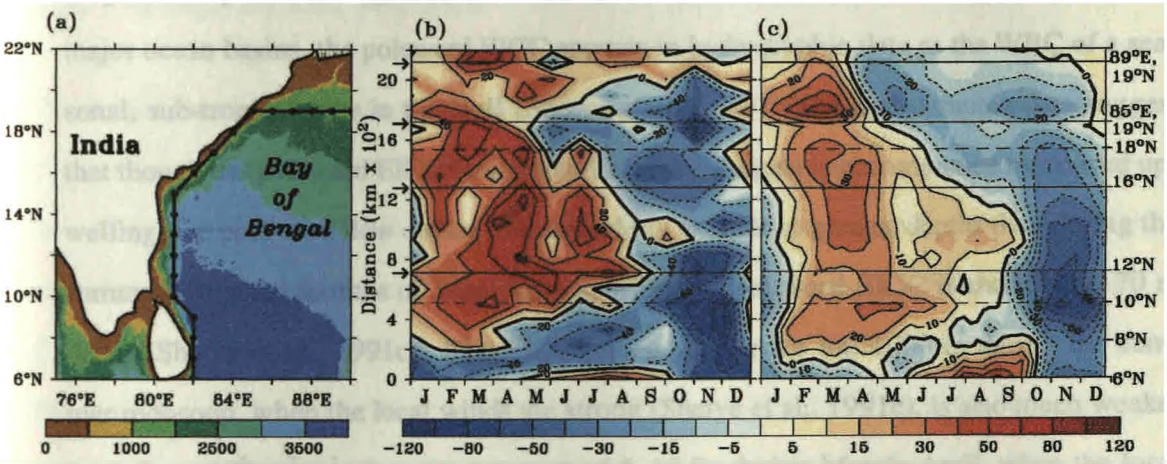

Figure 2.1: (a) The WBoB, showing the bathymetry (colour scale, m). The small circles and the associated line represent near-coastal locations along which the current climatologies shown in panels (b) and (c) were computed. (b) Monthly climatology of alongshore ship-drift currents (cm s^{-1}) (Mariano et al., 1995) as a function of distance (km) from the southern end at (82°E, 8°N). The solid horizontal lines represent the ADCP locations. 18°N and 10°N are marked by dashed horizontal lines; the former is where the shelf break breaks off the western boundary to mark the edge of the northern-boundary shelf and the latter roughly marks the divide between the two seasonal Ekman-pumping regimes in the basin (McCreary et al., 1996). the ordinate axis on the left shows the distance from (82°E, 8°N) in hundreds of km and the latitude is marked on the right ordinate axis. Above the dashed line marking 18°N, the ordinate axis marks the distance computed zonally from (85°E, 19°N) to (89°E, 19°N). In this part of the figure, the alongshore current is the zonal current because the shelf break runs roughly west–east. (c) As in panel (b), but for the weekly climatology of alongshore geostrophic currents (cm s^{-1}) (AVISO, 1996) based on data from January 2000 to December 2008.

The relationship of the EICC to the circulation in the rest of the BoB was first established

using hydrographic data. On the basis of a hydrographic survey along 13°N, Shcherbinin et al. (1979) showed the presence of a WBC (western boundary current) between 81°E and 82°E. While the existence of this WBC along the rest of the coast was confirmed using satellite measurements of sea surface temperature (SST) (Legeckis, 1987), a comprehensive description of the EICC was made possible through a series of hydrographic surveys (Shetye et al., 1991c, 1993, 1996). These data showed that though the EICC off the Indian east coast (i. e., poleward of 10°N) flows poleward during February–August, there is a difference between the pre-monsoon and summer-monsoon poleward flows. During February–May, the only time during the year when the circulation in the basin resembles that of the major ocean basins, the poleward EICC appears in hydrographic data as the WBC of a seasonal, sub-tropical gyre in the BoB (Shetye et al., 1993). The hydrographic data suggest that though the poleward EICC throughout February–August is accompanied by coastal upwelling, the poleward flow during February–May extends to greater depths than during the summer-monsoon months of June–August, when the poleward EICC is shallow ($\sim$ 70 m deep) (Shetye et al., 1991c). The EICC transport over the top 1000 m during the summer monsoon, when the local winds are strong (Shetye et al., 1991c), is also much weaker ($\sim$ 1 Sv $= 10^6$ m^{3}s^{-1}) than the transport of 5–10 Sv during March–April, when the local winds are much weaker (Shetye et al., 1993). A list of the transport estimates available for the EICC is given in Table 2.1 and shows that the transport of the equatorward EICC during October–December (Shetye et al., 1996) is comparable to that of the poleward EICC during February–May.

These hydrographic data also suggest the presence of an undercurrent (Shetye et al., 1991c, 1993, 1996) and recirculations or eddies associated with the EICC (Shetye et al., 1991c, 1993, 1996; Sanilkumar et al., 1997; Ali et al., 1998; Gopalan et al., 2000; Babu et al., 2003), but the resolution of the hydrographic data in time and space, particularly in the horizontal, make it difficult to interpret the signatures (Shetye et al., 1991c, 1993).

Reference	Location	Period (months)	Transport estimates in Sv ($10^6 m^3 s^{-1}$)
Shetye et al. (1991c)	10°N–20°N	July–August 1989	1 Sv poleward across 13°N.
Shetye et al. (1993)	10°N–20°N	March–April 1991	10 Sv poleward.
Murty et al. (1993)	12°N	April, September, and November 1997	3.25 Sv poleward during April, 3.16 Sv poleward during September, 6.64 Sv equatorward during November.
Shetye et al. (1996)	10°N–20°N	December 1991	7.7 Sv equatorward across 13°N
Sanilkumar et al. (1997)	10°N–20°N	9–23 March 1993	3–17 Sv poleward from 10°N to 18°N. At 14°N 3 Sv equatorward.
Babu et al. (2003)	12°N–20°N	22 March to 28 April 1987	12 Sv poleward.

Table 2.1: *Transport estimates of the EICC from hydrographic data.*

2.2 Theoretical studies

The hydrographic data collected in the Indian Exclusive Economic Zone (EEZ) during 1987–1994 (Shetye et al., 1990, 1991b,c, 1993, 1996) filled a major gap in our description of the EICC and WICC, permitting theoretical studies that aimed at explaining the observed seasonal cycle. Shetye and Shenoi (1988) and Shetye et al. (1993) used the Sverdrup theory (Sverdrup, 1947; Stommel, 1948) to estimate the EICC transport due to the Ekman-pumping field over the BoB, but a key drawback of this computation was the use of steady-state equations for a circulation whose seasonal cycle is stronger than the mean. Early numerical-modelling studies, which built on similar results from the Pacific (see, for example, Wyrtki, 1975; McCreary, 1976; Hurlburt et al., 1976) and Atlantic (see, for example, O'Brien et al., 1978; Picaut, 1983; McCreary et al., 1984) Oceans, showed that the winds over the EIO could have a significant impact on the circulation in the BoB, including the EICC, owing to long, baroclinic waves (Potemra et al., 1991; Yu et al., 1991). A comprehensive study of the dynamics of the Indian Ocean by McCreary et al. (1993) showed the importance of remote forcing from the EIO for the seasonal cycle of the EICC. A detailed analysis of the forcing mechanisms of the EICC was carried out by Shankar et al. (1996) and McCreary et al. (1996), who used LCS model to show that four dynamical processes contributed to the seasonal variation. Apart from the local alongshore winds and Ekman

pumping over the BoB, they showed that the winds over the EIO and the winds along the eastern boundary of the BoB (called "remote alongshore winds" by McCreary et al. (1996)) also contribute to forcing the observed EICC. All four mechanisms were noted to be important, with their relative contributions changing with time (McCreary et al., 1996). An analysis using an OGCM by Vinayachandran et al. (1996) led to similar results. These model simulations show that the reversal in current direction north of $\sim$ 18°N during the summer monsoon and off the east coast of Sri Lanka over most of the year is due to the variation in the amplitude of these forcing mechanisms during the year. For example, the equatorial winds, the remote alongshore winds in the eastern BoB (EBoB), and interior Ekman pumping force an equatorward EICC and it is only south of $\sim$ 18°N that the poleward EICC forced by the local alongshore winds is able to overcome this equatorward current during the summer monsoon (McCreary et al., 1996).

In all these models, the mechanisms for communicating the signal from the source, or forcing, region to remote locations were three long, baroclinic waves: the equatorial Rossby wave, the equatorial Kelvin wave, and the coastal Kelvin wave. The reflection of the equatorial Kelvin wave at the eastern boundary off Sumatra generates an infinity of meridional modes associated with the equatorial Rossby wave (Moore, 1968), but only the low-order modes have a real wavenumber and therefore constitute propagating Rossby modes. The high-order modes have an imaginary componnent in the zonal wavenumber, leading to evanescent waves that decay westward. Moore (1968) showed that these evanescent waves are identical to a β-plane coastal Kelvin wave poleward of the critical latitude, allowing energy to be carried away from the equatorial waveguide. Equatorward of the critical latitude, which occurs poleward of, or close to, the northern boundary of the BoB for the first baroclinic mode at the annual and semi-annual periods, the Rossby wave propagates into the interior of the BoB, allowing the equatorial winds to influence the seasonal cycle of circulation throughout the BoB. The Rossby wave propagates westward across the BoB, affecting

the EICC (Potemra et al., 1991; Yu et al., 1991; McCreary et al., 1993, 1996; Clarke and Liu, 1994; Vinayachandran et al., 1999); similar Rossby waves can be triggerred in the BoB by Ekman pumping (or wind curl) as well (Shetye and Shenoi, 1988; Shetye et al., 1993; Shankar et al., 1996; McCreary et al., 1993, 1996; Vinayachandran and Yamagata, 1998). The winds local to the east coast of India (and Sri Lanka) and the remote alongshore winds trigger coastal Kelvin waves (McCreary et al., 1993, 1996; Shankar et al., 1996), which propagate with the coast on their right in the northern hemisphere. Furthermore, the huge freshwater inflow into the BoB from rivers and rainfall implies a role for freshwater fluxes in forcing the seasonal geostrophic circulation in the WBoB (Sprintall and Tomczak, 1992; Shetye et al., 1993, 1996; Shankar, 1998, 2000; Shankar and Shetye, 1999, 2001; Han et al., 2001c; Han and McCreary, 2002; Han and Webster, 2002; Vinayachandran et al., 2002; Vinayachandran and Kurian, 2007; Wu et al., 2007).

The distance between the southern tip of Sri Lanka and the EIO ($\sim 6°$) exceeds the sum of the length scales for the gravest vertical (baroclinic) mode for the equatorial wave guide ($\sim 3°$) and the coastal wave guide south of the island ($\sim 2.5°$), permitting the passage of coastal Kelvin waves from the east to the west coast of India (Shankar et al., 2002), thereby affecting the WICC and linking the dynamics of the eastern Arabian Sea to that of the BoB and the EIO (McCreary et al., 1993; Shankar and Shetye, 1997; Bruce et al., 1994, 1998; Schott and McCreary, 2001; Shankar et al., 2002).

2.3 Satellite altimetry

The problem of space-time aliasing of the time-dependent circulation of the BoB in hydrographic data was ameliorated by satellite altimetry, which provides a quasi-synoptic view of the basin-scale circulation, permitting an analysis of the relationship between the EICC and the circulation in the rest of the BoB (Ali et al., 1998; Eigenheer and Quadfasel, 2000; Gopalan et al., 2000; Shankar et al., 2002; Gangopadhyay et al., 2013). The altimeter data

confirm that recirculations and eddies are part of the WBC system in the BoB. The altimeter data also permit an analysis of the EICC variability on time scales longer and shorter than the seasonal cycle.

At interannual time scales, the EICC is influenced by NSO (El Niño–the Southern Oscillation) and IOD (Indian Ocean Dipole) (Saji et al., 1999; Webster et al., 1999), the two major climate modes of the Indian Ocean (Clarke and Liu, 1994; Rao et al., 2002; Han and Webster, 2002; Srinivas et al., 2005; Jensen, 2007; Rao et al., 2009; Schott et al., 2009; Aparna et al., 2012). Using monthly-mean tide-gauge data, Clarke and Liu (1994) suggested that the interannual EICC would be coherent along the coast, but this inference was shown to be incorrect by Durand et al. (2009), who used altimeter data to show that it is decorrelated along the coast. One possible explanation for this alongshore decorrelation at interannual time scales, for which the length scales are expected to be large, was given by Shankar et al. (2010), who pointed to the existence of both minima and maxima of interannual variability along the WBoB. The minima (maxima) occurred along the southern (northern) part of the boundary, implying that the circulation at these time scales would not be correlated in these coastal stretches. This decorrelation can show up as eddies or recirculations, which have also been indentified in the altimeter data at interannual time scales (Durand et al., 2009; Chen et al., 2012).

Durand et al. (2009) noted that a similar alongshore decorrelation of the EICC occurred at intraseasonal time scales as well, but this decorrelation was attributed to the existence of eddies along the EICC path and the greater downward bending of the energy expected at these short time scales (Romea and Allen, 1983; Nethery and Shankar, 2007). Intraseasonal eddies associated with the EICC have received considerable attention in recent times (Durand et al., 2009; Kurian et al., 2010; Nuncio and Kumar, 2012; Cheng et al., 2013).

2.4 Direct current measurements

A major stumbling block in describing the intraseasonal variability of the EICC is the paucity of direct current measurements, which started only in the 1980s off the Indian east coast. A summary of these observations, which ranged from a day to a few weeks, is provided in Table 2.2. All these observations (Rao, 2004; Sarma and Rao, 1986; Chinthalu et al., 2002; Joseph et al., 2006; Sanilkumar et al., 2008; Mishra et al., 2011) are restricted to short durations and to the near-shore waters, precluding even a description of the seasonal EICC.

Period	Reference	Location/ Duration	Max. velocity/ Water column depth	Remarks
1 day	Rao (2004)	Central east coast (13°N–20°N)	37 cm s^{-1} / surface (shelf)	Variation in current along inner shelf off the east coast of India.
< 1 month	Sarma and Rao (1986, 1989)	Off river Godavari, 16.5°N/ 5 days (24-28 September 1980)	45.7 cm s^{-1} / 15 m (shelf)	Observational evidence of semidiurnal tides, internal waves.
	Chinthalu et al. (2002); Joseph et al. (2006)	North BoB, 16°N and 19°N/ 11 days (20-30 September 1997)	60 cm s^{-1} / 3 m (slope)	Current structure before and after the 1997 cyclone near Bangladesh.
≥ 1 month	Sanilkumar et al. (2008)	Off Yanam, 16.5°N / 40 days (August-October 2005)	54.5 cm s^{-1} / 5 m (shelf)	Current measurement after passage of cyclone.
	Mishra et al. (2011)	Gopalpur, 19°N / 97 days (May-August 2008)	74.5 cm s^{-1} /surface (shelf)	Impact of currents on beach profiles.
	Mukherjee et al. (2013)	Along east coast of India, 19°N-12°N / 3 years (May 2009 to February 2012)	160 cm s^{-1} / 40 m (slope)	Inertial currents on shelf and slope.

Table 2.2: List of major direct current measurements along the east coast of India. The estimated maximum velocity is listed in the fourth column.

2.5 Summary

In summary, the observations from the hydrography and ship-drift provide a climatological and seasonal perspective of the EICC. Using altimeter data, intraseasonal variability of the EICC can be measured. However, the altimeter data, cannot resolve satisfactorily periods shorter than a fortnight and are also restricted to providing estimates of the surface current. Direct current measurements were very few and also with short time duration, precluded any description of the intraseasonal or seasonal EICC.

A detailed description of the current measurements using long–term ADCPs off the east India of India and performance of an OGCM in simulating these observations are discussed in the later chapters of this thesis.

Chapter 3

Near-Inertial currents

In this chapter, we describe the EICC at near-Inertial periods, which are near the high frequency end of the intraseasonal part of the spectrum. Along with estimation of observed inertial periods (which may vary compared to theory (Kundu, 1976)), we have also analyzed seasonal and interannual variability of the near–Inertial currents. Here, we have used both shelf and slope ADCPs because the short duration of the continental shelf data ($<$ $\sim$one year) are also sufficient for describing inertial-current variability.

3.1 Introduction

Near-Inertial currents (NICs) are commonly observed in the ocean (Webster, 1968; Fu, 1981). They are generated by bursts in the wind, the generation being most efficient if the wind blows for half the local inertial period (Pollard, 1970; Jarosz et al., 2007). The current accelerates downwind, but turns clockwise (anticlockwise) in the northern (southern) hemisphere owing to the earth's rotation (Vandenbrouck et al., 2000). This difference in the clockwise and anticlockwise parts of the spectra shows a peak only in the vicinity of the inertial frequency f (Fu, 1981). The dominance of the clockwise part of the spectrum over the anticlockwise part starts at sub-Inertial periods, reaches a maximum near f, and decays

at supra–Inertial frequencies (Fu, 1981).

NICs have been observed in all parts of the ocean, whether it be the deep ocean (Gregg and Kunze, 1991; Zhai et al., 2005; Mori et al., 2005), the surface layers of the ocean interior away from continental boundaries (Leaman and Sanford, 1975; Haren et al., 1999), or the continental slope (Chen et al., 1996; Jarosz et al., 2007; Aken et al., 2005) or shelf (Huthnance, 1981; Shearman, 2005). In the Indian Ocean, however, the dearth of current measurements implies that studies of NICs are limited. They have been observed in drifting-buoy data in the South Indian Ocean (Shetye and Michael, 1988) and over most of the NIO (Saji et al., 2000). NICs have been observed in current-meter data from the BoB (Joseph et al., 2007) and the AS (Rao et al., 1996), and on the continental shelf off the Indian west coast (Shenoi and Antony, 1991).

A problem with the Indian-Ocean NICs studies is that they are based on short records (duration less than a month) (Shenoi and Antony, 1991; Rao et al., 1996) or deal with a specific event, typically the NICs excited by one storm (Joseph et al., 2007). These short records do not permit an analysis of the variability in both time and space. Specifically, is there a seasonality in the generation of NICs? Given the strong seasonality in the monsoon winds over the NIO, it is likely that the NICs show a strong seasonal variability. Likewise, are there spatial variations in the generation of NICs? For example, if we consider, say, the east coast of India (Figure 1.2), is the generation of NICs coherent along the coast, or does it vary along the coast? How important is the contribution of the NICs to the total current? Is there any difference between the theoretical and observed inertial period?

The chapter is organized as follows. The data and spectral analysis are presented in Section 3.2. The NICs on the shelf and slope are described in Section 3.3. Impact of storms and vertical propagation of NIC is discussed in Section 3.4. A comparison of observed NIC with a simple slab model is discussed in Section 3.5. Details sumary of NIC is discussed in Section 3.6.

3.2 Data

We have used all nine upward-looking ADCPs moorings on the continental shelf and slope along east coast of India (Figure 1.2, Table 1.1). On the slope, the bottom mounted ADCPs were located at a depth of $\sim$ 300–400 m from the surface, implying a loss of data in the top 30–40 m; these slope moorings were deployed in a water-column depth of $\sim$ 1100 m. On the shelf, the ADCPs were deployed just off the ocean bottom at a water-column depth of $\sim$ 100 m.

The slope (shelf) ADCPs had a frequency of 75 kHz (300 kHz) and recorded data at an interval of one hour (15 or 30 minutes). The accuracy of the velocity measurement was better than 1.8 cm s^{-1}. Data gaps in depth and time were filled using the method of Kutsuwada and McPhaden (2002). The tidal component of the current was removed using the Tidal Analysis Software Kit (TASK-2000) (Bell et al., 1998). A one-month control file was used to eliminate the tidal components with period less than a month. The de-tided currents were rotated by minimizing the cross-shore component below 100–150 m using a least-square approach; above this depth, the cross-shore component was often strong and could not be used to decompose the velocity field. Details of angle of rotation are given in Table 3.1.

The sign convention used is that the upwelling-favorable current is positive; the positive current is therefore poleward at Cuddalore, Kakinada, and Gopalpur and eastward at Paradip. In the description that follows, we use the terms spring, summer monsoon, and winter to refer to the periods February–April, June–August, and October–December, respectively. This distinction is based on the earlier literature and supported by the ADCP data; January, May, and September represent the transition between these seasons.

Mooring Location	Mooring Type	Angle of rotation (°)
Paradip	Slope	90
Gopalpur	Shelf	54
-do-	Slope	56
Kakinada	Shelf	45
-do-	Slope	42
Ramyapatnam	Shelf	27
-do-	Slope	24
Cuddalore	Shelf	27
-do-	Slope	30

Table 3.1: Angle of rotation at ADCPs observed locations. This angle is based on clockwise rotation of the meridional velocity.

3.3 NICs on the continental shelf and slope

We used the wavelet transform approach to obtain the spectra. Clockwise and anticlockwise components of the rotary spectra were calculated using the method of Paul and Miller (1996), and the wavelet transform of the velocity was converted as the sum of clockwise and anticlockwise components in time-frequency space. This analysis was applied to vertical averages of the current; the average was computed over a depth range of 40–250 m (20–80 m) on the slope (shelf).

At the northern hemisphere, inertial current rotate clockwise. So, as expected, the clockwise spectrum dominated over the anticlockwise spectrum in the neighborhood of the inertial frequency on the slope (Figure 3.1), indicating the existence of NICs.

On the shelf, the difference between the clockwise and anticlockwise spectra was much smaller (Figure 3.1), indicating weak generation of NICs on the east-coast shelf. Weak signatures of NICs were evident only off Ramayapatnam and Gopalpur. Similar results were obtained without vertical averaging: off the Indian east coast, NICs are weak on the shelf and strengthen offshore.

On the continental slope, the NICs is strongest off Paradip and weakest off Cuddalore.

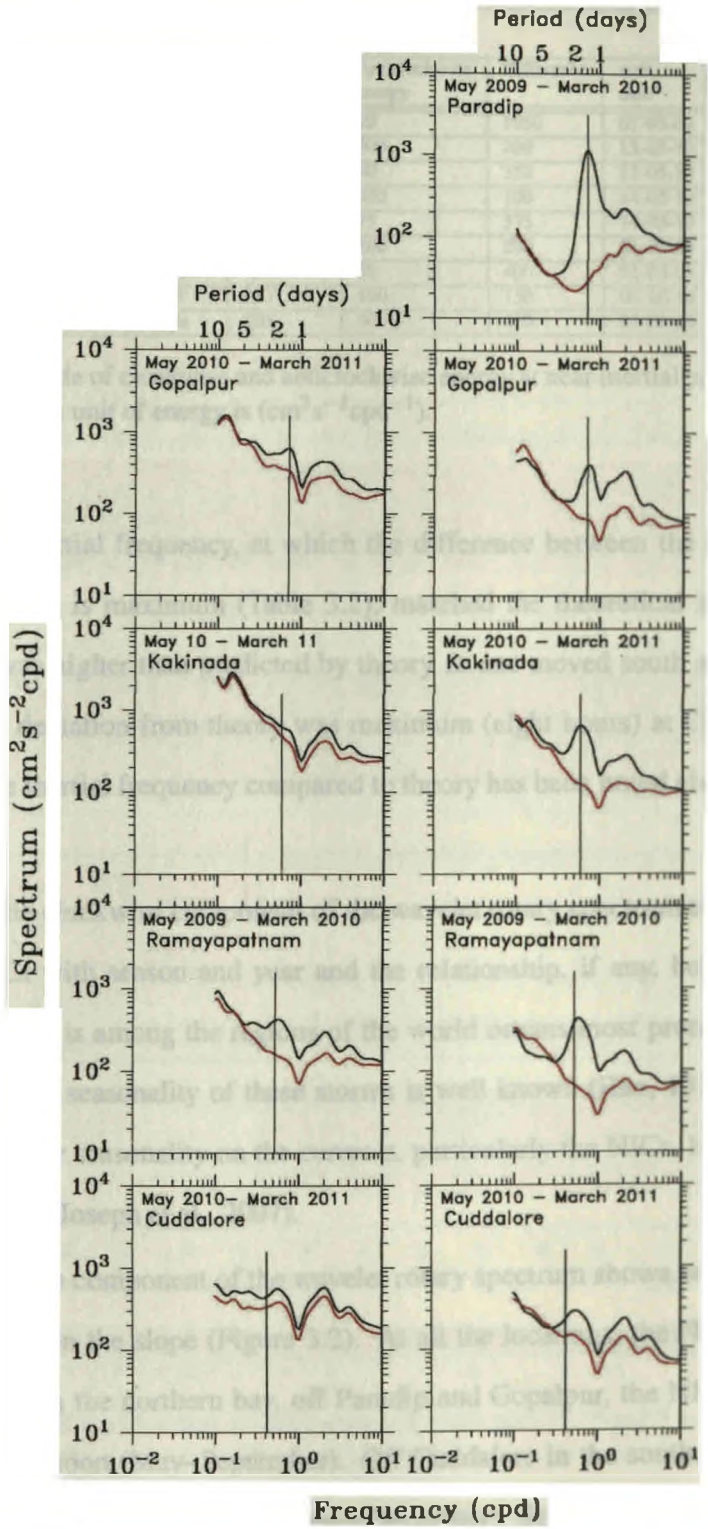

Figure 3.1: Clockwise (black) and anticlockwise (dashed line) rotary spectra (vertically averaged) of detided current for all locations. The vertical line indicates the theoretical inertial period ($T = \frac{2\pi}{f}$, where $f = 2\omega \sin\phi$; ω is the angular frequency of rotation of the earth and ϕ is the latitude) at the location. On the shelf (left panels), the data were vertically averaged over 20–80 m to compute these spectra; on the slope (right panels), the data were vertically averaged over 40–250 m.

Mooring Location	Mooring Type	Clockwise energy	Anticlockwise energy	Difference	start date	end Date
Paradip	Slope	1100	50	1050	01-05-09	31-03-10
Gopalpur	Shelf	600	400	200	13-05-10	19-03-11
-do-	Slope	400	50	350	13-05-10	19-03-11
Kakinada	Shelf	600	500	100	14-05-10	26-03-11
-do-	Slope	650	75	575	14-05-10	26-03-11
Ramayapatnam	Shelf	400	200	200	01-05-09	26-03-10
-do-	Slope	450	50	400	01-05-09	26-03-10
Cuddalore	Shelf	550	400	150	01-05-10	22-03-11
-do-	Slope	300	50	250	01-05-10	22-03-11

Table 3.2: Magnitude of clockwise and anticlockwise energy at near inertial periods for all shelf and slope locations. The unit of energy is ($cm^2s^{-2}cpd^{-1}$).

The observed inertial frequency, at which the difference between the clockwise and anticlockwise spectra is maximum (Table 3.2), matched the theoretical inertial frequency at Paradip, but was higher than predicted by theory as one moved south along the coast (Figure 3.1). The deviation from theory was maximum (eight hours) at Cuddalore. A similar increase in the inertial frequency compared to theory has been noted elsewhere too (Kundu, 1976).

We used the clockwise component of the wavelet rotary spectrum to determine the variability of NICs with season and year and the relationship, if any, between the NICs and storms. The BoB is among the regions of the world oceans most prone to cyclonic storms (Gray, 1967); the seasonality of these storms is well known (Rao, 1976), but the effect of the storms or their seasonality on the currents, particularly the NICs, has been studied only in isolated cases (Joseph et al., 2007).

The clockwise component of the wavelet rotary spectrum shows seasonality in the generation of NICs on the slope (Figure 3.2). At all the locations, the NICs are weak during January–April. In the northern bay, off Paradip and Gopalpur, the NICs are strong during the summer monsoon (May–September). Off Cuddalore in the south, the NICs are strong only during the winter monsoon (October–December). Seasonality is weaker in the central bay, off Kakinada and Ramayapatnam, with NICs being generated during both summer and winter monsoons.

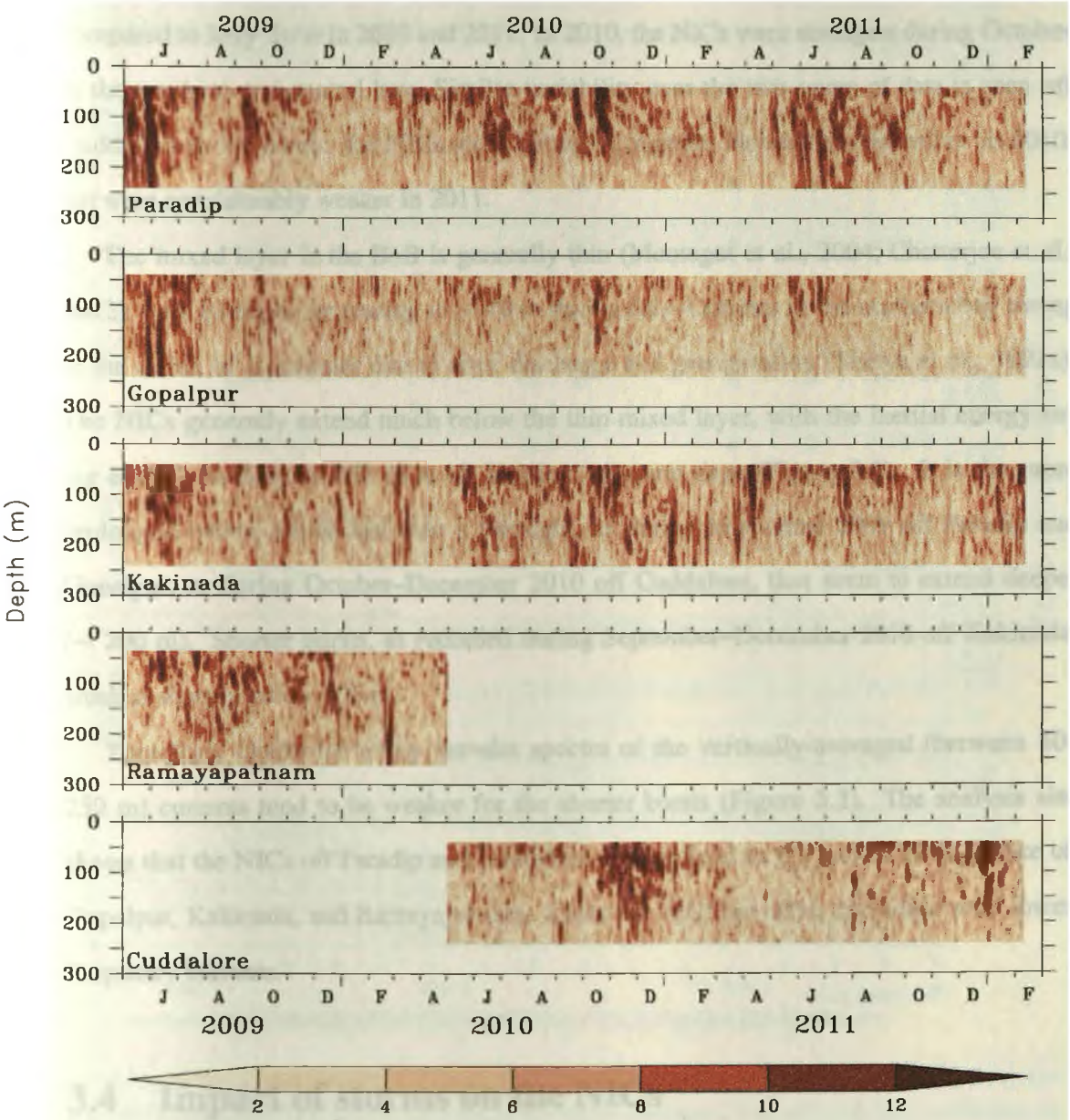

Figure 3.2: The clockwise component of the rotary spectrum ($cm^{-2}s^{-2}cpd^{-1}$) at the inertial period as a function of depth and time at all locations on the slope.

The data also show interannual variability in the generation of NICs. Off Paradip, Gopalpur, Kakinada, and Ramayapatnam, NICs were much stronger during May–June 2009 compared to May–June in 2010 and 2011. In 2010, the NICs were strongest during October in the northern and central bay. Similar variability over the two years of data is seen off Cuddalore in the south: the NICs were strong throughout November–December in 2010, but were considerably weaker in 2011.

The mixed layer in the BoB is generally thin (Montegut et al., 2004; Chatterjee et al., 2012), with its depth decreasing to $\sim$ 10 m during July–October in the northern bay owing to the influx of freshwater due to river discharge and precipitation (Shetye et al., 1991a). The NICs generally extend much below the thin mixed layer, with the inertial energy being evident as deep as 250 m at all locations at some time (Figure 3.2). It is the more prolonged bursts, which last over a fortnight, as during May–June 2009 off Paradip and Gopalpur, or during October–December 2010 off Cuddalore, that seem to extend deeper ($\sim$ 200 m). Shorter bursts, as recorded during September–December 2010 off Kakinada, weaken sharply below 100 m.

Therefore, clockwise rotary wavelet spectra of the vertically-averaged (between 40–250 m) currents tend to be weaker for the shorter bursts (Figure 3.3). The analysis also shows that the NICs off Paradip and Cuddalore are confined to the inertial band, unlike off Gopalpur, Kakinada, and Ramayapatnam, where the NICs are often associated with lower-frequency currents.

3.4 Impact of storms on the NICs

Is the seasonality observed in the generation of NICs related to the seasonality of storms over the BoB? It is known that storms, particularly depressions, are common in the northern BoB during the summer monsoon (Rao, 1976), when strong NICs are observed at the northern locations. During winter, the storms occur in the south (Rao, 1976; Gray, 1967), as do the

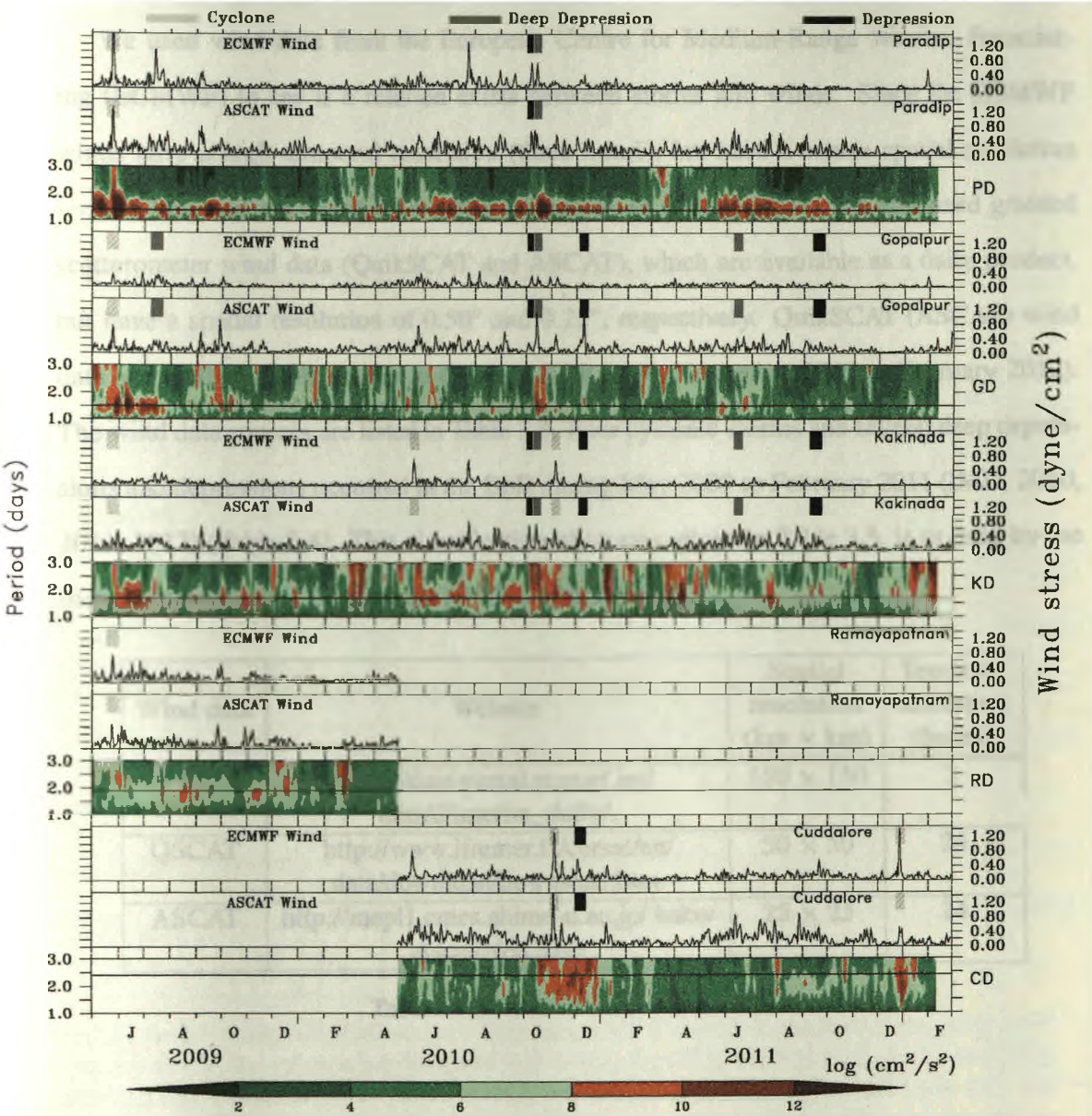

Figure 3.3: Four-day high-passed wind stress and clockwise wavelet rotary spectra (vertically averaged over 40–250 m) as a function of time for all the slope locations. The value of drag coefficient is based on Han and Webster (2002). Clockwise wavelet rotary spectra is plotted in every third panel from top. The classification of low–pressure systems into cyclones, deep depressions, and depressions is based on the reports of the India Meteorological Department (IMD, 2010, 2011, 2012). The black horizontal line indicates the theoretical inertial period at the location.

NICs.

We used wind data from the European Centre for Medium-Range Weather Forecasting (ECMWF) to see if a relation exists between storms and winds. Since the ECMWF winds have a high temporal resolution (three hours), but have a coarse spatial resolution ($\sim$ 150 km) and are based on a model reanalysis (Kallberg, 1997), we also used gridded scatterometer wind data (QuikSCAT and ASCAT), which are available as a daily product, but have a spatial resolution of 0.50° and 0.25°, respectively. QuikSCAT (ASCAT) wind data are used from May 2009 to October 2009 (from November 2009 to February 2012). The wind data sources are listed in Table 3.3. Four cyclonic storms and several deep depressions and depressions occurred in the BoB during May 2009 to February 2011 (IMD, 2010, 2011, 2012) (Table 3.4). This classification of storms, given in Table 3.5, is as used by the India Meteorological Department (IMD) (WMO, 2010).

Wind data	Website	Spatial resolution (km × km)	Temporal resolution (hours)
ECMWF	http://data-portal.ecmwf.int/ data/d/interim_daily/.	150 × 150	3
QSCAT	http://www.ifremer.fr/cersat/en/ data/download/download.htm.	50 × 50	24
ASCAT	http://mepl1.cmes.ehime-u.ac.jp/ kako/ Ascat/NetCDF/	25 × 25	24

Table 3.3: Details of wind-data sources.

The first cyclone, *Aila*, occurred in the northern bay during 23–25 May 2009 (Figure 3.4). *Aila* was a severe, destructive cyclone (IMD, 2010) and generated the strongest inertial currents during 2009–2012 in the bay (Figure 3.3). Since the maximum pressure drop (968 hPa) and the strongest winds during *Aila* were observed over the northern bay (Figure 3.4, Table 3.4), the strongest NICs were generated off Paradip and Gopalpur. The NICs continued even after the cyclone had crossed over land and were strongest immedi-

Cyclone/Storm	Cyclone genesis			Lowest pressure			wind speed		
	Start time	Position Lon. (°E)	Position Lat. (°E)	Mag. (hPa)	Position Lon. (°E)	Position Lat. (°N)	Mag. (kt)	Position Lon. (°E)	Position Lat. (°N)
Severe cyclonic storm *Aila* during 23–26 May 2009	0600	88.0	16.5	968	88.0	22.0	60	88.0	22.0
Deep depression during 20–21 Jul 2009	0300	88.5	21.0	988	88.0	21.0	30	88.0	21.0
Deep depression during 05–07 Sep 2009 Sep 2009	0000	88.0	20.5	988	87.5	21.0	30	87.5	21.0
Severe cyclonic storm *Laila* during 17–21 May 2010	0600	88.5	10.5	986	81.5	13.5	55	81.5	13.5
Depression during 07–09 Oct 2010	0300	84.5	16.5	996	85.5	18.5	25	85.5	18.5
Deep depression during 13–16 Oct 2010	0600	90.0	17.5	995	85.5	19.5	30	85.5	19.5
Severe cyclonic storm *Jal* during 04–08 Nov 2010	0000	92.0	8.0	988	84.5	11.0	60	84.5	11.0
Depression during 07–08 Dec 2010	0300	82.0	14.0	1000	82.0	14.0	25	82.0	14.0
Depression during 22–23 Sep 2011	0300	87.5	21.5	995	87.2	21.7	25	87.2	21.7
Deep depression during 19–20 Oct 2011	0000	90.5	20.0	1000	92.0	21.0	30	92.0	21.0
Severe cyclonic storm *Thane* during 25–31 Dec 2011	1200	88.5	8.5	972	80.6	12.0	75	80.6	12.0

Table 3.4: Details of storms, cyclones, and depressions that formed over the BoB during May 2009 to February 2012. The information presented here is based on IMD (2010), IMD (2011), and IMD (2012). The IMD classification of storms is based on the maximum wind speed (see Table 3.5). All times listed are in UTC (Indian Standard Time, or IST, is 5.5 hours ahead of UTC), wind speed is in nautical miles per hour (knots; 1 kt is 0.5 m s^{-1}.), and pressure in hpa (1 hPa is 100 pascals). Note that the time in the ADCP figures is in IST.

Weather system	Maximum wind speed (kt)
Low-pressure system	≤ 16
Depression	17–27
Deep depression	28–33
Cyclonic storm	34–47
Severe cyclonic storm	48–63
Very severe cyclonic storm	64–119
Super cyclonic storm	≥ 120

Table 3.5: IMD classification of storms. The maximum wind speed, used as the basis for classification, is given in knots (1 knot equals 0.5 m/s.) This table is based on WMO (2010).

ately following it (Figure 3.3). Note that the maximum pressure drop occurred as the cyclone crossed land (Figure 3.4). The winds were much weaker off Kakinada and the NICs here followed the cyclone, rather than occurring during its passage.

The second cyclone, *Laila*, was weaker (Table 3.4) and occurred during 17–20 May 2010; the maximum pressure (986 hPa) drop during *Laila* occurred in the central bay and the strongest NICs were therefore generated off Kakinada. (The effect of *Laila* must have been felt off Cuddalore as well, but the first mooring was deployed here shortly after the passage of the cyclone.)

The third cyclone, *Jal*, occurred during 4–8 November 2010. It was weaker than the earlier storms (Table 3.4) and its effect was restricted to the southern and central bay (Figure 3.4). Strong NICs were observed off Cuddalore and Kakinada (Figure 3.3).

The fourth cyclone, *Thane*, occurred during 25–31 December 2011 and was comparable to *Laila* (Table 3.4, Figure 3.4). Its effect was restricted to the southern bay, with NICs being generated off Cuddalore. Off Kakinada in the central bay, the currents generated at this time had a higher period ($\sim$ 3 days) than the NICs (Figure 3.3).

Apart from these four cyclones, there were several depressions and deep depressions during 2009–2012 (Table 3.4). NICs were generated during each of these events (Figure 3.3). Since these storms occur over the northern bay during the summer monsoon and the southern bay during the winter monsoon, the central bay is affected during both sea-

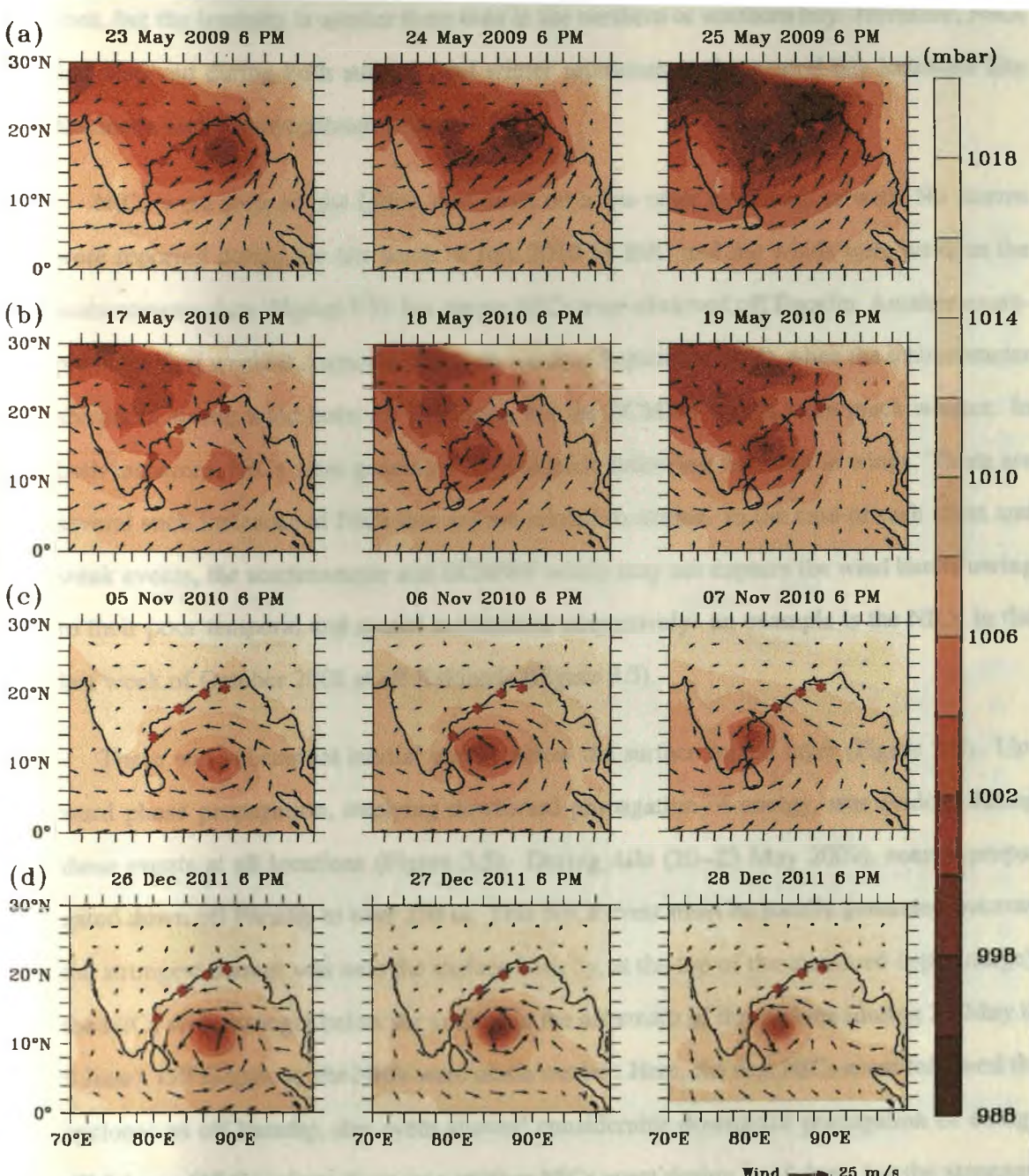

Figure 3.4: Sea-surface pressure and wind velocity vectors for the four cyclones that formed in the region during May 2009 to February 2012: (a) *Aila*, (b) *Laila*, (c) *Jal*, and (d) *Thane*. ECMWF wind velocity vectors are plotted over the atmospheric pressure at mean sea level. The red circles denote the mooring locations.

sons, but the intensity is weaker there than in the northern or southern bay. Therefore, NICs are observed during both summer and winter monsoons at the central-bay locations like Kakinada and Ramayapatnam (Figure 3.3).

NICs were seen off the Indian east coast on a few other occasions as well. No storms were reported during the last week of July 2010 by IMD and the winds were weak in the scatterometer data (Figure 3.3), but strong NICs were observed off Paradip. Another example is the first week of August and the last week of September 2010, when the scatterometer showed a strong wind burst off Kakinada, but the ECMWF winds were much weaker. In both instances, NICs were generated off Kakinada following the burst in winds. There are several such instances of NICs that are not related to storms. In the case of such short and weak events, the scatterometer and ECMWF winds may not capture the wind bursts owing to their poor temporal and spatial resolutions, respectively: an example is the NICs in the last week of October 2009 at off Kakinada (Figure 3.3).

There was substantial inertial energy below the surface mixed layer (Figure 3.2). Upward phase propagation, implying downward propagation of energy, was evident during these events at all locations (Figure 3.5). During *Aila* (20–23 May 2009), energy propagated down off Paradip to over 250 m. This NICs event must be locally generated because the strongest current was near the surface (strictly, at the top of the measured depth range); the NICs were stronger below the surface in the aftermath of the cyclone (during 25 May to 5 June). Off Gopalpur, the NICs were much weaker. Here, the first NICs event followed the cyclone; as off Paradip, this event showed considerable downward propagation of energy till 5 June. Off Gopalpur, there was another NICs event during 7–15 June, but the strongest currents during this period occurred at depths below 100 m, suggesting that the NICs were generated elsewhere. Downward energy propagation was evident in the ADCP data from all mooring locations during other storms as well; an example is shown for Kakinada and Cuddalore during cyclone *Jal* (Figure 3.5).

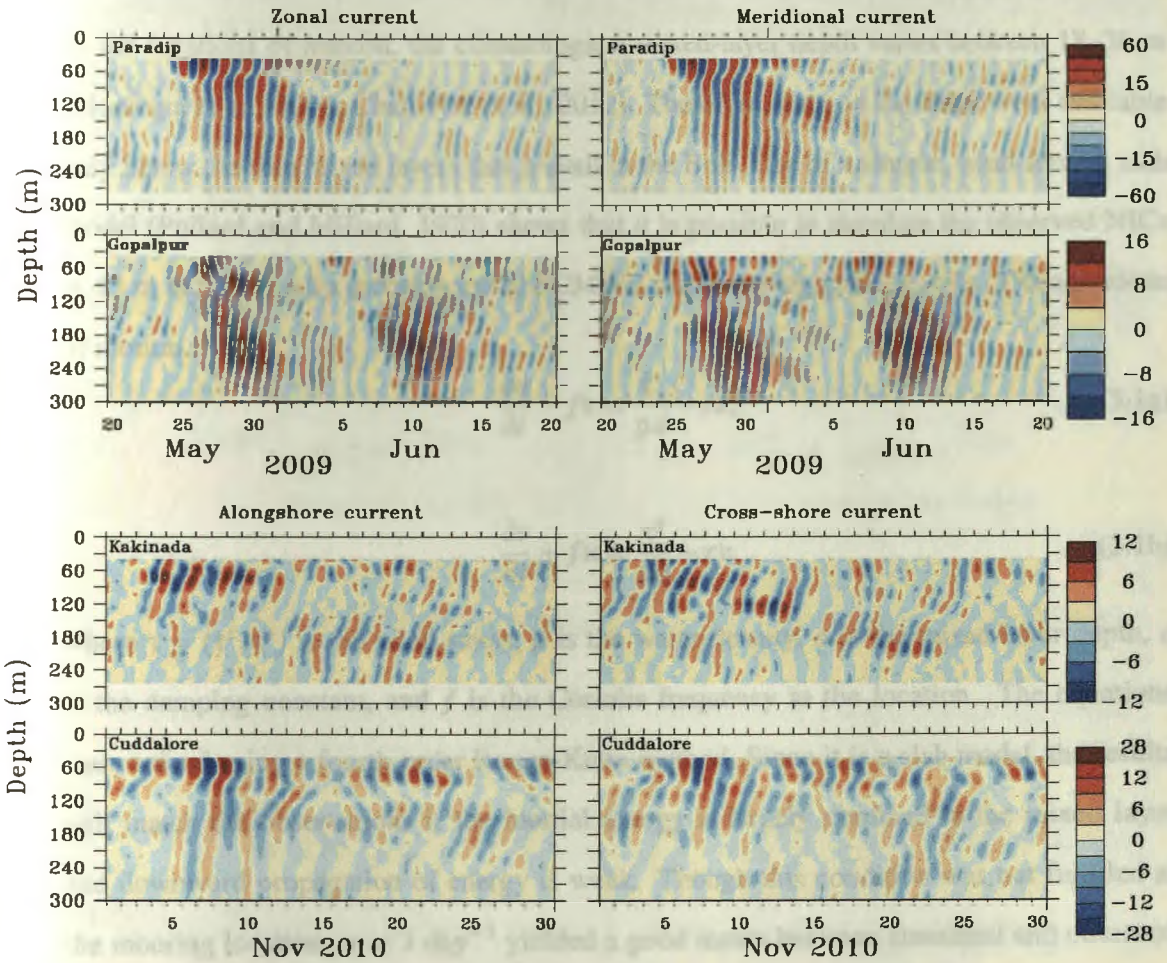

Figure 3.5: Upward phase propagation at the period of the NICs during severe storms. NICs are plotted as a function of depth and time during cyclone *Aila* at Paradip (first row) and Gopalpur (second row), and during cyclone *Jal* at Kakinada (third row) and Cuddalore (fourth row).

3.5 NICs in a simple slab model

At the locations of interest, the climatological mixed-layer depth varies between 18–30 m (Montegut et al., 2004; Chatterjee et al., 2012). Therefore, data on the slope were available only below the thin mixed layers that prevail in the BoB. Use of a simple, wind-forced, slab model (Pollard and Millard, 1970) shows that it is possible to simulate the observed NICs at 40 m at the Paradip mooring using ECMWF winds during cyclone *Aila*. The equations of motion are

$$\frac{\partial u}{\partial t} - fv = \frac{\tau^x}{\rho a} - cu; \tag{3.1a}$$

$$\frac{\partial v}{\partial t} + fu = \frac{\tau^y}{\rho a} - cv, \tag{3.1b}$$

where $\tau = (\tau^x, \tau^y)$ is the wind stress, ρ is the water density, a is the mixed-layer depth, c is the damping constant, and f is the Coriolis frequency at the location. The equations were solved using a fourth-order Runga-Kutta method. Since it is a slab model, the results will match the observations if the inertial energy is largely confined to the mixed layer and downward propagation of energy is weak. Though this condition was not fulfilled at the mooring locations, $c = 1$ day^{-1} yielded a good match between simulated and observed currents during cyclone *Aila* (Figure 3.6). The simulated current is valid only in the mixed layer and the observation is most likely to be below the mixed layer, suggesting that the match is likely to be due to the impact of the strong *Aila* winds extending below the mixed layer. The match was not as good at Gopalpur ($c = 2$ day^{-1}), where the NICs are weaker, and was poor at Kakinada ($c = 2$ day^{-1}) and Cuddalore ($c = 2$ day^{-1}) during cyclone *Jal* (Figure 3.6). Though this exercise is qualitative, it suggests that the NICs may extend even below the thin mixed layers in the BoB during severe storms.

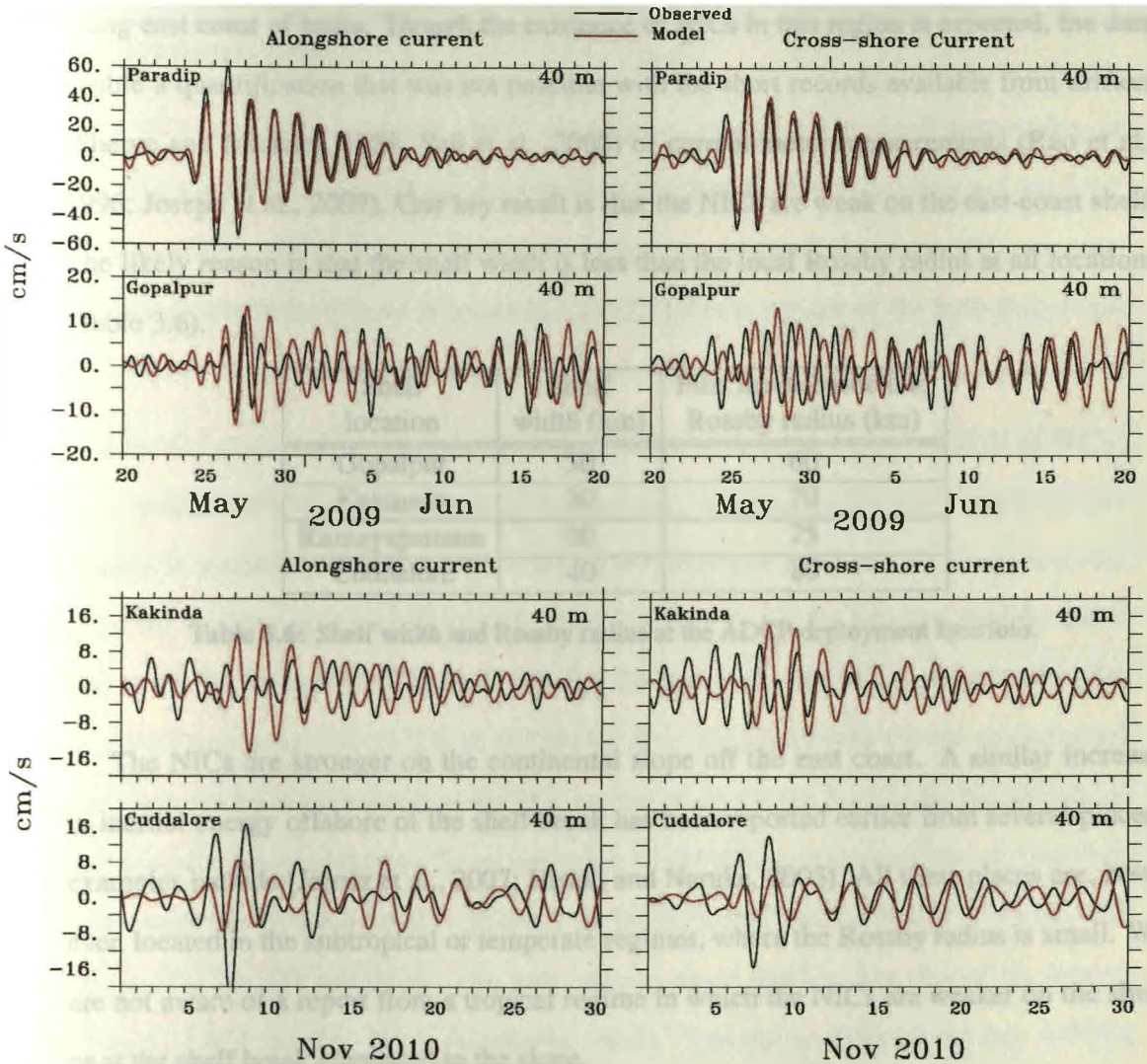

Figure 3.6: Comparison of observed (black) and simulated (dashed line) inertial currents at 40 m depth. Alongshore (left panels) and cross-shore (right panels) components of the NICs are plotted as a function of depth and time during cyclone *Aila* at Paradip (first row) and Gopalpur (second row), and during cyclone *Jal* at Kakinada (third row) and Cuddalore (fourth row).

3.6 Summary and discussion

We have used ADCP data from nine moorings to document the NICs in coastal waters along east coast of India. Though the existence of NICs in this region is expected, the data enable a quantification that was not possible with the short records available from drifters (Shetye and Michael, 1988; Saji et al., 2000) or current-meter measurements (Rao et al., 1996; Joseph et al., 2007). One key result is that the NICs are weak on the east-coast shelf. The likely reason is that the shelf width is less than the local Rossby radius at all locations (Table 3.6).

Shelf location	Shelf width (km)	First mode baroclinic Rossby radius (km)
Gopalpur	50	60
Kakinada	30	70
Ramayapatnam	60	75
Cuddalore	40	80

Table 3.6: Shelf width and Rossby radius at the ADCP deployment locations.

The NICs are stronger on the continental slope off the east coast. A similar increase in inertial energy offshore of the shelf break has been reported earlier from several places: examples include (Jarosz et al., 2007; Hisaki and Naruke, 2003). All these places are, however, located in the subtropical or temperate regimes, where the Rossby radius is small. We are not aware of a report from a tropical regime in which the NICs are weaker on the shelf or at the shelf break compared to the slope.

The slope ADCP data show a seasonality in the generation of the NICs. The NICs are not seen largely during January–April at all the mooring locations. They are prominent at the northern locations during May–September, when the strong winds associated with the summer-monsoon depressions and cyclones are observed in the region (Figures 3.2– 3.3). The storms shift southward following the summer monsoon, and so do the NICs, which are generated off Cuddalore during October–December. In the central part of the coast, the

NICs are seen during both summer and winter monsoon owing to effect of storms over the northern and southern bay. Though the data are of limited duration, they reveal considerable interannual variability in the generation of NICs. For example, the NICs were weaker in 2010–2011 than in 2009.

The NICs also exhibit upward phase propagation, implying downward propagation of energy (Figure 3.5), as has been noted elsewhere too (Kundu, 1976; Leaman and Sanford, 1975; Jarosz et al., 2007). During severe storms such as cyclone *Aila*, strong NICs are seen below the shallow mixed layer (Figures 3.2 and 3.5) that is typical of the BoB (Montegut et al., 2004; Chatterjee et al., 2012).

We have discussed the importance of low-pressure systems for the generation of NICs. Another process that has been noted as a generating mechanism for NICs is parametric subharmonic instability (PSI), in which energy is transferred from the tidal current to the NICs in the vicinity of a critical latitude, which is 28.8°N for the M_2 tide (Haren, 2005; Alford et al., 2007) and 14.52°N and 13.44°N for the K_1 and O_1 tides, respectively (Xie et al., 2009; Sun et al., 2011; Xie et al., 2011). The critical latitude for the semi-diurnal tide is north of the basin boundary, but that for the diurnal tides is close to the latitude of Ramayapatnam and Cuddalore. An examination of the tidal constituents shows, however, that the amplitude of the diurnal constituent K_1 is less than a quarter of that of the M_2 tide in the bay; for O_1, the amplitude is an order of magnitude smaller than that of M_2 (Murty and Henry, 1983; Sindhu, 2012; Admiralty, 2010). Spectral analysis of the raw ADCPs data also shows (figure not shown) that the diurnal tidal amplitudes are significantly weaker at Ramayapatnam and Cuddalore. Therefore, we rule out the possibility of PSI being a significant contributor to the NICs along the east coast of India.

One question of interest is whether the NICs make a significant contribution to the total current. A histogram of the ratio of the NICs to the total current (Figure 3.7b, c, d) shows that the NICs is comparable to the residual, i. e., non-tidal and sub-inertial, current on more

than nine days in a year off Paradip and Cuddalore; the magnitude of the NICs exceeds half that of the residual current on more than 16 days. Off Gopalpur and Kakinada, the NICs are not comparable to the residual current, the magnitude of the NICs being more than half the residual-current magnitude on just six days in a year.

The histogram of the ratios, however, does not give an idea of the magnitude of the NICs and also does not give a feel for the actual magnitudes of these currents. Therefore, in addition to the histogram, we show a correspondence (also called Kolmogorov-Smirnov) plot (Figure 3.7a) to show the magnitudes of these two components of the current. In the correspondence plot, the inertial current and residual current are separately sorted (not a unique sort) in ascending order over the entire data record, and the inertial current is plotted against the residual current. Unlike the histogram, which examines the ratio day by day, the correspondence plot merely provides a statistical idea of the current magnitudes. For example, the strong inertial current (over 40 cm s^{-1}) seen at Paradip implies a strong inertial current of that magnitude on some day during the period over which the data were collected. It is not necessary that the resdiual current magnitude was greater than 120 cm s^{-1} on that day. All that the correspondence plot gives us is the distribution of the magnitudes of the inertial and residual components. What is evident from the correspondence plot, however, is that the magnitude of the NICs seldom exceeds 10 cm s^{-1} ; it is higher than 30 cm s^{-1} only at Paradip and Cuddalore.

The NICs are therefore more important in the northern and southern bay, which experience more low-pressure systems than does the central part of the bay (Mooley and Shukla, 1989; Mohapatra and Mohanty, 2004). An implication is that forecasting models are likely to exhibit larger errors in the northern and southern BoB during storms owing to the need to simulate the NICs well. The NICs are not only stronger during these extreme weather events, but they are also sensitive to details of the storms, which are often not captured well by the atmospheric general circulation models, the source of the wind forcing for ocean-

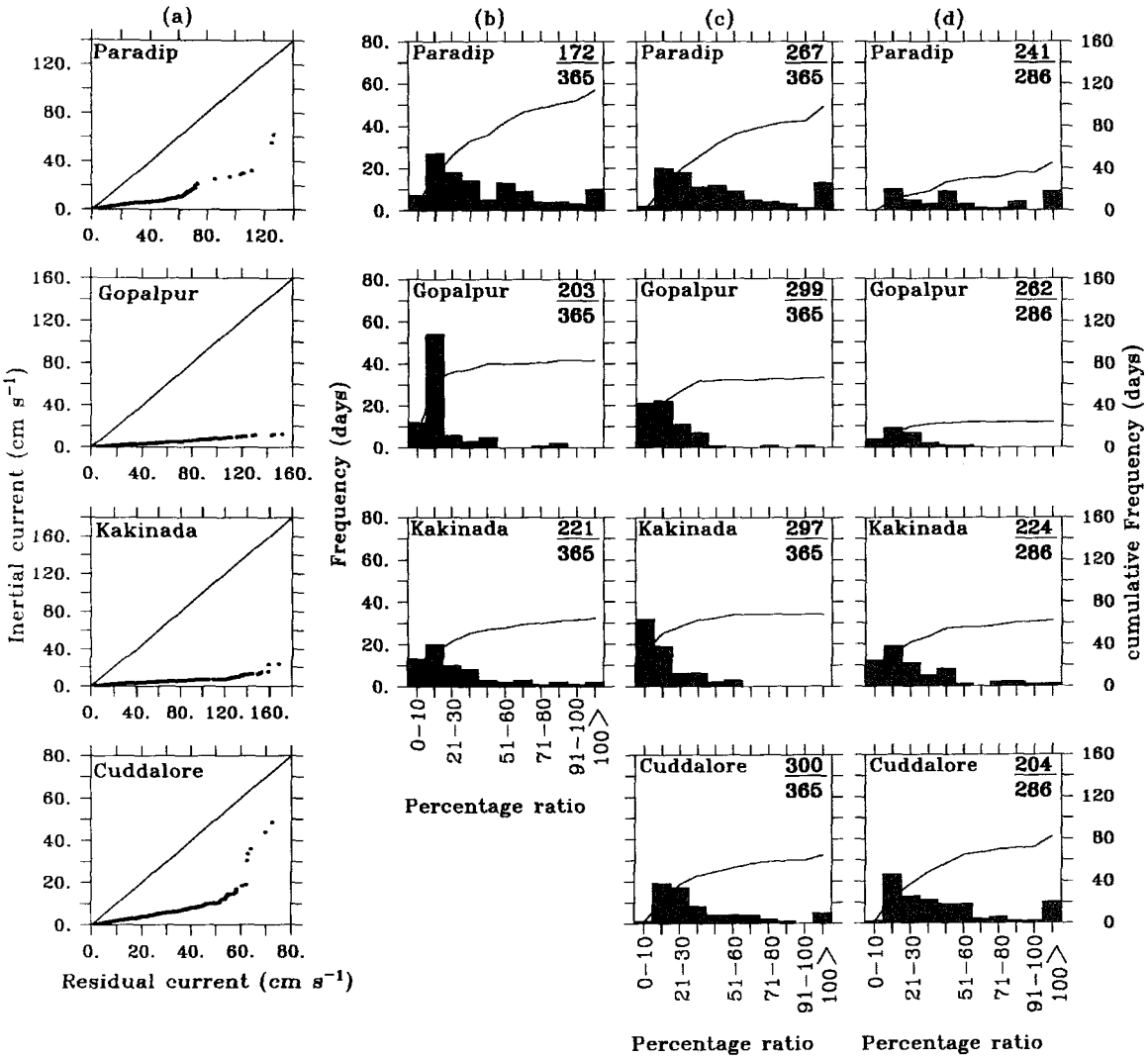

Figure 3.7: (a) Correspondence plot between magnitude of NICs and residual current from 1 May 2009 to 10 February 2012. (See the text in Section 3.6 for a description of the plot.) (b) Histograms showing the percentage contribution of NICs to the residual. The abscissa shows the ratio (as a percentage) of the daily NICs and the residual current magnitude; the frequency (left axis) shows the number of days in a year for which the ratio falls in the given ratio band. The black curve shows cumulative frequency (right axis). Histogram is computed considering data from 1 May 2009 to 30 April 2010 (365 days). The number in each panel (bold front) represent the number of days in which inertial and residual current magnitude are less than 5 cm s^{-1}. (c) Same as figure b but from 1st May 2010 to 30th April 2011 (365 days). (d) Same as figure b and c but from 1st May 2011 to 10th February 2012 (286 days).

forecasting models. Therefore, one can expect larger errors in the predicted current during such weather events.

Though the NICs not negligible during extreme events, they contribute much less to the EICC variability in the seasonal and intraseasonal parts of the spectrum. Hence, the rest of the thesis is devoted to the sub-Inertial EICC.

Chapter 4

Observed seasonal and intraseasonal variability of the sub-inertial EICC

In this chapter, we have analyzed seasonal and intraseasonal variability of the EICC at sub-inertial periods (periods more than inertial period) on four (Paradip, Gopalpur, Kakinada and Cuddalore) continental slope ADCP locations (Figure 1.2). We have not used data from the continental shelf and Ramyapatnam continental slope ADCPs due to non availability of continuous record for more than a year (Table 1.1). Based on accurate estimation of observed inertial periods at above four continental slope locations , we filtered out the NICs from the de-tided residual current using a 60 hour low-pass Butterworth filter to calculate sub-inertial alongshore and cross-shore currents (details of angle are given in Table 3.1).

This chapter is organized as follows. The alongshore and cross-shore currents are described in Sections 4.1 and 4.2, respectively. Section 4.3 concludes the chapter.

4.1 Alongshore current

The ADCPs observations show strong alongshore EICC at Gopalpur and Kakinada and a weaker EICC at Cuddalore and Paradip (Figure 4.1). In general, these data confirm what

was known about the EICC from earlier observations, but the current shows considerable variability within a season and across years. As inferred earlier from hydrography and ship drifts, the EICC is at its peak strength during spring, when it flows poleward over the top 40–300 m, the depth range sampled in these measurements. The peak value recorded was 160 cm s^{-1} at Kakinada during April 2010. The poleward flow weakens during the summer monsoon, particularly below 100 m, and it usually reverses (at 40 m) at Gopalpur and often at Cuddalore as well. During the summer monsoon of 2011, such an equatorward EICC is seen even at Kakinada, suggesting that the EICC during this year was equatorward throughout the east coast over at least part of the summer monsoon. Unlike for the spring EICC, an undercurrent is also seen on occasions during the summer monsoon, but the undercurrent is more prominent during winter, when it generally flows poleward under the equatorward surface current. The undercurrent is more commonly seen at Cuddalore than at the other locations.

A histogram (Figure 4.2a) shows that the alongshore current at Paradip is weaker than 25 cm s^{-1} over 80% (90%) of the time at 40 m (100 m). The peak strength at this location is 100 cm s^{-1} during the poleward (equatorward) burst in February–March 2010 (April–May 2011). At the other locations, the current is weaker than 25 cm s^{-1} just 60% of the time. The histogram is asymmetric with respect to direction, with poleward (eastward) flow dominating at Kakinada (Paradip) and equatorward flow dominating at Gopalpur. It is only at Cuddalore that the distribution tends to be more even. At Kakinada and Cuddalore, the poleward (equatorward) current is stronger than 25 cm s^{-1} 40% (23%) and 24% (20%) of the time, respectively; in contrast, at Gopalpur, the current is equatorward (poleward) 44% (22%) of the time. This asymmetry implies that the mean current over the record (of over a year) is not as weak as on the west-coast slope (Amol et al., 2014). The mean current is poleward at all depths at Kakinada and weakly poleward over the top 150 m at Cuddalore, but it is equatorward up to 180 m at Gopalpur (Figure 4.2b). At Paradip, the

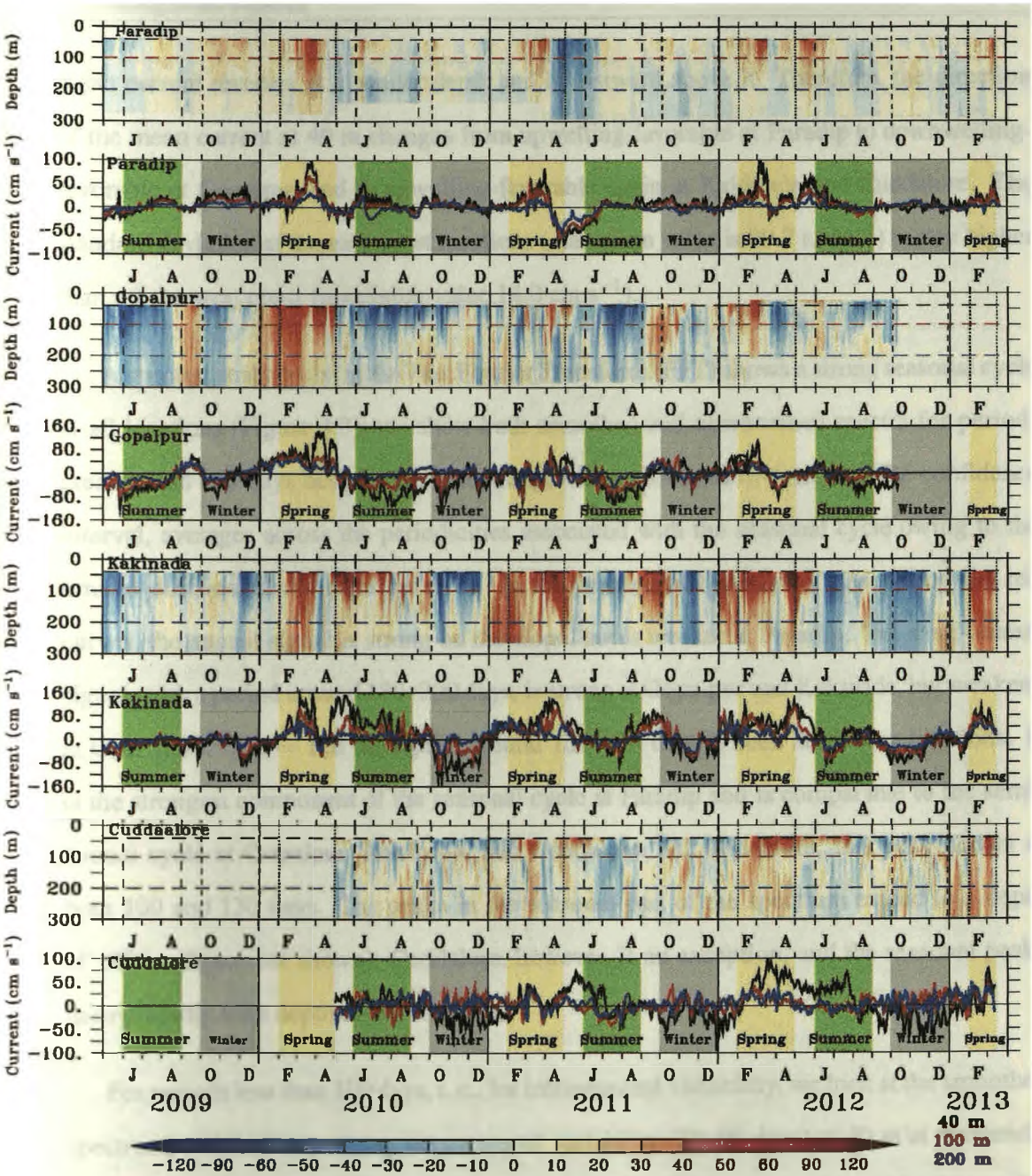

Figure 4.1: 2.5-day-low-pass-filtered, detided, residual alongshore currents (cm s^{-1}). At Paradip, the alongshore current is zonal and an eastward current is positive. At the other three locations, a poleward current is positive. This sign convention is used in all figures for the alongshore currents. The solid vertical lines mark the years. The dashed vertical lines in the odd panels and the yellow, green, and gray shading in the odd panels are used to denote the periods spring (February–May), summer monsoon (June–September), and winter (October–December), respectively. The dashed horizontal lines in the odd panels mark the 40 m (black), 100 m (red), and 200 m (blue) depths, and the currents at these depths are plotted in the respective colours in every even panel; the black horizontal line in these panels marks the zero current. The location name is at the top left corner in each panel. Note that the colour scale is not uniform.

mean current reverses at a similar depth and is eastward above it. Therefore, the direction of the mean current at 40 m changes from upwelling-favorable at Paradip to downwelling-favorable at Gopalpur and to upwelling-favorable again at Kakinada and Cuddalore. The standard deviation at the east-coast locations (maximum value is 29.7 cm s^{-1}) is also higher than off the west coast (maximum value 14.0 cm s^{-1}).

A spectral analysis using the Fast Fourier Transform (FFT) shows a strong seasonal cycle at all locations (Figure 4.3); we show both smoothed and unsmoothed spectra for periods greater than 100 days because the smoothing, which allows us to determine the confidence interval, averages across the periodicities associated with the seasonal cycle owing to the limited duration of the measurements. In the unsmoothed spectrum, denoted by the red curves, the annual signal is strong on the slope, but is weaker at Paradip. The semi-annual signal, with a period around 180–200 days, is strong at Gopalpur and Kakinada, but weakens at Cuddalore. The $\sim$ 120 days peak around 100–130 days is seen at all four locations. It is the strongest component of the seasonal cycle at Paradip and is comparable to the semi-annual cycle at Gopalpur, Kakinada, and Cuddalore. At Cuddalore, this peak occurs at both 100 and 130 days. The peaks in the seasonal part of the spectrum extend to a depth of 100 m (figure not shown); Cuddalore, however, is an exception, and the seasonal peaks decay rapidly with depth at this location.

For periods less than 100 days, i. e., for intraseasonal variability, we look at the smoothed spectrum, which shows strong intraseasonal variability (30–90 days) at 40 m at Kakinada. Comparison of the smoothed spectrum at seasonal and intraseasonal periods shows that the seasonal cycle is dominant at all locations except Cuddalore, where the difference in the spectral amplitude is within the 95% confidence limit. Peaks occur at 70 days at both Kakinada and Gopalpur, and it is possible that the 60-day peak at Cuddalore is part of this band, which is clearly separated from the peaks at the high-frequency limit of this band (30–40 days). With depth, the intraseasonal peaks tend to decrease fairly rapidly at all locations

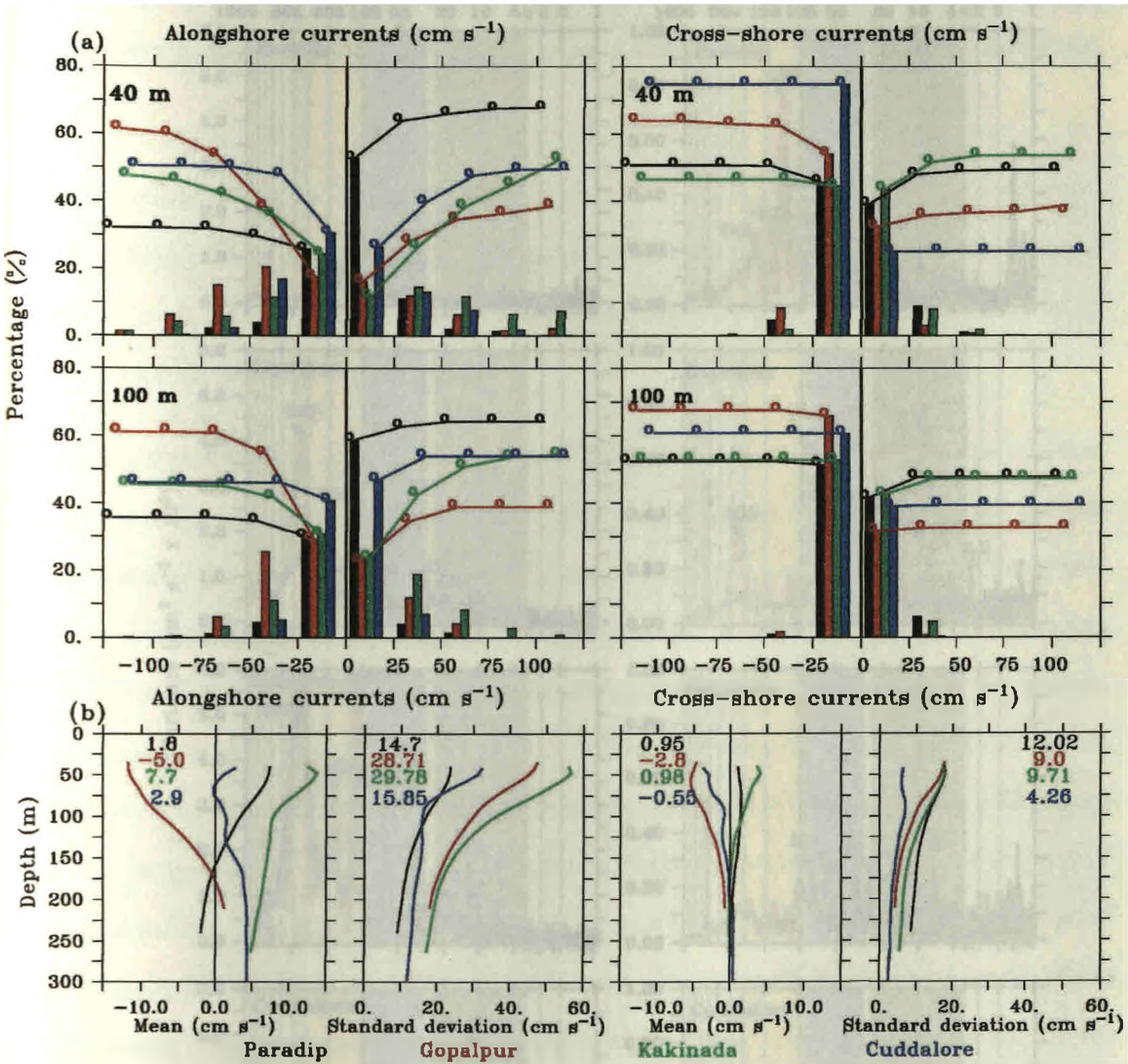

Figure 4.2: (a) Histogram and cumulative curve for both alongshore (left panels) and cross-shore currents (right panels) at 40 m (top panels) and 100 m (bottom panels) at the four ADCP locations. Here, Paradip, Gopalpur, Kakinada, and Cuddalore locations are represented by black, red, green, and blue colours, respectively. The histogram is calculated over a $\sim$ 25 cm s^{-1} bin (interval) and currents stronger than |100| cm s^{-1} are placed in a single bin. The histogram was computed using data from from May 2009 to April 2012 at Paradip, Gopalpur, and Kakinada and from May 2010 to April 2012 at Cuddalore. The cumulative curve, overlaid on the histogram, was drawn separately for negative and positive values of the current. The sum of the occurrences of both positive and negative values adds up to 100% at each location. (b) Statistical mean and standard deviation as a function of depth for both alongshore currents (left panels) and cross-shore currents (right panels). The colours are as in (a). The inset values in the top left corner show the total depth average mean and standard deviation for each location. The period over which the mean and standard deviation were computed is as for the histogram.

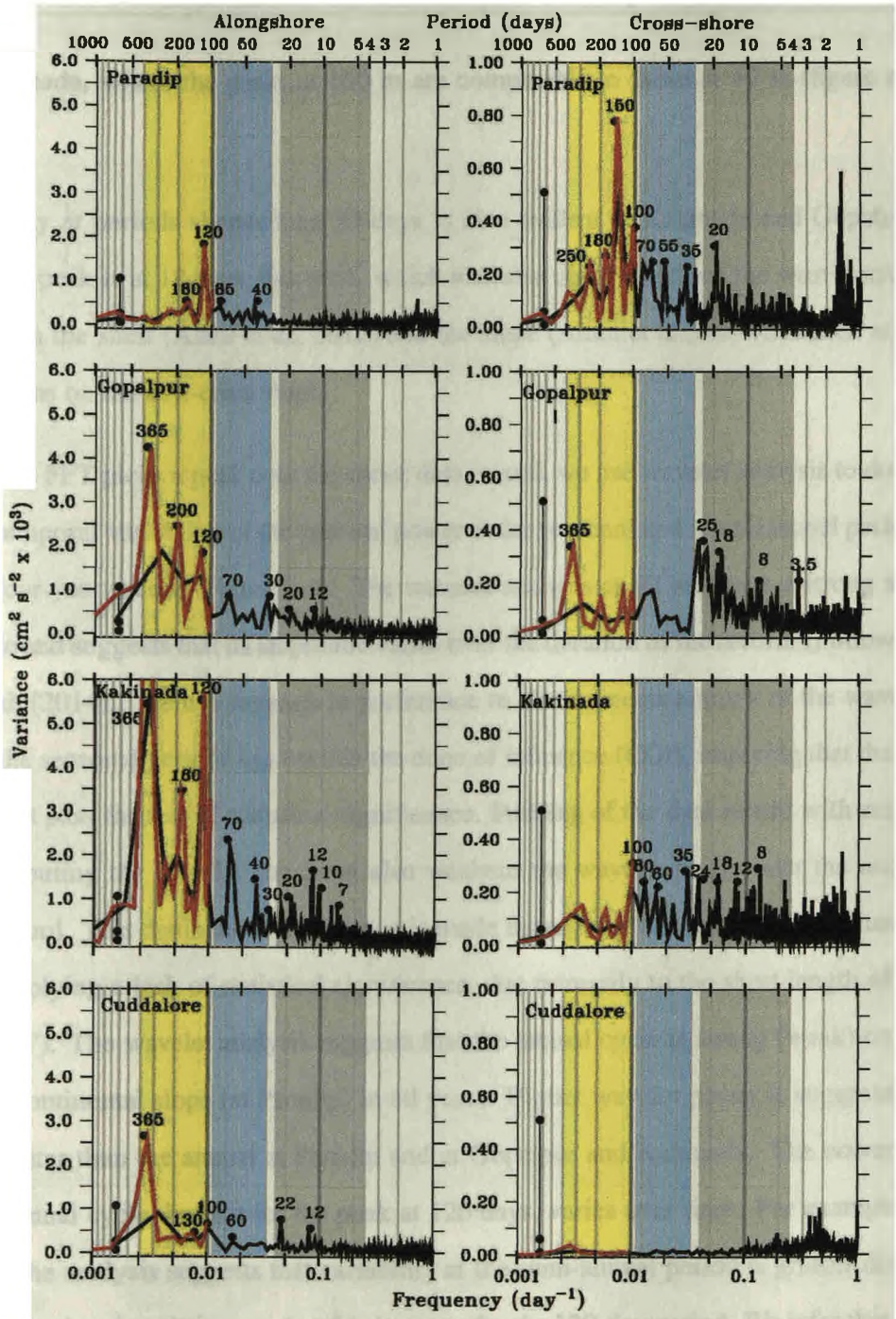

Figure 4.3: Variance preserving spectra (black curves) for the raw alongshore (left panel) and cross-shore (right panel) currents at 40 m. The spectra were smoothed using a three-point triangle filter after applying a 75% Tukey window to the detrended and detided data. The bar in the lower left corner of all figures represents the 95% confidence interval. The yellow, light blue, and gray shades highlight the seasonal cycle (100–400 days) and the intraseasonal (30–90 days) and high- frequency (4–25 days) bands, respectively. The dashed red curves show the raw spectra (not smoothed) for the seasonal band. The period for major peaks is listed.

except Kakinada, where the peaks at 100 m are comparable to those at 40 m (figure not shown).

Variability at periods shorter than 30 days is also evident at Kakinada and Gopalpur. One striking peak is at 12 days; this peak, which was also observed along the west coast of India on both the shelf (Amol et al., 2012) and the slope (Amol et al., 2014), is seen at all three locations on the east-coast slope.

Since the FFT picks a peak over the entire data record, we use wavelet analysis to document the temporal variability of the spectral power at the seasonal and intraseasonal periods over the four-year record (Figure 4.4). The wavelet analysis at 40 m shows a strong seasonal cycle and suggests that its amplitude varies over the duration of the record. (Following Amol et al. (2014), "we use *suggests* in preference to *shows* because much of the wavelet power at the seasonal periods lies outside the cone of influence (COI), implying that the result does not pass the test of statistical significance. Padding of the data record with zeroes before computing the wavelet transform also weakens the wavelet power near the end of the data record. This distinction in inference is made throughout this paper, with the use of *suggests* implying a lack of statistical significance, due primarily to the short length of the data record."). The wavelet analysis suggests that the annual cycle is strong (weak) on the east-coast continental slope (at Paradip) in all years. Higher wavelet power is suggested at periods greater than the annual at Paradip and at Gopalpur and Kakinada. The power for the semi-annual cycle, but not for the peak at 120 days, varies over time. For example, at Kakinada, the analysis suggests that variability at the semi-annual period is greater during 2011 compared to the other years, but this is not so for the 120-day period. We infer that this stronger interannual variability at the semi-annual period suggested by the wavelet analysis leads to the bigger peak at 120 days in the FFT (Figure 4.3); see the red curve depicting the unsmoothed spectrum). Nevertheless, seasonality in the power of the 120-day band is evident at Paradip, Gopalpur, and Kakinada, but not at Cuddalore, where it is seen primarily

from July 2011 to June 2012. Similar seasonality is seen in the variability at intraseasonal periods ranging from a few days to 90 days.

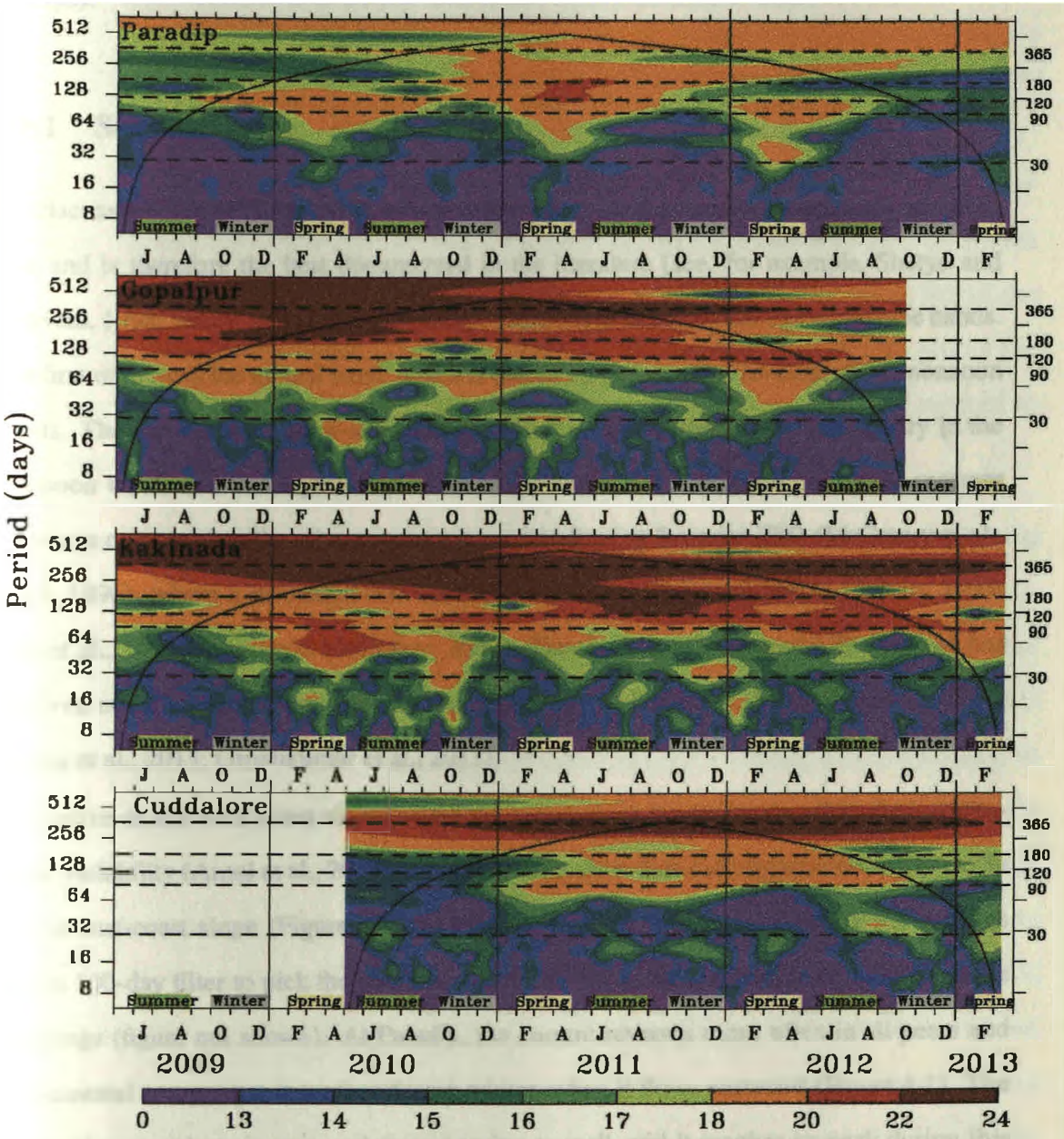

Figure 4.4: Morlet wavelet power spectra ($cm^2\ s^{-2}$) of alongshore currents at 40 m depth. The thick black line marks the cone of influence for the wavelet power spectra. The ordinate and wavelet power are plotted on a $\log_2$ scale. The horizontal dashed lines mark the 30-day, 90-day, 120-day, 180-day, and 365-day periods. Note that the colour scale is not uniform.

Based on the spectral (FFT and wavelet) analysis, we separated the spectrum into a

seasonal (period more than 100 days) and an intraseasonal component (periods less than 90 days).

4.1.1 Seasonal cycle

We discuss first the seasonal cycle, which is the variability that can be described by monthly data and is therefore the best documented in the literature (see, for example, Shetye and Gouveia, 1998; Schott and McCreary, 2001). Included in this seasonal cycle are three bands. The first of these is the annual band, which is forced by the seasonal reversal of the monsoon winds. The second is the semi-annual band, which exists because of the asymmetry in the monsoon winds and this asymmetry is due to the winds being stronger during the summer monsoon compared to the winter monsoon —, and forcing from the EIO (McCreary et al., 1993, 1996), where a resonance has been noted at the semi-annual period (Jensen, 1993; Han et al., 1999; Schott and McCreary, 2001). The third band is around 120 days and has received much less attention in the literature (Nethery and Shankar, 2007; Han et al., 2011; Cheng et al., 2013; Girishkumar et al., 2013).

Unlike on the west-coast slope, where the seasonal cycle was weaker than the intraseasonal variability (Amol et al., 2014), the ADCP data show that a strong seasonal cycle exists on the east-coast slope (Figure 4.1 and Figures 4.3–4.4). Low-pass-filtering the currents with a 100-day filter to pick the seasonal variability shows striking differences between the moorings (figure not shown). At Paradip, the current reverses more often in all years and the seasonal component is weaker during winter, when it flows eastward (Figure 4.1). The seasonal current here is eastward during spring as well, and it reaches its peak during this season. During the summer monsoon, the seasonal current at Paradip flows westward in 2011 and 2012 and eastward in 2010. Fewer reversals occur at the locations on the east-coast slope, with the EICC flowing poleward during spring and equatorward during winter. During the summer monsoon, the seasonal EICC is equatorward at Gopalpur, but can flow

in either direction at Kakinada and Cuddalore. To distinguish the annual cycle from the intra-annual components of the seasonal cycle, we use band-pass filters.

Filtering the data with a 300–400-day band-pass filter shows a strong annual cycle on the slope (Figure 4.5). A striking feature of the annual cycle is the upward phase propagation. On occasions, however, as during July–November 2009 at Gopalpur and Kakinada, or during October–December 2012 at Cuddalore, the phase propagates downward. The annual EICC on the slope tends to flow poleward (equatorward) during the first (second) half of the year. The annual cycle decays rapidly with depth at Cuddalore, but a depth-time plot of the wavelet power (figure not shown) suggests that the wavelet power at this period extends to greater depths at Kakinada and, to a lesser extent, at Gopalpur and Paradip.

Band-pass filtering with a 100–250-day filter shows stronger (weaker) currents at Paradip (Cuddalore); at Gopalpur and Kakinada, this intra-annual component of the seasonal cycle is weaker than the annual component, but is still significant (Figure 4.6). At Paradip, there are three full cycles each year, leading to the 120-day peak in the FFT; the intra-annual component is weak, however, following the summer monsoon, leading to the seasonality in the wavelet power spectrum (Figure 4.4). At all locations, the 120-day component strengthens the poleward or eastward EICC (Figure 4.6). If the number of current reversals during a year decreases, as happened at Gopalpur during 2010, the wavelet power tends to be stronger for the semi-annual cycle compared to the 120-day period (Figure 4.4); in 2010, the 100–250-day EICC flowed poleward at Gopalpur during spring and again during winter, with equatorward flow between them during the summer monsoon. The intra-annual current tends to reverse more often when the 120-day peak dominates this part of the seasonal cycle; an example is the stronger 120-day (semi-annual) variability at Kakinada during 2011–2012 (2009–2010). These current reversals in the 100–250-day band tend to occur over the top $\sim$ 300 m at all locations except Cuddalore, where the wavelet power in this band too tends to be trapped closer to the surface (Figure 4.7).

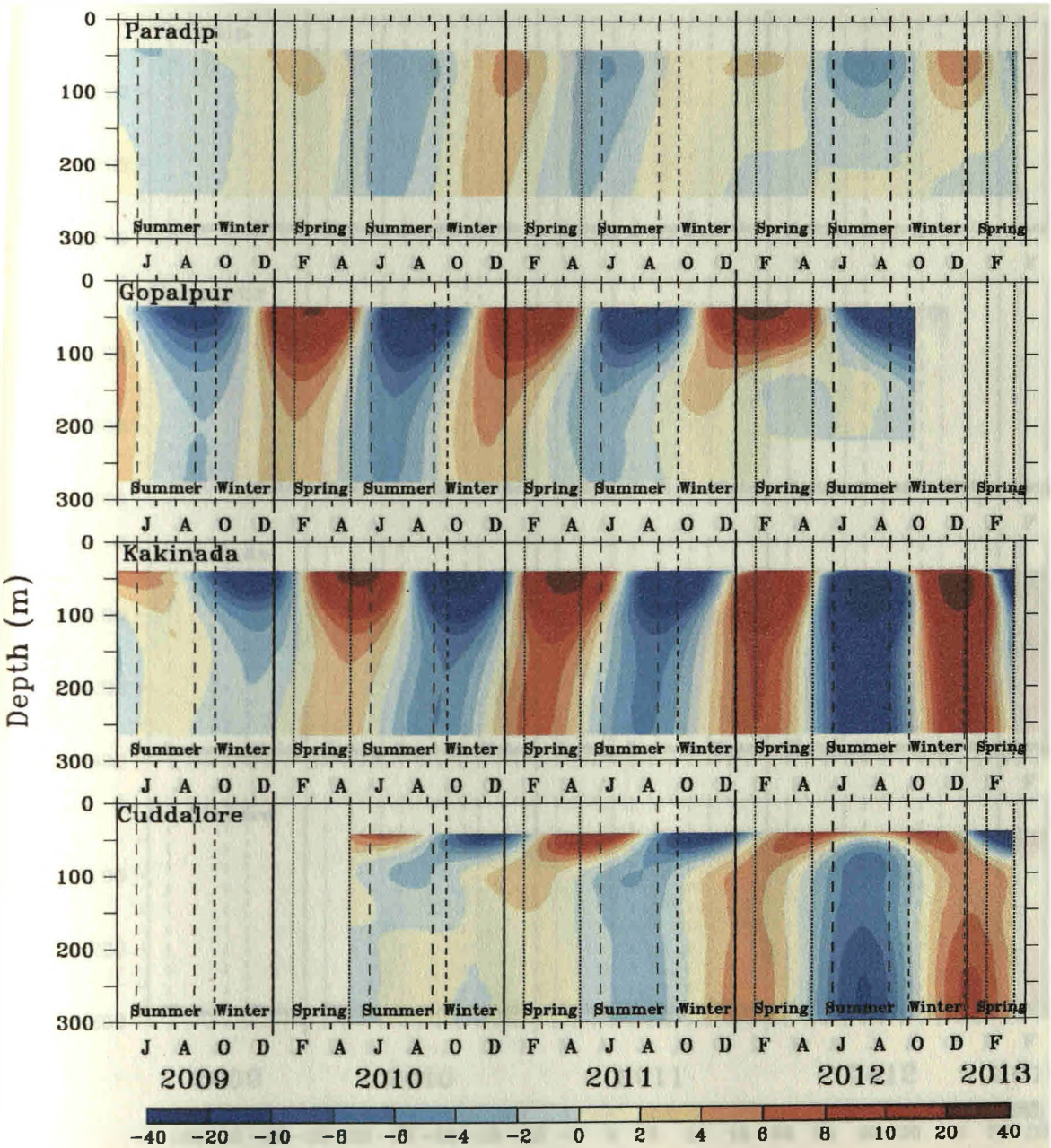

Figure 4.5: 300-400-day band-pass-filtered alongshore currents (cm s^{-1}). Note that the colour scale is not uniform.

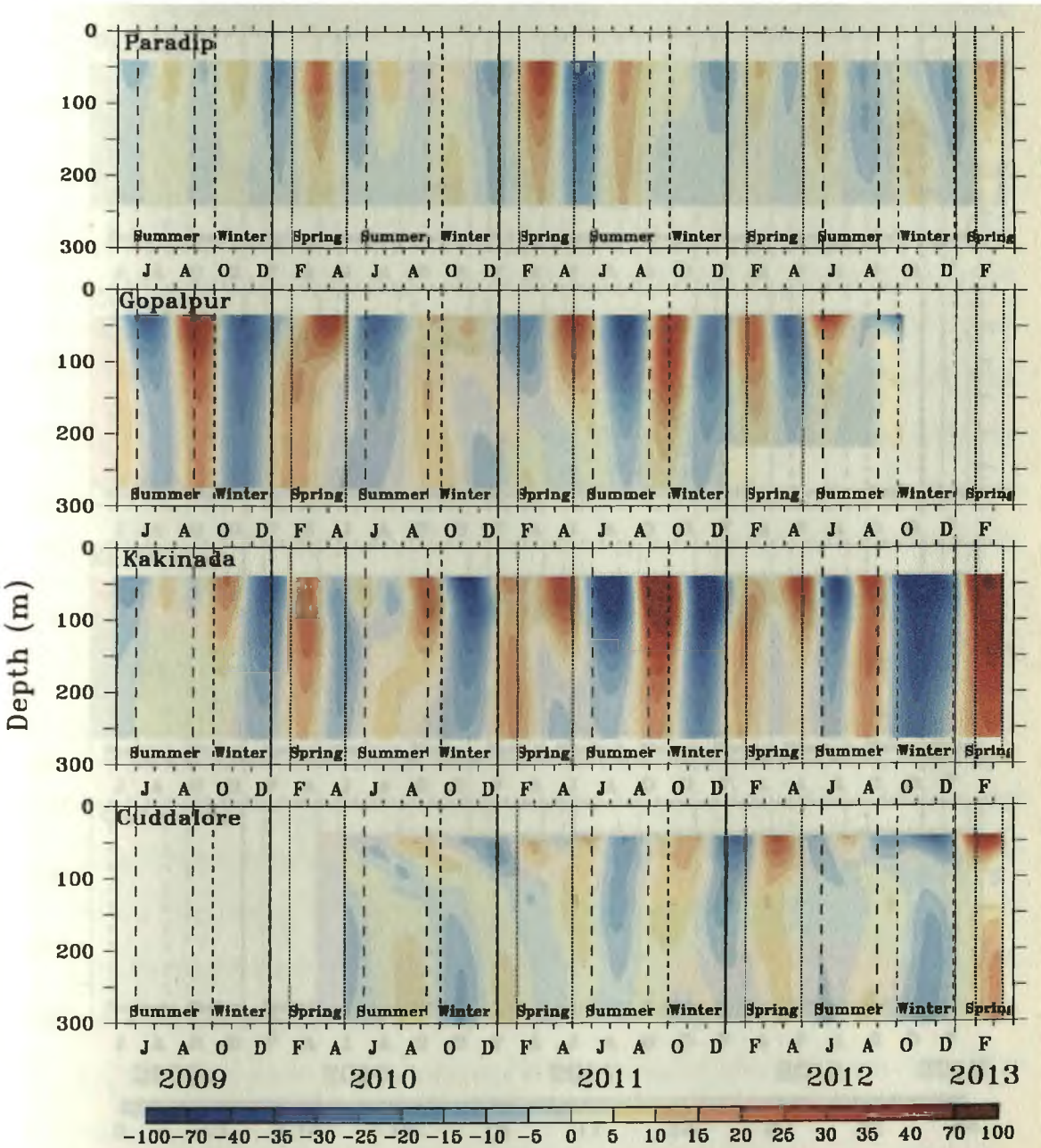

Figure 4.6: 100-250-day band-pass-filtered alongshore currents (cm s^{-1}). Note that the colour scale is not uniform.

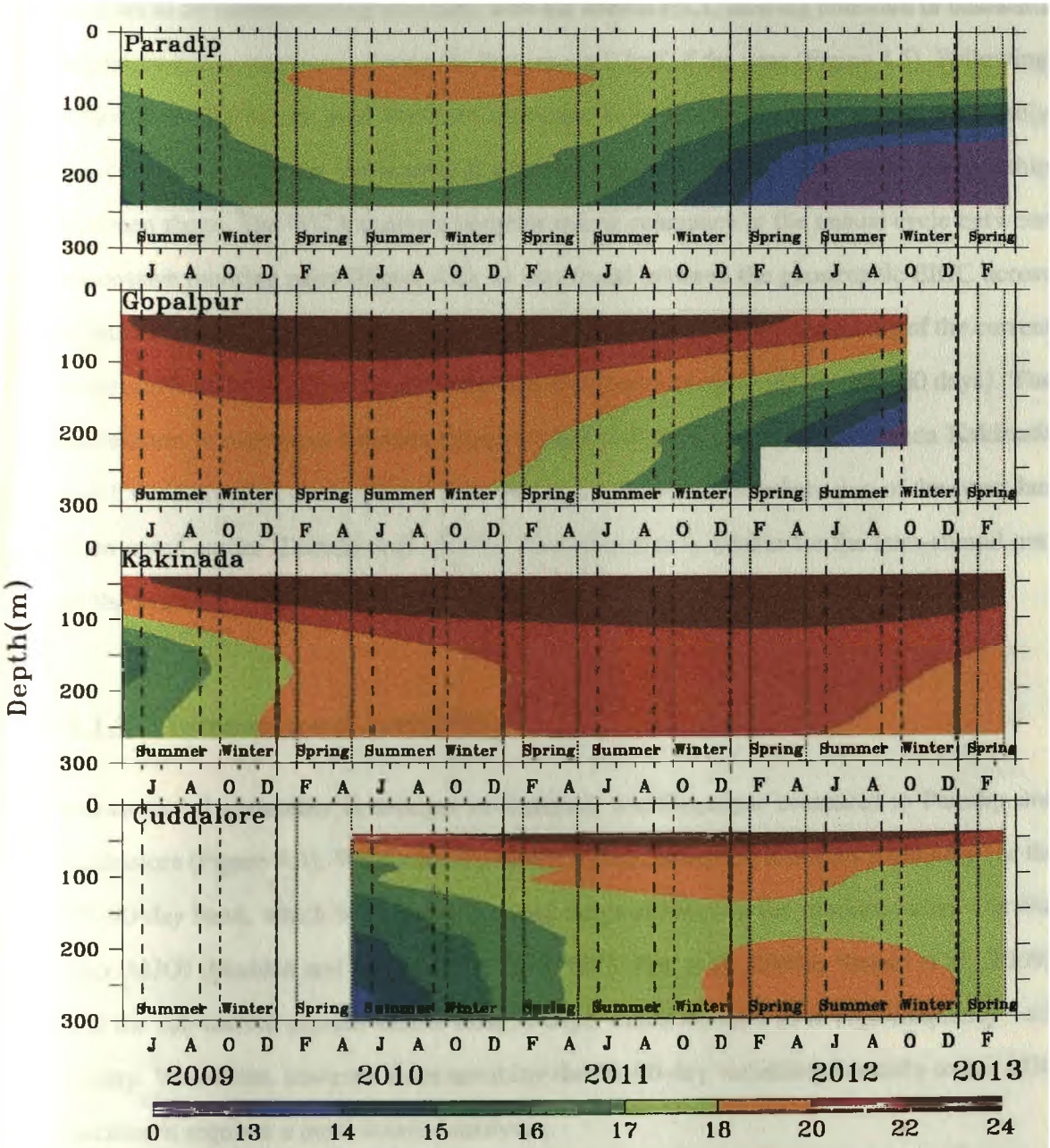

Figure 4.7: Vertical section of wavelet power ($cm^2\ s^{-2}$) for 360 day period. The ordinate and wavelet power are plotted on a $\log_2$ scale. Note that the colour scale is not uniform.

GOA UNIVERSITY LIBRARY GOA

Barring the obvious differences in the timing of the reversal, the annual component appears to be coherent along the coast, with the annual EICC flowing poleward or eastward (equatorward or westward) during the first (second) half of the year (Figure 4.5). Following Amol et al. (2014), we used Wavelet Coherence Analysis (WCA) to determine not merely the correlation between the current at adjacent moorings, but also the phase relationship between them. The WCA analysis suggests strong coherence at the annual cycle between successive mooring pairs (Figure 4.8), as was found between the geostrophic EICC across adjacent altimeter tracks by Durand et al. (2009). The differences in the timing of the current reversals lead, however, to significant phase differences of up to 90° (~ 90–100 days). The correlation is maximum between Gopalpur and Kakinada and weaker between Kakinada and Cuddalore; this weakening of the correlation towards the southern part of the coast has been noted earlier (Durand et al., 2009). The coherence is weaker for the intra-annual part of the seasonal cycle.

4.1.2 Intraseasonal variability

Intraseasonal variability is stronger at Kakinada and Gopalpur compared to Paradip and Cuddalore (Figure 4.3). We discuss the observed intraseasonal variability separately for the 30–90-day band, which is the general period range ascribed to the Madden-Julian Oscillation (MJO) (Madden and Julian, 1971, 1972, 1993; Han et al., 2001a; Vialard et al., 2009), and the sub-inertial periods shorter than 30 days, which we refer to as high-frequency variability. We refrain, however, from ascribing the 30–90-day variability formally to the MJO because it requires a more detailed analysis.

The current in the 30–90-day band is of the order of 40–70 (30–40) cm s^{-1} at Gopalpur and Kakinada (Paradip and Cuddalore) (Figure 4.9); these magnitudes are comparable to those of the seasonal component, i. .e., 80–90 (55–70) cm s^{-1}, at Gopalpur and Kakinada (Paradip and Cuddalore). The variability shows a seasonal pattern, with, in general, a peak

811

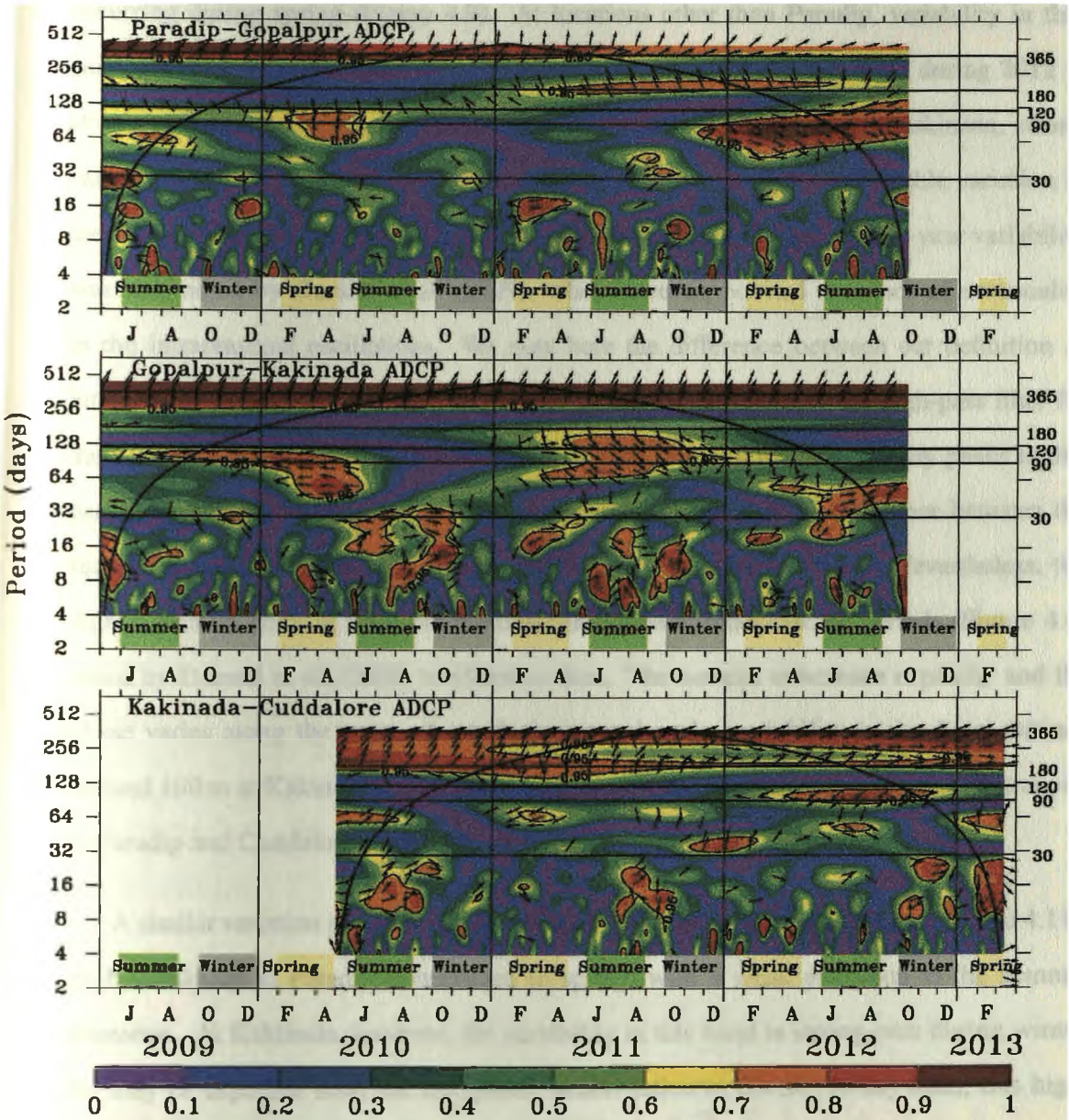

Figure 4.8: Wavelet coherence for the alongshore currents. The contour line shows the 5% significance level against red noise and the thick black line shows the cone of influence (COI). The arrows show the relative phase relationship with in-phase (anti-phase) pointing right (left). The first station leads (lags) the second station in anticlockwise (clockwise) direction. The arrows are shown only for wavelet coherence of 0.5 or more. In order from top to bottom, the panels show the wavelet coherence for the pairs (a) Paradip-Gopalpur, (b) Gopalpur-Kakinada, and (c) Kakinada-Cuddalore. Note that the ordinate (period) is plotted on a $\log_2$ scale. The horizontal solid lines mark the 30-day, 90-day, 120-day, 180-day, and 365-day periods.

T-811

occurring during spring (Figure 4.9). At locations other than Paradip, variability in this band occurs at other times as well. At Cuddalore, variability in this band during 2012 is stronger during the summer monsoon than in spring. At Gopalpur and Kakinada, strong variability in this band is seen over most of the year, but there is considerable variation in the pattern from year to year even within this four-year record. This year-to-year variability was also noted by Durand et al. (2009), who, however, pointed to a lack of seasonality in the intraseasonal oscillations. We note here the difference between our definition of intraseasonal variability and theirs: Durand et al. (2009) used a 250-day high-pass filter for their intraseasonal variability, thereby including the semi-annual and 120-day peaks in this part of the spectrum. Separating the higher periods brings out the difference between the seasonality at Paradip and the relative lack of it at the other locations. Nevertheless, the ADCP data do confirm the alongshore decorrelation at intraseasonal periods (Figure 4.8) noted by Durand et al. (2009) in altimeter data. The wavelet coherence is patchy and the phase varies along the coast. As with the annual cycle, variability in this band extends beyond 100 m at Kakinada and, to a lesser extent, Gopalpur, but tends to be surface-trapped at Paradip and Cuddalore (figure not shown).

A similar variation is seen in the 4–25-day, high-frequency band (Figures 4.10 and 4.11): high variability at Paradip is restricted to spring, with a weak extension to the summer monsoon. At Kakinada, however, the variability in this band is strong even during winter. As may be expected from the alongshore decorrelation in the 30–90-day band, this high-frequency band too decorrelates along the coast (Figure 4.8).

In the chapter 3, we have discussed that NIC along the east coast of India can be extended upto $\sim$ 200 m, which is much below the shallow mixed layers in the region (Montegut et al., 2004; Chatterjee et al., 2012). To see if the bursts at the high-frequency end of this 4–25-day band are related to the NICs, we checked the vertically averaged (over 40–200 m) wavelet power for the 1–32-day period range (Figure 4.12). The NICs are clearly separated from the

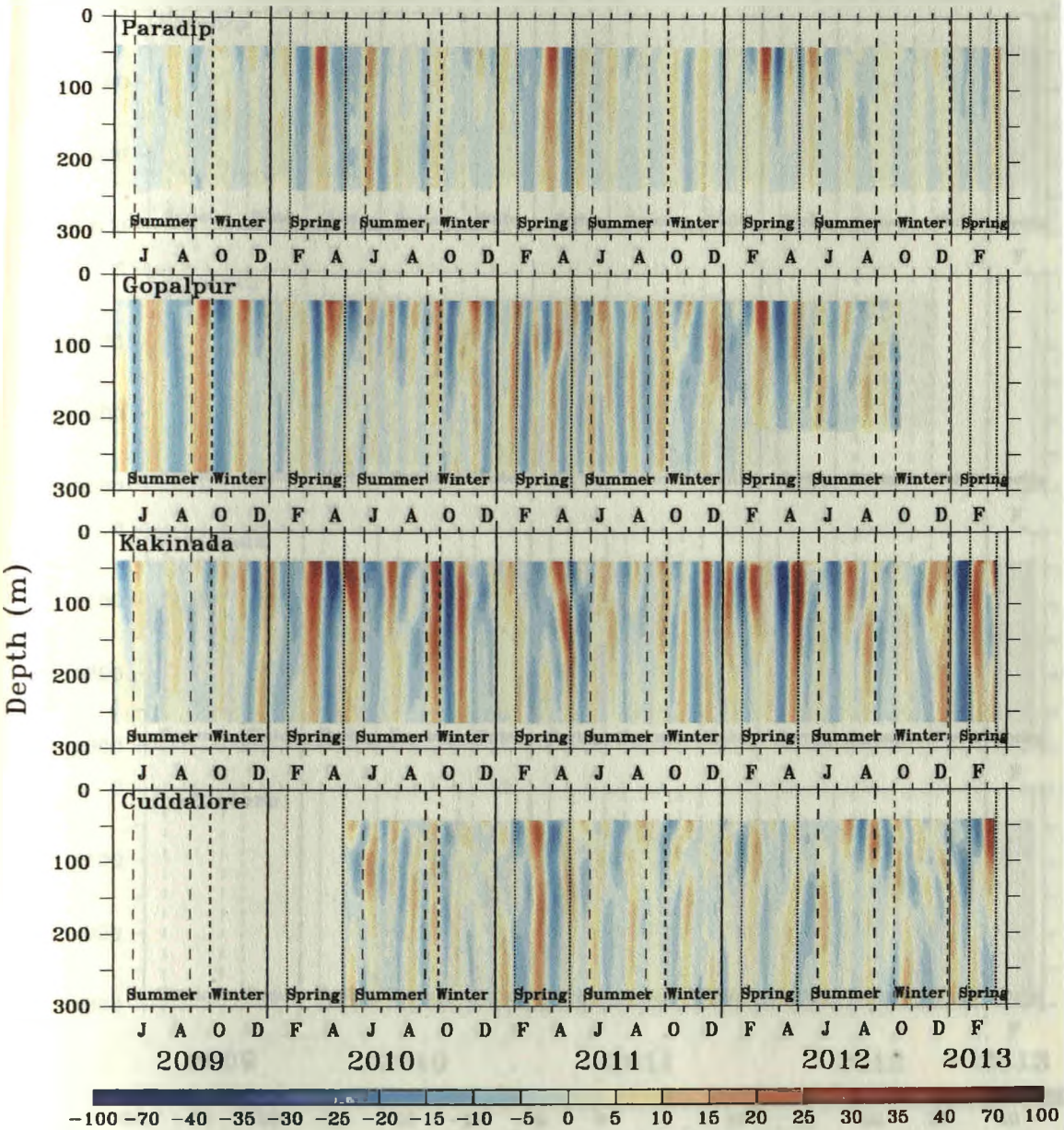

Figure 4.9: 30–90-day band-pass-filtered alongshore currents (cm s^{-1}). Note that the colour scale is not uniform.

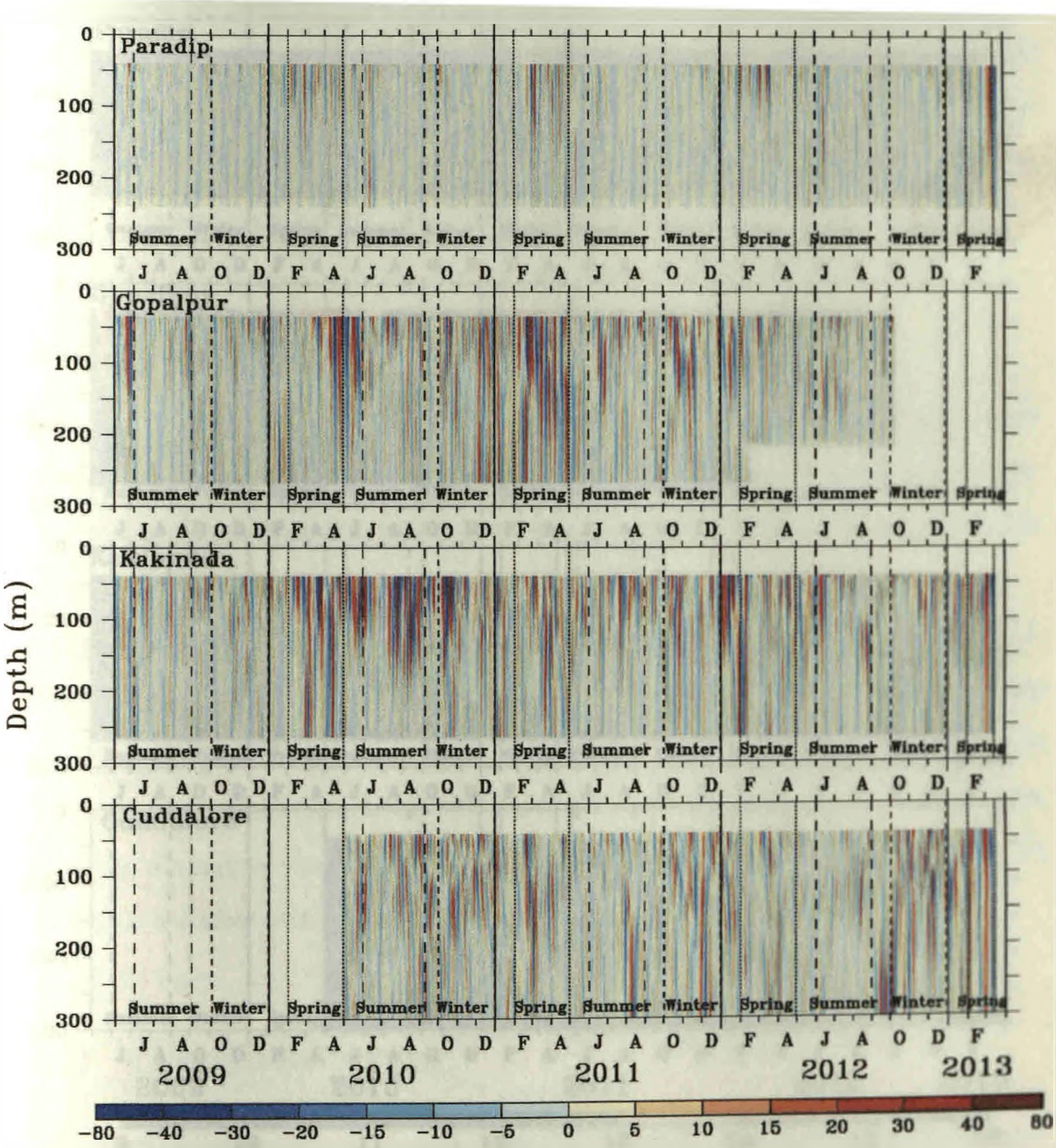

Figure 4.10: 4–25-day band-pass-filtered alongshore currents (cm s^{-1}). Note that the colour scale is not uniform.

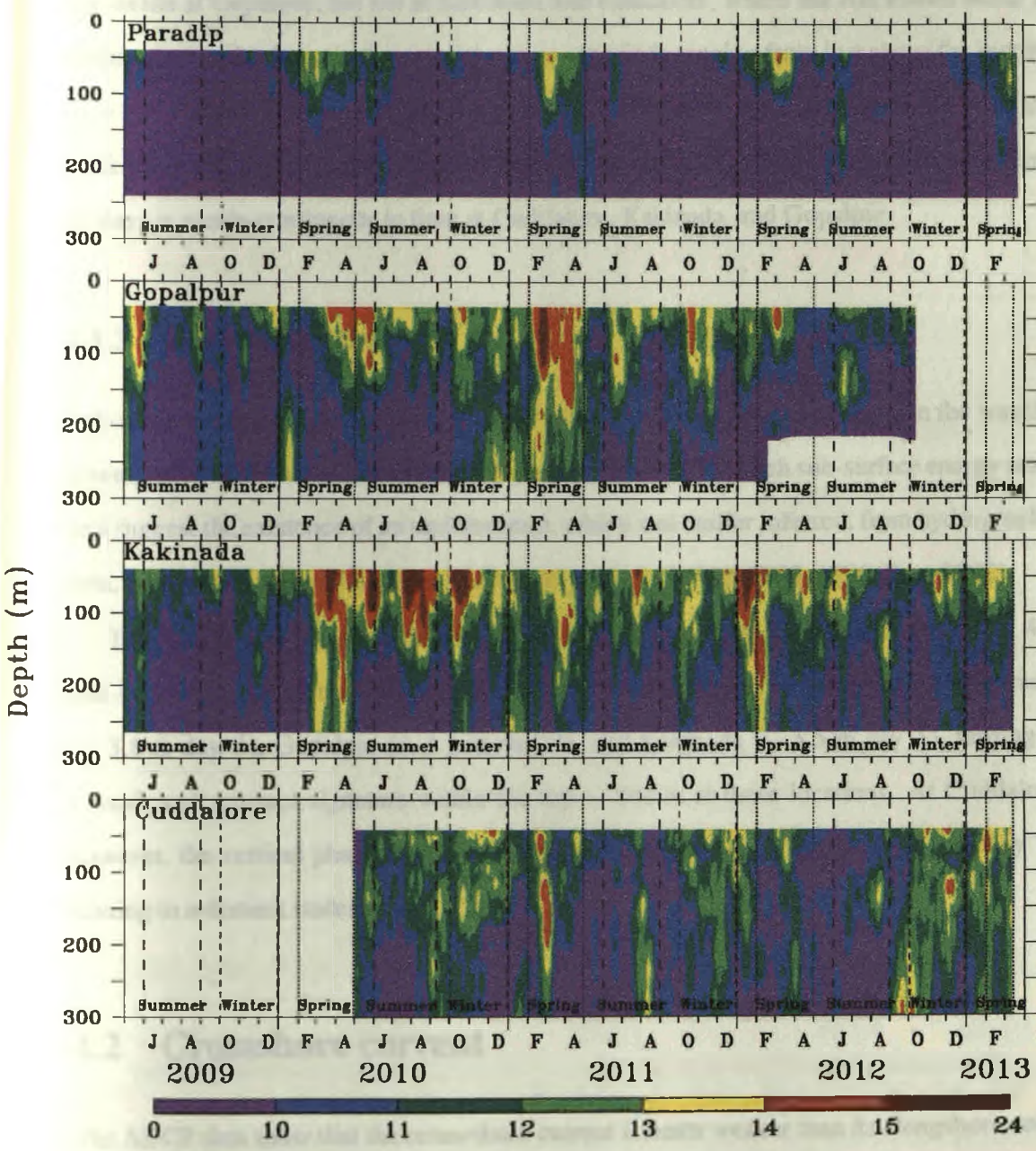

Figure 4.11: Vertical section of wavelet power ($cm^2\ s^{-2}$) for 4–25 day band. The ordinate and wavelet power are plotted on a $\log_2$ scale. Note that the colour scale is not uniform.

high-frequency band at Paradip, both in time as well as in frequency. A similar separation also exists at Gopalpur, but not at Kakinada and Cuddalore, where the NICs often occur in conjunction with a burst in the wavelet power at periods ranging from just above the inertial to $\sim$ 8–12 days. In contrast, allowing for the difference in the colour scale used for the weaker wavelet power in this frequency regime, the wavelet spectrum for periods exceeding 12 days is nearly continuous in time at Cuddalore, Kakinada, and Gopalpur.

4.1.3 Undercurrents

Sub-surface energy is not weak off the east coast: there are sub-surface cores in the wavelet power, particularly at the intraseasonal periods (Figure 4.11). Such sub-surface energy maxima suggest the existence of an undercurrent, which was earlier inferred, from hydrographic data, to exist along the Indian east coast (Shetye et al., 1991c, 1993, 1996; Rao, 2002).

The ADCP data provide evidence for upward phase propagation (Figures 4.5, 4.6, 4.9, and 4.10), but the vertical phase speed for the seasonal cycle is much higher at Paradip ($\sim$ 3.8 m day^{-1}), Gopalpur ($\sim$ 4.1 m day^{-1}), and Kakinada ($\sim$ 5.5 m day^{-1}), leading to a weak undercurrent signature within the top $\sim$ 300 m at these locations. At Cuddalore, however, the vertical phase speed is markedly less in the top $\sim$ 100 m ($\sim$ 0.7 m day^{-1}), leading to a distinct undercurrent (Figure 4.5).

4.2 Crossshore current

The ADCP data show that the cross-shore current is much weaker than its alongshore counterpart at Cuddalore (Figures 4.1 and 4.13). (The sign convention is that offshore (upwelling favourable) cross-shore currents are positive: at Paradip, this convention implies that a southward current is positive.) The cross-shore current is weaker than 25 cm s^{-1} all the time at Cuddalore and over almost 85% of the data record at the other three locations

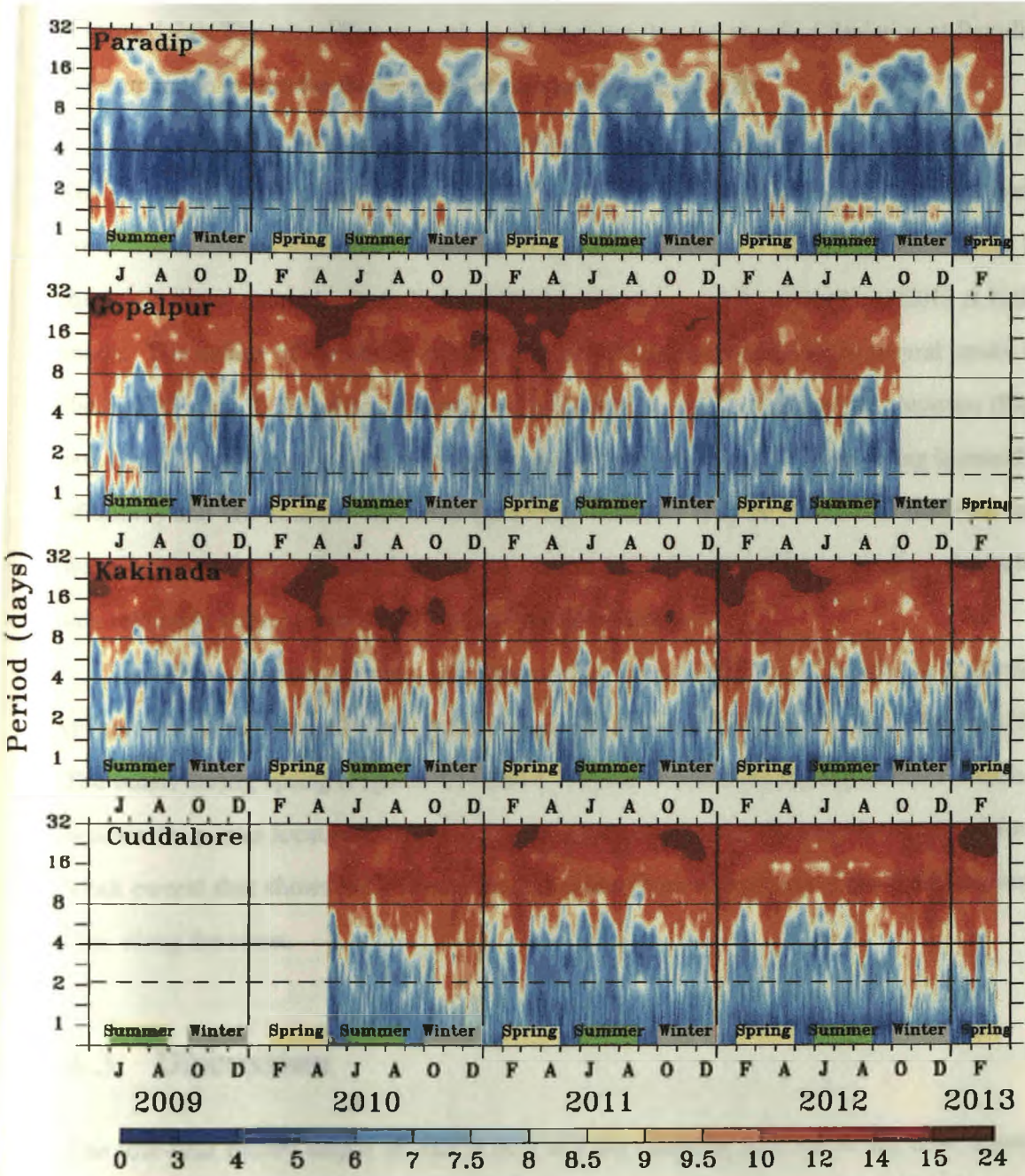

Figure 4.12: Vertically averaged, over 40–200 m, wavelet power ($cm^2\ s^{-2}$) for the 1–32-day band. The ordinate and wavelet power are plotted on a $\log_2$ scale. The 4-day and 8-day periods are highlighted by solid horizontal lines. The dashed horizontal line indicates the theoretical inertial period ($T = \frac{2\pi}{f}$, where $f = 2\omega \sin\phi$; ω is the angular frequency of rotation of the earth and ϕ is the latitude) at the location. Note that the colour scale is not uniform.

(Figure 4.2a). The mean flow is weak at all locations, but the standard deviation at Paradip is comparable to that for the alongshore component (Figure 4.2b).

A comparison at 40 m shows that the cross-shore current is weak in comparison to the alongshore component most of the time at Gopalpur and Kakinada (Figure 4.14), but there are a few instances when the cross-shore burst is comparable to the alongshore current at these locations: examples include April 2010 at Gopalpur and April 2011 and 2012 at Kakinada. The nature of variability observed at these two locations leads to several peaks in the FFT (Figure 4.3) and broad peaks, but with little power, in the wavelet spectrum (Figure 4.15). It is only at Paradip, where the cross-shore current peaks during spring (generally offshore) and the summer monsoon (generally onshore) (Figure 4.14), that the FFT and wavelet power tend to show a higher peak around 100–150 days. We discuss the reasons for this relatively strong cross-shore flow at Paradip in Section 4.3.

The WCA suggests a strong coherence at the annual cycle from Paradip to Kakinada (Figure 4.16), but it must be noted that the wavelet power at this period is low (Figure 4.15). The bursts during spring (Figures 4.14 and 4.15) lead to a statistically significant coherence beween these two locations, but with a large phase difference. As may be expected for a weak current that shows but a few bursts, the cross-shore component of the EICC decorrelates along the coast.

4.3 Discussion

The four-year record length of ADCP data and the sampling interval of one hour allow a hitherto unprecedented analysis of the variability of the EICC over a range of frequencies. Such an analysis was possible earlier for only the near-surface current with satellite altimeter data (Durand et al., 2009; Cheng et al., 2013), but these ADCP data provide a vertical profile over the depth range 40–300 m.

Analysis of the data shows a high coherence for the annual cycle along the coast (Fig-

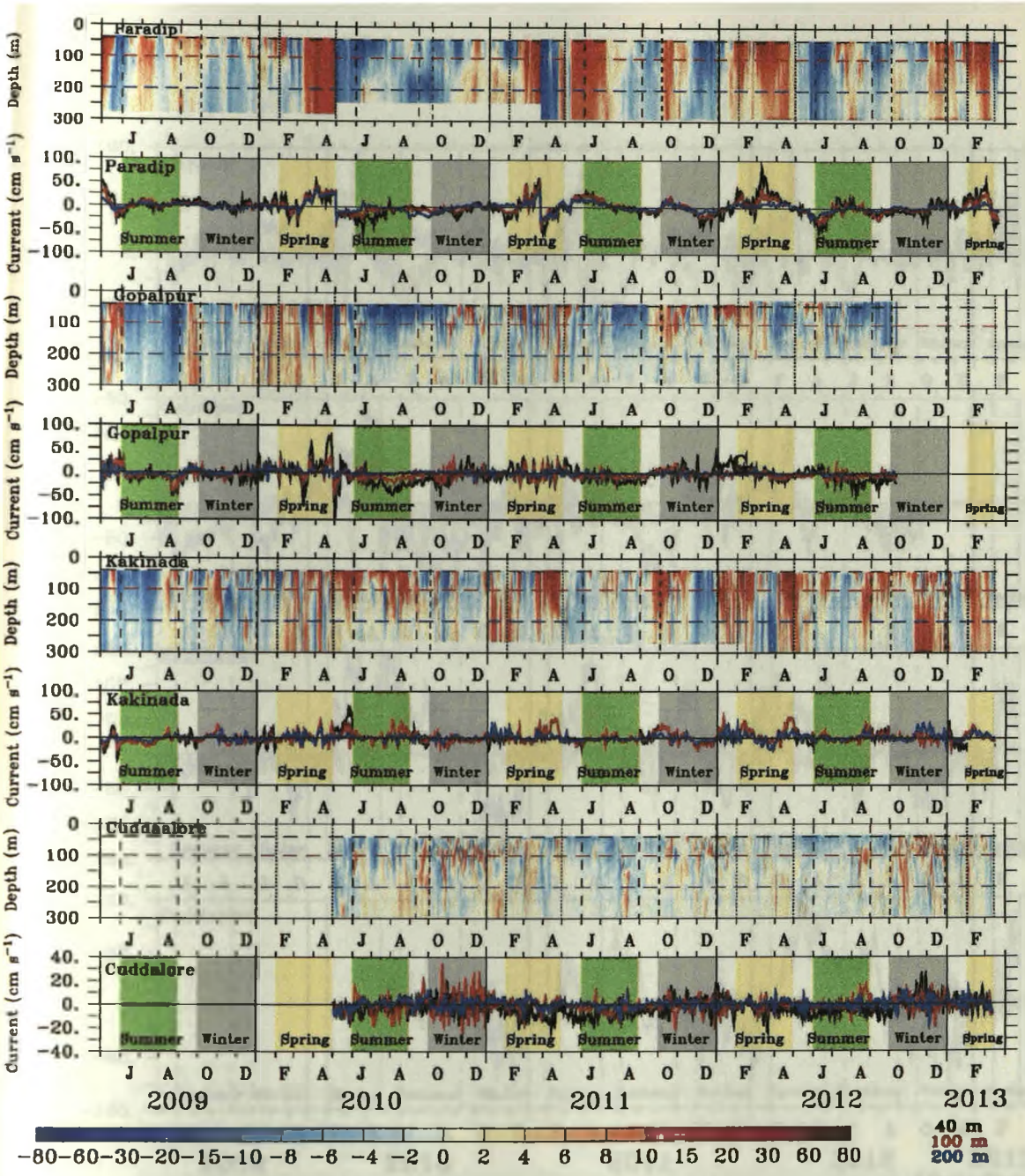

Figure 4.13: 2.5-day low-pass-filtered, detided, residual cross-shore current (cm s^{-1}). An upwelling favourable current is positive, which implies that the current is positive when it flows offshore (southward at Paradip). The solid vertical lines mark the years. The dashed vertical lines in the odd panels and the yellow, green, and gray shading in the odd panels are used to denote the periods spring (February–May), summer monsoon (June–September), and winter (October–December), respectively. The dashed horizontal lines in the odd panels mark the 40 m (black), 100 m (red), and 200 m (blue) depths, and the currents at these depths are plotted in the respective colours in every even panel; the black horizontal line in these panels marks the zero current. The location name is at the top left corner in each panel. Note that the colour scale is not uniform.

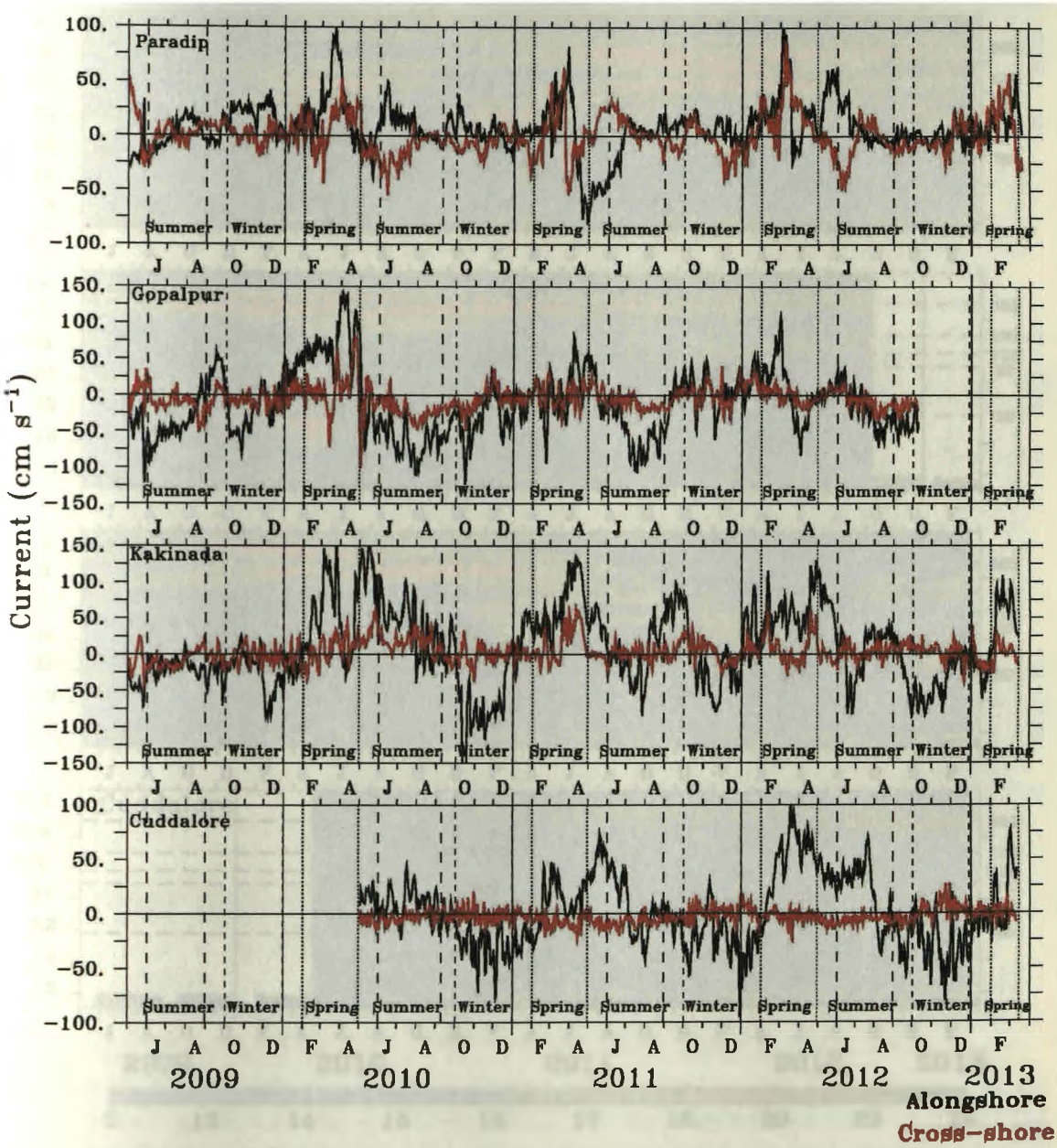

Figure 4.14: Comparison between alongshore (black) and cross-shore (red) currents (cm s^{-1}) at 40 m depth. The sign convention for the alongshore and cross-shore components is as in Figures 4.1 and 4.13, respectively.

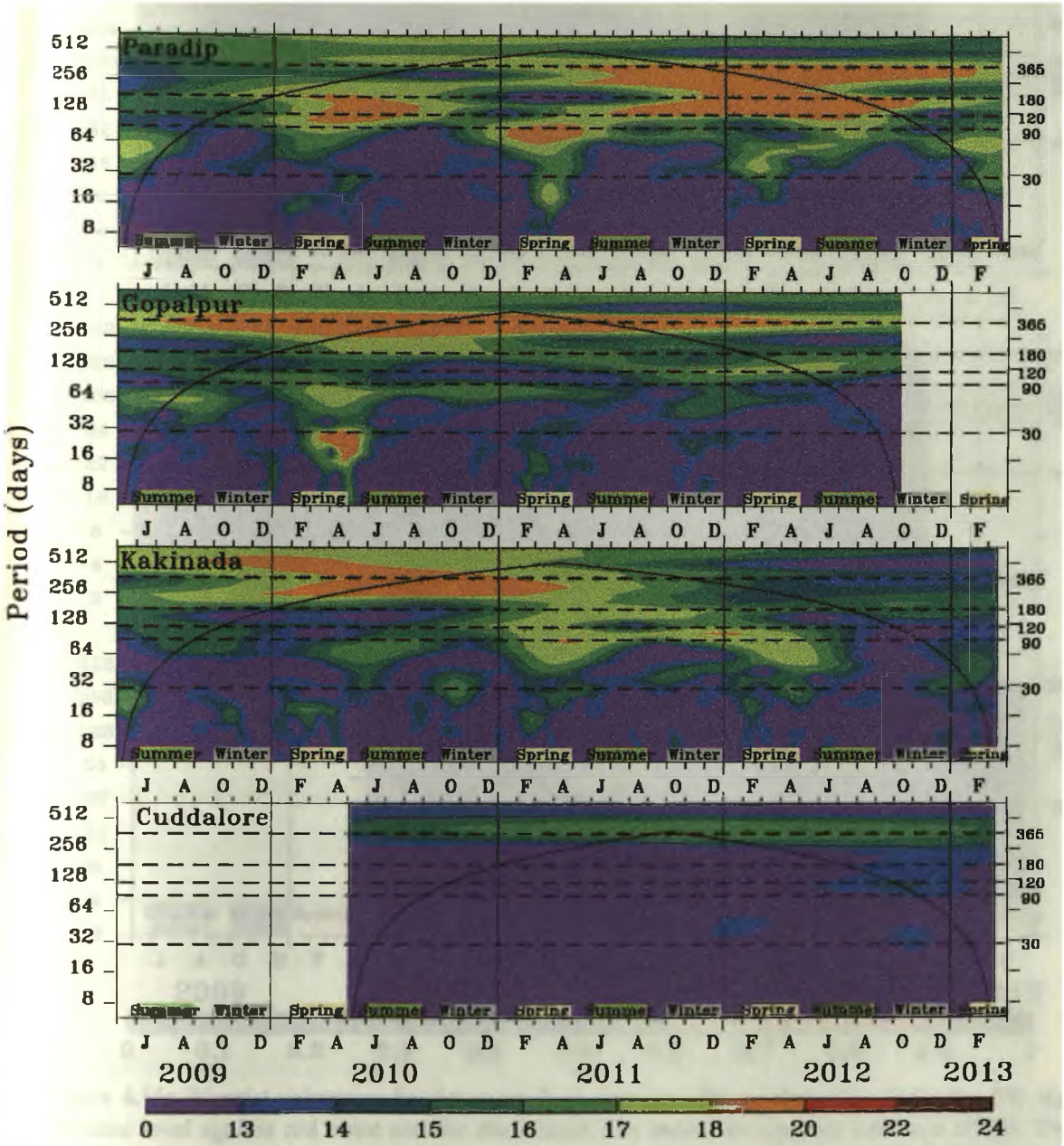

Figure 4.15: Morlet wavelet power spectra (cm^2s^{-2}) of the cross-shore currents at 40 m depth. The thick black line shows the cone of influence. The ordinate axis and wavelet power are plotted on a $\log_2$ scale. The horizontal dashed lines mark the 30-day, 90- day, 120-day, 180-day, and 365-day periods.

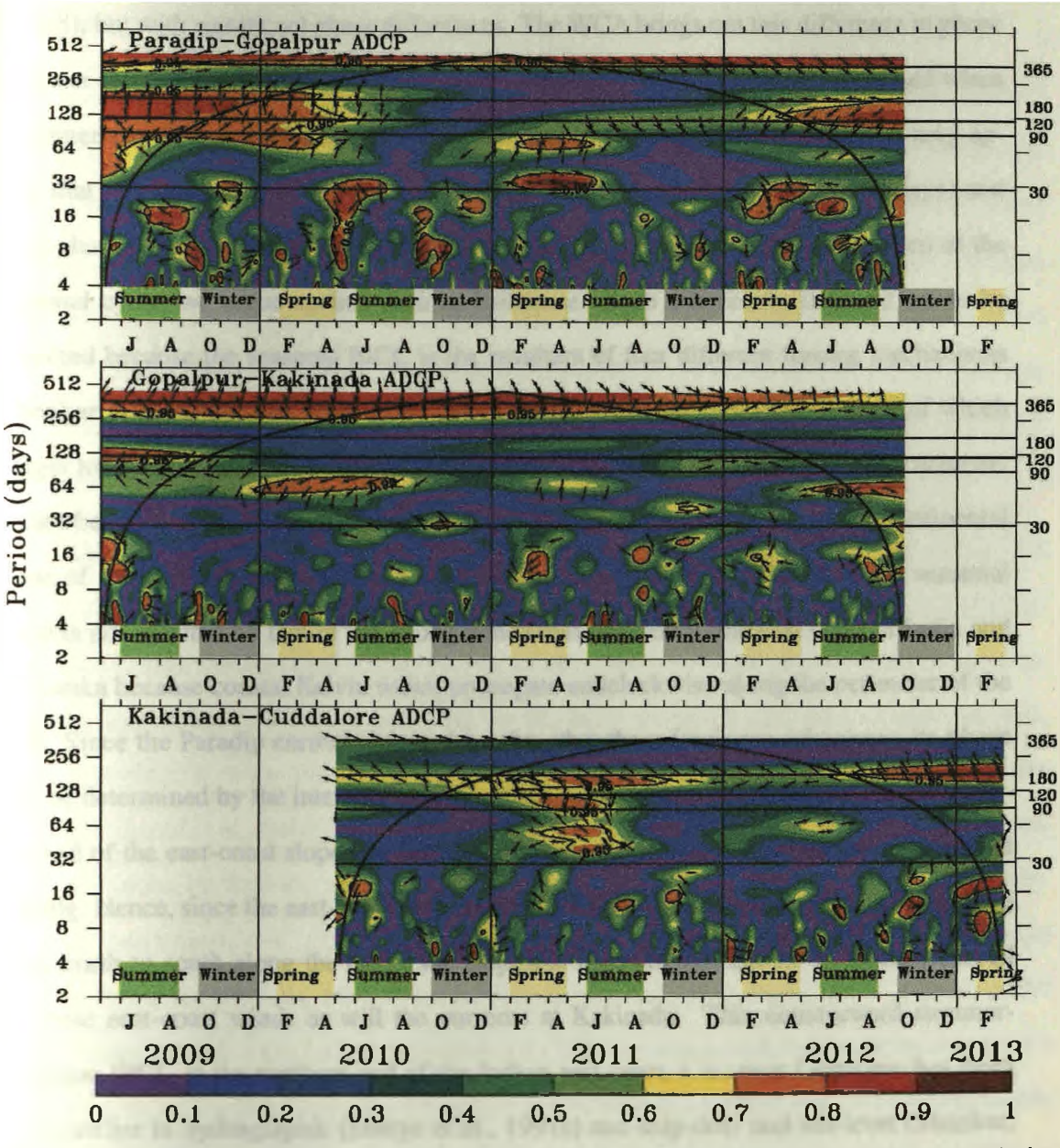

Figure 4.16: Wavelet coherence for the cross-shore currents. The contour line shows the 5% significance level against red noise and the thick black line shows the cone of influence (COI). The arrows show the relative phase relationship with in-phase (anti-phase) pointing right (left). The first station leads (lags) the second station in anticlockwise (clockwise) direction. The arrows are shown only for wavelet coherence of 0.5 or more. In order from top to bottom, the panels show the wavelet coherence for the pairs (a) Paradip-Gopalpur, (b) Gopalpur-Kakinada, and (c) Kakinada-Cuddalore. Note that the ordinate (period) is plotted on a $\log_2$ scale. The horizontal solid lines mark the 30-day, 90-day, 120-day, 180-day, and 365-day periods.

ure 4.8), but with significant phase differences. The WCA brings out this difference in phase between successive mooring pairs, presenting a facet of the variability that is missed when the coherence is evaluated using cross-correlations (figure not shown). Though it may appear that the weak coherence for the intra-annual EICC (period range 100–250 days) and large phase difference for the annual EICC suggest an alongshore decorrelation even of the seasonal cycle, we argue against such an inference. Such differences in phase are to be expected because the seasonal EICC is the resultant of four different forcing mechanisms (Shankar et al., 1996; McCreary et al., 1996; Vinayachandran et al., 1996), each of which trigger long, baroclinic waves. Differences in the timing of the reversal is therefore to be expected because of the location of the moorings. The Paradip mooring lies on the continental slope of the northern BoB (and at a deeper depth of $\sim$ 2000 m). Therefore, its seasonal cycle is not affected by that of the strong winds that are local to the east coast of India and Sri Lanka because coastal Kelvin waves propagate anticlockwise along the perimeter of the BoB. Since the Paradip current is forced by the other three forcing mechanisms, its phase will be determined by the interplay between them. The Gopalpur mooring lies at the northern end of the east-coast slope and is therefore at the northern edge of the east-coast wind forcing. Hence, since the east-coast response to the local winds is determined by integrating from north to south along the coast, the Gopalpur currents will not be as strongly forced by these east-coast winds as will the currents at Kakinada. This equatorward summer-monsoon EICC at the northern end of the Indian east coast, i. e., near Gopalpur, has been noted earlier in hydrographic (Shetye et al., 1991c) and ship-drift and sea-level (Shankar, 1998, 2000) data and has been attributed to forcing from the equator and to interior Ekman pumping (McCreary et al., 1993, 1996). Cuddalore's location near the 10°N separator for Ekman pumping over the BoB (McCreary et al., 1996) leads to the weaker coherence with Kakinada. In summary, the complex interplay among the four forcing mechanisms with respect to their amplitudes and phases can produce fairly complicated patterns even in the

seasonal EICC.

A striking feature of the seasonal cycle on the east coast is the strong peak around 120 days (Figures 4.3–4.4). Such a peak was not prominent off the west coast, where peaks at 100–110 (140) days were seen at Mumbai (Kollam). Nethery and Shankar (2007) noted this 120-day peak in the current measurements made by Schott et al. (1994) off the southern tip off Sri Lanka during 1991–1992, and it has been discussed by others subsequently (Han et al., 2011; Cheng et al., 2013; Girishkumar et al., 2013). What forces this 120-day peak at the mooring locations is not clear, but it dominates the seasonal cycle at Paradip in ADCP (Figure 4.4).

Intraseasonal variability in the 30–90-day band is weak at Paradip and Cuddalore, but the intraseasonal peaks at Kakinada and, to a lesser extent, Gopalpur, are significant (Figure 4.3). This intraseasonal variability varies seasonally, peaking during spring at all locations, but, except at Paradip, variability in this band extends to the other seasons as well. Nevertheless, it is the seasonal cycle that dominates the EICC variability, unlike for the WICC (Amol et al., 2014). The ADCP data also show variability at sub-inertial periods less than 30 days, particularly at Kakinada and Gopalpur. The 12-day period noted on the west-coast shelf (Amol et al., 2012) and slope (Amol et al., 2014) is seen on the east-coast slope as well, but the four-day band is not evident on the east coast (Figure 4.3). A burst in the 8–12-day band at Kakinada and Cuddalore is often accompanied by near-inertial currents (Figure 4.12), but there is a clear separation between the sub-inertial and near- inertial bands at Paradip and Gopalpur.

The ADCPs data show evidence of upward phase propagation, which indicates downward propagation of energy (Figure 4.5). This upward propagation of phase can introduce a lag between the ADCP current at 40 m (the topmost common depth level) and the surface current. Downward propagation of phase, seen off the west coast (Amol et al., 2014), is seen in the east-coast moorings as well; an example is seen at Cuddalore during June 2010

to April 2011 (Figure 4.6). A possible explanation for this downward phase propagation is the combination of vertical normal modes associated with locally and remotely forced currents.

The upward propagation of phase led to distinct undercurrents off the west coast (Amol et al., 2014). Off the east coast and at the Paradip mooring, however, the vertical phase speed is much higher compared to the west coast, the only exception being the much slower phase propagation in the top 100 m at Cuddalore (Figure 4.5). As a result, a distinct undercurrent is seen only at Cuddalore over most of the year; at other locations, the current is unidirectional over the top 300 m during spring, but an undercurrent does tend to form during the summer monsoon and winter. We note, however, that the ADCPs do not sample the top $\sim$ 40 m, and the short Gopalpur record with measurements till 24 m suggests that there can be occasions on which the surface current may even be directed opposite to that at 40 m.

Off the west coast, strong cross-shore currents were found at Kollam and Kanyakumari (see the loations at Figure 1.2), the two southernmost locations; the weakening of the cross-shore current at Goa and Mumbai (see the locations at Figure 1.2) farther north was attributed to the smaller length scale, the Rossby radius of deformation, at these locations (Amol et al., 2014). In contrast, off the east coast, the cross-shore currents are weakest at Cuddalore, the southernmost location (Figures 4.13 and 4.15). Cross-shore flows occur in bursts, typically during spring, at Kakinada and Gopalpur. It is only at Paradip, the northernmost location and therefore the one with the smallest length scale, that the cross-shore component is often comparable to the alongshore component during spring and the summer monsoon (Figure 4.14). Examination of the altimeter sea level suggests that such strong cross-shore flows are associated with eddy-like circulations (Figure 4.17).

The four-year-long ADCP data record off the Indian east coast provides an opportunity to validate available popular data products that are widely used in the absence of direct current measurements. Our next chapter is devoted to validate these data products.

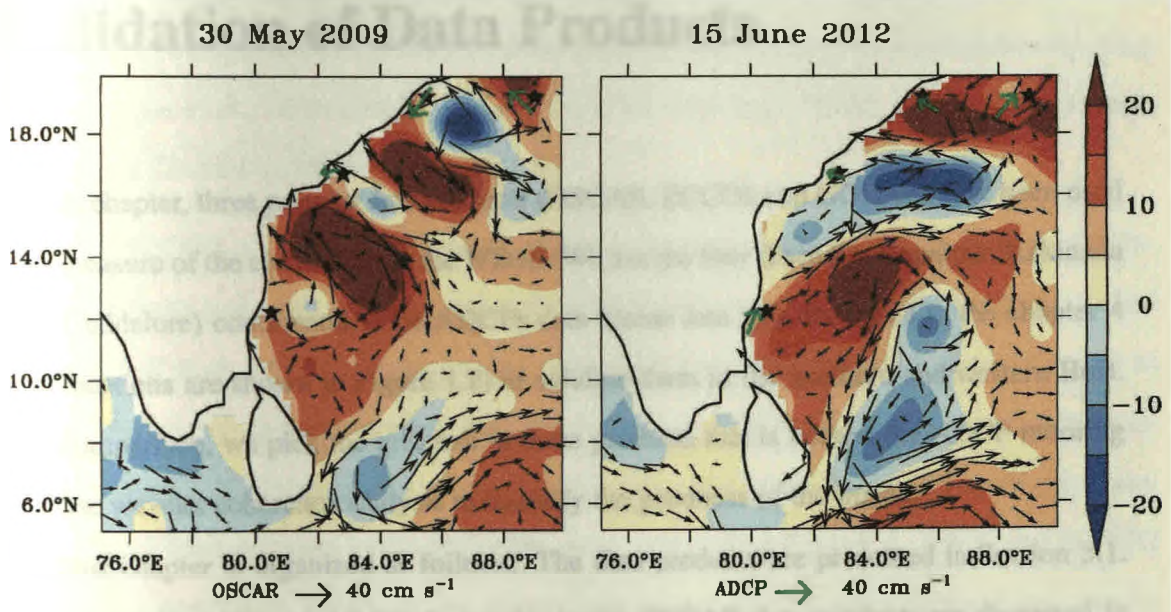

Figure 4.17: OSCAR currents and sea-level anomalies from altimeter (AVISO, 1996) for (a) 30 May 2009 and (b) 15 June 2012. The thick green arrows show the ADCP current vectors.

Chapter 5

Validation of Data Products

In this chapter, three popular data products (OSCAR, ECCO2 and GODAS) have been used as a measure of the circulation in the WBoB. We use the four (Paradip, Gopalpur, Kakinada and Cuddalore) continental slope ADCPs data (same data sets discussed in the chapter 4 and locations are shown in Figure 1.2) to validate them in the northern and western BoB. For comparison, we pick the grid cell in these products that is nearest the ADCP mooring and use wavelet coherence analysis to quantify the goodness of the match.

This chapter is organized as follows. The data products are presented in Section 5.1. A detailed validation of ADCP observations with OSCAR data products are discussed in Section 5.2. The performance of ECCO2 and GODAS are evaluated in Section 5.3. The results are briefly summarized in Section 5.4

5.1 Data Products

The first data product we use is OSCAR (Ocean Surface Currents Analyses Real-time) (Bonjean and Lagerloef, 2002), an ocean-surface-current data product in which the velocities are derived from satellite measurements. SLA (sea level anomaly) from altimeters, wind speed and direction from scatterometers, and SST are used in this diagnostic model to combine the

geostrophic, Ekman-Stommel, and thermal-wind relations, yielding a current-vector field representing the average current over the top 30 m on a 0.33° grid every five days. OSCAR has been used for several studies in the NIO (Chacko et al., 2012; Ratnam et al., 2009; Sreenivas et al., 2012) and has been validated against buoy measurements from the EIO and central BoB (Sikhakolli et al., 2013).

Unlike OSCAR, which is based on satellite data, the other two popular data products, ECCO2 (Estimating the Circulation and Climate of the Ocean, Phase II) (Stammer et al., 2002a,b; Menemenlis et al., 2005) and GODAS (Global Ocean Data Assimilation System) (Behringer et al., 1998; Behringer and Xue, 2004; Behringer, 2007), are based on Oceanic General Circulation Models (OGCMs).

In ECCO2, a cubed-sphere-model output interpolated on a 0.25° grid, in situ temperature, salinity and mean velocity from surface drifters are assimilated using an adjoint method (Marshall et al., 1997). The model has 50 vertical levels and thickness ranges from 10 m near the surface to approximately 450 m at a depth of 4150 m; the output is available every three days. ECCO2 has been used for a large number of oceanographic and interdisciplinary studies, including some in the NIO (Rao et al., 2012; Sreenivas et al., 2012) and the EIO (Pandey and Singh, 2010). A list of publications and reports since 2005 till date can be found at `http://ecco2.org/manuscripts`.

In GODAS, a real-time ocean analysis developed at the National Centers for Environmental Prediction (NCEP), is based on GFDL's (Geophysical Fluid Dynamics Laboratory) MOMv3 (Modular Ocean Model version 3) (Pacanowski and Griffies, 1998) and the data are assimilated in a 3D-VAR scheme (Derber and Rosati, 1989). The model has 40 vertical levels with 10 m bins in upper 200 m and the resolution is $1° \times 1°$ ($1° \times 0.33°$ near the Equator). GODAS is forced by the momentum, heat, and freshwater fluxes from the NCEP Atmospheric Reanalysis (version) 2. The output is available every five days. The product has been used for a few studies in the NIO (Rao et al., 2012; Chacko et al., 2012; Wu et al.,

2012) and a modified version of this product is used in the Indian Ocean Forecast System (INDOFOS) (Ravichandran et al., 2013).

5.2 Validation of OSCAR

Comparison of OSCAR and measured currents has been made earlier (Johnson et al., 2007; Sikhakolli et al., 2013) and these currents are regularly validated against moored buoys and global drifters (`http://www.oscar.noaa.gov/`). Except within 10° of the Equator, where its reliance on geostrophy implies a poor match with observations, OSCAR has shown fairly good correlation with the in-situ current data even though it underestimates the magnitude of the current (Johnson et al., 2007). In the EIO and the EBoB , Sikhakolli et al. (2013) showed that the OSCAR zonal current matched that measured by the RAMA (Research Moored Array for African-Asian-Australian Monsoon Analysis and Prediction) moorings (See Figure 1.2 for the location of these moorings) (McPhaden et al., 2009); the match for the meridional component, which showed fluctuations at higher frequencies, was not as good. There are, however, no studies validating OSCAR currents in the regime of the WBC represented by the EICC. We compare the OSCAR currents, which represent the average current over the top 30 m, to ADCPs currents at 40 m depth (the bin closest to the surface). To the best of our knowledge, the only validation of OSCAR against ADCPs data for a boundary current was made by Amol et al. (2014), who found a high coherence, but with significant phase differences, between ADCP currents off the Indian west coast and OSCAR at seasonal as well as intraseasonal periods; Amol et al. also noted that there were occasions when the OSCAR current was directed opposite to the ADCP current.

The five-day sampling interval of OSCAR currents implies that they should be able to resolve the seasonal (period greater than 100 days) and intraseasonal (30–90 days) bands, and we do see a reasonable match between OSCAR and ADCP currents (Figure 5.1). The match is particularly good at Paradip (see Table 5.1 for the correlations) owing to the domi-

Data type	Alongshore				Crossshore			
	P	G	K	C	P	G	K	C
OSCAR	**0.89**	**0.77**	**0.75**	**0.71**	**0.44**	**0.39**	**0.47**	**0.30**
ECCO2	**-0.36**	**0.53**	**0.28**	**0.64**	0.07	**0.10**	-0.02	**0.50**
GODAS	-0.03	**0.56**	**0.64**	**0.44**	**0.28**	**0.10**	**0.37**	**0.41**

Table 5.1: Correlation between currents from ADCP measurements and data products for both alongshore and cross-shore components of the current. P, G, K, and C represent Paradip, Gopalpur, Kakinada, and Cuddalore mooring respectively. Note that alongshore and cross-shore current at Paradip indicates zonal and meridional current, respectively. Correlation values in boldface notation exceed the 99% significance level; the significance of the correlations was computed by comparing the correlations for the filtered time series with the correlations obtained on applying the same Butterworth filter to random time series (Shankar, 1998).

nance of the seasonal cycle at this location. At other locations, the coherence is high for the annual cycle and in patches for the intra-annual periods, but the match is poor for intraseasonal variability (Figure 5.2), leading to a lower correlation (Table 5.1) than at Paradip. OSCAR is unable to capture the month-long bursts seen in the ADCP data at Gopalpur (examples include April 2010 and February and April 2012), Kakinada (examples include February–May 2010 and April 2011), and to a lesser extent, Cuddalore. The correlation is worse for the cross-shore component (Table 5.1).

5.3 Validation of ECCO2 and GODAS

Unlike with OSCAR, the comparison between the currents at 40 m from the ADCP and ECCO2 is poor at Paradip (Figure 5.1). The match is poor at Kakinada and Cuddalore as well, but is better at Gopalpur because the annual cycle is simulated well at this location (Figure 5.3). The coherence exceeds 0.8 for the annual cycle at Kakinada and Cuddalore, leading to a correlation of 0.64 for the later (Table 5.1), but there is a significant difference in phase between the ADCP and ECCO2 currents at Kakinada, leading to a low correlation (Table 5.1). This mismatch is seen even if we use the ECCO2 currents at 5 m or 55 m instead of 40 m. Furthermore, the correlations decrease with increasing depth (Figure 5.4a).

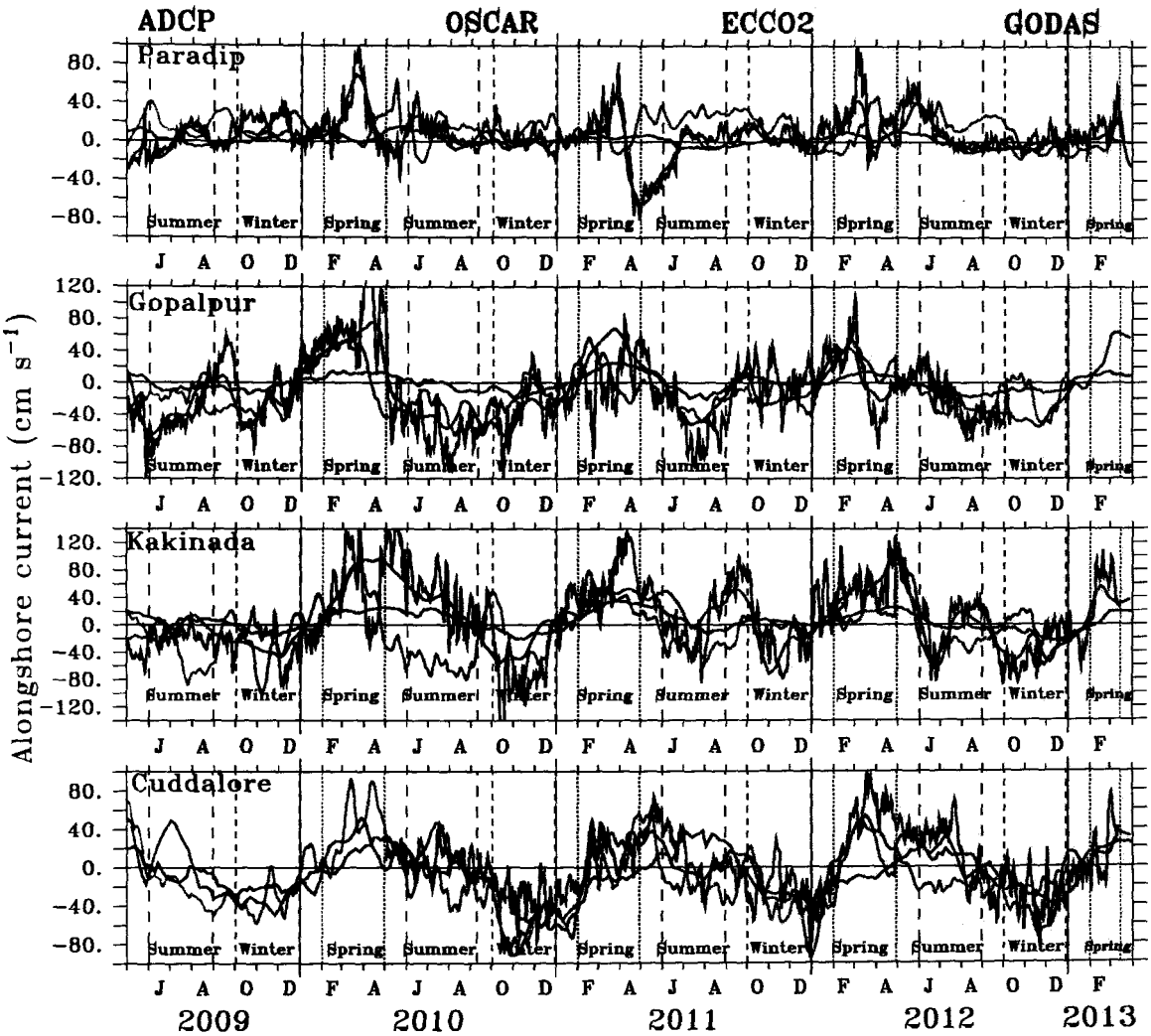

Figure 5.1: Comparison between alongshore currents (cm s^{-1}) measured by the ADCPs at 40 m and the alongshore currents from OSCAR, ECCO2, and GODAS. The ECCO2 and GODAS currents were picked at the same depth as the ADCP current, i. e., 40 m, but the OSCAR current represents an average over 0–30 m.

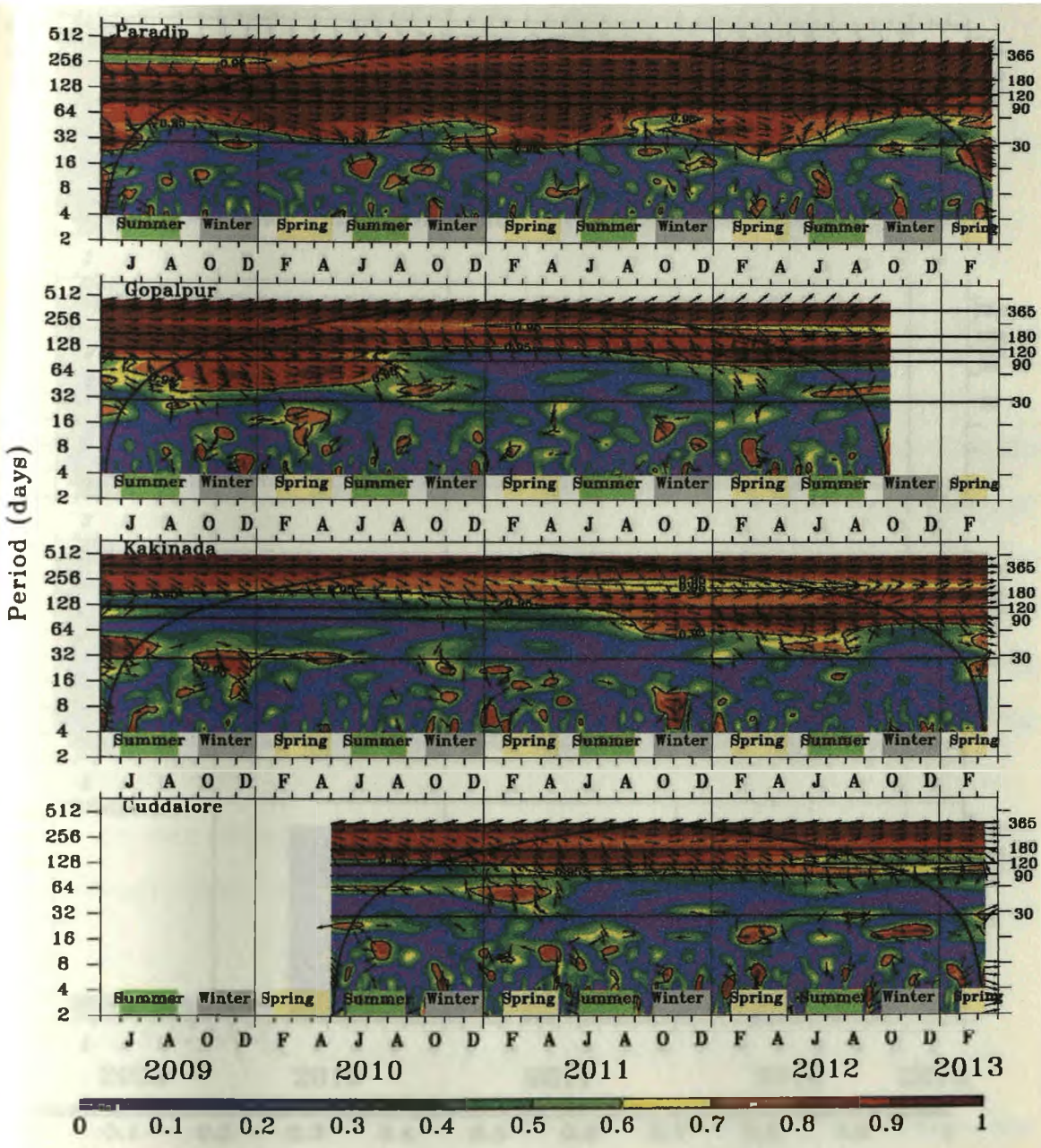

Figure 5.2: Wavelet coherence between ADCP and OSCAR alongshore currents. The contour line shows the 5% significance level against red noise and the thick black line shows the COI. The arrows show the relative phase relationship with in-phase (anti-phase) pointing right (left). The first station leads (lags) the second station in anticlockwise (clockwise) direction. The arrows are shown only for wavelet coherence of 0.5 or more. Note that the ordinate (period) is plotted on a $\log_2$ scale. The horizontal solid lines mark the 30-day, 90-day, 120-day, 180-day, and 365-day periods.

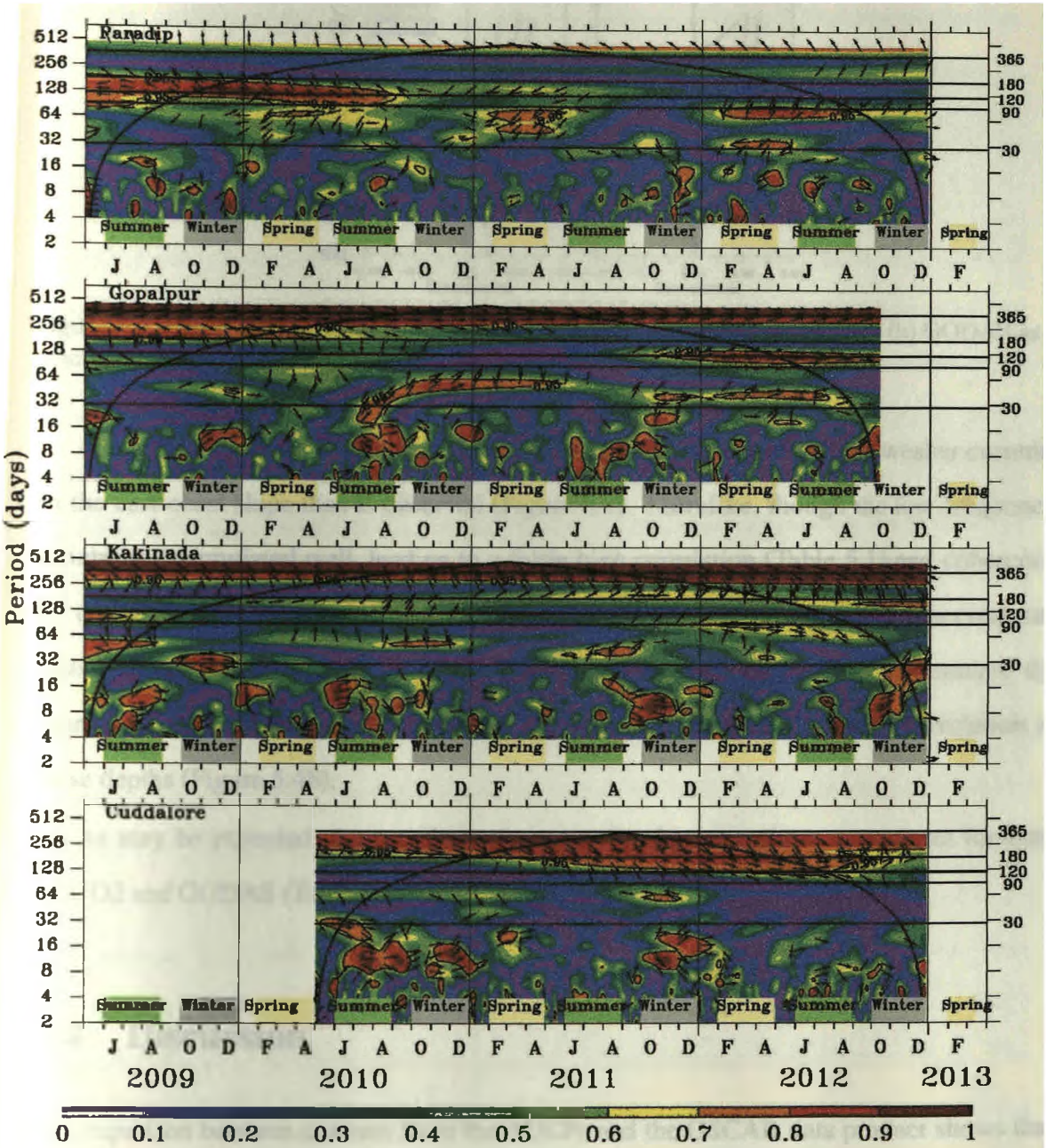

Figure 5.3: Wavelet coherence between ADCP and ECCO2 alongshore currents. The contour line shows the 5% significance level against red noise and the thick black line shows the COI. The arrows show the relative phase relationship with in-phase (anti-phase) pointing right (left). The first station leads (lags) the second station in anticlockwise (clockwise) direction. The arrows are shown only for wavelet coherence of 0.5 or more. Note that the ordinate (period) is plotted on a $\log_2$ scale. The horizontal solid lines mark the 30-day, 90-day, 120-day, 180-day, and 365-day periods.

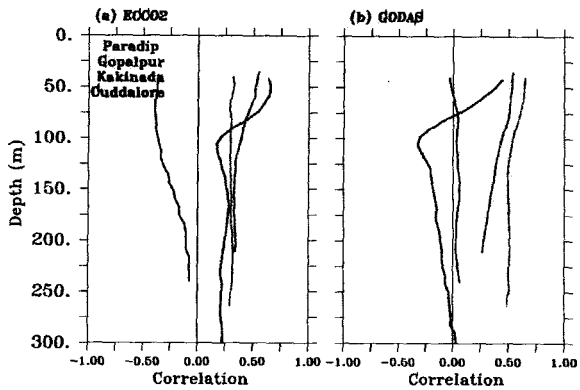

Figure 5.4: Correlation between alongshore currents from ADCP and (a) ECCO2 (b) GODAS as a function of depth.

As on the west-coast slope (Amol et al., 2014), GODAS simulates much weaker currents on the east-coast slope than is observed (Figure 5.1). Therefore, though the low-frequency variability is simulated well, leading to a fairly high correlation (Table 5.1) and coherence for the annual cycle (figure not shown), the match between the GODAS and observed currents is much worse than for ECCO2. Indeed, the inability of GODAS to simulate the change in current direction below 100 m at Cuddalore leads to a negative correlation at these depths (Figure 5.4b).

As may be expected, the correlation is worse for the cross-shore component for both ECCO2 and GODAS (Table 5.1).

5.4 Discussion

A comparison between currents from the ADCPs and the OSCAR data product shows that the latter is able to capture both seasonal and intraseasonal variability only for the Paradip mooring, where the match is remarkably good (Figures 5.1–5.2). At the other three locations, which are on the continental slope of the western boundary, the OSCAR currents are able to capture only the seasonal variability; the match at intraseasonal periods is reasonable, but there are several intraseasonal bursts that are seen in the ADCP data, but not in OSCAR.

A wavelet analysis of the OSCAR data at the four locations (Figure 5.5) shows similarities with the ADCP wavelet spectrum (Figure 4.4), but there are also significant differences. A WCA analysis for the OSCAR data from the mooring locations (Figure 5.6) leads to results similar to the ADCP WCA (Figure 4.8).

ADCP data shows evidence of upward phase propagation (see chapter 3). This upward propagation of phase can introduce a lag between the ADCP current at 40 m (the topmost common depth level) and the surface current. OSCAR is supposed to represent the current averaged over the top 30 m. The mixed layer in the BoB is shallower than 40 m at the mooring locations throughout the year (Montegut et al., 2004; Chatterjee et al., 2012) (Figure 5.7), and it is possible that the phase continues to propagate upward till the base of the mixed layer, which is within the averaging depth range of the OSCAR currents. Therefore, we examined the current data at Gopalpur during February–October 2012, when the data are available till 24 m because the ADCP was deployed at a shallower depth on the mooring line (Table 1.1). The 30-day low-pass-filtered current at 24 m is similar to the 40 m current in that both are in the same direction most of the time, but the magnitude range is less at 24 m (Figure 5.8). The two currents are in opposite directions during March–April because the equatorward current core is centred around 60 m and therefore represents an undercurrent. The result of these differences is that the 24 m current lags (leads) the 40 m current during February–March (March–April), but the weaker variability near the surface makes it difficult to decide if there is a definite change in phase from 40 m to 24 m. The OSCAR current seems to match the 40 m current better, unlike on the west coast, where the difference between the 24 m and 48 m ADCP currents and the OSCAR current was not as striking (Amol et al., 2014).

Apart from OSCAR, we validated the currents estimated from two model-based data products, ECCO2 and GODAS. As found off the west coast (Amol et al., 2014), the variability simulated by GODAS is weak, but ECCO2 fares better at the three locations on the

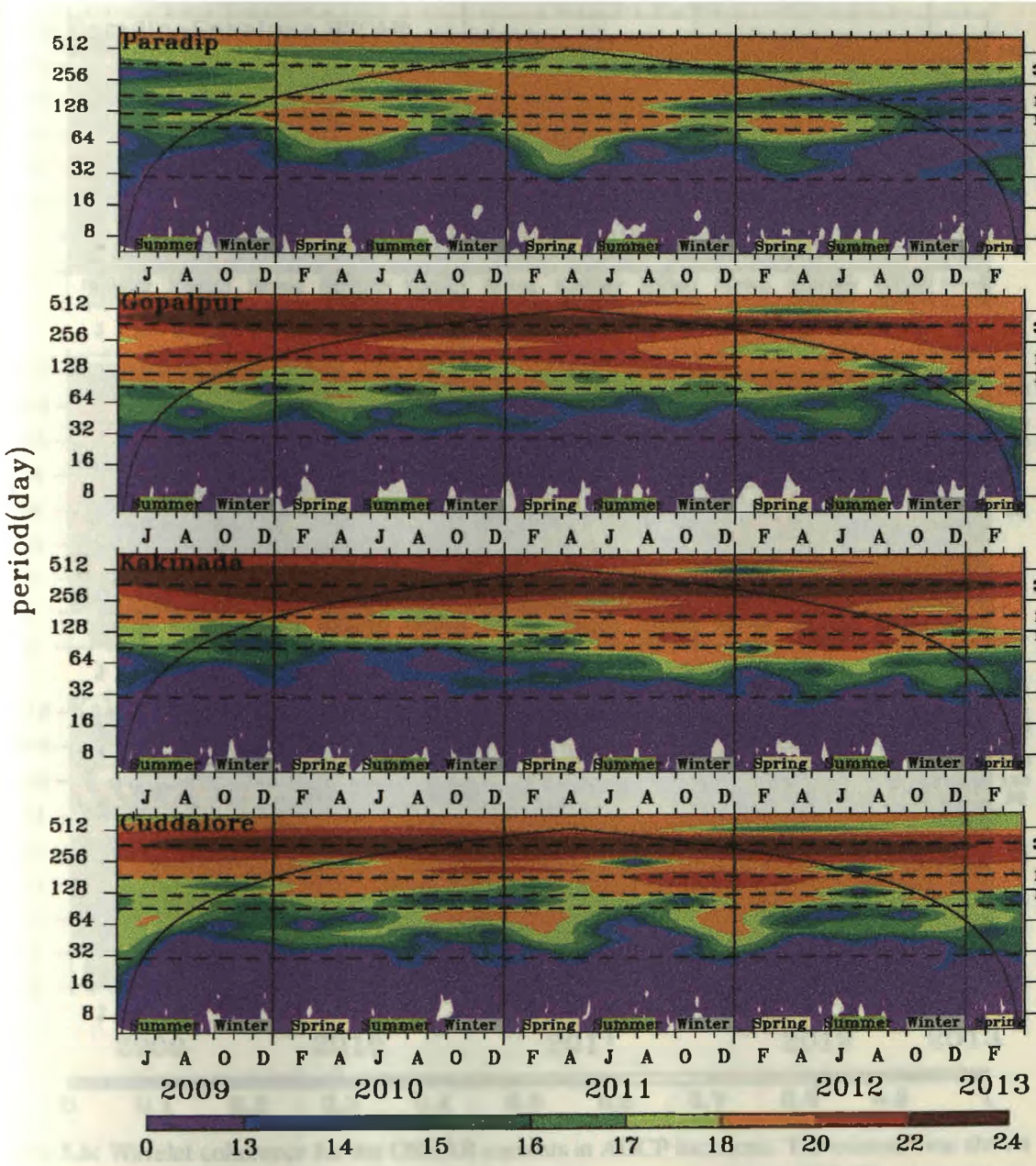

Figure 5.5: Morlet wavelet power spectra ($cm^2\ s^{-2}$) for OSCAR alongshore currents calculated at the ADCP locations. The thick black line shows the COI. The ordinate and wavelet power are plotted on a $\log_2$ scale. The horizontal dashed lines mark the 30-day, 90-day, 120-day, 180-day, and 365-day periods. Note that the colour scale is not uniform.

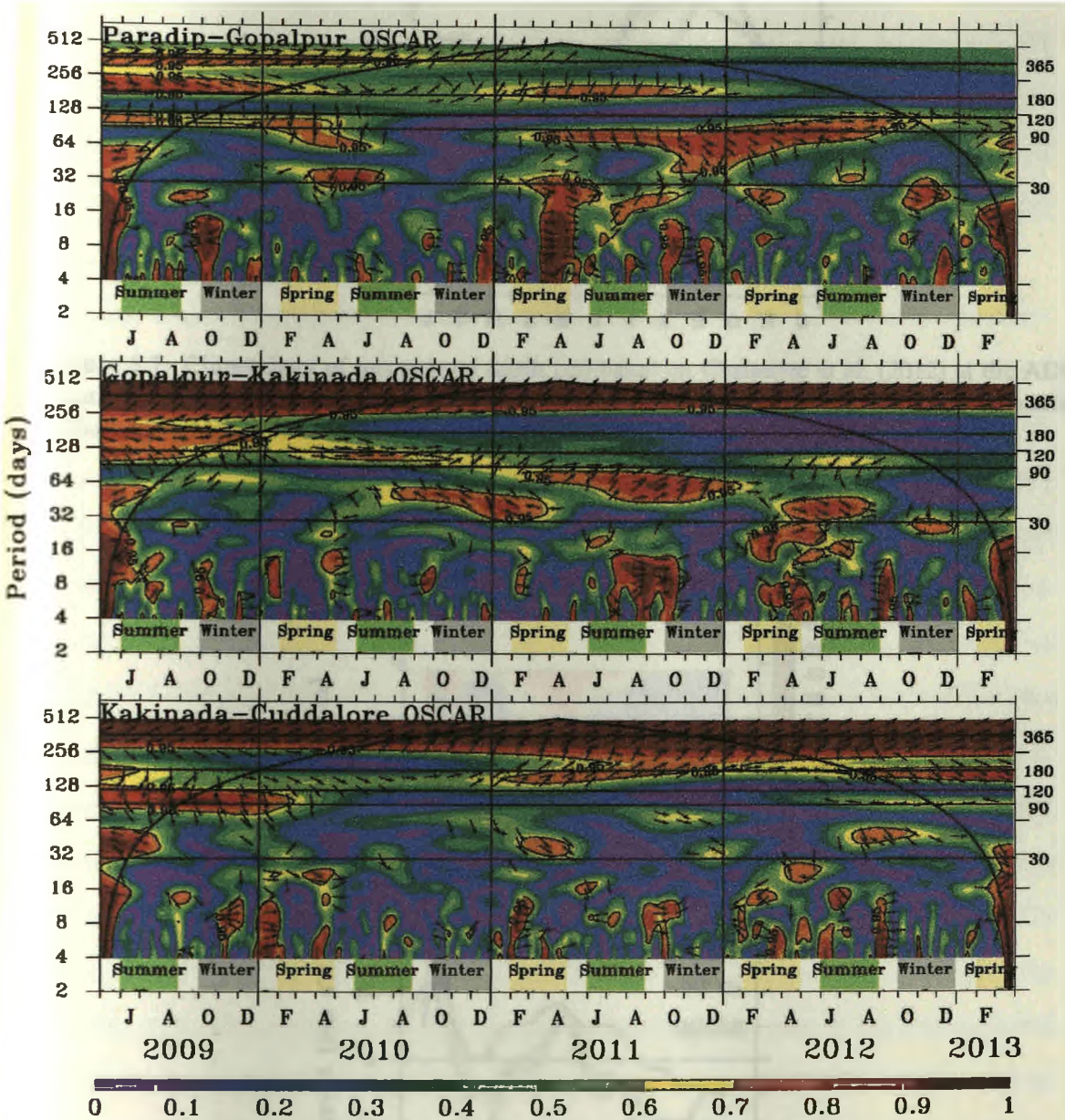

Figure 5.6: Wavelet coherence for the OSCAR currents at ADCP locations. The contour line shows the 5% significance level against red noise and the thick black line shows the COI. The arrows show the relative phase relationship with in-phase (anti-phase) pointing right (left). The first station leads (lags) the second station in anticlockwise (clockwise) direction. The arrows are shown only for wavelet coherence of 0.5 or more. Note that the ordinate (period) is plotted on a $\log_2$ scale. The horizontal solid lines mark the 30-day, 90-day, 120-day, 180-day, and 365-day periods.

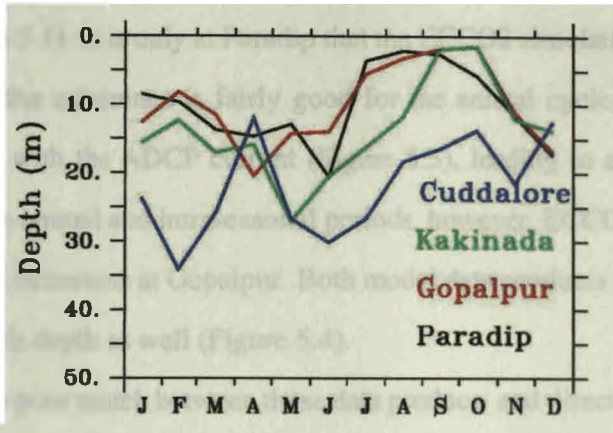

Figure 5.7: Climatology of mixed layer depth (m) based on Chatterjee et al. (2012) at the ADCP locations. The mixed layer depth is assumed to be the depth at which the density exceeds the surface density by 0.2 kg m^{-3}.

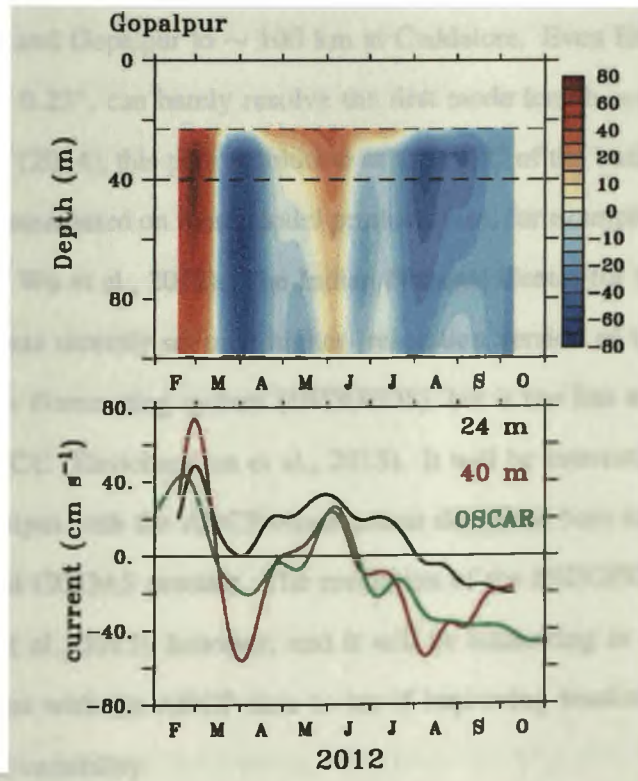

Figure 5.8: The top panel shows the 30-day low-passed currents as a function of depth at Gopalpur. The dashed horizontal lines mark the 24 m and 40 m water depth. The bottom panel shows the same 30-day low-passed currents at 24 m and 40 m and for the OSCAR product.

east-coast slope (Figure 5.1). It is only at Paradip that the ECCO2 simulation is really poor; at the other locations, the coherence is fairly good for the annual cycle, but the ECCO2 current is not in phase with the ADCP current (Figure 5.3), leading to a poor correlation (Table 5.1). At the intra-annual and intraseasonal periods, however, ECCO2 shows a match with the ADCP only on occasions at Gopalpur. Both model data products fail to capture the observed variability with depth as well (Figure 5.4).

A key reason for the poor match between these data products and direct current measurements is likely to be the coarse model resolution (Johnson et al., 2007; Amol et al., 2014). GODAS has a horizontal resolution of 1°, which is too coarse for resolving the characteristic cross-shore length scale, the Rossby radius of deformation, of even the gravest baroclinic mode off the east coast of India. The Rossby radius for the first vertical mode varies from $\sim$ 60 km at Paradip and Gopalpur to $\sim$ 100 km at Cuddalore. Even ECCO2, with a horizontal resolution of 0.25°, can barely resolve the first mode length scale at Paradip. As noted by Amol et al. (2014), this poor resolution of the WBC of the basin has implications for any budget estimates based on these model products (see, for example, Rao et al., 2012; Chacko et al., 2012; Wu et al., 2012). The Indian National Centre for Ocean Information Services (INCOIS) has recently set up a higher- resolution version of the GODAS model for the Indian-Ocean Forecasting system (INDOFOS), but it too has a 0.5° resolution in the regime of the EICC (Ravichandran et al., 2013). It will be interesting to compare the INCOIS GODAS output with the ADCP observations described here to see if it performs better than the global GODAS product. The resolution of the INDOFOS models is being improved (Francis et al., 2013), however, and it will be interesting to compare the high-resolution simulations with the ADCP data to see if improving resolution is sufficient to capture the observed variability.

Hence, in the next chapter, we use a high resolution OGCM simulating the observed EICC on the continental slope.

Chapter 6

Numerical simulation of the EICC

In this chapter, our aim is to simulate the observed variability of the EICC as seen in the four ADCP moorings. We use two numerical models, an OGCM, MOM and a linear, continuously model (LCS). MOM has been used extensively in modelling studies of the NIO (Kurian and Vinayachandran, 2007; Vinayachandran et al., 2007, 2012; Chatterjee et al., 2013, 2017); the LCS model has also been used extensively to analyse processes (Shankar et al., 1996; McCreary et al., 1996; Shankar and Shetye, 1997; Shankar et al., 2002, 2010; Miyama et al., 2003; Nethery and Shankar, 2007; Aparna et al., 2012; Chatterjee et al., 2013, 2017; Suresh et al., 2013) because it can be used more effectively to separate local and remote forcing effects.

We have four aims in this chapter. First, we evaluate the performance of a state-of-the-art OGCM in simulating the observed variability of the EICC on the continental slope. We show that MOM simulates well the observed annual cycle of the EICC, but the performance degrades for the intra-annual and intraseasonal components. Second, we test the importance of model resolution and nonlinearity. We show that even a 0.25° resolution suffices to simulate the observed variability in the EIO, but higher resolution is required to simulate currents in the BoB. Resolution also matters in the NBoB because of the significant role of instabilities. Third, we assess the role of stratification: we test the importance of the back-

ground density profile in the LCS model, showing that the stratification plays an important role in determining the magnitude of the surface current. Stratification affects both locally and remotely forced components, but has a stronger impact on the former. Fourth, we analyse the response of the EICC to remote forcing from the EIO. We show that the response of both sea level and current is similar at the annual and intra-annual time scales, but significantly different at intraseasonal time scales. This difference implies that the intraseasonal variability of the EICC owes less to remote forcing from the EIO than to local forcing.

The chapter is organised as follows. In Section 6.1, we describe the models used, and the model experiments. The model performance is validated in Section 6.3. The forcing mechanisms of the EICC at annual, intra-annual, and intraseasonal time scales are discussed in Section 6.4, and 6.5 shows that sea level and current off the east coast of India respond differently to remote forcing from the EIO at intraseasonal periods. The implication of stratification for the response to local and remote forcing is discussed in Section 6.6, and the impact of horizontal resolution and the effect of nonlinearity are discussed in Section 6.7. Section 6.8 concludes the chapter.

6.1 Ocean models

We use version 4p1 of MOM (MOM4p1; Griffies, 2009) and our model setup follows Chatterjee et al. (2013) and Chatterjee et al. (2017). Our LCS model configuration is similar to those in several earlier studies (McCreary et al., 1996; Shankar et al., 2010; Aparna et al., 2012; Chatterjee et al., 2013, 2017). The model physics parametrization of MOM4p1 are summarized in Table 6.1. Details of MOM4p1 model configurations and forcings are discussed in Appendix A.

Details of LCS model configurations and forcings are described in the Appendix B. Since the LCS model is linear, it is easy to separate the contribution of local and remote forcing to the EICC. The forcing by alongshore winds is isolated using a modified conti-

Physical processes	*Details of scheme and reference*
Horizontal and vertical advection of tracer	Multi-dimensional piece-wise parabolic method (MDPPM) (Colella and Woodward, 1984; Lin, 2004)
Horizontal friction	Combination of Smagorinsky, Laplacian, and biharmonic viscosities (Griffies and Hallberg, 2000)
Shortwave penetration into the upper ocean	Chlorophyll scheme (Morel and Antoine, 1994)
Neutral physics	Laplacian neutral diffusion (Griffies et al., 1998) and Laplacian GM skew diffusion (Griffies, 1998)
Vertical mixing	K-profile parametrization (KPP) scheme (Large et al., 1994)
Vertical diffusivity	Bryan and Lewis (1979)
Vertical mixing due to tide	Simmons et al. (2004)
Computation of potential temperature, density, and freezing temperature of sea water	Feistel (2003)

Table 6.1: Details of MOM4p1 model parameterisation schemes along with references.

nental boundary condition; this boundary condition has been used in several earlier studies (Shankar et al., 1996; McCreary et al., 1996; Chatterjee et al., 2017).

6.2 Numerical experiments

To isolate the processes, we carry out several experiments with both models, MOM4p1 and LCS. The main or control runs for both models, called MOMCR and LCSCR, respectively, are for a $0.1° \times 0.1°$ horizontal resolution.

The numerical experiment with MOM tests the impact of horizontal resolution. We carry out a simulation with a resolution of $0.25° \times 0.25°$ and this experiment is labelled MOM25. The configurations and forcing are the same, but the Smagorinsky viscosity coefficients are different for the two resolutions. For the $0.1° \times 0.1°$ ($0.25° \times 0.25°$) resolution, the value of Smagorinsky mixing coefficient for Laplacian viscosity is 0.06 (0.10), with velocity scale 0.04 m s^{-1}; for biharmonic viscosity, the Smagorinsky mixing coefficient is 0.002 (0.01) with velocity scale 0.005 m s^{-1}.

The LCS model is more amenable to experimentation because it is linear. We use it to separate the response to local and remote forcing, which is due to alongshore winds away from the western boundary of the bay, Ekman pumping over the bay, and the zonal winds over the EIO. These experiments are described in detail in Section 6.4; we refrain

from giving more details of the numerical experiments here because the context for the experiments is not apparent at this stage. A second set of experiments is carried out for idealised wind forcing to show the role of vertical normal modes; these experiments are described in Section 6.5. The third set of experiments tests the impact of stratification, which determines the vertical-mode structure. We carry out six experiments with density profiles from different locations in the EIO and the BoB; these experiments are described in detail in Section 6.6.

6.3 The control runs

In this section, we describe the results of the control runs, MOMCR and LCSCR. Though the impact of resolution is formally discussed in Section 6.7 in the context of the ADCP mooring off Paradip, we present the current simulations for MOM25 here to show that resolution is more important for simulating the currents in the bay. We compare the model currents with RAMA current observations in the EEIO and EBoB and with the ADCP current observations in the WBoB. In the EEIO and EBoB, the comparison is made for both zonal and meridional components. In the WBoB, the comparison is made for the allongshore component.

6.3.1 Current simulations in the EEIO and EBoB

Both MOMCR and LCSCR simulate the zonal and meridional current well in the EEIO; the measurement is at 10 m at 90°E on the equator and at 1.5°N (Figure 6.1); the correlations exceed 0.6 for MOMCR for the zonal component and all correlations are significant at the 90% level (Table 6.2). The correlation is weaker for the meridional component and this difference is particularly striking for LCSCR (Table 6.3). Note, however, that the variability of the meridional component is dominated by intraseasonal variability, with the seasonal cy-

Simulation	RAMA (u)		
	0°	1.5°N	15°N
MOMCR	**0.68**	**0.68**	**0.41**
MOM25	**0.66**	**0.70**	**0.25**
LCSCR	**0.53**	**0.60**	**0.38**
MOMCR (300-400 day BP)	0.61	0.83	0.74
MOM25 (300-400 day BP)	0.76	0.71	0.71
LCSCR (300-400 day BP)	-0.33	0.72	0.68
MOMCR (100-250 day BP)	0.51	**0.76**	0.53
MOM25 (100-250 day BP)	0.43	**0.81**	0.28
LCSCR (100-250 day BP)	**0.67**	0.65	0.31
MOMCR (30-90 day BP)	**0.82**	**0.73**	0.23
MOM25 (30-90 day BP)	**0.83**	**0.79**	0.13
LCSCR (30-90 day BP)	**0.61**	**0.73**	-0.18

Table 6.2: Correlation between RAMA currents (10 m depth) and model currents. Correlations are shown for zonal (u) components of the current. The RAMA moorings are deployed at 90°E in the BoB at several latitudes. Correlation values in boldface notation exceed the 90% significance level, and "BP" implies "band-pass filter".

cle practically invisible (Figure 6.1); in contrast, variability at lower frequencies is evident in the zonal component. The key reason for this difference is the dominance of the symmetric meridional modes, the Kelvin wave (meridional mode number -1) and the gravest Rossby mode (meridional mode number 1) at the lower frequencies. Studies show that the Yanai wave, which is anti-symmetric (meridional mode 0) is a dominant contributor to the meridional current at the equator (Sengupta et al., 2004; Masumoto et al., 2005; Chatterjee et al., 2013). Small phase differences in the model current can lead to a large decrease in the correlation and such differences are more likely at the higher frequencies, leading to the weaker correlations for the meridional current.

The performance of both models degrades away from the equator (Figure 6.1); at 15°N, the correlations are weaker and the decrease is much greater for the meridional component (Table 6.3). The degradation in the model simulations is not restricted to 15°N, but is seen at 4°N, 8°N, and 12°N as well (Figure 6.2 and Table 6.4). While LCSCR is almost as good as MOMCR in the neighbourhood of the equator, the difference between the OGCM and

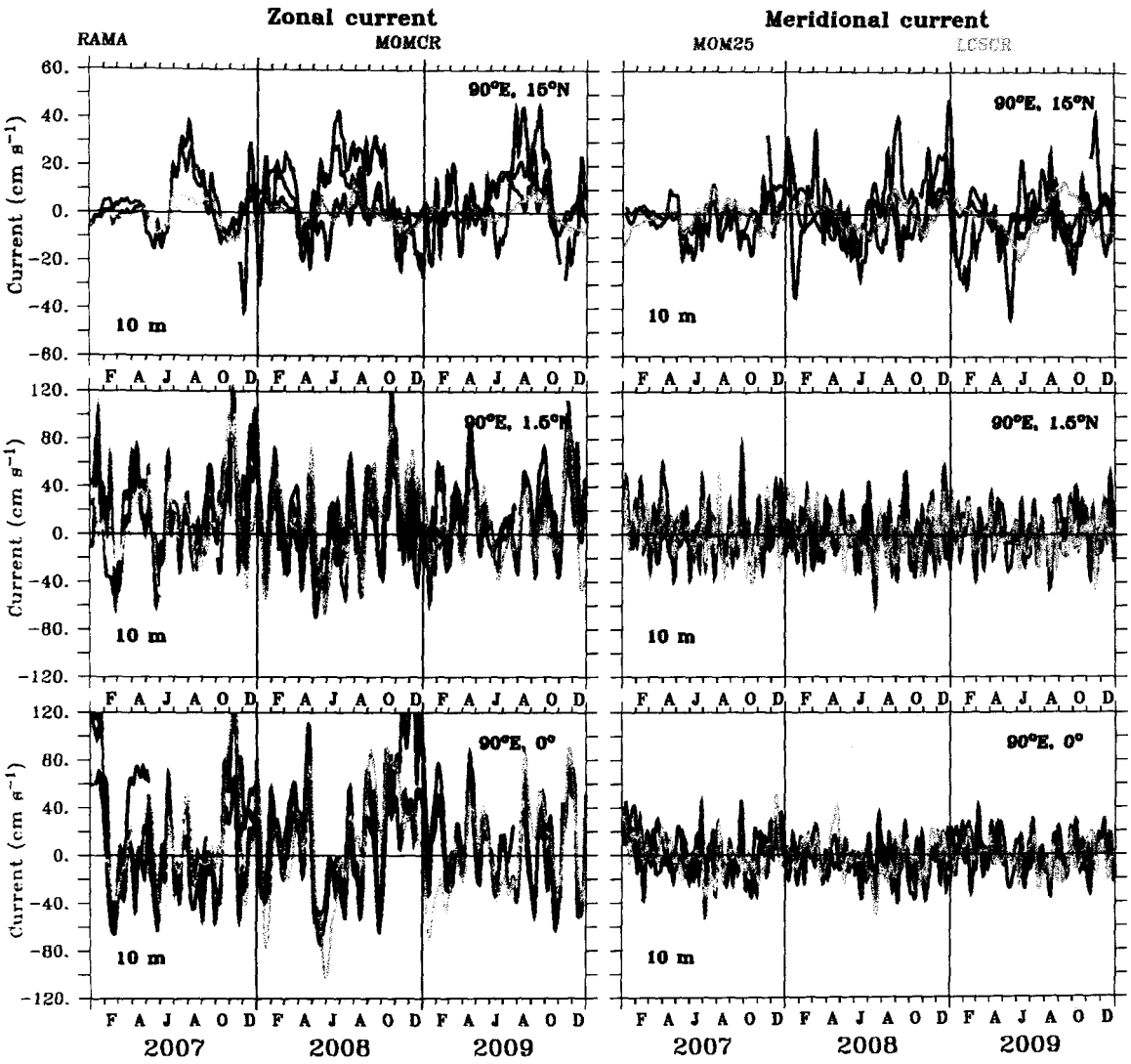

Figure 6.1: Comparison between zonal (left panels) and meridional (right panels) components of the current measured at 10 m by the RAMA moorings (locations marked by the red stars in Figure 1.2) and the current components simulated by MOMCR, MOM25, and LCSCR. The comparison is shown at 90°E for the EEIO (0° and 1.5°N) and the EBoB (15°N).

linear model is striking away from the equator (Figure 6.1 and 6.2).

Chatterjee et al. (2013) had used a resolution of $0.25° \times 0.25°$ for their simulation of Yanai waves in the EIO. Experiment MOM25 shows that the performance of MOM4p1 at this coarser resolution is comparable in the equatorial regime, but degrades away from the equator (Figure 6.1, 6.2; Tables 6.2, 6.3, 6.4). This experiment suggests that the larger

Simulation	RAMA (v)		
	0°	1.5°N	15°N
MOMCR	**0.52**	**0.58**	**0.15**
MOM25	**0.53**	**0.57**	**0.12**
LCSCR	**0.39**	**0.40**	**0.08**
MOMCR (300-400 day BP)	0.49	0.09	0.73
MOM25 (300-400 day BP)	0.54	0.05	0.91
LCSCR (300-400 day BP)	0.85	0.61	0.83
MOMCR (100-250 day BP)	0.29	0.61	0.46
MOM25 (100-250 day BP)	0.33	0.02	0.36
LCSCR (100-250 day BP)	0.41	0.41	0.16
MOMCR (30-90 day BP)	**0.37**	**0.53**	-0.08
MOM25 (30-90 day BP)	**0.33**	**0.47**	-0.06
LCSCR (30-90 day BP)	-0.01	0.17	-0.05

Table 6.3: Correlation between RAMA currents (10 m depth) and model currents. Correlations are shown for meridional (v) components of the current. The RAMA moorings are deployed at 90°E in the BoB at several latitudes. Correlation values in boldface notation exceed the 90% significance level, and "BP" implies "band-pass filter".

Data type	RAMA (u)			RAMA (v)		
	12	8	4	12	8	4
MOMCR	**0.17**	**0.70**	**0.27**	**0.23**	**0.19**	**0.59**
MOM25	0.10	**0.54**	**0.28**	**0.42**	**0.24**	**0.55**
LCSCR	**0.29**	**0.15**	-0.01	**0.48**	**0.61**	0.07

Table 6.4: Correlation between RAMA currents (10 m depth) and model simulations of zonal (u) and meridional (v) components of the current. The RAMA moorings are deployed at 90°E in the BoB at several latitudes. Correlation values in boldface notation exceed the 99% significance level.

length scales in the vicinity of the equator permit simulation of the equatorial currents with a coarser resolution than is required for the shorter length scales in the tropical regime. The performance of the LCS model also suggests that the dynamics of the currents in the EIO is more linear, perhaps due to the larger length scales, than in the BoB.

A decomposition into period bands based on a wavelet analysis (Figure 6.3, 6.4) shows

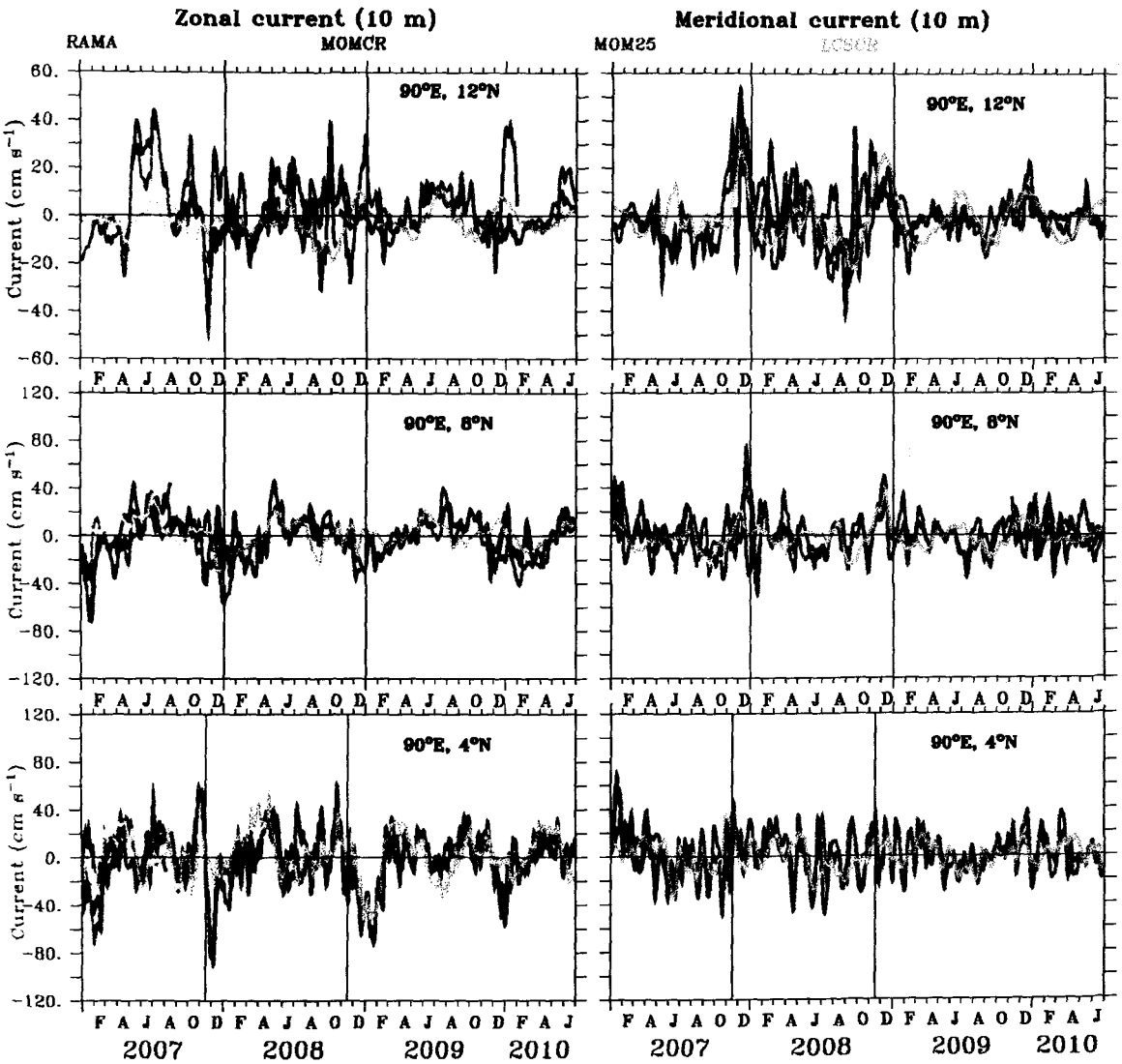

Figure 6.2: Comparison between zonal (left panels) and meridional (right panels) components of the current measured at 10 m by the RAMA moorings (locations marked by the red stars in Figure 1.2) and the current components simulated by MOMCR, MOM25, and LCSCR. The comparison is shown at 90°E for the EBoB (4°N, 8°N, and 15°N).

that the simulation in the equatorial regime is good in the annual (300–400 days), intra-annual (100–250 days), and intraseasonal (30–90 days) bands, but the off-equatorial simulation is not good even for the annual and intra-annual bands (Table 6.2, 6.3, Figure 6.5, 6.6). Note that the higher correlation for these band-passed currents are not necessarily statistically significant at the 90% level because the averaging decreases the number of degrees of freedom, implying that a higher correlation is needed for the same level of statistical significance obtained for the unfiltered data (Shankar, 1998; Shankar and Shetye, 1999).

6.3.2 Current simulations in the WBoB

The decline in model performance in the EBoB does not have a major impact on the ability of the models to simulate the EICC. The EICC is simulated well in both MOMCR and LCSCR (Figure 6.7) and the correlations for all three slope locations (Gopalpur, Kakinada, and Cuddalore) are significant at the 90% level (Table 6.5). MOMCR simulates the EICC well, with significant deviations from the observed current restricted to some seasons at each location: the summer monsoon of 2010 and spring of 2012 at Gopalpur, the winter monsoon of 2011 at Kakinada, and the summer monsoon of 2011 at Cuddalore. LCSCR matches MOMCR, with the significant discrepancy between the two models restricted to the summer monsoon of 2011 at Cuddalore. The MOMCR current is stronger at the surface compared to 40 m, but no such difference is seen in LCSCR (Figure 6.7); we discuss the difference between surface and 40-m currents in greater detail in Section 6.6.

The wavelet power is lower in MOMCR compared to the observations (Figure 6.8a). MOMCR simulates a much weaker EICC at intraseasonal time scales; at the annual time scale, the difference in wavelet power is less, but the simulated EICC is still weaker than in the observations. Unlike the annual cycle, which is strong throughout the period analysed, the variability in the intra-annual (100–250 days) and intraseasonal (30–90 days) bands varies over time. Some of this variation is simulated well in MOMCR, but some of it is not.

For example, MOMCR does not capture the observed intra-annual variability at Gopalpur and, to a lesser extent, Kakinada, during 2009–2010; the intra-annual variability during

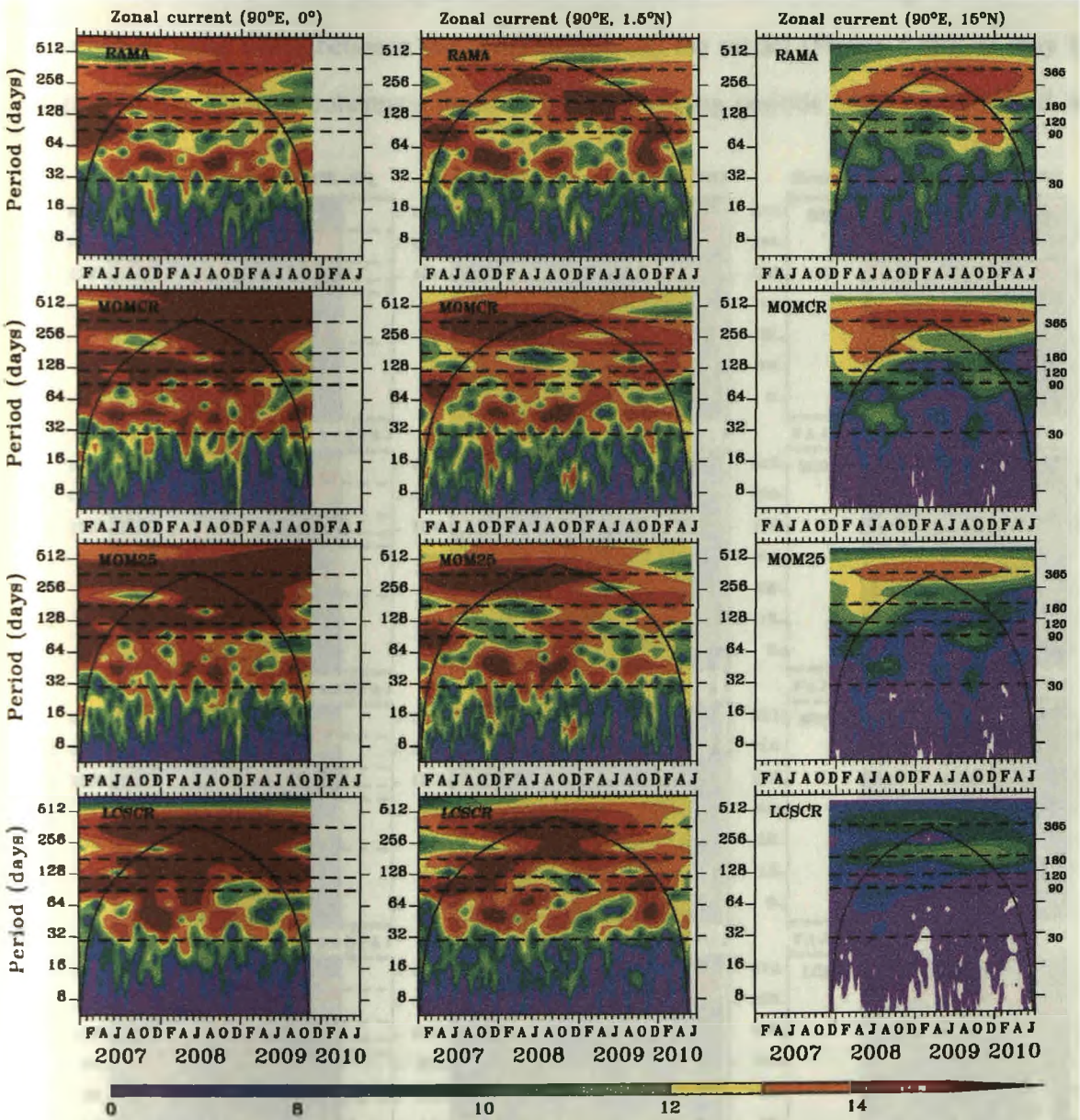

Figure 6.3: Morlet wavelet power spectra ($cm^2\ s^{-2}$) of the zonal currents at 10 m for RAMA observations and the model simulations MOMCR, MOM25, and LCSCR. The mooring locations are along 90°E in the EEIO (0° and 1.5°N) and the EBoB (15°N); see Figure 1.2. Note that the colour scale is not uniform. The thick black line marks the COI. The ordinate and wavelet power are plotted on a $\log_2$ scale. The horizontal dashed lines mark the 30-day, 90-day, 120-day, 180-day, and 365-day periods.

2011–2012 is simulated better. Furthermore, the strong intraseasonal variability observed during spring 2010 at Kakinada and spring 2012 at Gopalpur appear weak in MOMCR. That these intraseasonal events are captured in the model, however, leads to a higher wavelet coherence at these times between the observations and the model (Figure 6.8b); as may be expected, the wavelet coherence tends to be weak during periods when the observed in-

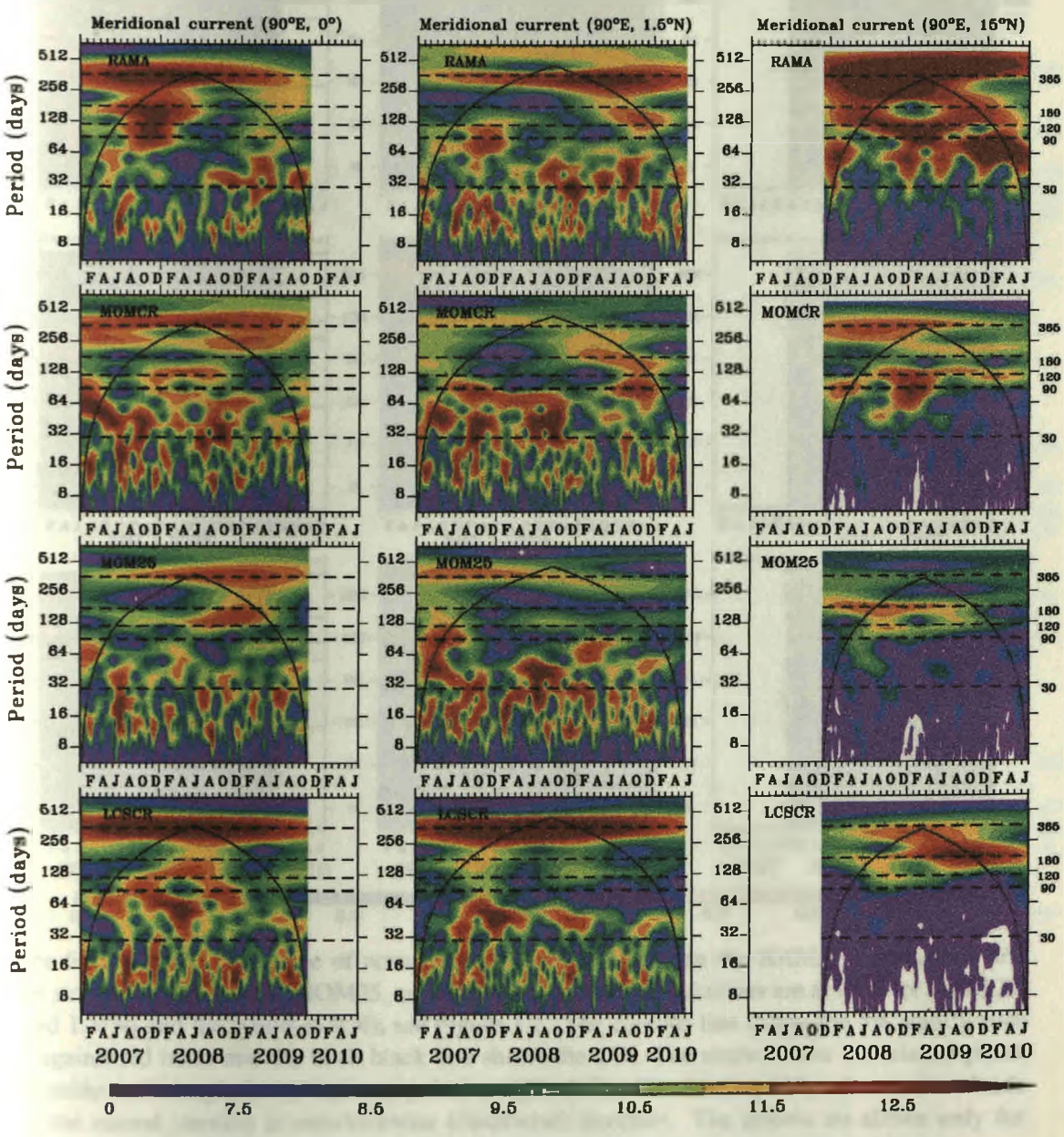

Figure 6.4: As in Figure 6.3, but for the meridional component of the current.

traseasonal variability is weak. The inability to simulate some of these intraseasonal events leads to a weaker overall correlation for the intraseasonal and intra-annual bands (Table 6.5).

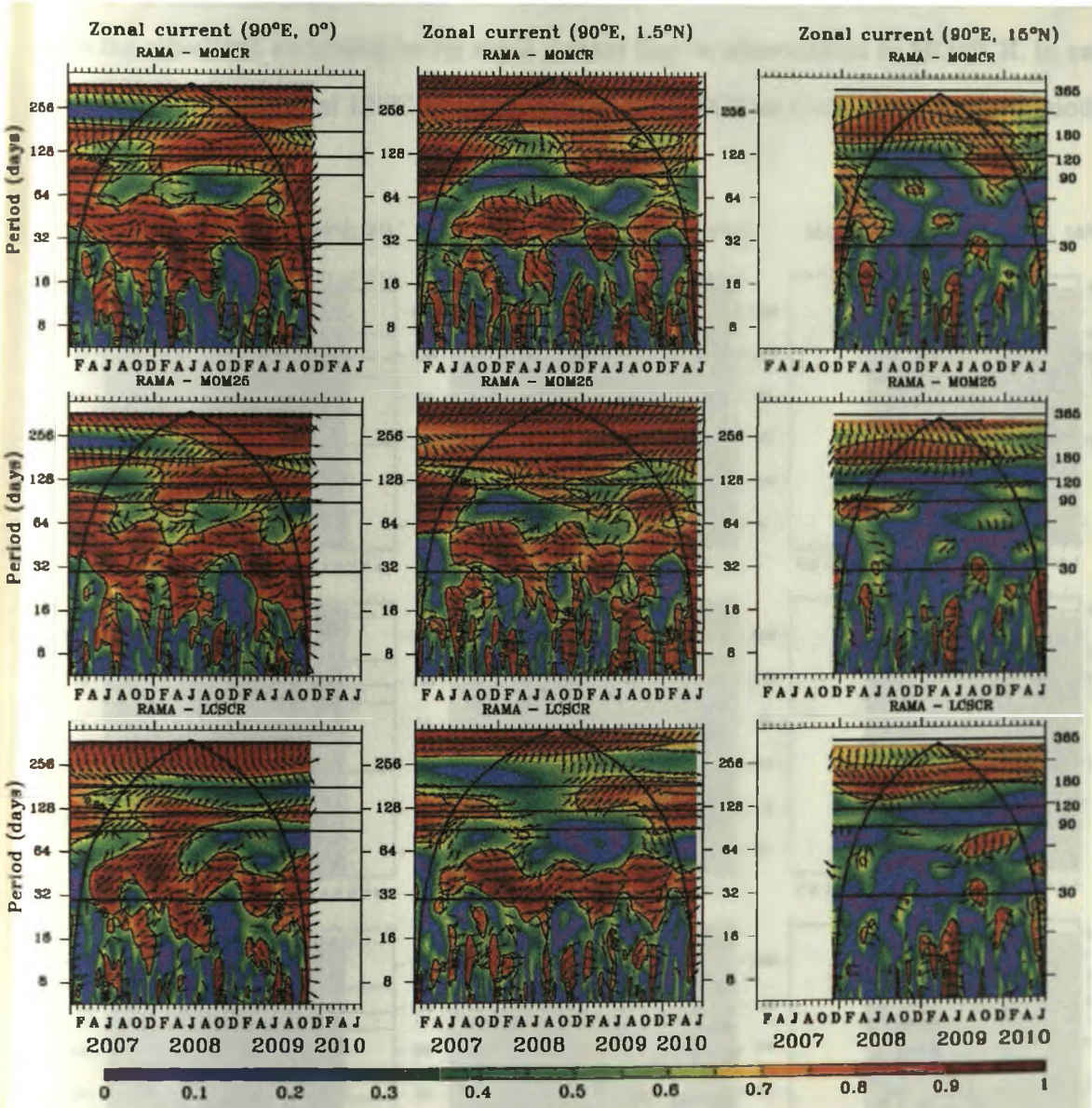

Figure 6.5: Wavelet coherence of zonal current (cm^2s^{-2}) between the RAMA observations and model simulations MOMCR, MOM25, and LCSCR. The mooring locations are at 90°E for the EEIO (0° and 1.5°N) and the EBoB (15°N); see Figure 1.2. The contour line shows the 5% significance level against red noise and the thick black line shows the COI. The arrows show the relative phase relationship, with in-phase (anti-phase) pointing right (left). The first variable (observation) leads (lags) the second (model) in anticlockwise (clockwise) direction. The arrows are shown only for wavelet coherence of 0.5 or more.

The EICC in LCSCR is weaker than in MOMCR, but LCSCR simulates the intra-annual variability better (Figure 6.8), with the correlation being much higher for LCSCR at Gopalpur (Table 6.5). The major deficiency of LCSCR is seen in the intraseasonal band, with the simulated variability being much weaker than in observations or MOMCR. In particular, the intraseasonal EICC is much weaker in LCSCR at Cuddalore, with the model

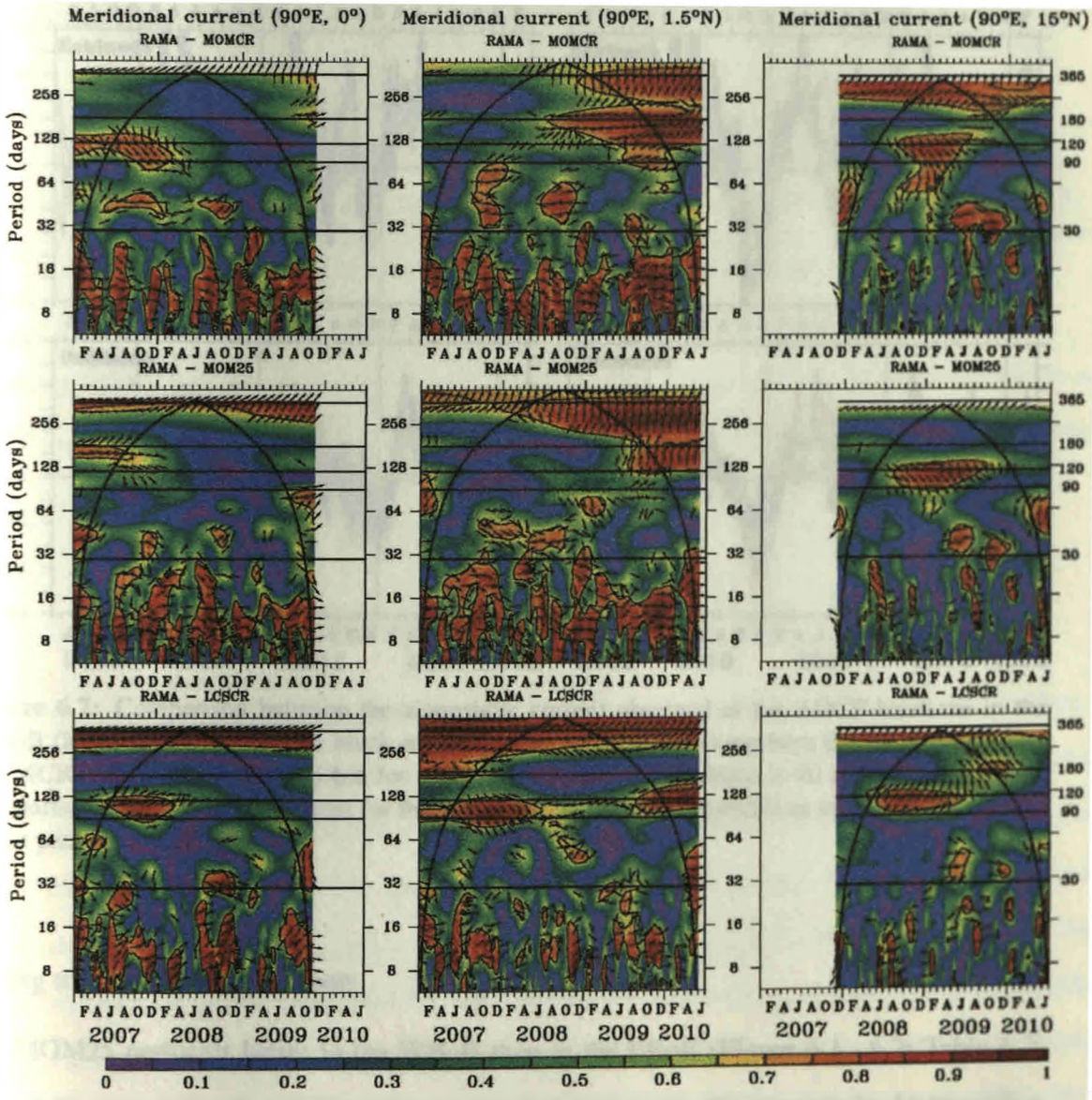

Figure 6.6: As in Figure 6.5, but for the meridional component of the current.

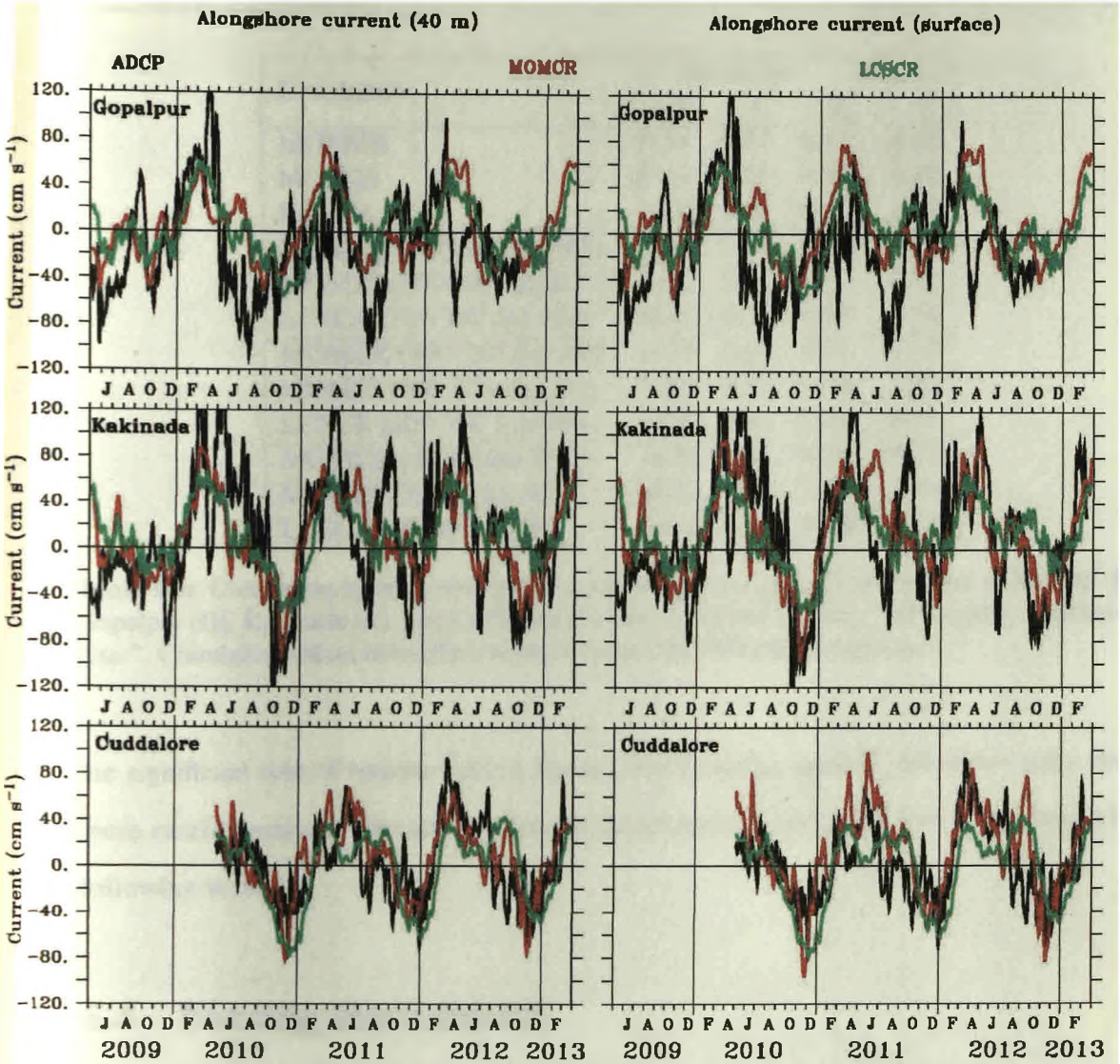

Figure 6.7: Comparison between the alongshore current observed at the ADCP locations in the WBoB (locations marked by the black stars in Figure 1.2) and the alongshore current simulated by MOMCR, and LCSCR. The top bin for which ADCP data are available is 40 m, but we show the comparison with this measurement for the simulation at 40 m (left panels) as well as at the surface (right panels).

failing to simulate several events.

MOM25 performs better in the WBoB than in the EBoB (Figure 6.1, 6.2; Table 6.2, 6.3, 6.5), suggesting that the inability to simulate accurately the currents in the transition regime between the EIO and the WBoB does not imply a poor EICC simulation. Given

Simulation	Location			
	P	G	K	C
MOMCR	**0.15**	**0.42**	**0.62**	**0.68**
MOM25	-0.01	**0.53**	**0.69**	**0.69**
LCSCR	-0.04	**0.51**	**0.60**	**0.61**
MOMCR (300-400 day BP)	-0.33	0.87	**0.95**	**0.99**
MOM25 (300-400 day BP)	-0.26	0.82	0.93	0.92
LCSCR (300-400 day BP)	-0.43	0.75	**0.97**	0.88
MOMCR (100-250 day BP)	0.29	0.02	0.34	0.52
MOM25 (100-250 day BP)	0.10	0.38	0.38	0.61
LCSCR (100-250 day BP)	0.33	0.45	0.41	0.55
MOMCR (30-90 day BP)	0.04	**0.41**	**0.26**	0.11
MOM25 (30-90 day BP)	0.10	**0.37**	0.28	0.04
LCSCR (30-90 day BP)	0.1	0.15	0.04	-0.19

Table 6.5: Correlation between alongshore currents from the ADCP observations at Paradip (P), Gopalpur (G), Kakinada (K), and Cuddalore (C) with simulated currents. "BP" implies "band-pass filter". Correlation values in boldface notation exceed the 90% significance level.

the significant role of remote forcing highlighted by earlier studies, this aspect calls for a more careful analysis. Hence, we separate the response to local and remote forcing in the following section.

6.4 Forcing mechanisms

Wavelet analysis shows that the EICC can be decomposed into three bands: annual, intra-annual, and intraseasonal (Figure 6.8). Hence, we analyse the EICC response to local and remote forcing for these three bands; the current is band-pass filtered using a fourth-order Butterworth filter. Local forcing is defined to be the wind blowing along the WBoB, from the northern end of the Indian east coast (21°N), which is just north of Gopalpur, to the southern tip of Sri Lanka (6.5°N). As noted earlier, remote forcing consists of three mechanisms: the winds blowing along the northern and eastern boundaries of the BoB, Ekman pumping over the BoB, and the winds blowing along the equator (Shankar et al., 1996; McCreary et al., 1996; Vinayachandran et al., 1996). A list of these experiments is given in

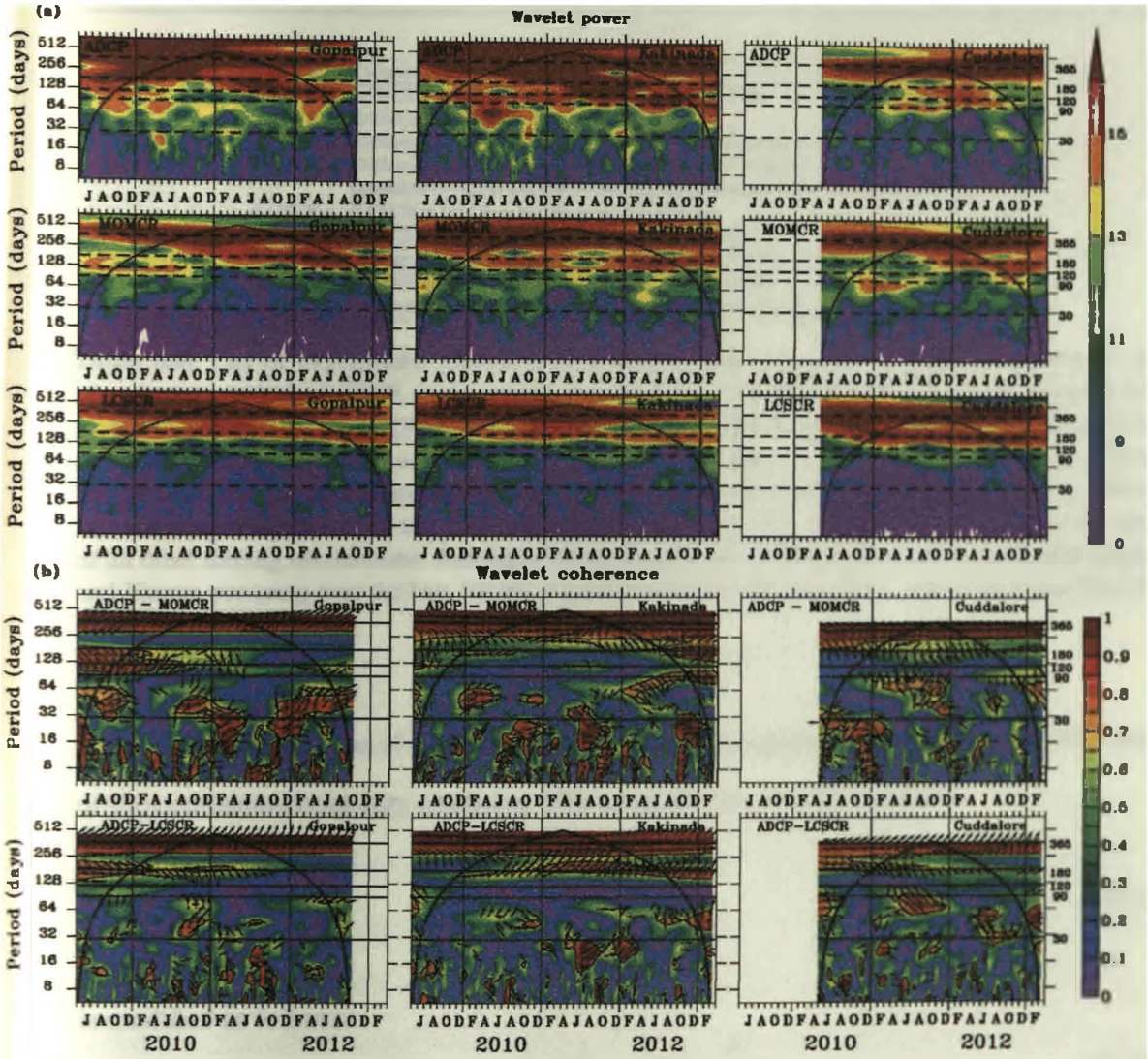

Figure 6.8: **(a)** Morlet wavelet power spectra ($cm^2\ s^{-2}$) of the alongshore currents at 40 m for ADCP observations in the WBoB and the model control runs, MOMCR and LCSCR; note that the colour scale is not uniform. The thick black line marks the COI. The ordinate and wavelet power are plotted on a $\log_2$ scale. The horizontal dashed lines mark the 30-day, 90-day, 120-day, 180-day, and 365-day periods. **(b)** Wavelet coherence of alongshore current ($cm^2 s^{-2}$) between the ADCP observations in the WBoB and model control runs, MOMCR and LCSCR. The contour line shows the 5% significance level against red noise and the thick black line shows the COI. The arrows show the relative phase relationship, with in-phase (anti-phase) pointing right (left). The first variable (observation) leads (lags) the second (model) in anticlockwise (clockwise) direction. The arrows are shown only for wavelet coherence of 0.5 or more.

Table 6.6.

As done in earlier papers that used the LCS model (see McCreary et al., 1996), we

Experiment	Description
$LCSCR_R$	LCSCR with modified boundary condition in WBoB
$LCSCR_{WB}$	Difference of LCSCR and $LCSCR_R$
$LCSCR_{EIO}$	Difference of LCSCR and LCSCR with equatorial damper
$LCSCR_{EB}$	Difference of LCSCR and LCSCR with modified boundary condition in NBoB and EBoB (including Andaman and Nicobar Islands)
$LCSCR_{BI}$	LCSCR-($LCSCR_{WB}$+$LCSCR_{EIO}$+$LCSCR_{EB}$)
$LCSCB_R$	LCSCB with modified boundary condition in WBoB
$LCSCB_L$	Difference of LCSCB and LCSCB with modified boundary condition in WBoB
$LCSNB_R$	LCSNB with modified boundary condition in WBoB
$LCSNB_L$	Difference of LCSNB and LCSNB with modified boundary condition in WBoB

Table 6.6: List of experiments related to local and remote forcing of the EICC. The first set of experiments, with the LCSCR configuration, are described in Section 6.4, and use the density profile from Moore and McCreary (1990). The other two sets use density profiles from the central bay (CB) and northern bay (NB); these experiments (see Table 6.9) are described in Section 6.6. The subscripts "L" and "R" for the stratification experiments denote local and remote forcing, respectively. Here, local forcing is equivalent to the "WB" experiment in Section 6.4, while remote forcing is the sum of all other forcing mechanisms: forcing by alongshore winds in NBoB and EBoB, equatorial winds, and Ekman pumping over the bay. Model parameters for the CR and other experiments are listed in Table 6.8.

separate the contribution of alongshore winds, whether local or remote, using a modification of the continental boundary condition. The usual, closed, no-slip condition

$$u_n = v_n = 0 \tag{6.1}$$

is modified as follows:

$$\tilde{u_n} = \vec{n}.\vec{v_n} = -\vec{n}.\vec{k} \times \frac{\vec{F_n}}{f}; \tag{6.2a}$$

$$\tilde{v_n} = \vec{k} \times \vec{n}.\vec{v_n} = 0. \tag{6.2b}$$

In Equation (6.2), $\vec{n}$ is the unit vector normal to the boundary that points into the bay along its western and northern boundaries and the east coast of the Andaman and Nicobar Islands, and out of the bay along its northeastern and eastern boundaries and along the west coast of the Andaman and Nicobar Islands; $\vec{k}$ is the unit vector directed upward and f is the Coriolis frequency. $\tilde{u_n}$ and $\tilde{v_n}$ are velocity components perpendicular and parallel to the boundary. This modification allows the local Ekman flow to pass through the continental

boundary over the stretch of the coastline where it is applied, implying that there is no coastal upwelling or downwelling due to the local winds. As a consequence, coastal Kelvin waves are not generated over this stretch of the coastline, filtering out the local response to the alongshore winds. Owing to the linearity of the LCS model, the difference between LCSCR and this run gives the response to the alongshore wind forcing over this part of the coastline. One experiment, $LCSCR_{WB}$, uses this approach to isolate the effect of alongshore winds blowing in the WBoB, and another experiment, $LCSCR_{EB}$, to isolate the effect of the alongshore winds in the NBoB and EBoB; in $LCSCR_{EB}$, the winds blowing along the coasts of the Andaman and Nicobar Islands are also clubbed with the continental winds to isolate the effect of all alongshore winds in the EBoB. The stretches of the coastline over which the winds are thus filtered in these two experiments is shown in Figure 6.9a.

To isolate the response to equatorial forcing, we use a damper in the EIO east of 80°E between 6.5°S and 6.5°N; this damper absorbs the energy of the incident equatorial Kelvin wave and the difference between LCSCR and this run, called experiment $LCSCR_{EIO}$, gives the response in the bay to forcing from the equator (McCreary et al., 1996). The response to Ekman pumping over the bay, called experiment $LCSCR_{BI}$ (where the "BI" stands for "bay interior"), is obtained by subtracting the results of the simulations with the equatorial damper and the modified continental boundary conditions applied along both sets of boundaries defined in $LCSCR_{WB}$ and $LCSCR_{EB}$ (Table 6.6; McCreary et al., 1996).

Shankar et al. (1996) and McCreary et al. (1996) showed that all four forcing mechanisms (one local, three remote) contribute significantly to the seasonal cycle of the EICC at different times of the year. Splitting the seasonal cycle into annual and intra-annual components shows that the annual cycle at Kakinada and Cuddalore is driven by the local winds and Ekman pumping over the bay; the response to equatorial winds and the alongshore winds in NBoB and EBoB are not small, but interfere destructively as they are out of phase (Figure 6.10). At Gopalpur, the response to local forcing is weak because this mooring is

located close to the northern end of the WBoB, implying that it is close to the lower limit of the integral for the Kelvin wave that is generated along this boundary (Shankar et al., 1996). Hence, the annual EICC at Gopalpur is driven almost completely by Ekman pumping over the bay. Kakinada and Cuddalore lie farther down the coast and this increasing distance along the integral path implies a stronger response at these locations to the local alongshore winds. For the intra-annual band, the contribution of alongshore winds, whether in the WBoB or NBoB or EBoB, is much weaker than that of the equatorial winds; this dominance of the equatorial forcing in this band is not surprising as the EIO is known to exhibit strong semi-annual variability (Knox, 1976; Luyten and Roemmich, 1982) owing to resonance at this period (Jensen, 1993). The EIO also shows a significant response around 120 days (Han et al., 2011).

The intraseasonal EICC is weaker in the LCS model than in the observations or MOMCR (Figure 6.8), suggesting that nonlinear effects are important, but the linear model solutions are nevertheless useful to gain some insight into the relative importance of the forcing mechanisms. For the reason discussed above, the contribution of local forcing is weak at Gopalpur, but significant at Kakinada and Cuddalore (Figure 6.11). Hence, the intraseasonal response at Gopalpur is dominated by forcing from the equator and by remote alongshore winds.

This relatively weak response of the EICC to equatorial forcing at intraseasonal periods compared to the intra-annual band is curious because the equatorial current shows roughly equal strength in the intraseasonal and intra-annual bands (Figure 6.12). The model solutions suggest that intra-annual variability is stronger at 70°E, but the current in the intraseasonal band is comparable at 85°E. We have used here the solution at 70°E and 85°E solution because these locations occur near the middle of the regime associated with the Wyrkti Jet (Wyrtki, 1973) and the Madden-Julian oscillation (MJO; Madden and Julian, 1971, 1972, 1993) and to the east of this regime, respectively: the patch of winds associated with the

Wyrkti Jet and MJO lies between 60–80°E (Prerna et al., 2017). Furthermore, recent studies have suggested a significant impact of the Madden-Julian oscillation (Madden and Julian, 1971, 1972, 1993), which is a dominant mechanism for equatorial currents in the Indian Ocean (Han et al., 2001b; Prerna et al., 2017), in the BoB (Vialard et al., 2009; Cheng et al., 2013), and even the eastern Arabian Sea (Vialard et al., 2009).

The LCS model experiments suggest that the response in the EICC regime is different for sea level and current and that this difference is a function of the period (Figure 6.12). The decrease in sea level from the EIO to 17°N (Kakinada) along the Indian east coast is negligible for the intra-annual band, but the current magnitude decreases to almost half when we look at the response to the equatorial winds ($LCSCR_{EIO}$). In the intraseasonal band, however, the decrease in the current magnitude is much greater (by ~85%) than in the sea level. In the following section, we analyse this difference in the response to equatorial forcing and show that it is due to the excitation of high-order vertical modes.

6.5 Importance of high-order vertical modes

When the LCSCR response is broken down to individual modes, we find that the sea level is determined almost completely by the first two modes, with a small contribution from the third mode; higher modes are not required to estimate the model sea level (Figure 6.13b). Even modes 5–10, however, make a significant contribution to the current (Figure 6.13a). The high-order modes are less important for the current in the intra-annual band compared to the intraseasonal band, which shows considerable variation with both year and season. The contribution of the high-order modes to the intraseasonal current component varies with year and is related to the interannual variability of the length scale of the intra-annual or intraseasonal zonal wind stress along the equator because the band-passed response of a vertical mode depends on the length scale of the band-passed wind stress (Reppin et al., 1998; Prerna et al., 2017).

The total field is determined by summing over the vertical normal modes and the contribution of high-order modes leads to the formation of beams that take energy down along the equator (McCreary, 1984). Such beams are seen in the LCS model for both, the eastward propagating Kelvin wave and the westward propagating, reflected Rossby wave. The Kelvin (Rossby) beam for the intra-annual band is denoted by the eastward (westward) and downward bending of the red (blue) contours around 65°–85°E (85°–90°E) above (below) $\sim$120 m in the upper panel of Figure 6.13c. For the intraseasonal band, the Kelvin beam is denoted by the eastward and downward bending of the blue contours around $\sim$ 67°–85°E. The bending angle is given by $\theta = \frac{\sigma}{N_b}$, where σ is the forcing frequency and $N_b(Z)$ is the background Brünt-Vaïsala frequency (McCreary, 1984). As θ increases with decreasing (increasing) period (frequency), the beam bends at a steeper angle at intraseasonal periods. Therefore, the reflected Rossby wave is much weaker in the intraseasonal band owing to a weak incident (and, consequently, weak reflected) signal in the depth regime shown in Figure 6.13c.

The forcing in LCSCR is complex and we carry out idealised experiments to show the differing impact of high-order modes on sea level and current. These experiments are similar to those described in McCreary (1984) and Chatterjee et al. (2013). (Similar experiments with the LCS model were animated during a school conducted at the CSIR-National Institute of Oceanography, India in 2010. The relevant experiments on equatorial beams, titled "Experiments J", may be downloaded from http://www.nio.org/index/option/com_eventdisplay/task/view/tid/4/sid/114/eid/143.) The model configuration in these experiments is as in LCSCR, but the forcing is restricted to a patch of zonal wind stress in the central EIO (CEIO). The forcing has the form

$$\tau^x = \tau_0 X(x) Y(y) T(t); \tag{6.3a}$$

$$\tau^y = 0, \tag{6.3b}$$

where τ^x (τ^y) is the zonal (meridional) wind stress and

$$X(x) = 0.5\{1 + \cos[2\pi(x - x_c)/L_w]\}, \quad x_w \leq x \leq x_e, \tag{6.3c}$$

$$Y(y) = 0.5\{1 + \cos[2\pi(y - 0°)/4°]\}, \quad -2° \leq y \leq 2°, \tag{6.3d}$$

$$T(t) = \sin(\sigma t). \tag{6.3e}$$

In Equation (6.3), $\sigma = \frac{2\pi}{P}$, where P is the forcing period; x_w, x_c, and x_e are the western edge, centre, and eastern edge of the wind patch, respectively, and $L_w = x_e - x_w$ is the zonal length scale associated with the forcing. The advantage with this "half-cosine" forcing form is that it produces a weak wind curl; the wind stress is set to zero outside the forcing region.

We conduct four experiments, two each with $P = 60$ days and $P = 180$ days. The wind is switched off after six (four) cycles for $P = 60$ days ($P = 180$ days). In one experiment for each period, $x_c = 70°$E and $L_w = 20°$, representing a long forcing length scale; in the other experiment for each period, $x_c = 77°$E and $L_w = 6°$, representing a short forcing length scale. These four experiments are listed in Table 6.7. We show the results at the centre of the forcing patch (70°E or 77°E), to its east (85°E), and near Kakinada (83°E, 17°N).

Since a downwelling equatorial Kelvin wave, with eastward zonal current at the equator, reflects as a downwelling Rossby wave, with westward zonal current at the equator to ensure no flow into the eastern boundary (Moore, 1968), the currents associated with the incident and reflected waves tend to cancel, but not the sea level (Figure 6.14). Hence, the zonal current at both intra-annual (experiments LCS180$^{20°}$ and LCS180$^{6°}$) and intraseasonal (experiments LCS060$^{20°}$ and LCS060$^{6°}$) periods decreases sharply east of the forcing region owing to the interference between the incident Kelvin and reflected Rossby waves. An infin-

Experiment	Period (days)	L_w	x_w	x_c	x_e
$LCS180^{20°}$	180	20°	60°E	70°E	80°E
$LCS060^{20°}$	60	20°	60°E	70°E	80°E
$LCS180^{6°}$	180	6°	74°E	77°E	80°E
$LCS060^{6°}$	60	6°	74°E	77°E	80°E

Table 6.7: List of LCS model experiments related to vertical normal modes (Section 6.5). $LCS180^{20°}$ implies a 180-day forcing with a zonal length scale $L_w = 20°$; x_w, x_c, and x_e denote the western edge, the middle, and the eastern edge of the wind forcing patch, respectively.

ity of meridional Rossby modes are required to satisfy the no-normal-flow condition at the eastern boundary, leading to energy tending to propagate poleward along the eastern boundary as coastal Kelvin waves (Moore, 1968). Therefore, energy leaks from the equatorial wave guide into the coastal wave guide at the eastern boundary, influencing the circulation in the BoB (Yu et al., 1991; Potemra et al., 1991; McCreary et al., 1993, 1996; Shetye, 1998; Shankar et al., 2002). (Strictly, in the inviscid analysis of Moore (1968), the coastal Kelvin waves exist only poleward of the critical latitude for a periodic forcing. Equatorward of this latitude, Rossby waves carry the signal westward into the interior. This balance sets up instantaneously in an inviscid system and the westward propagating Rossby waves come into existence instantaneously at all latitudes. The inclusion of viscosity complicates the analysis and numerical simulations suggest that the westward propagating waves appear later at higher latitudes. Hence, energy appears to propagate poleward even equatorward of the critical latitude in numerical models.)

This reflection process, coupled with the shallow bending for the intra-annual period, makes it difficult to make a clear case for the greater weakening of the current at intraseasonal periods (Fig. 6.14a,c). Nevertheless, separation of the response into modes, as done earlier for LCSCR (Fig. 6.13a,b), shows clearly the significant contribution made by the high-order modes, including modes 5–10, to the current (Fig. 6.15a). Modes 3–10 contribute ~40% (~45%) to the current at the intra-annual (intraseasonal) period for $L_w = 20°$

(Fig. 6.15a).

The zonal length scale of the wind forcing determines which vertical modes will respond more strongly: the modes preferrentially excited are those with a horizontal length scale of the order of or greater than that of the forcing. A vertical normal mode is a mathematical construct and a more physical argument for the coupling links the length scale of the forcing to the vertical scale of the beam, which descends into the ocean at a specific angle θ. The vertical extent of the beam is given by $L_w \tan(\theta)$ (Fig. 6.15c,d) and all the modes superpose to make this beam. For the Kelvin wave, the zonal length scale of the response is $L_K = c_n P$ (because $c_n = \frac{\sigma}{k}$, where k is the zonal wavenumber), implying that higher modes are preferentially excited as the forcing length scale decreases (Fig. 6.15a–d); this decrease in the zonal length scale is evident in the shorter horizontal length scales in Fig. 6.15b compared to Fig. 6.15a. The characteristic (or Kelvin wave) speeds are listed for the first 10 modes in Table 6.8. For $P = 180$ days ($P = 60$ days), the length scale is $\sim$22.5° ($\sim$19.5°) for the third (first) mode, implying that these modes will be excited when the forcing length scale is 20°. When the forcing length scale decreases to 6°, the mode that matches this zonal length scale is the tenth (fourth) for $P = 180$ days ($P = 60$ days), and the zonal length scale associated this mode is $\sim$7° ($\sim$5.5°). Though the bending angle depends only on the forcing period and stratification and is independent of the forcing length scale, the shorter horizontal and vertical length scales associated with the high-order modes are subject to greater friction owing to its Laplacian form, leading to increased damping for the high-order modes. (Inclusion of biharmonic friction, as in MOM4p1, implies even greater horizontal friction at shorter length scales.)

Hence, the sea level, which is determined mostly by the first two or three modes, correlates better from the EIO to the WBoB (Fig. 6.15e,f) than does the current (6.15a,b), which is impacted more by the high-order modes that are strongly damped (by both horizontal and vertical friction) and cause energy to escape the surface layer into the deeper ocean

(Fig. 6.15c,d). In the equatorial ocean, this difference is a consequence of sea level depending on F_n and current on $\frac{F_n}{c_n}$ (McCreary, 1980, 1981). Even off the equator, however, a similar difference occurs in the sea-level and current response because the current depends on the horizontal gradient of sea level rather than on sea level, implying that the smaller contribution made by the high-order modes to sea level matters more for the current owing to the short horizontal length scales associated with these modes. (The relevant length scale is the Rossby radius of deformation, which is $\approx$ 340 km (160 km) at the equator for the first (fifth) baroclinic mode and $\approx$ 60 km (14 km) at 17°N for the first (fifth) baroclinic mode.) Therefore, even the local alongshore winds in the WBoB can excite significant currents at high-order vertical modes even though the contribution of these modes to the sea level is negligible.

In the equatorial ocean, another complication for the periodic forcing assumed in this idealised experiment is the existence of a critical latitude, $y_{cr} = \frac{c_n}{2\sigma}$ (Moore, 1968; McCreary, 1980, 1981). For $P = 60$ days, $y_{cr} \sim 10°$; for $P = 180$ days, $y_{cr} \sim 30°$. At the intra-annual periods, the critical latitude lies poleward of Kakinada ($\sim$17°N), implying that the sea level and current there are influenced both along the coastal wave guide (via the Kelvin wave) and the propagation of Rossby waves across the bay. Due to significance influence of eastern boundary radiative Rossby wave pack at intra-annual periods, interpretation of any intra-annual lag in phase between the equatorial signal and that near Kakinada became difficult. At intraseasonal periods, in contrast, the critical latitude lies equatorward of Kakinada, implying that Rossby wave propagation is not possible at this latitude, obviating the need for separating these two processes. Note that the critical latitude exists only for a periodic forcing and is therefore relevant to the experiment with idealised, sinusoidal wind forcing. For the intraseasonal band, the sea level at Kakinada in LCS060$^{20°}$ lags that at 70°E at the equator by $\sim$25 days, comparable to the predicted lag of $\sim$20 days for the first vertical mode; the longer lag may be attributed to the non-negligible contribution of the second vertical mode,

whose phase speed is lower than that of the first mode (Table 6.8).

6.6 Impact of stratification

All the LCS model simulations in the preceding sections use the density profile of Moore and McCreary (1990) to determine the vertical normal modes. This profile was constructed to illustrate the dynamics of the western EIO (WEIO) and is therefore more representative of the stratification in this region. The mixed layer, at ~58 m, is deeper for this profile than in the BoB (Chatterjee et al., 2012). Figure 6.16 shows the density profile from Moore and McCreary (1990) and from six different regimes of the EIO (including the WEIO) and the BoB. These profiles are based on an averaging of the density from Chatterjee et al. (2012) within a limited domain in the WEIO, CEIO, EEIO, southern BoB (SBoB), central BoB (CBoB), and NBoB: the averaging domains are shown in Figure 6.9a and the coordinates of these boxes are given in Table 6.9. The density profile in the WEIO, where the MLD is ~48 m, is significantly different from that in the BoB: in the NBoB, the MLD is 18 m (Table 6.8) owing to rainfall and the inflow of freshwater from rivers (Shetye, 1993). As a consequence, the vertical profile of the Brünt-Vaïsala frequency also varies considerably in space (Figure 6.16).

Results from the EIO show that the fall Wyrtki Jet (Wyrtki, 1973) is stronger than the one in spring (McPhaden et al., 2015) owing to the thermocline in fall being shallower and concentrating the transport in the surface layer over a smaller depth range (Han et al., 1999). We test the implication of the spatial variation in stratification for the EICC by conducting six experiments, one each with a density profile from the WEIO, CEIO, EEIO, SBoB, CBoB, and NBoB; the experiments are listed in Table 6.9. The mode structures for these regions are strikingly different, with the much stronger second mode in the profile of Moore and McCreary (1990) being replaced by a dominant first mode in the EEIO and the BoB. The mode and wind coupling coefficients for all experiments, including LCSCR, are listed

Parameter	Mode	LCSCR	LCSWE	LCSCE	LCSEE	LCSSB	LCSCB	LCSNB
	1	264	252	252	262	270	273	269
	2	167	153	155	165	165	166	164
	3	105	91	92	94	97	97	96
Charcteristic speed	4	75	65	68	68	74	64	74
(c_n, cm s^{-1})	5	60	53	54	55	56	57	57
	6	49	43	45	46	47	48	48
	7	42	37	38	39	40	41	40
	8	37	32	33	34	35	36	36
	9	33	29	29	30	31	32	32
	10	30	26	27	27	28	28	29
	1	313	215	194	167	157	155	147
	2	186	261	224	288	285	289	246
	3	865	1013	642	1180	419	384	265
Mode coupling	4	956	561	450	672	447	692	285
coefficient ($\mathcal{H}_n$, m)	5	1877	728	661	804	586	473	258
	6	1869	822	596	867	504	399	280
	7	1982	737	642	809	713	569	340
	8	1581	983	850	1054	626	480	359
	9	1492	1083	774	876	656	517	449
	10	4176	970	835	781	673	593	527
	1	0.98	0.98	0.98	0.99	0.99	0.99	0.99
	2	0.95	0.95	0.96	0.98	0.98	0.98	0.98
	3	0.89	0.88	0.92	0.95	0.95	0.95	0.96
Wind coupling	4	0.81	0.79	0.85	0.90	0.93	0.91	0.94
coefficient (Z_n)	5	0.72	0.69	0.77	0.86	0.88	0.88	0.90
	6	0.62	0.57	0.68	0.80	0.83	0.84	0.87
	7	0.49	0.46	0.59	0.74	0.78	0.78	0.82
	8	0.40	0.34	0.49	0.67	0.72	0.73	0.78
	9	0.31	0.23	0.39	0.59	0.66	0.67	0.73
	10	0.23	0.14	0.30	0.52	0.59	0.58	0.68
MLD (m)		48	48	38	44	28	24	18

Table 6.8: Values of LCS mode parameters (characteristic mode speed and mode and wind coupling coefficients) for the LCS model experiments related to stratification (see Table 6.9). LCSCR is the control run and uses the density profile from Moore and McCreary (1990). All simulations are carried out at a horizontal resolution of $0.1° \times 0.1°$ and the horizontal mixing coefficient for all experiments is 5×10^6 cm^2 s^{-1}. The vertical mixing coefficient is $\nu = \frac{A}{N_b^2}$ and $A = 1.3 \times 10^{-4}$ cm^2 s^{-3} for all experiments. Density profiles for all experiments are given in Figurere 6.16. The computation of mode parameters from density is described in Appendix B. The mixed layer depth (MLD) is assumed to be the depth at which the density exceeds the surface density by 0.2 kg m^{-3}.

Experiment	Region	Latitude	Longitude
LCSWE	WEIO	2°S–2°N	42°–46°E
LCSCE	CEIO	2°S–2°N	60°–64°E
LCSEE	EEIO	2°S–2°N	84°–88°E
LCSSB	SBoB	11°–13°N	85°–89°E
LCSCB	CBoB	14°–16°N	85°–89°E
LCSNB	NBoB	17°–19°N	85°–89°E

Table 6.9: List of LCS model experiments related to stratification. The density profiles used for these experiments are taken from the annual climatology of Chatterjee et al. (2012) and averaged over the latitude and longitude ranges listed in columns 3 and 4, respectively. These regions are shown by the red rectangles in Figure 6.9a.

in Table 6.8. The strength of a mode depends on the ratio of the wind coupling coefficient to the mode coupling coefficient. Higher the ratio, called the effective coupling coefficient, stronger is the response of that mode (McCreary, 1980, 1981; Moore and McCreary, 1990). The list in Table 6.8 shows that the mode (effective) coupling coefficient is smallest (highest) for the second mode for LCSCR, but for the first mode in the other six experiments, including LCSWE, which uses the profile from the WEIO based on Chatterjee et al. (2012). The mode (effective) coupling coefficient also increases (decreases) more slowly with increasing mode number for the profiles from the BoB, with the highest (lowest) mode (effective) coupling coefficient, and therefore strongest response, for the tenth mode occurring for the profile from the NBoB (experiment LCSNB).

The change in stratification does not have a significant impact on the simulation of currents in the EIO or EBoB (Table 6.10, 6.11) or at 40 m in the WBoB (Figure 6.18, Table 6.12) because the MLD is shallower than 40 m for five of the seven profiles (Table 6.8). We have seen earlier (Section 6.3.2) that the EICC in MOMCR is stronger at the surface than at 40 m, but no such difference is seen in LCSCR (Figure 6.7): the EICC in LCSCR does not change from the surface to 40 m because the MLD in LCSCR is deeper than 40 m. Changing the background stratification results in an increase in the EICC strength at the surface (Figure 6.17), as in MOMCR, owing to the decrease in MLD, and the simulated

Experiment	RAMA (u)					
	0°	1.5°N	4°N	8°N	12°N	15°N
LCSCR	**0.53**	**0.59**	**0.17**	**0.15**	**0.29**	**0.38**
LCSWE	**0.49**	**0.55**	**0.33**	**0.12**	**0.13**	0.09
LCSCE	**0.47**	**0.51**	**0.30**	**0.17**	**0.17**	**0.14**
LCSEE	**0.50**	**0.52**	**0.29**	**0.16**	**0.17**	**0.25**
LCSSB	**0.43**	**0.43**	**0.28**	**0.23**	**0.17**	**0.25**
LCSCB	**0.40**	**0.39**	**0.25**	**0.24**	**0.17**	**0.25**
LCSNB	**0.35**	**0.31**	**0.26**	**0.32**	**0.20**	**0.25**

Table 6.10: Correlation between RAMA currents (10 m depth) and model currents; correlations are shown for zonal (u) components of the current for the stratification experiments listed in Table 6.9. The RAMA moorings are deployed at 90°E in the BoB at several latitudes (Figure 1.2). Correlation values in boldface notation exceed the 90% significance level.

Run	RAMA (v)					
	0°	1.5°N	4°N	8°N	12°N	15°N
LCSCR	**0.39**	**0.40**	**0.42**	**0.61**	**0.48**	0.08
LCSWE	**0.37**	**0.40**	**0.34**	**0.59**	**0.40**	-0.03
LCSCE	**0.38**	**0.41**	**0.34**	**0.59**	**0.41**	-0.03
LCSEE	**0.42**	**0.48**	**0.35**	**0.60**	**0.45**	**0.11**
LCSSB	**0.42**	**0.50**	**0.31**	**0.55**	**0.45**	**0.18**
LCSCB	**0.41**	**0.50**	**0.27**	**0.54**	**0.45**	**0.20**
LCSNB	**0.36**	**0.47**	**0.27**	**0.53**	**0.45**	**0.17**

Table 6.11: Correlation between RAMA currents (10 m depth) and model currents; correlations are shown for and meridional (v) components of the current for the stratification experiments listed in Table 6.9. The RAMA moorings are deployed at 90°E in the BoB at several latitudes (Figure 1.2). Correlation values in boldface notation exceed the 90% significance level.

surface current correlates better with the observed current, which is measured at 40 m (Table 6.13). The difference between the currents simulated for the three EIO profiles or for the SBoB and CBoB profiles are not significant (Figure 6.17); hence, we present results only for LCSCR, LCSCB, and LCSNB in the rest of this section.

The simulation at Kakinada shows maximum improvement in LCSNB during May–September and December 2010, when the increase in current strength leads to a better match with the observations than for LCSCR (Figure 6.17). This increase in the current strength does not, however, always imply an improved simulation. For example, the weak poleward

Data type	ADCP Alongshore			
	P	G	K	C
LCSCR	-0.04	**0.51**	**0.60**	**0.61**
LCSWE	0.07	**0.50**	**0.56**	**0.58**
LCSCE	0.07	**0.49**	**0.50**	**0.58**
LCSEE	**0.15**	**0.46**	**0.57**	**0.58**
LCSSB	**0.20**	**0.48**	**0.59**	**0.57**
LCSCB	**0.21**	**0.48**	**0.59**	**0.57**
LCSNB	**0.23**	**0.52**	**0.57**	**0.59**

Table 6.12: Correlation between alongshore currents from the ADCP observations at Paradip (P), Gopalpur (G), Kakinada (K), and Cuddalore (C) with simulated currents for the stratification experiments listed in Table 6.9. Both ADCP and model currents are at 40 m. Correlation values in boldface notation exceed the 90% significance level.

Experiment	Location			
	P	G	K	C
LCSCR	-0.04	**0.48**	**0.58**	**0.61**
LCSWE	0.07	**0.50**	**0.56**	**0.58**
LCSCE	0.06	**0.48**	**0.56**	**0.57**
LCSEE	**0.15**	**0.45**	**0.58**	**0.58**
LCSSB	**0.18**	**0.45**	**0.59**	**0.56**
LCSCB	**0.19**	**0.44**	**0.60**	**0.55**
LCSNB	**0.15**	**0.41**	**0.58**	**0.53**

Table 6.13: Correlation between alongshore currents from the ADCP observations at Paradip (P), Gopalpur (G), Kakinada (K), and Cuddalore (C) with simulated currents for the stratification experiments listed in Table 6.9. Correlation values in boldface notation exceed the 99% significance level.

flow at Cuddalore during May–July 2011 in LCSCR is replaced by an equatorward flow in LCSCB and LCSNB; though this change essentially represents an increase in the current strength, it implies a poorer match with the poleward flow in observations. Likewise, the poleward current simulated by LCSCR during September–October 2011 matches the observations better than the weakly equatorward flow in LCSNB. In general, however, the change in stratification has a greater impact on the simulation at Kakinada and Cuddalore than at Gopalpur.

Since the EICC is forced both locally and remotely, it is useful to separate such impacts of stratification on the locally and remotely forced components. The experiments separating the local and remote responses are listed in Table 6.6. In these experiments, we do not separate the three processes contributing to remote forcing, but lump them together under, say, $LCSNB_R$; the corresponding local response is denoted by $LCSNB_L$. As may be expected from the strikingly different mode structures (Table 6.8), the change in background stratification has a significant impact on both local and remote components: the current is stronger in both cases for LCSNB compared to LCSCR (Figure 6.19).

The change in stratification affects both local and remote components of the current, but the seasonality and spatial variations in the strength of the local and remote forcing mechanisms are evident in the stratification experiments (Figure 6.19). For example, the change in the local response due to stratification is more during the summer monsoon, when the local forcing is strong, and marginal during February–April, when the local forcing and response are weak (see Figure 6.10; Shankar et al., 1996; McCreary et al., 1996). Likewise, the change in stratification has a weaker impact on the local response at Gopalpur than at Kakinada or Cuddalore (Figure 6.19) for the reasons discussed in Section 6.4. The poorer EICC simulation during May–July and September–October at Cuddalore in LCSNB or LCSCB compared to LCSCR is due to the stronger remotely forced component, which overwhelms the locally forced component even more in these simulations than in LCSCR

(Figure 6.19). Similarly, the poorer performance of LCSCB and LCSNB at Gopalpur during September–October 2011 is due to the much stronger remotely forced component. The complex interplay of the local and remote responses leads to a better simulation at some times and at some places, but a poorer simulation on other occasions when we compare the response to a change in the background stratification.

Low-order and high-order modes respond differently to the wind owing to the presence of vertical mixing in the LCS model (McCreary, 1980, 1981). Vertical mixing in this model has the form $\nu = \frac{A}{N_b^2}$, where A is a constant. The relevant terms in the momentum equations have the factor $\frac{A}{c_n^2}$ (see, for example, McCreary, 1980; Shankar et al., 1996), implying that the low-order modes, which are associated with a higher c_n (Table 6.8), are less affected by vertical mixing, and therefore changes in stratification, than the high-order modes. Physically, the low-order (high-order) modes have fewer (more) zero crossings in the mode structure and are therefore weakly (strongly) affected by vertical mixing (McCreary, 1980). Therefore, the low-order (high-order) modes in this model tend to adjust to a state of Sverdrup (Ekman) balance and they are efficient in radiating energy away from the forcing region in the form of Kelvin and Rossby waves (McCreary, 1980; Shankar et al., 1996). These modes are more significant for remote forcing and the remote response is dominated by the first two modes (Figure 6.20). In contrast, the stronger Ekman response of the high-order modes (McCreary, 1980) implies a stronger impact of these modes on the local response (Shankar et al., 1996; McCreary et al., 1996). The much stronger response, for the BoB stratification, at Kakinada during the summer monsoon is due to the stronger local response for the high-order modes (Figure 6.20).

Even though the effective coupling coefficient for the high-order modes is greater for the BoB stratification compared to LCSCR, these modes will be excited only if the length scale of the wind forcing fits these modes. For the annual band (300–400 days), the band-pass-filtered alongshore wind stress has a length scale of $\sim 14^\circ$, which matches the ~ 12

length scale for the tenth mode (based on the c_n values in Table 6.8; Figure 6.9d); the length scale for the first mode is an order of magnitude larger. Hence, when the local wind stress increases in May–June at Kakinada (Figure 6.9c), the contribution of the high-order modes to the local response exceeds that of the low-order modes (Figure 6.20).

Unfortunately, the spatial invariance of the background stratification implies that the local response due to these modes strengthens at Cuddalore as well (figure not shown); hence, using the BoB stratification experiments does not improve the simulation at Cuddalore (Figure 6.19). The heat and salt equations in this model are linearised about an assumed "steady thermohaline-driven background state" (McCreary, 1980) and this assumption is fundamental to the formulation of the model. Indeed, this assumption of a constant background stratification is a key linearisation of an inherently nonlinear system. The foregoing discussion shows that this limitation of a constant background stratification is a major weakness of the LCS model. In the real ocean and in an OGCM like MOM4p1, the density field varies in the horizontal and in time, implying that the mode coupling coefficient also varies in space and time (Figure 6.21). The temporal variation of this coefficient is less in the WEIO than in the BoB. In the NBoB, the coefficient for modes 4–5 is comparable to that for the first mode in some months, suggesting that the response in the OGCM will change in time even for the same wind forcing.

Hence, though the LCS model is invaluable for analysing processes, it has a fundamental limitation owing to its linearity and this limitation must be kept in mind when interpreting the model results.

6.7 Role of nonlinear dynamics

The nonlinearity due to the spatial and temporal variation in the vertical mode structure is not the only nonlinear effect ignored in the LCS model. The linearisation involves a neglect of the nonlinear advective terms, which leads to the much smoother circulation patterns

produced by the LCS model (Figure 6.22b). In this section, we discuss briefly the effect of nonlinear dynamics on the EICC; in particular, we show that nonlinearity is critical for simulating the current observed at the Paradip ADCP mooring (Figure 1.2b).

We have separated the Paradip mooring from the others for two reasons. First, unlike the other three moorings, it lies on the continental slope of the northern bay rather than off the east coast of India (Section 3.2); the deeper water column (~2000 m compared to ~1100 m) leads to the cross-shore component (meridional) being of the same order as the alongshore component (zonal) (Figure 6.22a). Second, the variability of the current at this location is different: the annual cycle is weak and the wavelet spectrum is dominated by the ~120-day period [Figure 6.23, top panels] (chapter 4).

The MOMCR simulation at Paradip is not as good as at the other locations. MOMCR simulates the strong observed alongshore (zonal) current during spring 2010 and 2011, but not during spring 2012. Even in the first two years, however, there is a phase mismatch, with the peak model current lagging (leading) the observed peak current by about a month in 2010 (2011) (Figure 6.22a, 6.23, 6.24). The MOMCR simulation of the cross-shore (meridional) current is worse, but the model does still capture some of the observed variability at the ~120-day period. The LCSCR simulation of both alongshore and cross-shore currents is poor, but comparable to that of MOM25 (Figure 6.22, 6.23, 6.24), the coarser-resolution MOM experiment (Sections 3.2, 6.3.2).

The altimeter SLA during March–April shows the presence of mesoscale circulations with a length scale of ~ 2° (~200 km) near the Paradip ADCP mooring (Figure 6.22b) in all three years. MOMCR simulates these "eddies" fairly well in 2010 and 2011, but is unable to capture the strong cyclonic eddy in 2012. These eddies are not captured in LCSCR, as expected of a linear model, and also in MOM25 owing to its coarser resolution.

We estimate the eddy kinetic energy (EKE) and eddy potential energy (EPE) following Böning and Budich (1992) and Eden and Böning (2002). EKE and EPE are defined as

follows:

$$\mathrm{EKE} = \frac{1}{2}\left(u'^2 + v'^2\right); \tag{6.4}$$

$$\mathrm{EPE} = -\frac{g\rho'}{2\rho\,(\partial\rho_\theta/\partial z)}, \tag{6.5}$$

where ρ_θ is the seasonal and horizontal mean potential density within the BoB; $\rho' = \rho - \bar{\rho}$, $u' = u - \bar{u}$, and $v' = v - \bar{v}$; $\bar{\rho}$ is the seasonal mean density and $\bar{u}$ and $\bar{v}$ are the zonal and meridional components, respectively of the seasonal mean current. In my thesis, we use a cutoff of 151 days to define the seasonal mean.

An eddy grows by taking potential and kinetic energy from the mean flow. Conversion from mean potential energy (MPE) to EPE is known as baroclinic conversion (E_{BC}) and that from mean kinetic energy (MKE) to EKE is knows as barotropic conversion (E_{BT}); E_{BC} and E_{BT} represent the terms $T2$ and $T4$, respectively in Equations (14) and (16) in Böning and Budich (1992) and are defined as follows (Böning and Budich, 1992; Eden and Böning, 2002; Cheng et al., 2013):

$$E_{\mathrm{BC}} = -\frac{g}{\rho(\partial\rho_\theta/\partial z)}\left(u'\rho'\frac{\partial\bar{\rho}}{\partial x} + v'\rho'\frac{\partial\bar{\rho}}{\partial y}\right); \tag{6.6}$$

$$E_{\mathrm{BT}} = -\left[u'u'\frac{\partial\bar{u}}{\partial x} + u'v'\left(\frac{\partial\bar{v}}{\partial x} + \frac{\partial\bar{u}}{\partial y}\right) + v'v'\frac{\partial\bar{v}}{\partial y}\right]; \tag{6.7}$$

Positive values of E_{BC} (E_{BT}) indicate baroclinic (barotropic) instability, with conversion of mean potential (kinetic) energy to eddy potential (kinetic) energy; negative values of E_{BC} (E_{BT}) indicate conversion from eddy potential (kinetic) to mean potential (kinetic) energy.

Since the variability in the intra-annual and intraseasonal bands can be forced not only by instabilities, but also by intra-annual and intraseasonal wind variability, we forced MOM at both resolutions with the wind forcing low-pass-filtered using a cutoff of 150 days. The

choice of the cutoff is dictated by the need to retain the variability around 120 days in the eddy part of the variability. These MOM experiments are called MOMCRF and MOM25F for the $0.1° \times 0.1°$ and $0.25° \times 0.25°$ resolutions, respectively. Since the wind forcing in these experiments does not include any variability at periods less than 150 days, the simulated variability around 120 days and in the intraseasonal band are due to instabilities associated with the mean current, which is dominated by the annual (and semi-annual) components. Estimation of eddy energy is based on the deviation from the mean. We use a 151-day Parzen window to estimate the seasonal mean; as with the forcing cutoff, this choice too is dictated by the need to retain the variability around 120 days in the eddy part of the variability. MOMCRF simulates the strong observed current during March–April 2010 (Figure 6.22a). Since both MOMCR and MOMCRF simulations are comparable, the strong intra-annual and intraseasonal variability simulated by MOMCR during March–April 2010 can be attributed to instabilities. During March–April 2011, however, there is a significant difference between MOMCR and MOMCRF, with the latter failing to simulate the strong current. We infer that this variability during March–April 2011 in MOMCR must be forced directly by the wind variability around this band. During 2012, since MOMCR does not simulate the observed current at Paradip, neither does MOMCRF.

The analysis shows patches of strong eddy kinetic energy (EKE) and eddy potential energy (EPE) near the Paradip mooring (Figure 6.25). The eddy grows by extracting both kinetic and potential energy from the mean flow. As expected, resolution matters for simulating the eddies and instabilities. The coarser resolution of MOM25 makes it less capable of resolving the mesoscale eddies, leading to marginal differences between the currents simulated by MOM25 and MOM25F (Figure 6.22a) and much lower estimates of EKE and EPE. The increase in horizontal resolution in MOMCR has a significant impact on the barotropic instability (panels for E_{BT} in Figure 6.25; see Equation (6.7)) and less on the baroclinic instability (panels for E_{BC} in Figure 6.25; see Equation 6.6. Though the simulation shows that

both instabilities are important at this location, the eddy grows by extracting energy from the mean flow via barotropic instability. In 2012, when MOMCR fails to simulate the observed current at Paradip, EKE and barotropic instability are weaker than in 2010 and 2011 (Figure 6.26). The results suggest considerable interannual variability in the eddy activity and the generation of instabilities.

The role of the eddies and instabilities is not restricted to the NBoB, where the Paradip mooring is located. Cheng et al. (2013) showed that eddy activity is strong in the WBoB at intraseasonal periods. Our analysis also shows that EKE, EPE, barotropic instability, and baroclinic instability are important in the regime of the EICC at Gopalpur, Kakinada, and Cuddalore (Figure 6.25). Such nonlinear interactions were ignored in the analysis with the LCS model, but they account for a part of the observed variability of the EICC.

6.8 Summary

The objective of this chapter was to simulate the current variability observed in the four ADCP moorings deployed on the continental slope of the WBoB and NBoB. The data show that the annual cycle (300–400 days) dominates the EICC variability, but with significant variability superimposed on it in the intra-annual (100–250 days) and intraseasonal (30–90 days) bands (Figure 6.7). For simulating the currents, we have used two numerical models, an OGCM (MOM4p1) and a simple, linear model. The linear (LCS) model has been used extensively in the literature to analyse the forcing mechanisms of the circulation in the NIO. In carrying out this analysis, we separate the three moorings at Gopalpur, Kakinada, and Cuddalore in the WBoB from the mooring, named Paradip, in the NBoB (Figure 1.2) because the current variability in this mooring is different.

We listed four specific aims in the introduction and we summarise the results before discussing the strengths and weaknesses of this work and the approach.

Our first aim was to evaluate the performance of a state-of-the-art OGCM in simulat-

ing the observed variability of the EICC on the continental slope. The results (Section 6.3) show that MOM, run at a horizontal resolution of $0.1° \times 0.1°$, simulates well the observed annual cycle of the EICC, but the performance degrades for the intra-annual and intraseasonal components (Figure 6.7). The performance of the LCS model is comparable to that of the OGCM (Figure 6.7), permitting its use for analysing local and remote contributions to the EICC. Such an analysis has been done earlier for the seasonal, climatological cycle (Shankar et al., 1996; McCreary et al., 1996), but we have extended it to a comparison with direct current measurements. The annual EICC is largely forced by the local alongshore winds in the WBoB and Ekman pumping over the interior BoB (Section 6.4; Figure 6.10). The contribution of local forcing is expectedly weak at Gopalpur owing to the direction of propagation of the Kelvin waves (anticlockwise along the perimeter of the BoB). The intra-annual EICC is dominated by remote forcing from the EIO (Figure 6.10). The intraseasonal EICC is affected by both local and remote forcing (Figure 6.11), but the intraseasonal variability is weaker in the linear model compared to the observations or the OGCM (Figure 6.7), suggesting the importance of nonlinear processes. Since the intraseasonal variability is not uniform in time, the coherence between the simulated and observed current also varies in time (Figure 6.8).

Our second aim was to test the importance of model resolution and nonlinearity. The results (Section 6.3) show that even a linear model or an OGCM with a $0.25° \times 0.25°$ resolution suffice to simulate the observed variability in the EIO, but their performance degrades in the EBoB (Figure 6.1). The LCS model and the OGCM at the coarser resolution also perform poorly in the NBoB (Section 6.7), where the Paradip mooring is located (Figure 6.22). Estimates of eddy kinetic energy (EKE) and instability computations show that eddies extract energy from the mean flow via both barotropic and baroclinic instabilities, but the barotropic instability is more important in the NBoB as well as the WBoB (Figure 6.25). An important result is that the poorer performance of the models in the EBoB does not imply

a poor simulation of the EICC owing to the significant forcing by local alongshore winds and Ekman pumping in the BoB.

Our third aim was to assess the role of stratification in the simulation of the EICC. This assessment is important owing to a limitation of the LCS model: the background density profile is invariant in space and time. Experiments with different background density profiles (Figure 6.9a and 6.16) in the LCS model (Section 6.6) show that the stratification in the EIO and BoB lead to significantly different structures for the vertical normal modes. We see a shift from the second-mode-dominance in the profile of Moore and McCreary (1990), which has been used in several earlier studies (see, for example, Shankar et al., 1996; McCreary et al., 1996), to a first-mode-dominance for profiles from the BoB (Table 6.8). The change in stratification leads to a stronger EICC for the NBoB or CBoB stratifications compared to the EIO stratifications and this increase in magnitude of the surface current is seen for both locally and remotely forced components (Figure 6.19). The effective (mode) coupling coefficient also decreases (increases) more slowly with mode number for the BoB profiles, making the high-order modes more significant. As a consequence, the high-order modes (5–10) contribute significantly to the locally forced EICC, but the remotely forced component is weakly affected by these modes (Figure 6.20).

Our fourth aim was to analyse the response of the EICC to remote forcing from the EIO. This analysis is important because altimeter SLA is used often to infer the remote forcing of the BoB circulation by the equatorial winds (see, for example, Vialard et al., 2009). Simulations with the LCS model, forced by realistic and idealised winds, show that the SLA is determined primarily by the first two vertical modes, with a weak contribution from the third mode (Section 6.5, Figure 6.13 and 6.15). The high-order modes are not important for the SLA, but contribute significantly to the current, particularly in the intraseasonal band (Figures. 6.13,6.15). The significant contribution from the high-order modes leads to downward propagation of energy in the form of beams along the equator (Figure. 6.12,6.14; McCreary,

1984). Hence, the SLA propagates almost undiminished from the EIO to the WBoB, but the current decays more rapidly away from the forcing regime in the CEIO (Figure 6.12–6.15). Since the beam bends more for the intraseasonal band compared to the annual or intra-annual band (Figure 6.14), the impact of remote forcing from the EIO is weaker for the intraseasonal EICC compared to the annual or intra-annual EICC (Figures. 6.12,6.14). It is important to keep this distinction between SLA and currents in mind when analysing the impact of remote forcing by events like the MJO on the circulation in the BoB. This bending of beams is not restricted to the EIO, but is likely to occur even for the coastal Kelvin waves: such a bending due to coastal Kelvin beams (Nethery and Shankar, 2007) has been invoked to explain the observed alongshore decorrelation of the intraseasonal current in the WBoB (discussed in the chapter 4) and the eastern Arabian Sea (Amol et al., 2012, 2014).

In summary, the results show that a linear model or a coarse-resolution OGCM work well for simulating the currents in the EIO, but the performance degrades away from the equator in the EBoB. In spite of this poorer performance in the EBoB, where the circulation may be strongly affected by the presence of the Andaman and Nicobar Islands (Chatterjee et al., 2017), the linear model simulates fairly well the observed variability of the EICC owing to the strong impact of local forcing. It is likely that even higher resolution is required to capture the short-scale effect of the Andaman and Nicobar Islands on the circulation in the EBoB. Model resolution is also important owing to the significant role of eddies and instabilities in the NBoB and the regime of the EICC.

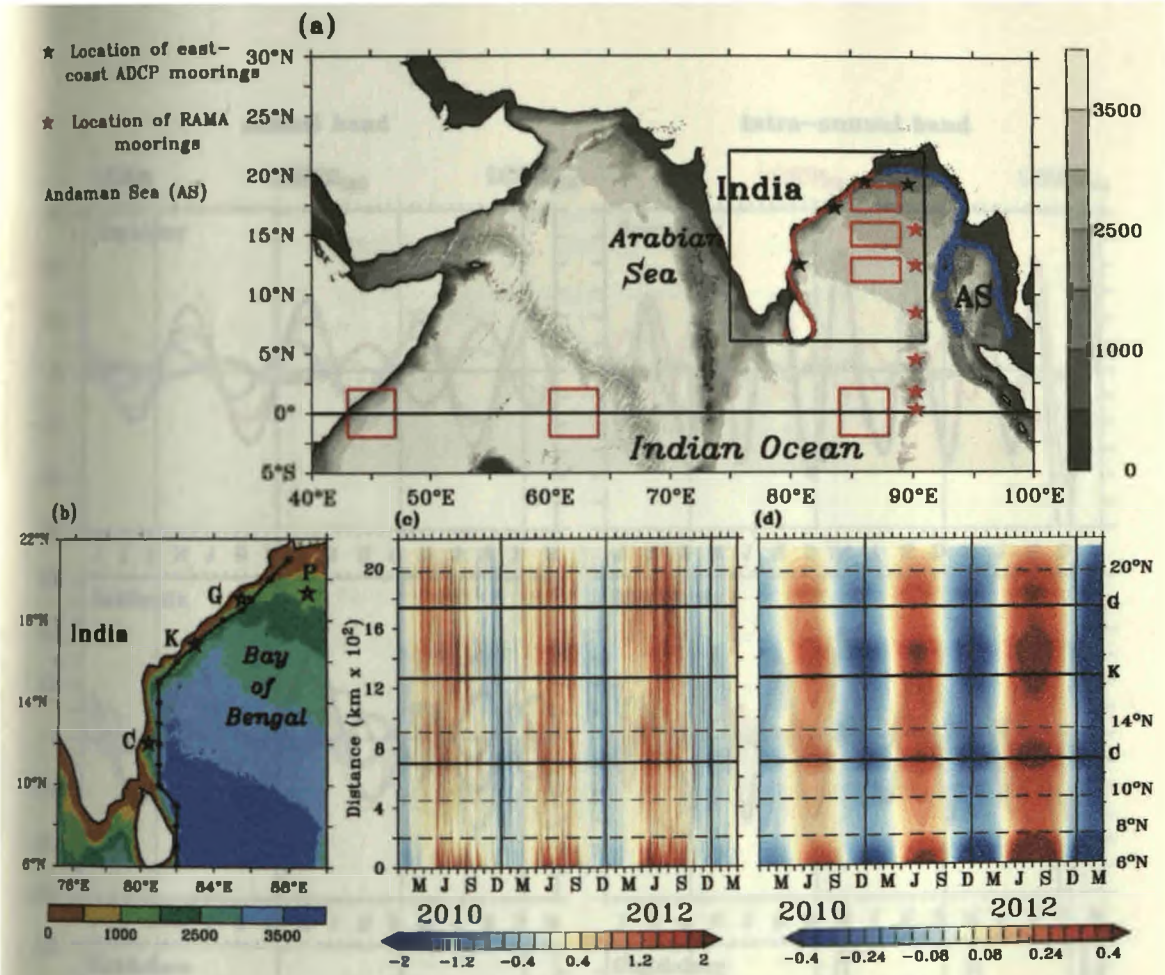

Figure 6.9: **(a)** Region of interest in the North Indian Ocean (NIO). The greyscale shading shows the bathymetry (m). The black box marked by solid lines is the western BoB (WBoB) region shown in panel (b). The three ADCP moorings on the continental slope in the WBoB and the ADCP mooring in the northern BoB (NBoB) are shown by the black stars. The red stars denote the RAMA moorings. The red boxes denote the domains used for averaging the density profiles for the stratification experiments discussed in Section 6.6. The red curve along the western margin of the BoB denotes the stretch of the coast along which the modified continental boundary condition is applied in Experiment $LCSCR_{WB}$ in Section 6.4; the red curve along the eastern and northern margins of the BoB and along the coastline of the Andaman and Nicobar Islands denotes the stretch of the coast for application of this boundary condition in Experiment $LCSCR_{EB}$. **(b)** The WBoB, showing the bathymetry (colour scale, m) and the location of the ADCP moorings (black stars). The solid line with closed circles denotes the stretch of the coast for which the alongshore wind stress is shown in panels (c) and (d). **(c)** Alongshore wind stress (dyne cm^{-2}) as a function of distance (km) from the southern end of the coastal stretch at (82°E, 6°N). The solid horizontal lines represent the ADCP locations. The latitudes are marked by the dashed lines. **(d)** As in panel (c), but for the 300–400-day band-pass-filtered alongshore wind stress (dyne cm^{-2}). A fourth-order Butterworth filter is used for the filtering operation.

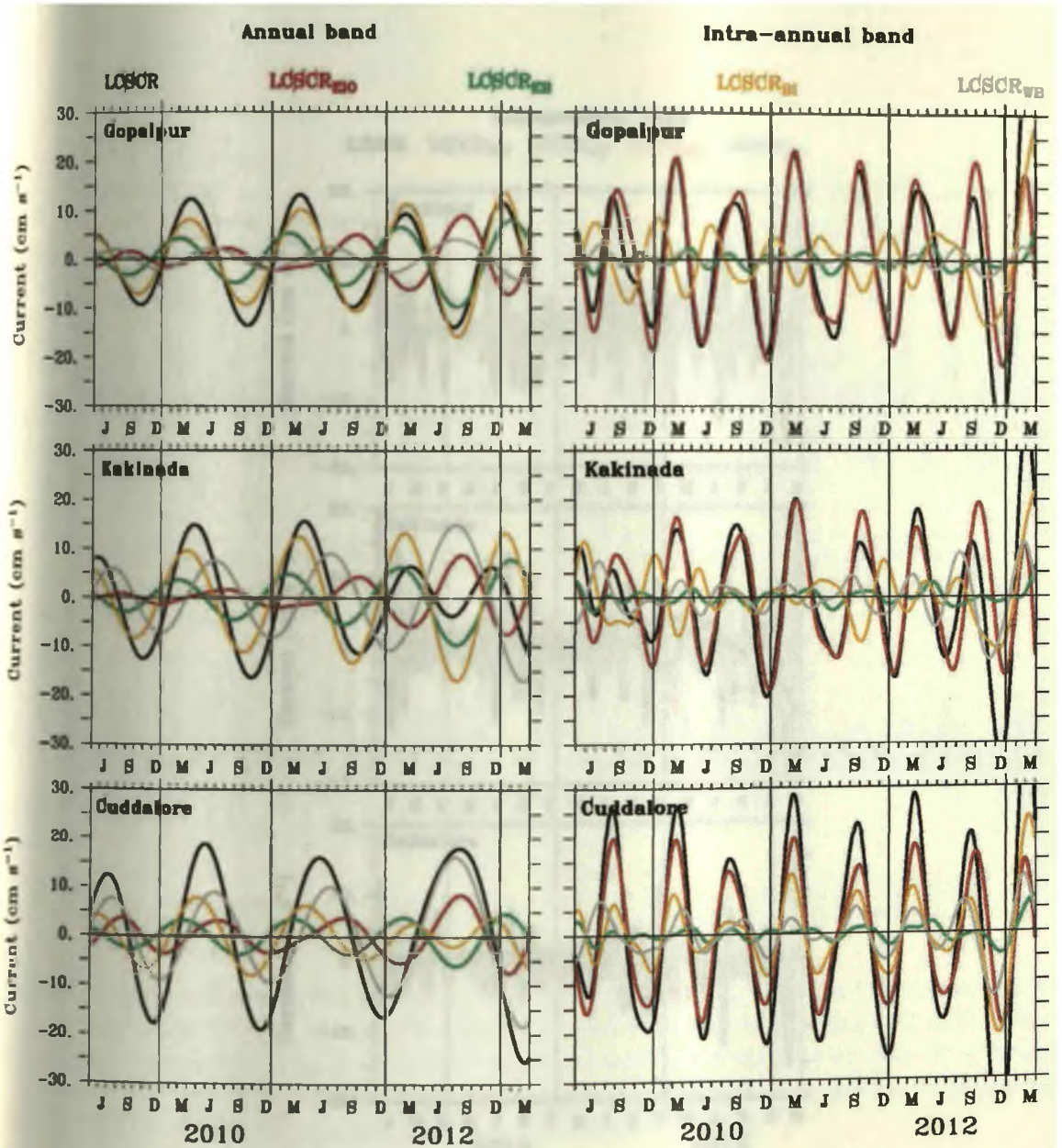

Figure 6.10: Alongshore surface current in the annual (300–400 days, left panels) and intra-annual (100–250 days, right panels) for the LCS model experiments described in Section 6.4. The experiments LCSCR$_{WB}$, LCSCR$_{EIO}$, LCSCR$_{EB}$, and LCSCR$_{BI}$ are listed in Table 6.6. The intraseasonal current is shown in Figure 6.11.

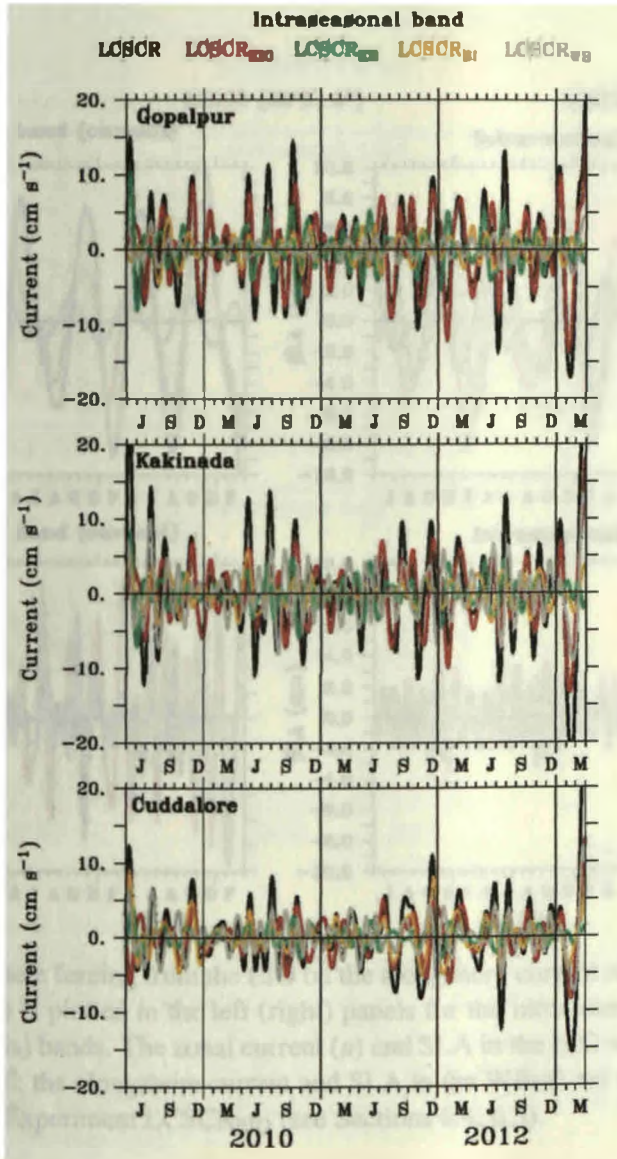

Figure 6.11: As in Figure 6.10, but for intraseasonal (30–90 days) band.

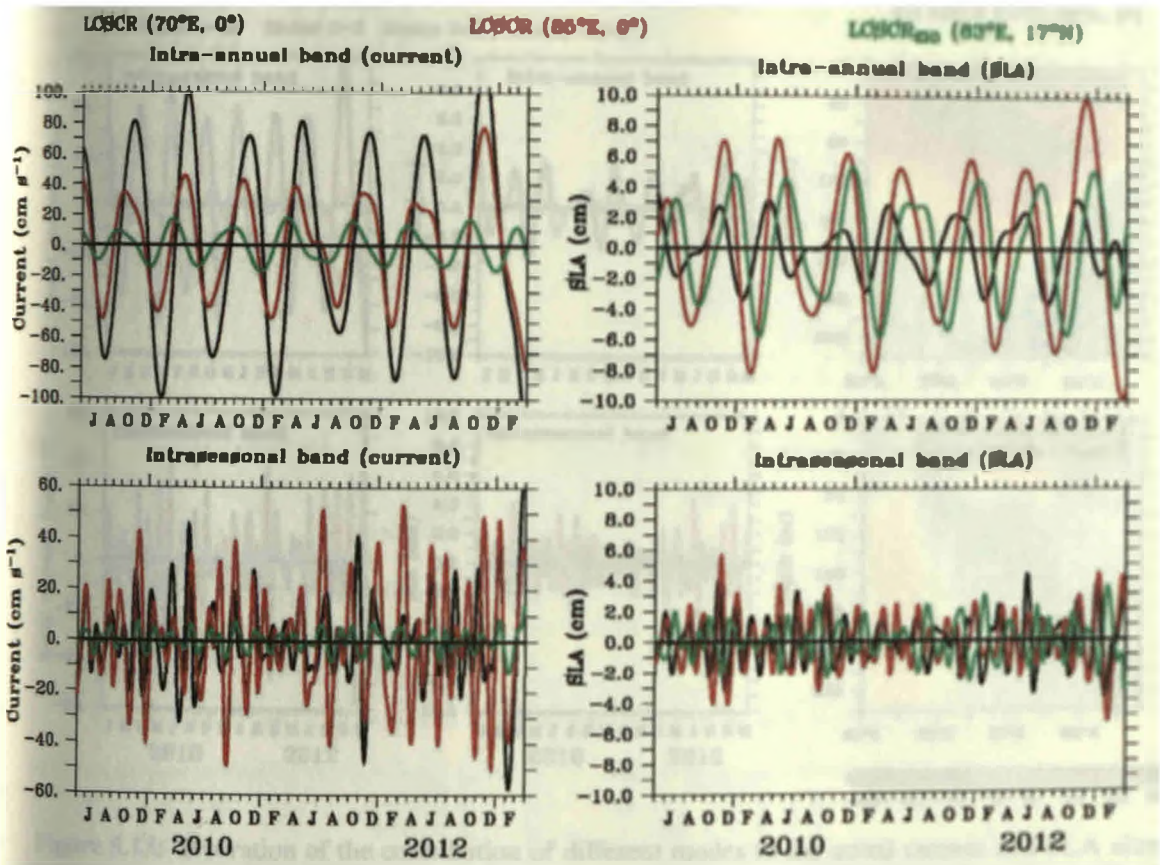

Figure 6.12: Impact of remote forcing from the EIO on the alongshore current and SLA in the EICC regime. The current (SLA) is plotted in the left (right) panels for the intra-annual (top panels) and intraseasonal (bottom panels) bands. The zonal current (u) and SLA in the EIO are from LCSCR and are shown for 70° and 85°E; the alongshore current and SLA in the WBoB are shown off Kakinada (83°E, 17°N) are are from Experiment $LCSCR_{EIO}$ (see Sections 6.4, 6.5).

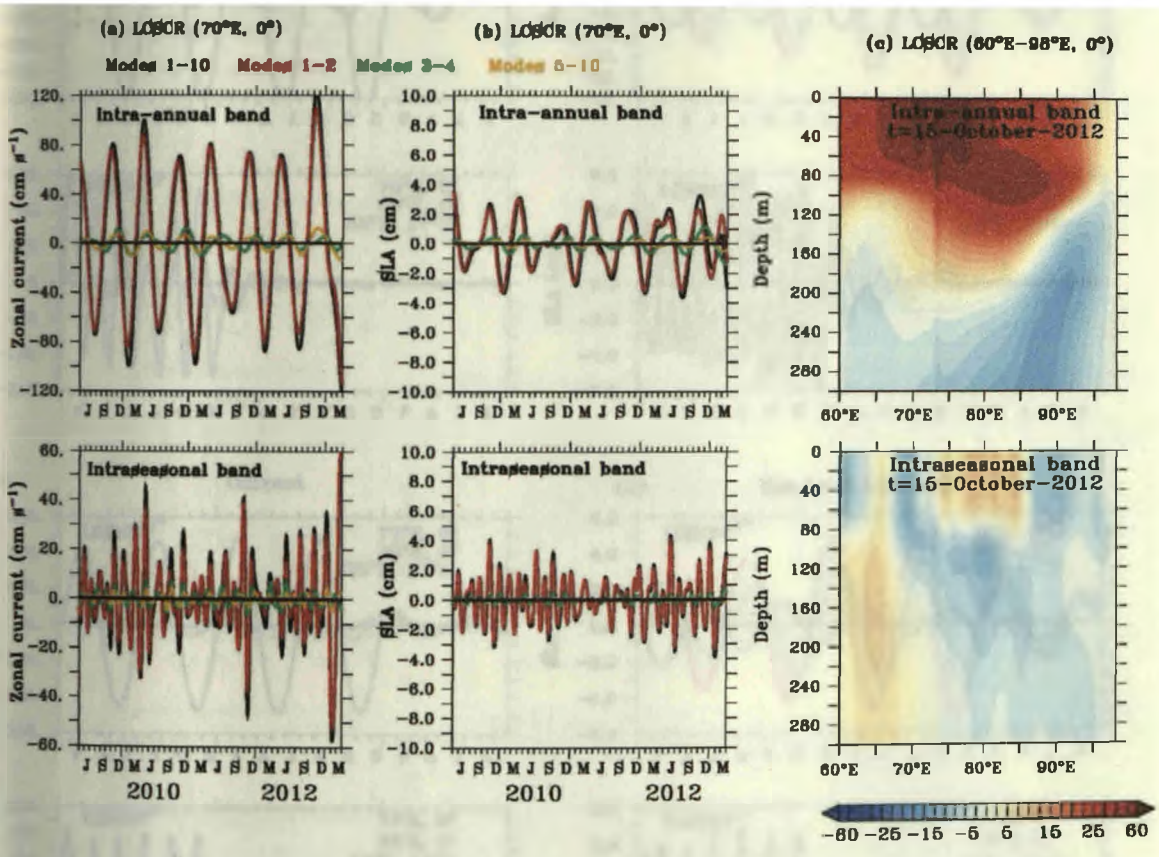

Figure 6.13: Separation of the contribution of different modes to the zonal current and SLA simulated by LCSCR in the EIO. **(a)** Surface zonal current simulated by LCSCR in the EIO (85°E, 0°) for the intra-annual (top panel) and intraseasonal (bottom panel) bands. The curves shown are for a summation of the contribution to the first ten modes (black), modes 1–2, (red), modes 3–4 (green), and modes 5–10 (yellow). **(b)** As in (a), but for SLA. **(c)** vertical section of zonal current along the equator between 60°–96°E for the intra-annual (top panel) and intraseasonal (bottom panel) bands; the snapshots are for 15 October 2012.

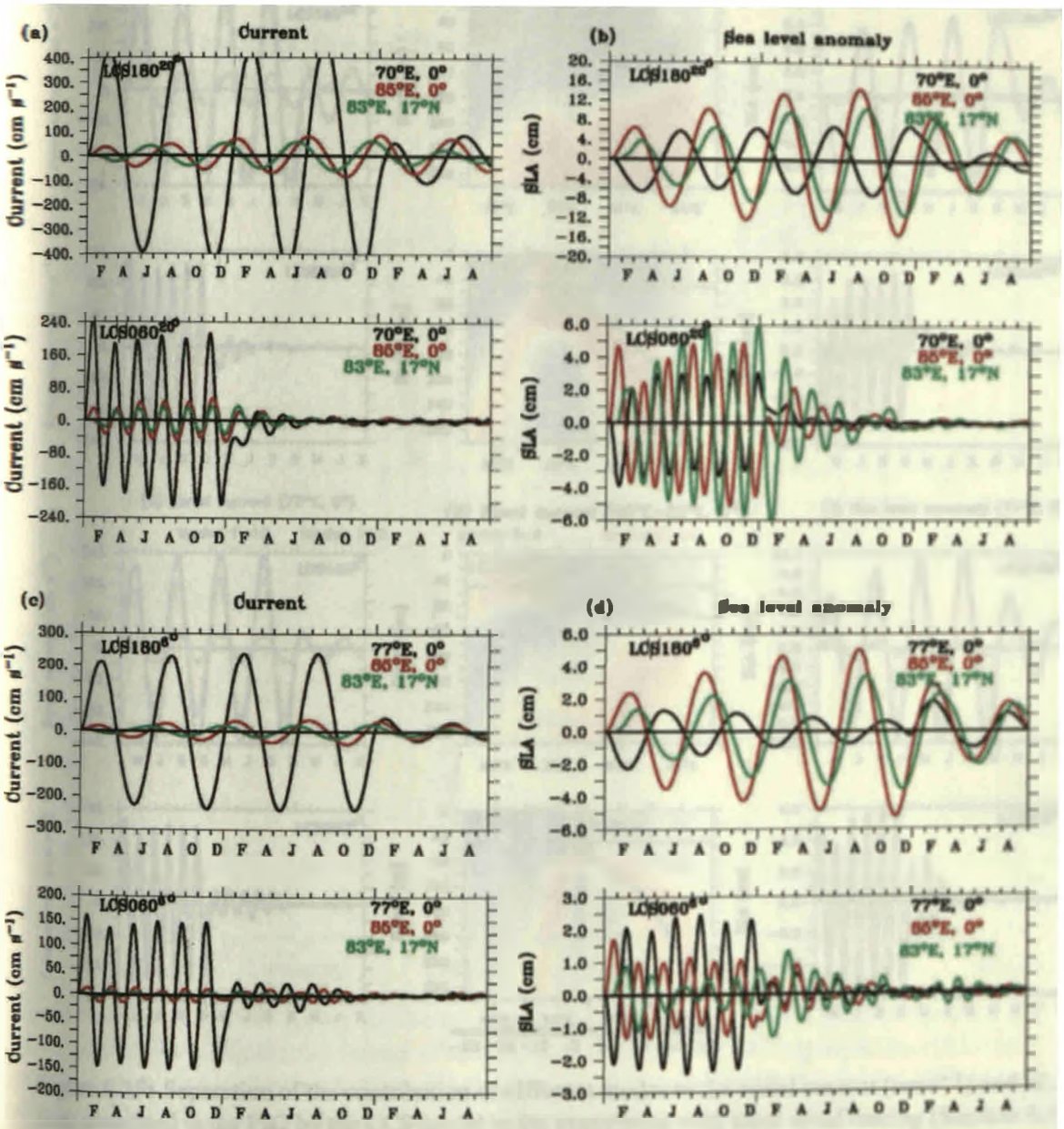

Figure 6.14: Results of the simulations with ideal wind forcing (Section 6.5). Current (SLA) is plotted in the left (right) panels for the four experiments listed in Table 6.7. The surface zonal current at the equator is plotted at the centre of the wind-forcing patch (black curve; 70°E and 77°E for the forcing length scale of 20° and 6°, respectively) and to its east (red curve; 85°E); the alongshore current in the WBoB is plotted near Kakinada (green curve; 83°E, 17°N). **(a)** Experiment LCS180$^{20°}$. **(b)** Experiment LCS060$^{20°}$. **(c)** Experiment LCS180$^{6°}$. **(d)** Experiment LCS060$^{6°}$.

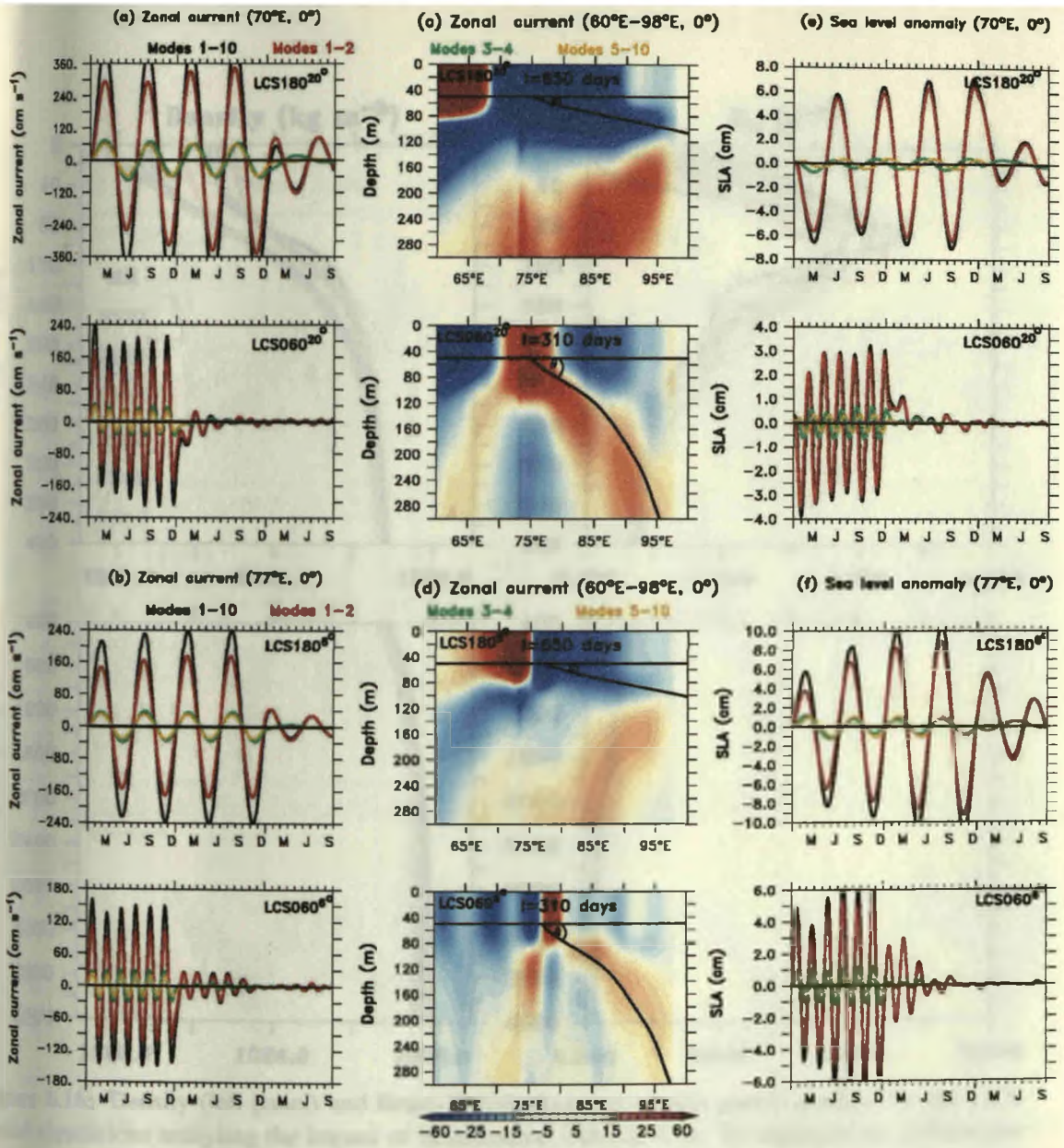

Figure 6.15: Separation of the contribution of different modes to the zonal current (cm s^{-1}) and SLA (cm) simulated in the EIO by the LCS model in the experiment with ideal wind forcing (Section 6.5). As in Fig. 6.13, surface zonal current (left panels), a section of the zonal current along the equator (60°–96°E; middle panels), and SLA (right panels) are plotted. The curves in the left and right panels are for a summation of the contribution to the first ten modes (black), modes 1–2, (red), modes 3–4 (green), and modes 5–10 (yellow). **(a)** Zonal current as a function of time for LCS180$^{20°}$ (top) and LCS060$^{20°}$ (bottom) at 70°E at the equator. **(b)** Zonal current as a function of time for LCS180$^{6°}$ (top) and LCS060$^{6°}$ at 77°E (bottom) at the equator. θ is the bending angle given by $\frac{\sigma}{N_b(z)}$, where σ is the forcing frequency and $N_b(z)$ is the background Brünt-Vaïsala frequency used in LCSCR. **(c)** Depth-longitude section for day 650 of the zonal current for LCS180$^{20°}$ (top) and LCS060$^{20°}$ (bottom) at 70°E at the equator. **(d)** Depth-longitude section for day 310 of the zonal current for LCS180$^{6°}$ (top) and LCS060$^{6°}$ at 77°E (bottom) at the equator. **(e)** As in (a), but for SLA. **(f)** As in (b), but for SLA.

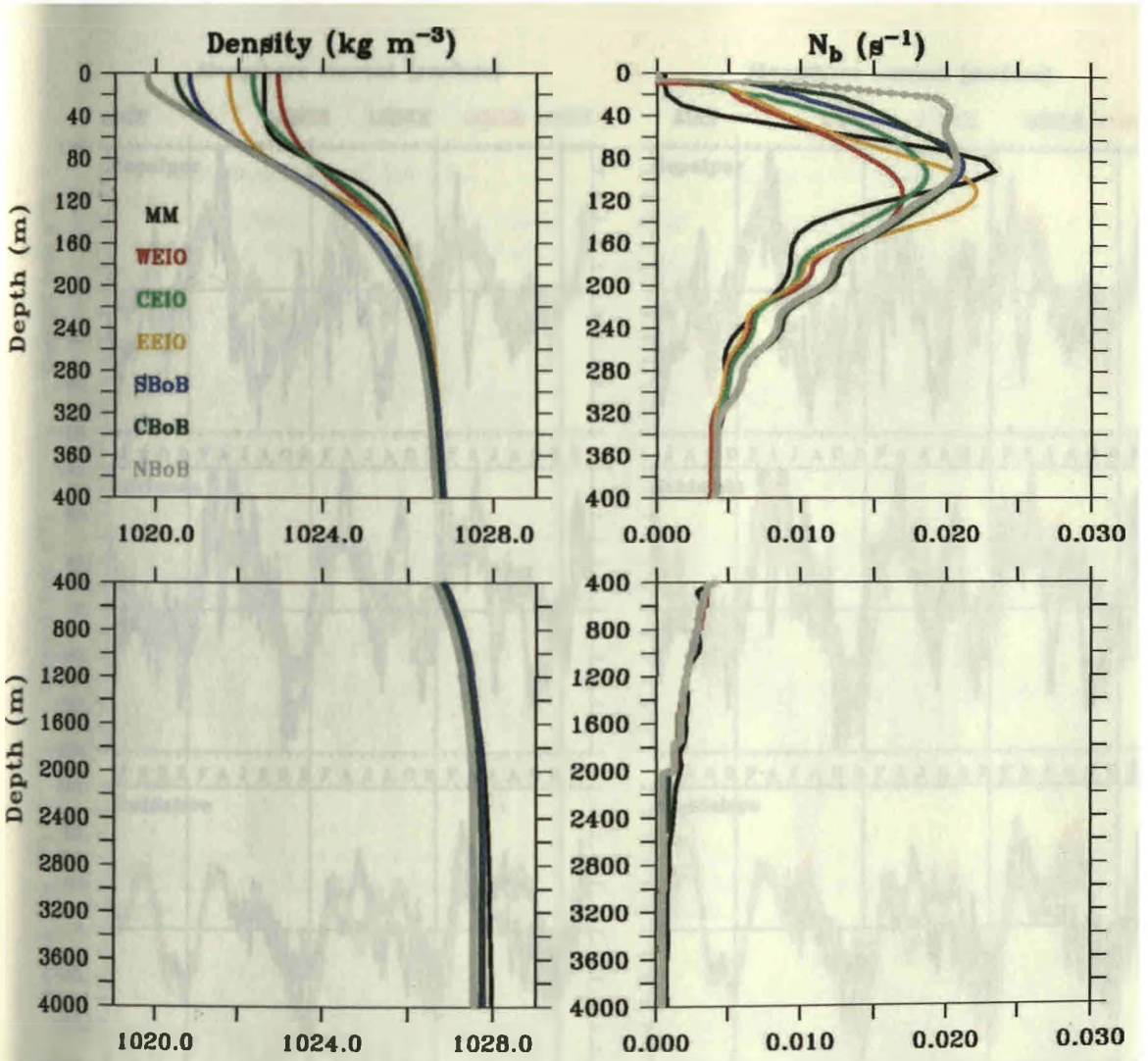

Figure 6.16: Density (left panel) and Brünt-Vaïsala-frequency (right panel) profiles for the LCS model simulations analysing the impact of stratification (Section 6.6). To highlight the differences near the surface and in the thermocline, the profiles are shown separately for the top 400 m (top panels) and for 400–4000 m (bottom panels). The simulations include LCSCR, which uses the stratification from Moore and McCreary (1990, profile MM); this density profile was constructed on the basis of a current-meter profile in the WEIO (ONeill, 1984). The profiles used in Experiments LCSWE, LCSCE, LCSEE, LCSSB, LCSCB, and LCSNB are denoted by WE, CE, EE, SB, CB, and NB, respectively, and represent averages of density in the WEIO, CEIO, EEIO, SBoB, CBoB, and NBoB, respectively. These averages were computed over the domains shown in Figure 6.9 using the annual climatology of Chatterjee et al. (2012).

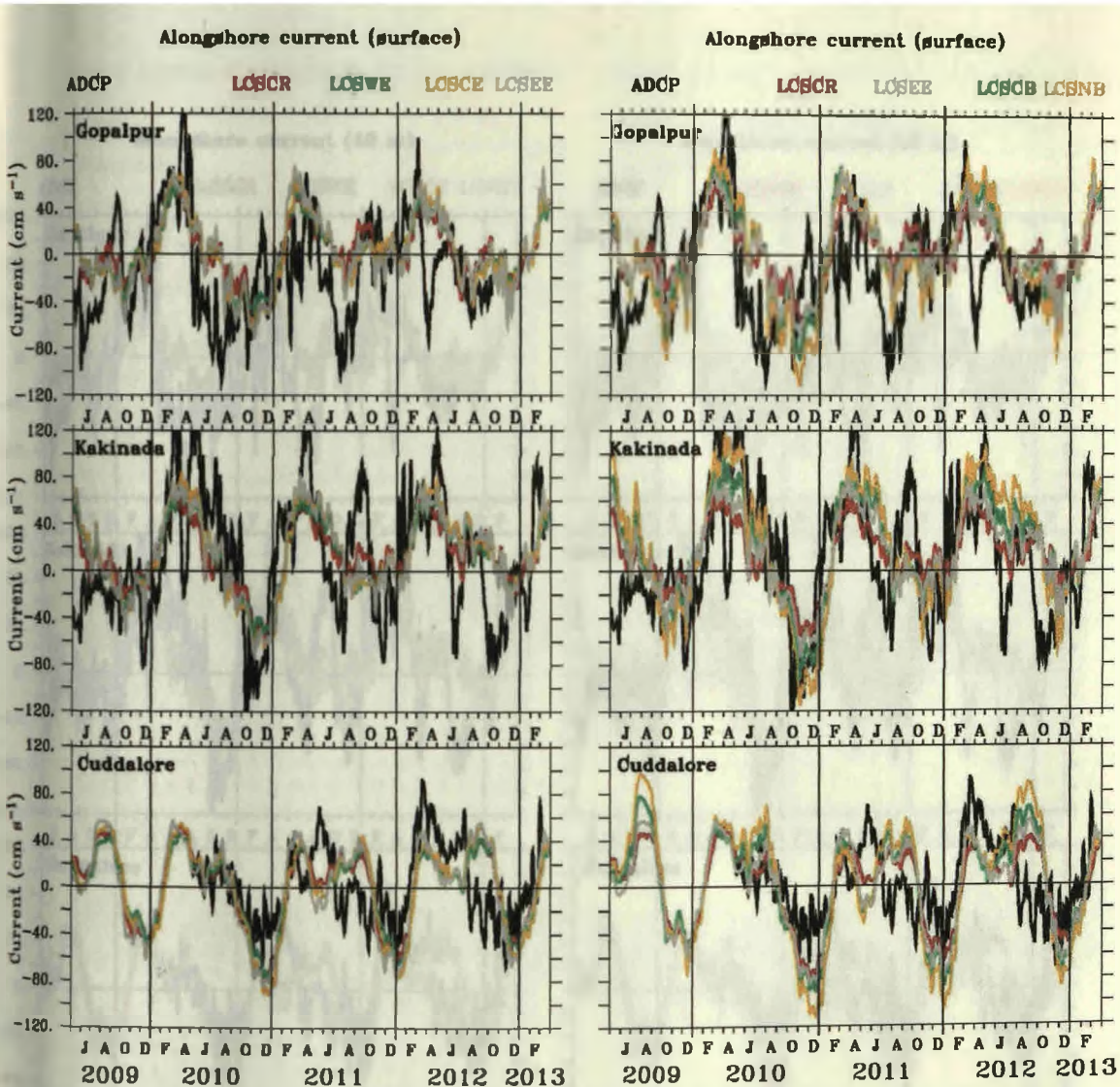

Figure 6.17: Impact of stratification on the LCS model simulation of the EICC (Section 6.6). The experiments are listed in Table 6.9 and use the density profiles shown in Figure 6.16. The ADCP current is at 40 m, but the model currents are shown for the surface. To avoid clutter, we have split the results into two panels for each location and have not shown the curve for LCSSB as it is almost the same as that for LCSCB. The ADCP current and the currents simulated by LCSCR and LCSEE are repeated in the panels on the left and right; LCSEE is repeated to highlight the transition from the EIO to the BoB.

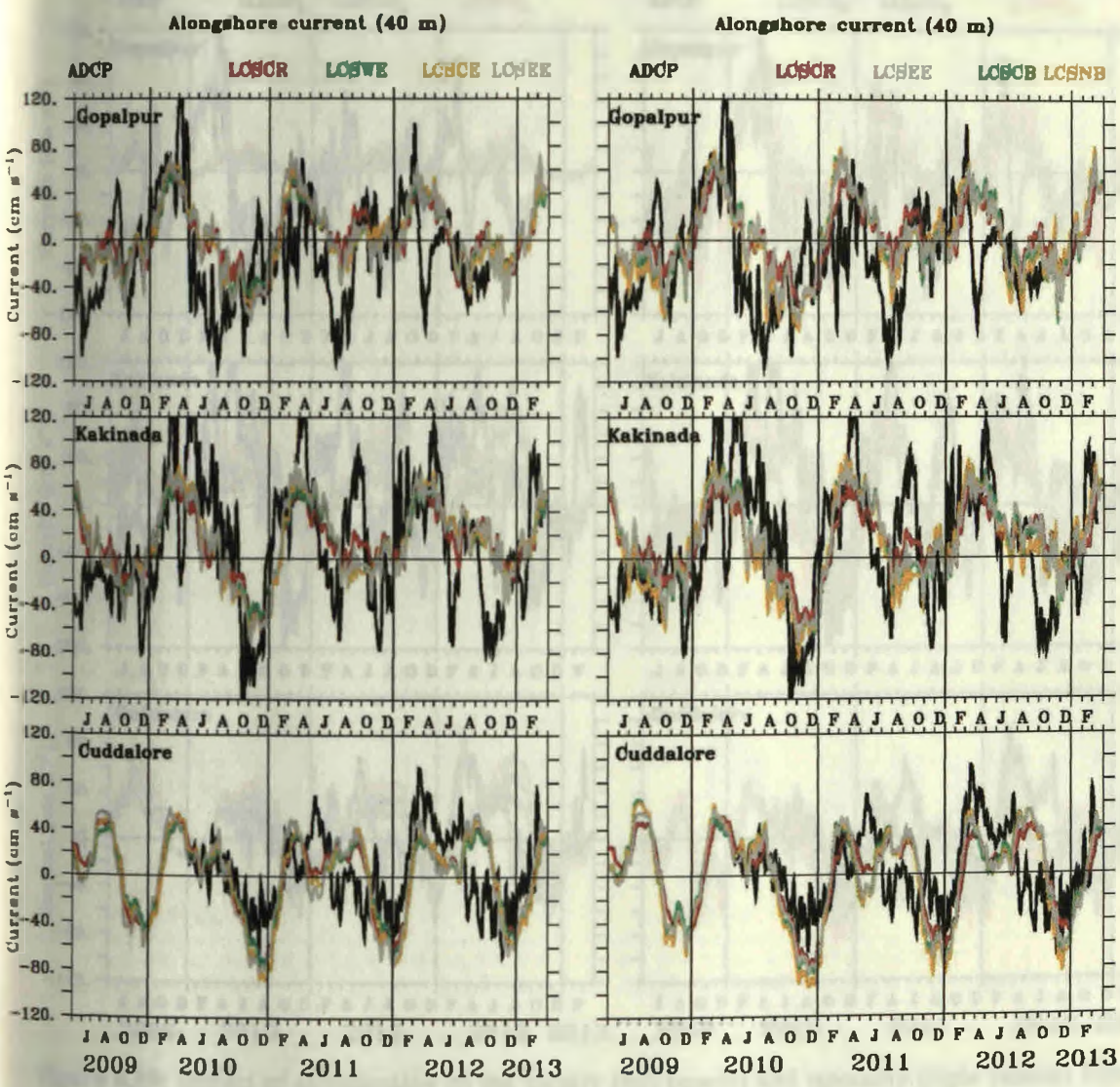

Figure 6.18: Same in Figure 6.17, but at 40 m.

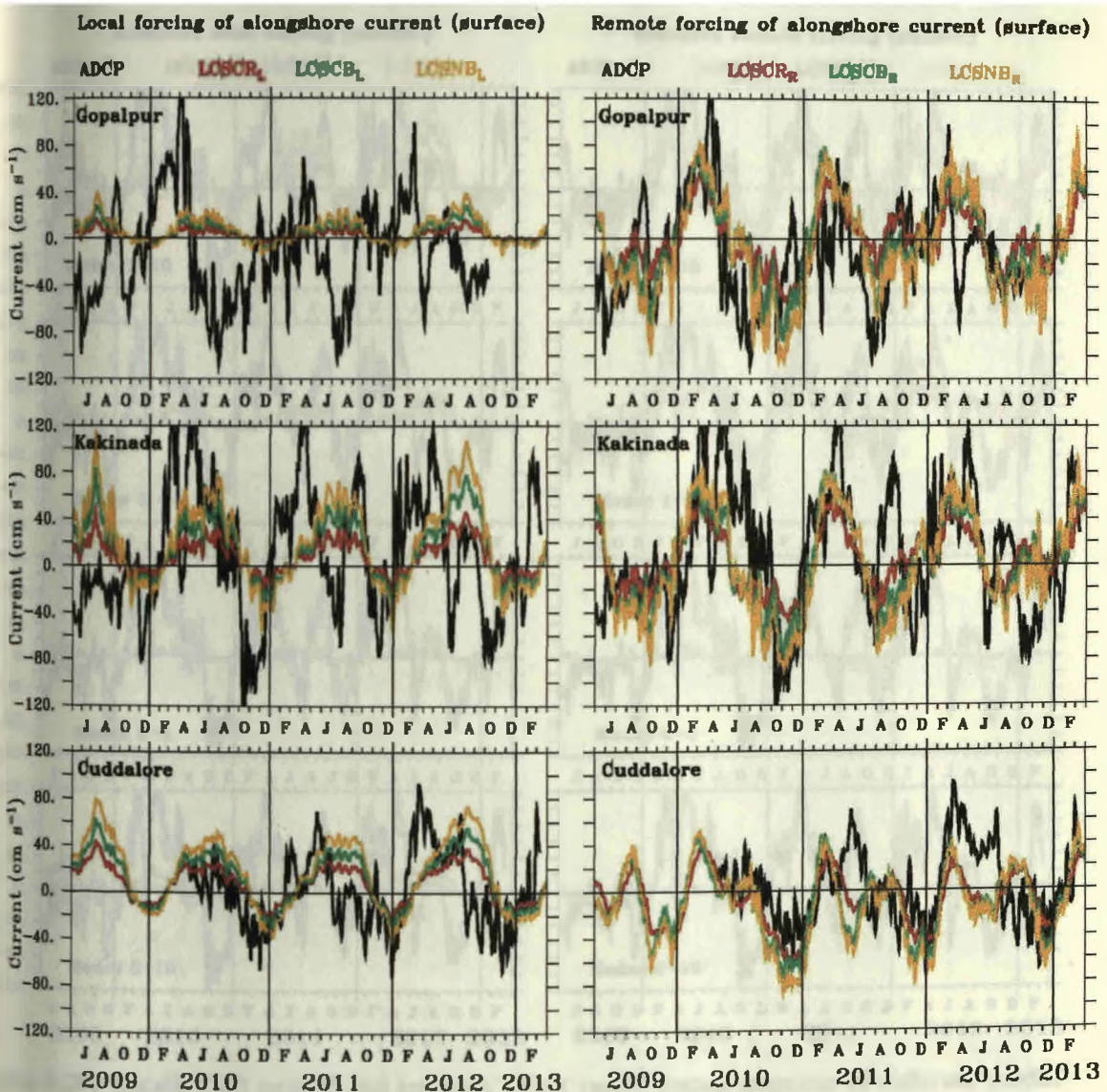

Figure 6.19: Impact of stratification on the locally (left panels) and remotely (right panels) forced components of the EICC (Section 6.6). Alongshore current from the ADCP observations (40 m, repeated in left and right panels) and the LCS model experiments LCSCR, LCSCB, and LCSNB (see Table 6.9) is plotted. The model current is at the surface.

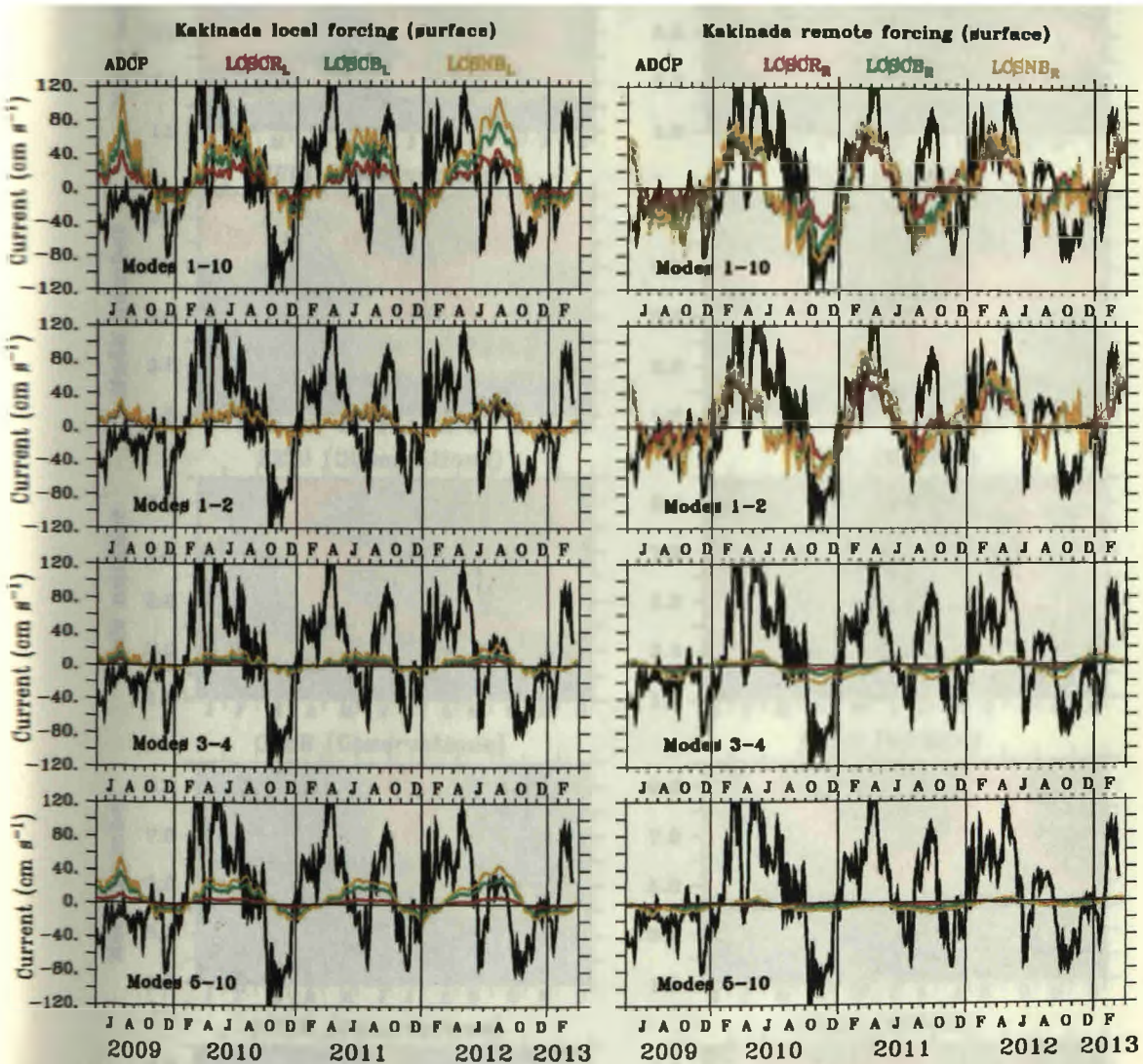

Figure 6.20: Locally (left panels) and remotely (right panel) forced response of different modes at Kakinada (Section 6.6). The alongshore current is plotted for the ADCP observations (40 m, repeated in left and right panels) and the LCS model experiments LCSCR, LCSCB, and LCSNB (see Table 6.9). From top to bottom, the panels show the response summed over the first ten modes (top row), modes 1–2 (second row), modes 3–4 (third row), and modes 5–10 (bottom row).

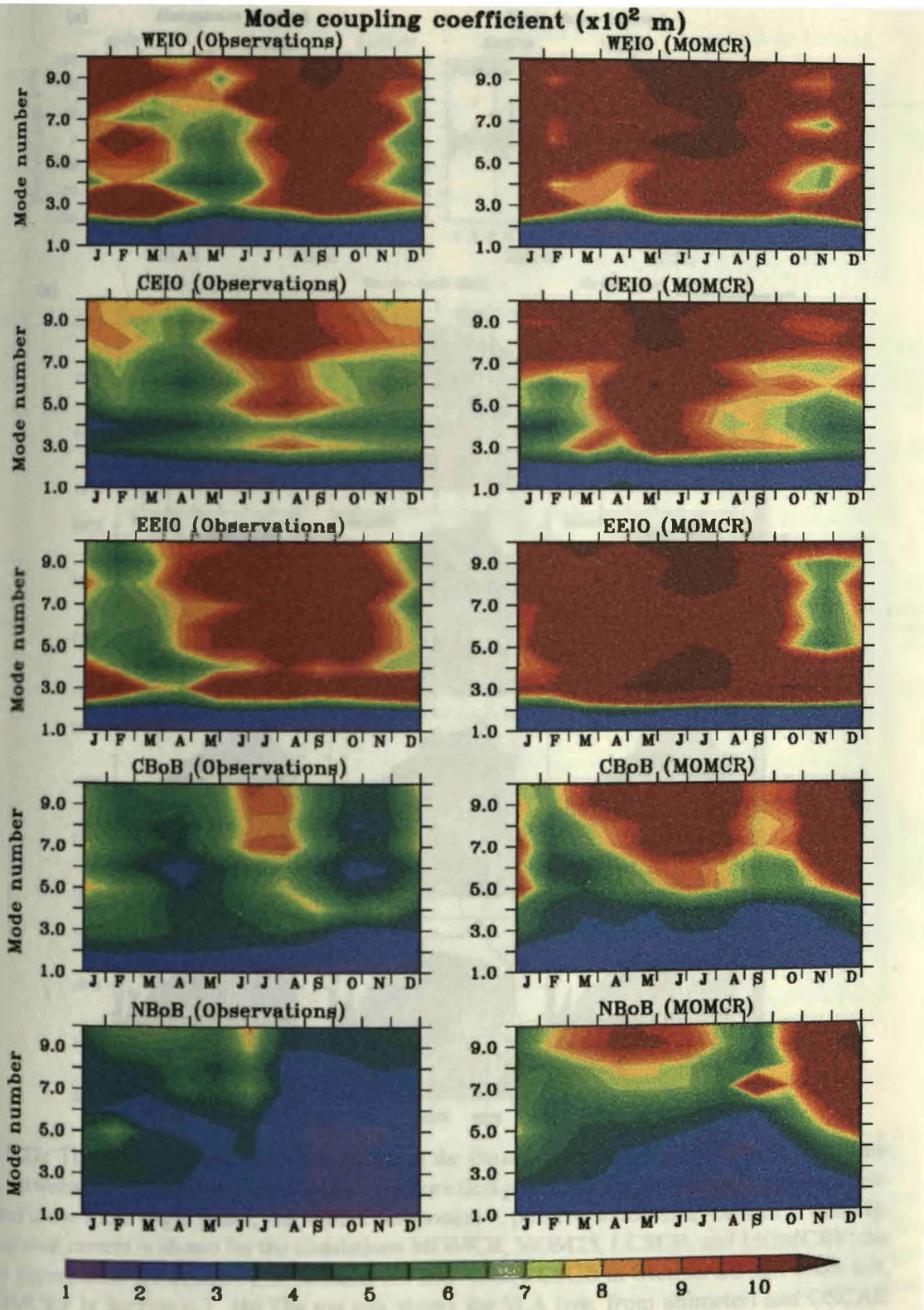

Figure 6.21: Mode coupling coefficient computed for the annual climatology of Chatterjee et al. (2012) (left panels) and MOM4p1 (right panels). The coefficients are computed for a monthly climatology of the density field in MOM4p1. The locations in the WEIO, CEIO, EEIO, CBoB, and NBoB are shown in Figure 6.9a and the coordinates of the averaging domains are listed in Table 6.9.

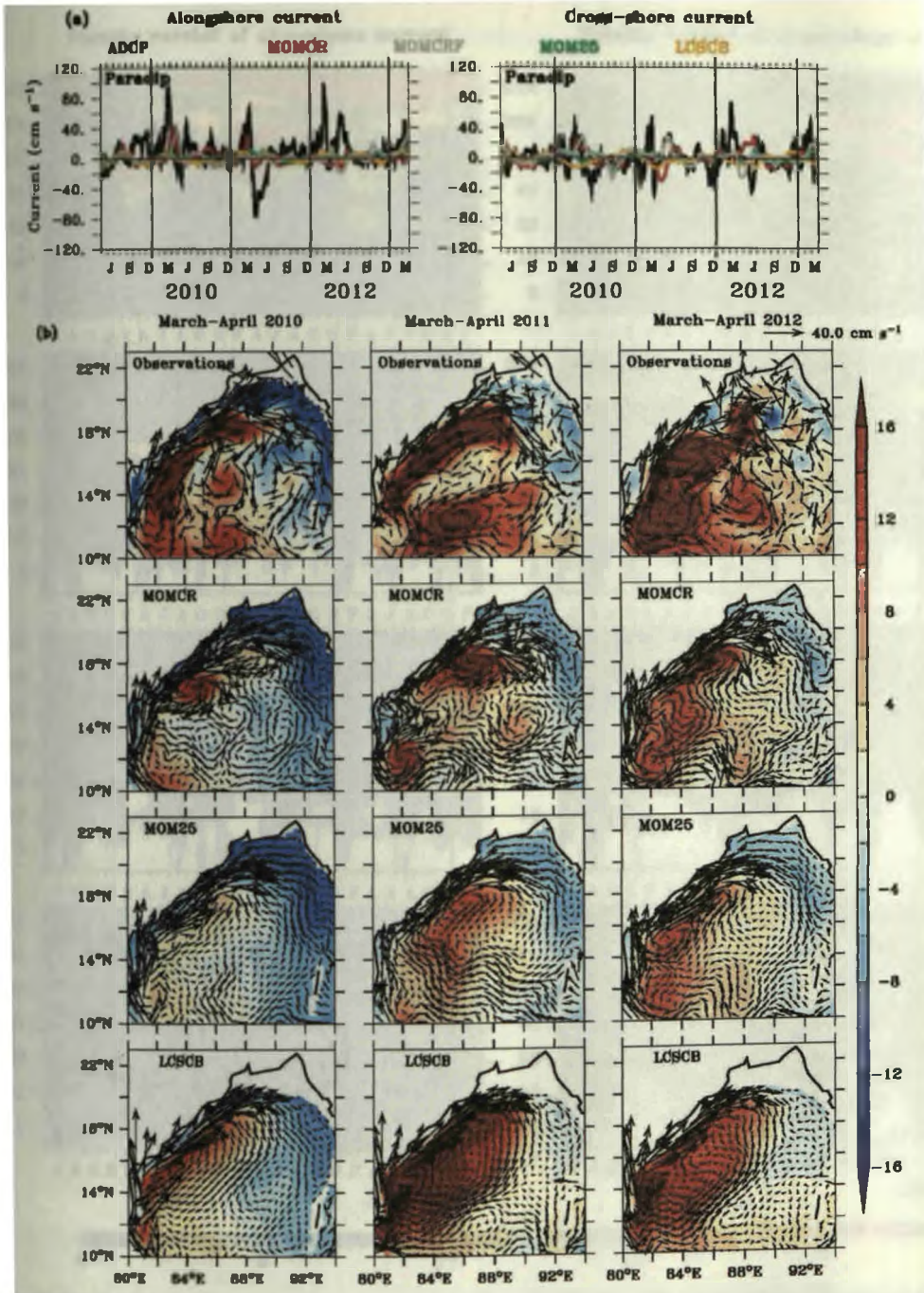

Figure 6.22: The observed and simulated current at the Paradip mooring (Figure 6.9a,b). **(a)** Comparison between the observed and simulated alongshore (left panel; zonal component u, positive eastward) and cross-shore (right panel; meridional component v, positive *southward*) current at Paradip. The simulated current is shown for the simulations MOMCR, MOM25, LCSCB, and MOMCRF; the first two experiments are described in Sections 3.2 and 6.3.2, LCSCB in Section 6.6 and Table 6.9, and MOMCRF in Section 6.7. **(b)** The top row shows the SLA (cm, from altimeter) and OSCAR current during March–April of 2010, 2011, and 2012. The next three rows show the SLA and surface current for the simulations MOMCR, MOM25, and LCSCB. (The result for LCSNB is similar to that for LCSCB. The values are averages during 10 March to 10 April)

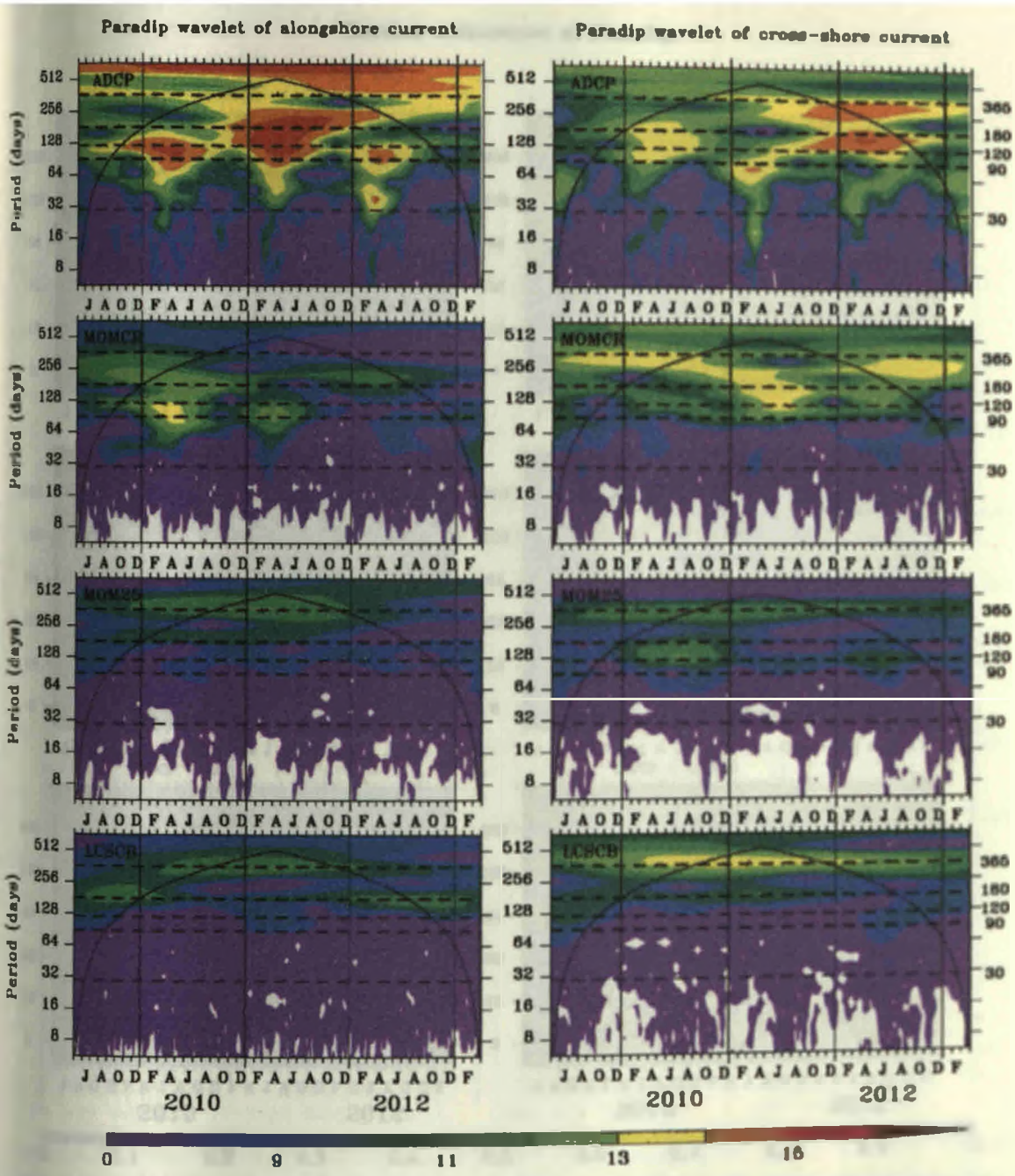

Figure 6.23: Morlet wavelet power spectra ($cm^2\ s^{-2}$) of alongshore (zonal, left panels) and cross-shore (meridional) components of the current at 40 m depth at the Paradip mooring location (Figure 6.9a,b). The wavelet spectra are plotted for the ADCP data (top row) and the model simulations MOMCR (second row), MOM25 (third row), and LCSCB (bottom row). The thick black line marks the cone of influence. The ordinate and wavelet power are plotted on a $\log_2$ scale. The horizontal dashed lines mark the 30-day, 90-day, 120-day, 180-day, and 365-day periods. Note that the colour scale is not uniform.

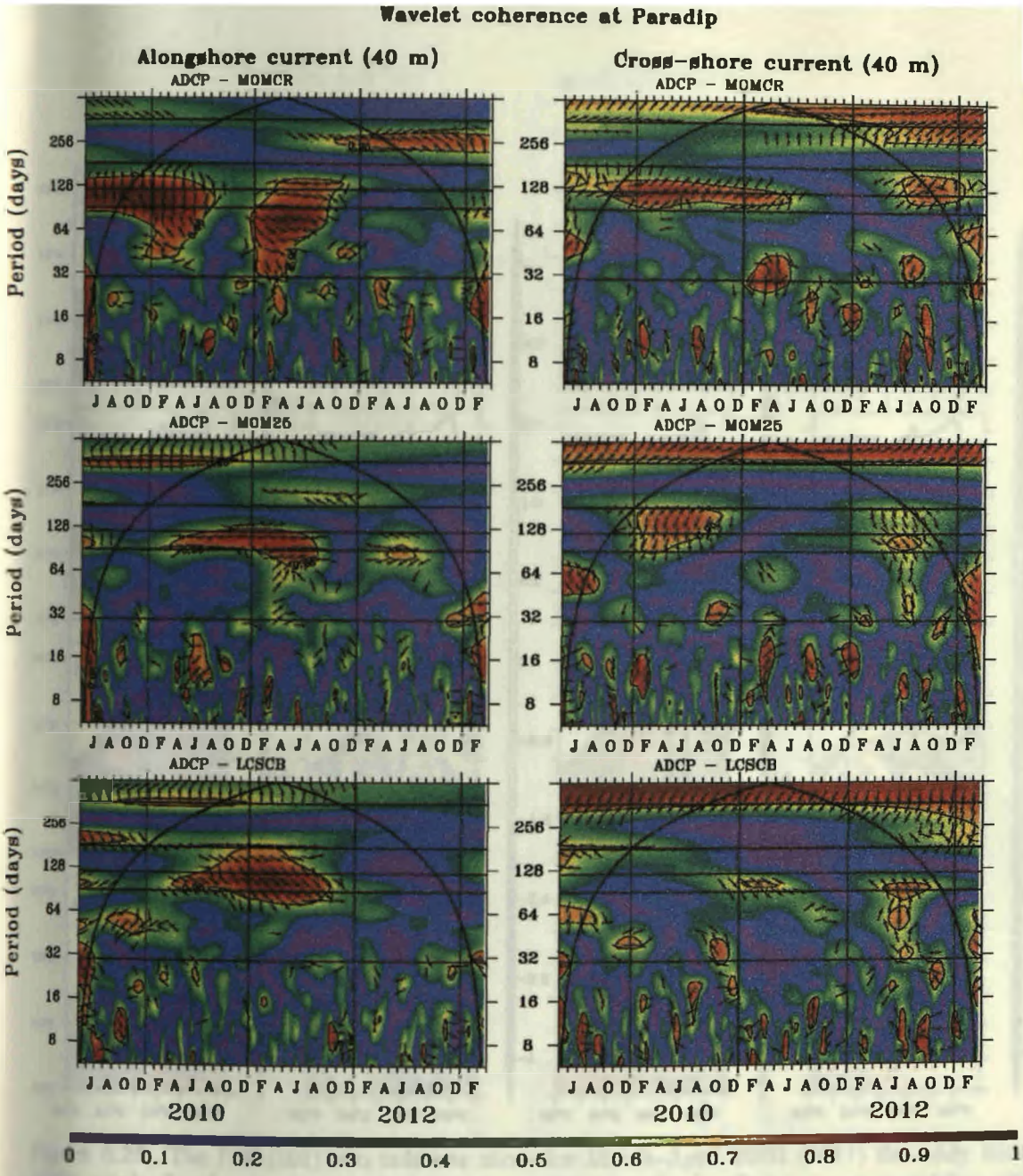

Figure 6.24: Wavelet coherence of the alongshore current at Paradip between the ADCP observations and the model simulations MOMCR, MOM25, and LCSCB; the result for LCSCR is almost identical to that for LCSCB. The contour line shows the 5% significance level against red noise and the thick black line shows the COI. The arrows show the relative phase relationship, with in-phase (anti-phase) pointing right (left). The first variable (observation) leads (lags) the second (model) in anticlockwise (clockwise) direction. The arrows are shown only for wavelet coherence of 0.5 or more.

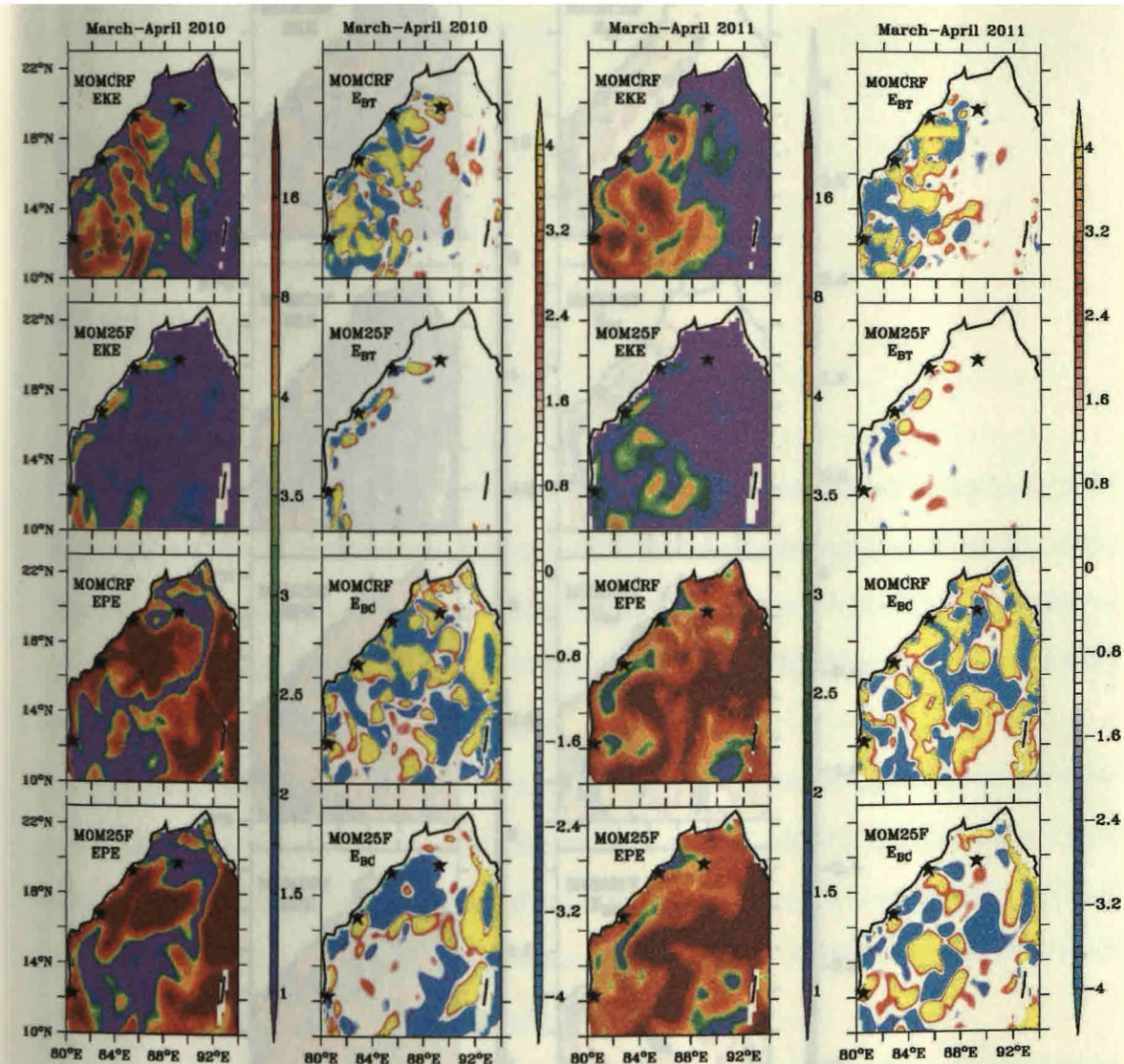

Figure 6.25: The first (last) two columns show for March–April 2010 (2011) the eddy kinetic (EKE, 10^{-3} m^2 s^{-2}) energy, eddy potential energy (EPE, 10^{-3} m^2 s^{-2}), barotropic instability (E_{BT}, 10^{-3} m^2 s^{-3}), and baroclinic instability (E_{BC}, 10^{-3} m^2 s^{-3}). The estimates are shown for the simulations MOMCRF and MOM25F and the values are averages during 10 March to 10 April.

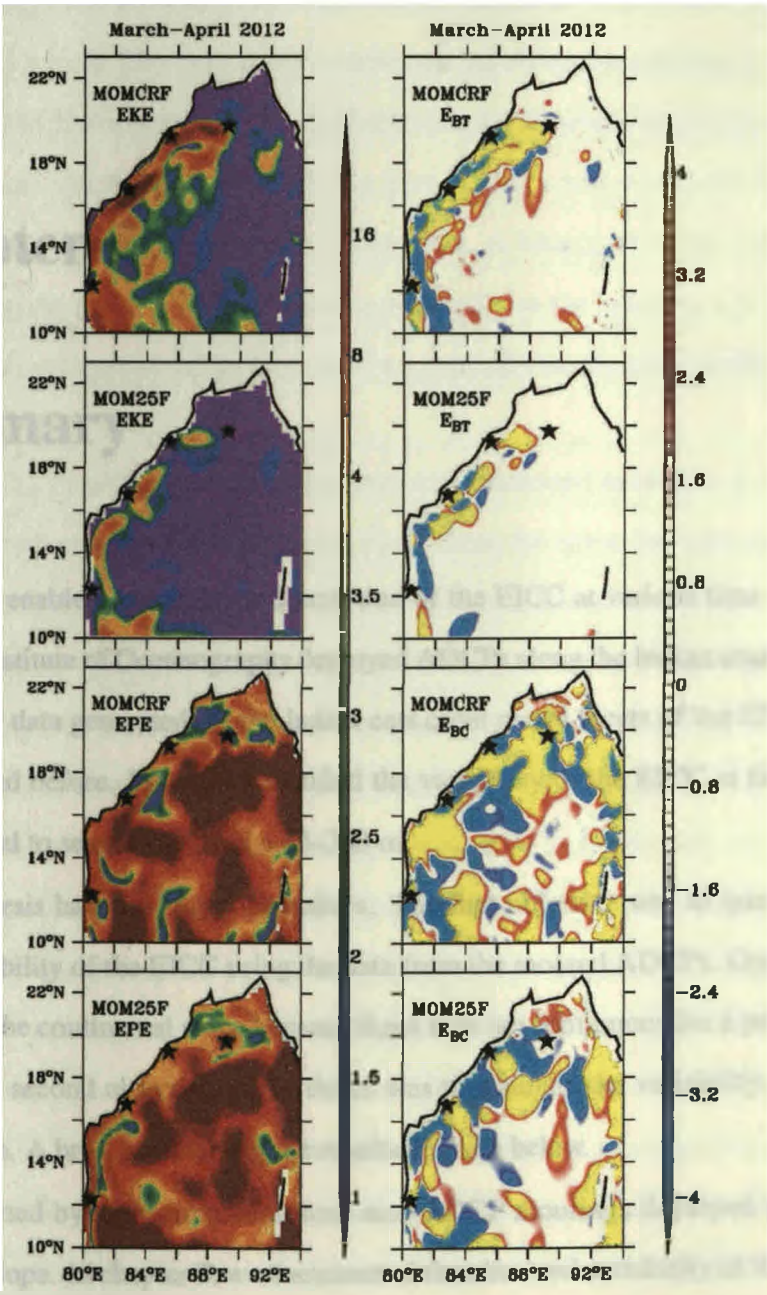

Figure 6.26: The left (right) panels show for March–April 2012 (average between 10 March and 10 April) the eddy kinetic energy (EKE, 10^{-3} m^2 s^{-2}), eddy potential energy (EPE, 10^{-3} m^2 s^{-2}), barotropic instability (E_{BT}, 10^{-3} m^2 s^{-3}), and baroclinic instability (E_{BC}, 10^{-3} m^2 s^{-3}). The estimates are shown for the simulations MOMCRF and MOM25F.

Chapter 7

Summary

In order to enable a quantitative description of the EICC at various time scales, the CSIR-National Institute of Oceanography deployed ADCPs along the Indian coast from May 2009. The ADCP data generated off the Indian east coast reveal facets of the EICC that could not be described before. We have quantified the variability of the EICC at time scales ranging from inertial to seasonal between 40–300 m.

This thesis had two major objectives. The first objective was to quantify the intraseasonal variability of the EICC using the data from the moored ADCPs. Our focus was on the data from the continental slope because these data are continuous for a period of about four years. The second objective of the thesis was to simulate the variability observed in these ADCP data. A brief summary of the results is given below.

We started by presenting data from nine ADCP moorings deployed on the continental shelf and slope. In chapter 3, we documented the observed variability of the EICC at inertial time scales. One key result is that the NICs are weak on the east-coast shelf. The likely reason is that the shelf width is less than the local Rossby radius at all locations. The NICs are stronger on the continental slope off the east coast. The slope ADCP data show a seasonality in the generation of the NICs. The NICs are not seen during January–April at all the mooring locations. They are prominent at the northern locations during May–September,

when the strong winds associated with the summer-monsoon depressions and cyclones are observed in the region. The storms shift southward following the summer monsoon, and so do the NICs, which are generated off Cuddalore during October–December. In the central part of the coast, the NICs are seen during both summer and winter monsoon owing to effect of storms over the northern and southern bay. A histogram of the ratio of the NICs to the total current shows that the NICs is comparable to the residual, i. e., non-tidal and sub-inertial, current on more than nine days in a year off Paradip and Cuddalore.

Observations from the sub-inertial currents were discussed in chapter 4. Analysis of the data shows a high coherence for the annual cycle along the coast, but with significant phase differences, and low coherence at intra-annual and intraseasonal time scales. A striking feature of the seasonal cycle on the east coast is the strong peak around 120 days. Intraseasonal variability in the 30–90-day band is weak at Paradip and Cuddalore, but the intraseasonal peaks at Kakinada and, to a lesser extent, Gopalpur, are significant. This intraseasonal variability varies seasonally, peaking during spring at all locations, but, except at Paradip, variability in this band extends to the other seasons as well. The data also show evidence of upward phase propagation, which indicates downward propagation of energy. The upward propagation of phase leads to distinct undercurrents off the west coast. Off the east coast and at the Paradip mooring, however, the vertical phase speed is much higher compared to the west coast, the only exception being the much slower phase propagation in the top 100 m at Cuddalore. As a result, a distinct undercurrent is seen only at Cuddalore over most of the year; at other locations, the current is unidirectional over the top 300 m during spring, but an undercurrent does tend to form during the summer monsoon and winter. The cross-shore currents are weakest at Cuddalore, the southernmost location, and occur in bursts, typically during spring, at Kakinada and Gopalpur. It is only at Paradip that the cross-shore component is often comparable to the alongshore component during spring and the summer monsoon. Examination of the altimeter sea level suggests that such strong cross-shore flows

are associated with eddy-like circulations.

In order to validate ocean current data products, we compared three popular data products with the slope ADCP data in chapter 5. A comparison between currents from the ADCPs and the OSCAR data product shows that the latter is able to capture both seasonal and intraseasonal variability only for the Paradip mooring, where the match is remarkably good. At the other three locations, which are on the continental slope of the western boundary, the OSCAR currents are able to capture only the seasonal variability; the match at intraseasonal periods is reasonable: there are several intraseasonal bursts that are seen in the ADCP data, but not in OSCAR. One possible reason for this phase mismatch between the ADCP current at 40 m and the OSCAR current, which represents the current in the 0–30 m depth range, is the vertical phase propgation. The variability simulated by GODAS is weak, but ECCO2 fares better at the three locations on the east-coast slope

In chapter 6, we simulate the variability of the EICC observed in the ADCP data from the continental slope. For this purpose, we have used two numerical models, an OGCM (MOM4p1) and a simpler, linear model. The results show that MOM, run at a horizontal resolution of $0.1° \times 0.1°$, simulates well the observed annual cycle of the EICC, but the performance degrades for the intra-annual and intraseasonal components. The performance of the LCS model is comparable to that of the OGCM, permitting its use for analysing local and remote contributions to the EICC. The annual EICC is largely forced by the local alongshore winds in the WBoB and Ekman pumping over the interior BoB. The contribution of local forcing is expectedly weak at Gopalpur owing to the direction of propagation of the Kelvin waves (anticlockwise along the perimeter of the BoB). The intra-annual EICC is dominated by remote forcing from the EIO. The intraseasonal EICC is affected by both local and remote forcing, but the intraseasonal variability is weaker in the linear model compared to the observations or the OGCM, suggesting the importance of nonlinear processes.

Our results also show that even a linear model or an OGCM with a $0.25° \times 0.25°$ resolu-

tion suffices to simulate the observed variability in the EIO, but their performance degrades in the EBoB. The LCS model and the OGCM at the coarser resolution also perform poorly in the NBoB. Estimates of eddy kinetic energy (EKE) and instability computations show that eddies extract energy from the mean flow via both barotropic and baroclinic instabilities, but the barotropic instability is more important.

We have also discussed the role of stratification in simulating EICC. The change in stratification from the EIO to the BoB leads to a stronger EICC for the NBoB or CBoB stratifications compared to the EIO stratifications, and this increase in magnitude of the surface current is seen for both locally and remotely forced components. For the BoB profiles, the high-order vertical modes couple more strongly than for the EIO profiles, leading to a stronger locally forced component. These high-order modes, which lead to energy propagating down into the ocean in the form of beams, are important only for the current and do not contribute significantly to the sea level. Hence, the sea-level signal propagates almost undiminished from the EIO to the WBoB, but the current decays more rapidly away from the forcing regime in the central EIO. It is important to keep this distinction between sea level and currents in mind when analysing the impact of remote forcing by intraseasonal events like the Madden-Julian Oscillation on the circulation in the BoB.

The highlights of the thesis are as follows.

- **Description of inertial current along east coast of India**: This thesis presents the first description of near-inertial current (NICs) off the east coast of India

- **Description of sub-inertial EICC**: This thesis also presents a detailed description of the sub-inertial variability of the EICC as observed in the ADCP data.

- **Validation of ocean-current data products**: Comparison of popular ocean-current data products with the ADCP observations shows that the models need significant improvement for simulating the EICC.

- **Simulating the EICC**: This thesis shows how well a state-of-the-art OGCM is able to simulate the EICC. Experiments with the OGCM and a simpler model are used to analyse the processes. The results show that the models today are capable of simulating the annual cycle of the EICC, but have difficulty in simulating the intra-annual and intraseasonal variability. The numerical experiments show the importance of stratification nonlinearity, suggesting that increasing model resolution is necessary.

These ADCP data are expected to provide a fillip to theoretical studies of intraseasonal variability, just as the hydrographic data in the Indian EEZ (Shetye et al., 1990, 1991b,c, 1993, 1996; Shetye and Gouveia, 1998) did for the seasonal cycle of circulation in the 1990s. The changes in phase seen between adjacent moorings even for the annual cycle will provide the modelling community with a data set to test the quantitative skills of the models even for the low-frequency variability. At intraseasonal time scales, the EICC decorrelates even more strongly along the coast and the comparison with data-assimilated model products like ECCO2 and GODAS shows that the models have a long way to go before they can simulate the variability observed in the EICC.

Model resolution is important owing to the significant role of eddies and instabilities in the NBoB and the regime of the EICC. The LCS model, owing to its linearity, cannot account for the contribution of these nonlinear processes. Another significant linearisation in the LCS model is the assumption of a constant background density profile. One unfortunate consequence of the constant background density profile in the LCS model is that it simulates a stronger EICC for the NBoB stratification not only at Kakinada, where this increase in magnitude constitutes an improvement, but also at Cuddalore, where the increase in magnitude leads to a poorer match with the observed current. In the real ocean, the stratification changes in the horizontal and also over time, and these changes are incorporated in an OGCM. Unfortunately, the OGCM, when forced by realistic winds and realistic air-sea fluxes, is far too complex to permit an analysis of the impact on the circulation of the spatial

and temporal changes in stratification.

The observations are continuing and a long time series of direct current measurements will allow an evaluation of the impact on the EICC of the major climate modes of the NIO (see, for example, Schott et al., 2009), i. .e. ENSO (El Niño and Southern Oscillation) (Philander, 1983; Meyers et al., 2007) and the IOD (Indian Ocean Dipole) (Saji et al., 1999; Webster et al., 1999). Earlier studies, typically based on altimeter data, suggest that both ENSO (Clarke and Liu, 1994; Somayajulu et al., 2003; Aparna et al., 2012) and IOD (Rao et al., 2002; Jensen, 2007; Aparna et al., 2012) have an impact on the western boundary of the Bay of Bengal. Another interesting question is whether a long time series of direct current measurements will show the minimum of interannual variability noted in altimeter sea level by Shankar et al. (2010) along the southern part of the western boundary of the bay. Along the northern part of this boundary, there was a maximum of interannual variability. Will this distinction be seen in the ADCP data? This question is important because such a difference in the variability will lead to an alongshore decorrelation of the interannual EICC, as found by Durand et al. (2009) using the MAP altimeter data set in contrast to the study of Clarke and Liu (1994), who used tide-gauge data to suggest that the EICC should be coherent along the coast at these sub-seasonal time scales.

Appendix A

MOM4p1 Model configuration

We have used an ocean general circulation model like MOM4p1 (Griffies, 2009). MOM4p1 model is configured for the IO similar with Kurian and Vinayachandran (2007); Vinayachandran et al. (2007, 2012); Chatterjee et al. (2013). MOM4p1 is a B-grid hydrostatic Boussinesq, free surface ocean model with generalized depth and pressure based vertical and generalized orthogonal horizontal coordinates.

A.1 Equation of motion and coordinate systems

The solution algorithm of MOM4p1 is based on Boussinesq hydrostatic equations written in geopotential vertical coordinates. The resulting primitive equation of motion are (Griffies and Adcroft, 2008)

$$[\partial_t + (f\,\vec{z} + \omega)\wedge]\mathbf{v} + \nabla_z \varepsilon + \rho_o^{-1}\nabla_z p = \rho_o^{-1}\nabla.\tau; \tag{A.1a}$$

$$\Phi_{,z} + \rho^{-1} p_{,z} = 0; \tag{A.1b}$$

$$\nabla_z.\mathbf{u} + w_{,z} = 0; \tag{A.1c}$$

$$\theta_{,t} + \nabla_z.(\mathbf{u}\theta) + (w\theta)_{,z} = S_\theta; \tag{A.1d}$$

$$S_{,t} + \nabla_z.(\mathbf{u}S) + (wS)_{,z} = S_s; \tag{A.1e}$$

$$\rho = \rho(\theta, S, p). \tag{A.1f}$$

In these equations (A.1a)–(A.1f), ω, ε and τ each assume their hydrostatic forms accordingly:

$$\omega = \nabla \wedge \mathbf{u}; \tag{A.2}$$

$$\varepsilon = \mathbf{u}.\mathbf{u} + \Phi; \tag{A.3}$$

$$\nabla.\tau = \partial_z(\kappa_{\text{model}}\mathbf{u}_{,z}) + \nabla.\tau_{horizontal\ strain}. \tag{A.4}$$

There are seven equations(A.1) with seven unknowns u (zonal velocity), v (meridional velocity), w (vertical velocity), p (pressure), θ (temperature), S (salinity), ρ (temperature). v= (u, v) is the velocity vector. The in-situ density ρ can be diagnosed from the equation of state (A.1f) using pressure at lagged time step (Griffies et al., 2001). Hydrostatic pressure p can be diagnosed by vertical equation (A.1b). Horizontal velocity u is solved using equation A.1a. The vertical velocity component can be calculated using equation A.1c. Tracers θ and S can be predicted using equation A.1d and A.1e.

ectionModel grid and domain

The model domain comes from the Indian Ocean between 30°S–30°N and 30°–120°E. It is configured for two different resolutions (0.25° and 0.1°)in both longitudinal and latitudinal directions (see Figure A.1). There are 40 vertical levels in the model with a 5 m resolution in the top 60 m. The vertical topography of model is based on modified the ETOPO2 bathymetry (Sindhu et al., 2007). The narrow channel between Indian and Sri Lanka remains closed in the model. The narrow channels between the Red Sea or Persian Gulf into the Arabian Sea are broadened and deepened. The part of the Pacific Ocean is removed from model grid. The minimum ocean depth is set to 15 m and single isolated land points are removed.

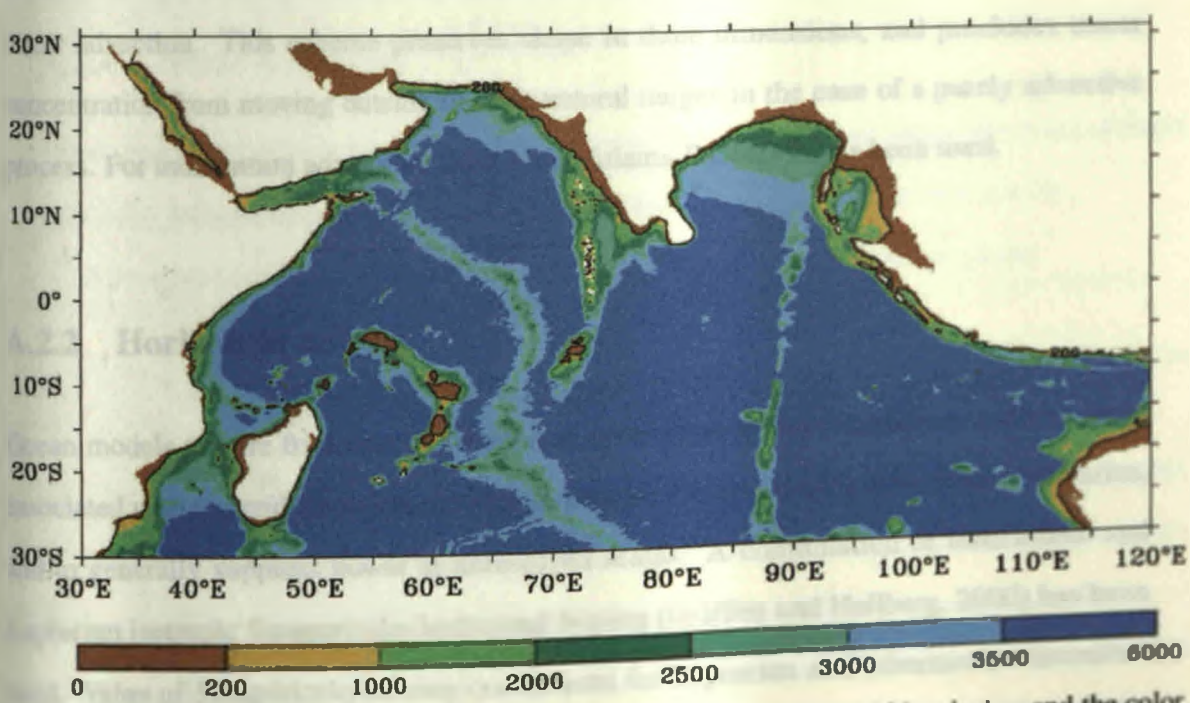

Figure A.1: 0.1 degree MOM model grid. The black contour represents 200 m isobar and the color pallets show the depth in meter.

A.2 Model physics parametrization

OGCMs are tools used to numerically simulate the large space-time scales which characterize the ocean climate system. Realistic simulation of physical integrity requires both an ability to accurately represent the various phenomena which are resolved, and an ability to parameterize those scales of variability which are not resolved. For example, the representation of momentum and tracer transport falls under the class of problems addressed by numerical advection schemes and vertical coordinates of the model, whereas parameterizing sub-grid-scale transport is linked to turbulence closure considerations.

A.2.1 Advection

We have used the multi-dimensional piece-wise parabolic method (MDPPM) method for tracer advection. This scheme preserves shape in three dimensions, and precludes tracer concentration from moving outside of their natural ranges in the case of a purely advective process. For momentum advection, third order Adams-Bashforth has been used.

A.2.2 Horizontal mixing

Ocean models require frictional dissipation in order to suppress instabilities such as those associated with the grid Reynolds number, to provide a vorticity sink at western boundaries, and to generally suppress power at unresolved scales. A combination of biharmonic and Laplacian isotropic Smagorinsky horizontal friction (Griffies and Hallberg, 2000) has been used. Value of Smagorinsky mixing coefficients for Laplacian and biharmonic viscosities are 0.10 (0.06) with velocity scales =0.04 m s^{-1} and 0.01 (0.002) with velocity scale=0.005 m s^{-1} respectively for 0.25° (0.1°) model.

A.2.3 Vertical mixing

It is well known that vertical mixing in the ocean plays a prominent role in regulating the sea surface temperature (SST) , a critical oceanic parameter in controlling the exchanges of energy and momentum between the ocean and atmosphere. We have used K-profile Parameterization (KPP) for vertical mixing (Large et al., 1994). The KPP scheme does not assume a priori that the boundary layer is well mixed and explicitly predicts an ocean boundary layer depth. Within this boundary layer, the turbulent mixing is parameterized using a nonlocal bulk Richardson number (value is set to 0.3 here) and the similarity theory of turbulence. Below the boundary layer, the vertical mixing is parameterized through the local gradient Richardson number and a background mixing. The background vertical diffusivity and viscosity (due to constant internal wave activity) were set to 1.34 x 10^{-7} m^2 s^{-1} and 1.00 x 10^{-4} m^2 s^{-1} respectively.

A.2.4 Neutral Physics

Tracer transport in the ocean interior has a strong tendency to occur along directions defined by locally referenced potential density (i.e., neutral directions), rather than across.

Advective stirring of tracer in a volume conserving $z^\star$-model takes the form

$$\partial_t T = -\nabla.(\mathbf{u}\mathrm{T}) - \partial_z(\mathrm{wT}); \tag{A.5}$$

where ∇ is the horizontal gradient operator taken along constant z surfaces. In the absence of explicit knowledge of the neutral directions, advection schemes in z-models rely on numerical accuracy to approximate the isopycnal transport processes.

In our model set-up, neutral physics consists of neutral diffusion (Redi, 1982) and GM skew-diffusion (Gent and Mcwilliams, 1990), are implemented according to Griffies et al. (1998); Griffies (1998). GM skew-diffusivity is computed as a function of the flow; the

length scale is determined by the Rossby radius and the time scale is determined by the Eddy growth rate. Neutral fluxes are tapered to zero in regions where slope of ocean topography is steeper than 1/500 with the *tanh* taper scheme of Danabasoglu and McWilliams (1995).

A.2.5 Shortwave Radiation

Absorption of shortwave radiation within the upper ocean is one of the most important factor which determines the temperature of the mixed layer. Low (high) chlorophyll levels allow shortwave radiation to penetrate to deeper (shallow) depths (Morel and Maritorena, 2001). We have used the chlorophyll based Morel and Antoine (1994) scheme, which represent space-time variation of chlorophyll and calculates the vertical profile of shortwave absorption in three partitions, using exponential functions. The first partition handles infrared part (with wavelengths > 750 nm) of the solar radiation, which is not influenced by the presence of biological materials and is absorbed within the upper few centimeters of the water column. The second and third partition deals with the ultraviolet and visible parts of solar radiation (between wave lengths 300 and 750 nm).

A.2.6 Tidal dissipation

To resolve vertical dissipation and mixing due to barotropic and baroclinic tidal energy, we have used baroclinic tidal scheme of Simmons et al. (2004) and Lee et al. (2006) for barotropic tide. Baroclinic tidal scheme includes vertical dissipation due to internal gravity wave breaking close to rough bottom topography.

A.2.7 Boundary condition

A set of boundary condition is required for solving equation of motion. Kinematic type of boundary condition defines ocean model domain and describe its volume budget. Dynamic boundary condition prescribe the flux of momentum, heat, salt, precipitation etc.

Surface boundary condition

We have assumed that volume sources/sinks are present only at ocean surface, leads to the balance of volume per unit area within an ocean column. The surface kinematic boundary condition is defined as

$$(\partial_t + \mathbf{u}.\nabla)\eta = q_w + \mathrm{w} \qquad \text{at} \quad Z = \eta; \tag{A.6}$$

Here η is the sea surface height. w is the vertical component of the velocity and q_w is the volume transport per time per horizontal area across the free surface.

The surface dynamic boundary condition for momentum flux takes the form

$$\rho\kappa\mathbf{u}_{,z} = \tau^{wind} \qquad \text{at} \quad Z = \eta; \tag{A.7}$$

where ρ is the water density, κ is the viscosity and τ is the wind stress.

Lateral boundary condition

At the land boundaries on the western and northern side of the model domain, no-flux condition for tracers and no-normal flow conditions for velocity have been applied. Sponge layers of width 3.5° have been applied at the open boundaries on the south and east. Within the sponge layer, temperature and salinity are restored to climatological values (Chatterjee et al., 2012).

Bottom boundary condition

The boundary flux passing through the bottom is ignored and hence the normal component of velocity vector vanishes at the ocean bottom:

$$\vec{n}.\mathbf{v} = 0 \qquad \text{at} \quad Z = -H. \tag{A.8}$$

Field	Data Source	Frequency	Reference
Wind stress (N m^{-2})	QuikSCAT	Daily	www.ifremer.fr/cersat/en/data/data.html
Wind stress (N m^{-2})	ASCAT	daily	ftp://ftp.ifremer.fr/ifremer/cersat/products
SW rad. down (W m^{-2})	NCEP	daily	Kalnay et al. (1996)
LW rad. down (W m^{-2})	NCEP	daily	Kalnay et al. (1996)
Air temperature, K	NCEP	daily	Kalnay et al. (1996)
Specific humidity, kg/kg	NCEP	daily	Kalnay et al. (1996)
Precipitation (m s^{-1})	TRMM	daily	ftp://disc2.nascom.nasa.gov/data/TRMM
ChlorophyII (mg m^{-3})	SeaWiFS	Monthly	http://nomads.gfdl.noaa.gov

Table A.1: List of data sources used in the MOM4p1 model. QuikSCAT wind product is used upto 31 December 2008. From 01 January 2009, ASCAT wind product is used upto end of model simulations (31 March 2013)

where v=(u,w) is the three dimensional velocity field and $\vec{n}$ is the unit vector normal to the ocean bottom.

A.3 Forcing

The forcing field plays an important role in the accuracy of the model simulation. Errors in the forcing fields and the limitation of the model, together or alone, can give rise to undesired results. We have started our model with climatological temperature and salinity from Chatterjee et al. (2012) and equation of state from rest. The complete model forcing is given in Table A.1 .

Special care has been taken for salinity simulation in the IO. Sea surface salinity are relaxed to climatological values from Chatterjee et al. (2012) with a time scale of 30 days.

Appendix B

LCS model configuration

Our LCS model configuration is similar with McCreary et al. (1996), Shankar et al. (2010), Aparna et al. (2012) and Chatterjee et al. (2013). A brief summary of the model is given here.

B.1 Equations of motion

The equations of motion are linear and starts from state of rest of u (zonal velocity), v (meridional velocity) and p (pressure) with background Brunt–Vaisala frequency (N_b). The ocean bottom is assumed to be flat. The final equations of motion for u, v and p is given below, where

$$(\partial_t + \frac{A}{c_n^2})u_n - fv_n + p_{nx} = F_n + \nu_2 \nabla^2 u_n; \tag{B.1a}$$

$$(\partial_t + \frac{A}{c_n^2})v_n + fu_n + p_{ny} = F_n + \nu_2 \nabla^2 v_n; \tag{B.1b}$$

$$(\partial_t + \frac{A}{c_n^2})\frac{p_n}{c_n^2} + u_{nx} + v_{ny} = 0. \tag{B.1c}$$

A is the vertical mixing parameter with value of 1.3 x 10^{-4} cm^2s^{-3}, n is the mode number,

c_n is the characteristic mode speed, ν_2 horizontal mixing parameter, $F_n = \tau^x Z_n/(\bar{\rho}\mathcal{H}_n)$ and $G_n = \tau^y Z_n/(\bar{\rho}\mathcal{H}_n)$. Both, $Z_n = \int_{-D}^{0} Z(z)\psi_n dz$ and $\mathcal{H}_n = \int_{-D}^{0} \psi_n^2 dz$ determines how strongly wind couples with each mode. The value of Z(z) is calculated using a smoother ramped functions like

$$Z(z) = \begin{cases} \frac{2}{3h}, & -h < z \leq 0 \\ \frac{2(z+2h)}{3h^2}, & -2h < z \leq -h \\ 0, & \end{cases} \tag{B.2}$$

where h is the mixed layer depth of density profile. The depth of the basin is in meters and $\bar{\rho}$ is assumed to be 1 gm cm^{-3}. τ^x and τ^y represents zonal and meridional wind stress respectively. ψ_n is the eigenfunction of n'th mode which is calculated using

$$(\frac{1}{N_b^2}\psi_{nz})_z = -\frac{1}{c_n^2}\psi_n(z); \tag{B.3a}$$

$$\psi_{nz}(-D) = \psi_{nz}(0); \tag{B.3b}$$

$$\psi_n(0) = 1. \tag{B.3c}$$

and the resultant solutions are calculated using

$$(\frac{1}{N_b^2}\psi_{nz})_z = -\frac{1}{c_n^2}\psi_n(z); \tag{B.4a}$$

$$\psi_{nz}(-D) = \psi_{nz}(0); \tag{B.4b}$$

$$\psi_n(0) = 1. \tag{B.4c}$$

and the resultant solutions of u, v and p are calculated using

$$u = \sum_{n=0}^{N} u_n \psi_n; \tag{B.5a}$$

$$v = \sum_{n=0}^{N} v_n \psi_n; \tag{B.5b}$$

$$p = \sum_{n=0}^{N} p_n \psi_n. \tag{B.5c}$$

B.2 Computation of the vertical mode structure in the LCS model

The computation of the vertical mode structure in the linear, continuously stratified (LCS) model follows the standard procedure (McCreary, 1980, 1981; Shankar et al., 1996; McCreary et al., 1996). In this model, the heat equation is linearised about a steady, thermohaline-driven background state. To specify this background state, we need the vertical profile of the mean density field. The vertical normal modes are then computed from the vertical profile of the Brünt-Vaïsala frequency (N_b), which is given by

$$N_b^2 = -\frac{g}{\bar{\rho}} \frac{\partial \rho_b}{\partial z}. \tag{B.6}$$

where g is the acceleration due to gravity, ρ_b is the background or average density (a function of the vertical coordinate, z, alone), and $\bar{\rho}$ is the average density of water (assumed to be 1.2 gm cm^{-3}). The mode shape (eigenfunction, ψ_n) and mode or characteristic speed

(eigenvalue, c_n) for the nth mode are given by

$$\frac{1}{N_b^2}(\psi_{nz})_z = -\frac{1}{c_n^2}\psi_n, \tag{B.7}$$

where the subscript z implies differentiation with respect to z. The mode speed, c_n, is the speed of the Kelvin wave in this model. The surface and bottom boundary conditions associated with Equation (B.7) are

$$\frac{1}{N_b^2}\psi_{nz} = 0 \quad \text{at} \quad z = 0, -D, \tag{B.8}$$

where D is the depth of the flat-bottomed ocean. For the numerical simulations in this paper, $D = 4000$ m.

Two coupling coefficients, the mode coupling coefficient $\mathcal{H}_n$ and the wind coupling coefficient $\mathcal{Z}_n$), determine how strongly the wind forcing couples with each mode. These coefficients are computed as follows.

$$\mathcal{Z}_n = \int_{-D}^{0} Z(z)\psi_n dz; \tag{B.9a}$$

$$\mathcal{H}_n = \int_{-D}^{0} \psi_n^2 dz. \tag{B.9b}$$

The value of $Z(z)$ in Equation (B.9a) is computed using a smooth, ramped function like the one given in McCreary et al. (1996):

$$Z(z) = \begin{cases} \frac{2}{3h}, & -h < z \leq 0 \\ \frac{2(z+2h)}{3h^2}, & -2h < z \leq -h \\ 0 & \text{otherwise} \end{cases} \tag{B.10}$$

In Equation (B.10), h is the mixed-layer depth estimated from the density profile. This ramp structure is used to smoothen the density jump at the base of the mixed layer. The strength of an individual mode's response is determined by its effective coupling coefficient, which is the ratio of the wind coupling coefficient and the mode coupling coefficient ($\frac{Z_n}{\mathcal{H}_n}$).

B.3 Model grid, domain and forcing

The model has a flat bottom and its basin geometry is defined by the 200 m isobath; we use a realistic coastline and resolve the Andaman and Nicobar Islands as well as in MOM4p1 because the LCS model is also run at a resolution of $0.1° \times 0.1°$ (Figure B.1). The model equations are linearised about a uniform background density state and the variables are decomposed into vertical normal modes (McCreary, 1980, 1981). We sum over the first 10 vertical modes to obtain the solutions. Calculation of modes for the control run (LCSCR) is based on the background density (or Brünt–Vaïsala frequency, N_b) profile used by Moore and McCreary (1990). A brief description of the computation of mode structure from the density profile is given in Section B.2. The model is spun up from a state of rest; the model ocean is forced initially by QuikSCAT winds from January 2000 and a switch is made to ASCAT winds from January 2009.

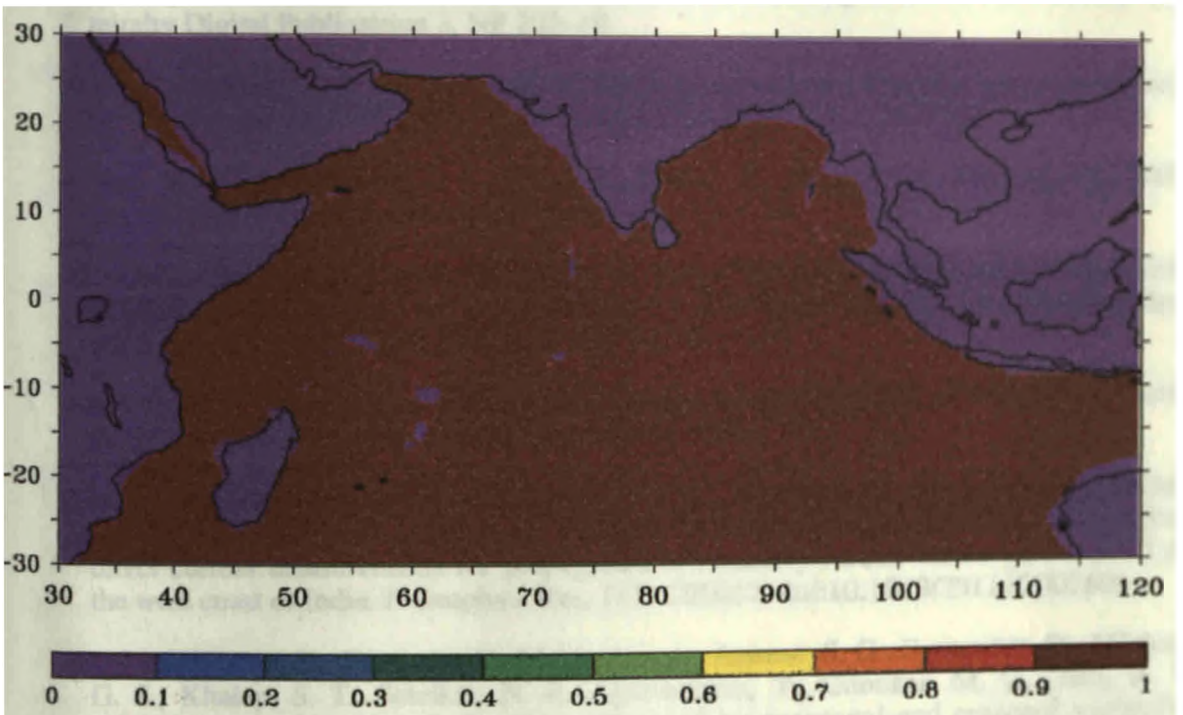

Figure B.1: 0.1 degree LCS model grid land mask. 0 (1) value represent land (ocean).

References

Admiralty, 2010. Indian Ocean and South China Sea (Including Tidal Stream Tables). Admiralty Digital Publicatrion 3, NP 203–10.

Aken, H. V., Maas, L. R. M., Haren, H. V., 2005. Observations of inertial wave events near the continental slope off Goban Spur. J. Phys. Oceanogr. 35, 1329–1340.

Alford, M. H., MacKinnon, J. A., Zhao, Z., Pinkel, R., Klymak, J., Peacock, T., 2007. Internal waves across the Pacific. Geophys. Res. Lett. 34.

Ali, M. M., Sharma, R., Cheney, R., 1998. An atlas of the north Indian Ocean eddies from TOPEX altimeter derived sea surface heights. Indian Space Research Orginazation Special Publication ISRO-SAC-SP-69-98, 8pp and 39 plates.

Amol, P., 2014. Intraseasonal variability of currents along west coast of India. Ph.D thesis. Goa University, Department of Marine Science, India.

Amol, P., Shankar, D., Aparna, S. G., Shenoi, S. S. C., Fernando, V., Shetye, S. R., Mukherjee, A., Agarvadekar, Y., Khalap, S., Satelkar, N. P., 2012. Observational evidence from direct current measurements for propagation of remotely forced waves on the shelf off the west coast of India. J. Geophys. Res. 117, C05017, doi:10.1029/2011JC007606.

Amol, P., Shankar, D., Fernando, V., Mukherjee, A., Aparna, S. G., Fernandes, R., Michael, G. S., Khalap, S. T., Satelkar, N. P., Agarvadekar, Y., Gaonkar, M. G., Tari, A. P., Kankonkar, A., Vernekar, S. P., 2014. Observed intraseasonal and seasonal variability of the West India Coastal Current on the continental slope. J. Earth Syst. Sci. 125(5), 1045–1074.

Aparna, S. G., McCreary, J. P., Shankar, D., Vinayachandran, P. N., 2012. Signatures of the Indian Ocean Dipole and El Nino-Southern Oscillation events in sea level variations in the Bay of Bengal. J. Geophys. Res. 117, doi10.1029/2012JC008055.

AVISO, 1996. AVISO User Handbook. Technical Report. Toulouse, France.

Babu, M. T., Sarma, Y. V. B., Murthy, V. S. N., Vethamony, P., 2003. On the circulation in the Bay of Bengal during northern spring inter-monsoon (march april 1987). Deep–Sea Res. Part II, 5, 855–865, doi:10.1016/S0967–0645(02)00609–4.

Behringer, D. W., 2007. The Global Ocean Data Assimilation System (GODAS) at NCEP. In: 11th Symp. on Integrated Observing and Assimilation Systems for Atmosphere, Oceans, and Land Surface . Vol. 3.3. Amer. Meteor. Soc., San Antonio, TX.

Behringer, D. W., Ji, M., Leetmaa, A., 1998. An Improved Coupled Model for ENSO prediction and implications for ocean initialization. Part I: The Ocean Data Assimilation System. Mon. Wea. Rev. 126, 1013–1021.

Behringer, D. W., Xue, Y., 2004. Evaluation of the global ocean data assimilation system at NCEP: The Pacific Ocean. In: Eighth Symposium on Integrated Observing and Assimilation Systems for Atmosphere, Oceans, and Land Surface. Vol. 2.3. Amer. Meteor. Soc., Washington State Convention and Trade Center, Seattle, Washington, pp. 11–15.

Bell, C., Vassie, J., Woodworth, P., 1998. POL-PSMSL Tidal Analysis Software Kit 2000 (TASK-2000), Technical Report. Proudman Oceanogr. Lab., U. K Bidston Obs. Merseyside.

Birol, F., Roblou, L., Lyard, F., Llovel, W., Durand, F., Renault, L., Dewitte, B., Morrow, R., Mnard, Y., 2006. Towards using satellite altimetry for the observation of coastal dynamics. In 15 Years of Progress in Radar Altimetry Symposium Venice, Italy.

Böning, C., Budich, R. G., 1992. Eddy dynamics in a primitive equation model: Sensitivity to horizontal resolution and friction. J. Phys. Oceanogr. 22, 361–381.

Bonjean, F., Lagerloef, G. S. E., 2002. Diagnostic Model and Analysis of the Surface Currents in the tropical Pacific Ocean. J. Phys. Oceanogr. 32 (10), 2938–2954.

Bruce, J. G., Johnson, D. R., Kindle, J. C., 1994. Evidence for eddy formation in the eastern Arabian Sea during the northeast monsoon. J. Geophys. Res. 99, 7651–7664.

Bruce, J. G., Kindle, J. C., Kantha, L. H., Kerling, J. L., Bailey, J. F., 1998. Recent observations and modeling in the Arabian Sea Laccadive High region. J. Geophys. Res. 103, 7593–7600.

Bryan, K., Lewis, L. J., 1979. A water mass model of the World Ocean. J. Geophys. Res. 84(5), 2503–2517.

Chacko, N., Ravichandran, M., Rao, R. R., Shenoi, S. S. C., 2012. An anomalous cooling event observed in the Bay of Bengal during June 2009. Ocean Dynam. 62, 671–681, doi:10.1007/s10236–012–0525–9.

Chatterjee, A., Shankar, D., McCreary, J. P., Vinayachandran, P. N., 2013. Yanai waves in the western equatorial Indian Ocean. J. Geophys. Res. 118.

Chatterjee, A., Shankar, D., Shenoi, S. S. C., Reddy, G. V., Michael, G. S., Ravichandran, M., Gopalkrishna, V. V., Rao, E. P. R., Bhaskar, T. V. S. U., Sanjeevan, V. N., 2012. A new atlas for temperature and salinity for North Indian Ocean. J. Earth Syst. Sci. 121 (3), 559–593.

Chatterjee, A., Shankar, D., Vinayachandran, P. N., McCreary, J. P., 2017. Role of the Andaman Sea in the dynamical connection between the equatorial Indian Ocean and Bay of Bengal. J. Geophys. Res. 122, 1–19.

Chen, C., Reid, R., Nowlin, W., 1996. Near-inertial oscillations over the Texas-Louisiana shelf. J. Geophys. Res.. 101, 3509–3524.

Chen, G., Wang, D., Hou, Y., 2012. The features and interannual variability mechanism of mesoscale eddies in the Bay of Bengal. Cont. Shelf. Res. 47, 178–185.

Cheng, X., Xie, S.-P., McCreary, J. P., Qi, Y., Du, Y., 2013. Intraseasonal variability of sea surface height over the Bay of Bengal. J. Geophys. Res. 118, 1–15, doi:10.1002/jgrc.20075.

Chinthalu, G. R., Seetaramayya, P., Ravichandran, M., Mahajan, P. N., 2002. The Bay of Bengal and tropical cyclones. Curr. Sci. 82, NO–4, 379–381.

Clarke, A. J., Liu, X., 1994. Interannual sea level in the northern and eastern Indian ocean. J. Phys. Oceanogr. 24, 1224–1235, doi:10.1017/1520–0485.

Colella, P., Woodward, P. R., 1984. The Piecewise Parabolic Method (PPM) for Gas-Dynamical Simulations. J. Comput. Phys. 54, 174–201.

Cutler, A. N., Swallow, J. C., 1984. Surface currents of the Indian ocean. Technical report. 187, Inst. of Oceanogr. Sci., Wormley, England.

Danabasoglu, G., McWilliams, J. C., 1995. Sensitivity of the global ocean circulation to parameterizations of mesoscale tracer transports. J. climate 8, 2967–2987.

Derber, J., Rosati, A., 1989. A global oceanic data assimilation system. J. Phys. Oceanogr. 19, 1333–1347.

Durand, F., Shankar, D., Birol, F., Shenoi, S. S. C., 2009. Spatiotemporal structure of the East India Coastal Current from satellite altimetry. J. Geophys. Res. 114, C02013, doi:10.1029/2008JC004807.

Durand, F., Shankar, D., de B. Montegut, C., Shenoi, S. S. C., 2008. Estimating boundary currents from satellite altimetry: A case study for the east coast of India. J. Oceanogr. 64, 831–845, doi:10.1007/s10872–008–0069–2.

Eden, C., Böning, C., 2002. Sources of eddy kinetic energy in the Labrador Sea. J. Phys. Oceanogr. 32, 3346–3363.

Eigenheer, A., Quadfasel, D., 2000. Seasonal variability of the Bay of Bengal circulation inferred from TOPEX/Poseidon altimetry. J. Geophys. Res. 105, 3243–3252.

Feistel, R., 2003. A new extended Gibbs thermodynamics potential of seawater. Prog. Oceanogr. 58, 43–114.

Francis, P. A., Vinayachandran, P. N., Shenoi, S. S. C., 2013. The Indian ocean forecast System. Curr. Sci 104(10), 1354–1368.

Fu, L. L., 1981. Observations and models of inertial waves in the deep ocean. Reviews of Geophysics and Space Physics 19, 141–170.

Gangopadhyay, A., Bharatraj, G. N., Chaudhuri, A. H., Babu, M. T., Sengupta, D., 2013. On the nature of meandering of the springtime western boundary current in the Bay of Bengal. Geophys. Res. Lett. 40, 2188–2193.

Gent, P. R., Mcwilliams, J. C., 1990. Isopycnal mixing in ocean circulation models. J. Phys. Oceanogr. 20, 150–155.

Girishkumar, M. S., Ravichandran, M., Han, W., 2013. Observed intraseasonal thermocline variability in the Bay of Bengal. J. Geophys. Res. 118, 1–14, doi:10.1002/jgrc.20245.

Gopalan, A. K. S., Gopalakrishna, V. V., Ali, M. M., Sharma, R., 2000. Detection of BoB eddies from TOPEX and sea truth observations. J. Mar. Res. 58, 721–734.

Gray, W., 1967. Global view of the origin of tropical disturbances and stroms. Technical Report, Colorado State University, 112.

Gregg, M. C., Kunze, E., 1991. Shear and strain in Santa Monica Basin. J. Geophys. Res. 96, 16709–16719.

Griffies, S., 1998. The Gent-McWilliams Skew-flux. J. Phys. Oceanogr. 28, 831–841.

Griffies, S., Gnanadesikan, A., Pacanowski, R., Larichev, V., Dukowicz, J., Smith., R., 1998. Isoneutral diffusion in a z-coordinate ocean model. J. Phys. Oceanogr. 28, 805–830.

Griffies, S. M., 2009. Elements of MOM4p1. Tech. Report. NOAA/Geophys. Fluid Dyn. Lab., Available online at www.gfdl.noaa.gov.

Griffies, S. M. ., Hallberg, R. W., 2000. Biharmonic friction with a smagorinsky viscosity for use in large-scale eddy-permitting ocean models. Mon. Weath. Rev. 128, 2935–2946.

Griffies, S. M., Adcroft, A. J., 2008. Formulating the equation of ocean models. Ocean Modelling in an Eddying Regime. 177, 281–317.

Griffies, S. M., Harrison, M. J., Pacanowski, R. C., Rosati, A., 2004. A technical guide to MOM4. GFDL Ocean Group Tech. Report. NOAA/Geophys. Fluid Dyn. Lab., Available online at www.gfdl.noaa.gov.

Griffies, S. M., Pacanowski, R., Schmidt, M., Balaji, V., 2001. Tracer conservation with an explicit free surface method for z-coordinate ocean models. Mon. Weather Rev. 129, 1081–1098.

Han, W., Lawrence, D. M., Webster, P. J., 2001a. Dynamical response of equatorial Indian Ocean to intraseasonal winds: zonal flow. Geophys. Res. Lett. 28, 4215–4218.

Han, W., Lawrence, D. M., Webster, P. J., 2001b. Dynamical response of equatorial Indian Ocean to intraseasonal winds: zonal flow. Geophys. Res. Lett. 28, 4215–4218.

Han, W., McCreary, J. P., 2002. Modeling salinity distributions in the Indian Ocean. J. Geophys. Res. 106, 859–877.

Han, W., McCreary, J. P., Anderson, D. L. T., Mariano, A. J., 1999. On the dynamics of the eastward surface jets in the equatorial Indian Ocean. J. Phys. Oceanogr. 29, 2191–2209.

Han, W., McCreary, J. P., Kohler, K., 2001c. Influence of Precipitation minus evaporation and Bay of Bengal rivers on dynamics, thermodynamics and mixed-layer physics in the upper indian Ocean. J. Geophys Res. 106, 6895–6916, doi:10.1029/2000JC000403.

Han, W., McCreary, J. P., Masumoto, Y., Vialard, J., Duncan, B., 2011. Basin resonances in the equatorial Indian Ocean. J. Phys. Oceanogr. 41, 1252–1270.

Han, W., Webster, P., 2002. Forcing mechanisms of sea level inter-annual variability in the Bay of Bengal. J. Phys. Oceanogr. 32, doi:10.1175/1520–0485(2002)032<0216.

Haren, H., 2005. Tidal and near-inertial peak variations around the diurnal critical latitude. Geophys. Res. Lett. 32.

Haren, H., Maas, L., Zimmerman, J. T. F., Ridderinkhoaf, H., Malschaert, H., 1999. Strong inertial currents and marginal internal wave stability in the central North Sea. Geophyscial Research Letters 26, 2993–2996.

Hastenrath, S., Greischar, L. L., 1986. The monsoonal current regimes of the tropical Indian Ocean. Observed surface flow fields and their geostrophic and wind-driven components. J. Geophys. Res. 96, 12619–12633.

Hellerman, S., Rosenstein, M., 1983. Normal monthly wind stress over the world ocean with error estimates. J. Phys. Oceanogr. 13, 1093–1104.

Hisaki, Y., Naruke, T., 2003. Horizontal variability of near-inertial oscillations associated with the passage of a typhoon. J. Geophys. Res. 108, 3382.

Hurburt, H. E., Thompson, J. D., 1976. A numerical model of the Somali Current. J. Phys. Oceanogr. 6, 646–664.

Hurlburt, H. E., Kindle, J. C., O'Brien, J. J., 1976. A numerical simulation of the onset of El Niño. J. Phys. Oceanogr. 6, 621–631.

Huthnance, J. M., 1981. Waves and currents near the continental shelf edge. Progress in Oceanography 10, 193–226.

IMD, 2010. Cyclonic disturbances over north Indian Ocean during 2009: A report. Tech. Rep. 5/2010, India Meteorological Department, Cyclone Warning Divison, New Delhi, India.

IMD, 2011. Cyclonic disturbances over north Indian Ocean during 2010: A report. Tech. Rep. 1/2011, India Meteorological Department, Cyclone Warning Divison, New Delhi, India.

IMD, 2012. Cyclonic disturbances over north Indian Ocean during 2011: A report. Tech. Rep. 1/2012, India Meteorological Department, Cyclone Warning Divison, New Delhi, India.

Jarosz, E., Hallock, Z., Teague, W., 2007. Near-inertial currents in the DeSoto Canyon region. Continental Shelf Research. 27, 2407–2426.

Jensen, T. G., 1993. Equatorial variability and resonance in a wind-driven Indian Ocean model. J. Geophys. Res. 98, 22533–22552.

Jensen, T. G., 2007. Wind–driven response of the northern Indian Ocean to climate extremes. J. Climate.. 20, 2978–2993, doi:10.1175/JCLI4150.1.

Johnson, E. S., Bonjean, F., Lagerloef, G. S. E., Gunn, J. T., 2007. Validation and Error analysis of OSCAR sea Surface Currents. J. Atmos. Ocean Tech. 24, 688–701.

Joseph, K. J., Balchand, A. N., Hareeshkumar, P. V., Rajesh, G., 2007. Inertial oscillations forced by September 1997 cyclone in the Bay of Bengal. Current Science. 92, 790–794.

Joseph, K. J., Balchand, A. N., V.Hareeshkumar, P., Rajesh, G., 2006. Inertial oscillation forced by the September 1997 cyclone in the Bay of Bengal. Curr. Sci. 92, NO–6, 790–794.

Kallberg, P., 1997. Aspects of the Re-analysed climate. ECMWF Re-Analysis Project Report Series, Part 2. Technical Report 89, ECMWF.

Kalnay, E., kanamitsu, M., Kistler, R., Collins, W., Deaven, D., Gandin, L., Iredell, M., Saha, S., White, G., Woollen, J., Zhu, Y., Chelliah, M., Ebisuzaki, W., Higgins, W., Janowiak, J., Mo, K. C., Ropelewski, C., Wang, J., Leetmaa, A., Reynolds, R., Jenne, R., Joseph, D., 1996. The NCAP/NCAR 40-year Reanalysis project. Bull. Amer. Meteorol. Soc. 77 (3), 437–471.

Knox, R. A., 1976. On a long series of measurements of Indian Ocean equatorial currents near Addu Atoll. Deep-Sea Res. 23, 211–221.

Krishnamurti, T. N., 1971. Tropical east–west circulations during northern summer. J. Atmos. Sci., 28, 1342–1347.

Kundu, P. K., 1976. An analysis of inertial oscillations observed near Oregon coast. J. Phys. Oceanogr. 6, 879–893.

Kurian, J., Vinayachandran, P. N., 2007. Mechanisms of formation of Arabian Sea mini warm pool in a high resolution OGCM. J. Geophys. Res. 112.

Kurian, P., Ikeda, M., Valsala, V. K., 2010. Mesoscale variability along the east coast of India in spring as revealed from satellite data and OGCM simulations. J. Oceanogr. 66, 273–289, doi:10.1007/s10872–010–0024–x.

Kutsuwada, K., McPhaden, M., 2002. Intraseasonal variations in the Upper Equatorial Pacific Ocean prior to and during the 1997-98 El-Niño. J. Phys. Oceanogr. 32, 1133–1149.

Large, W. G., McWilliams, J. C., Doney, S. C., 1994. Oceanic vertical mixing: a review and a model with a nonlocal boundary layer parameterization. Rev. Geophys. 32 (4), 363–403.

Leaman, K. D., Sanford, T. B., 1975. Vertical energy propagation of inertial waves: A vector spectral analysis of velocity profiles. J. Geophys. Res. 80, 1975–1978.

Lee, H. C., Rosati, A., Spelman., M., 2006. Barotropic tidal mixing effects in a coupled climate model: Oceanic conditions in the northern Atlantic. Ocean Modelling. 11, 464–477.

Leetma, A., 1972. The response of the Somali Current to the southwest monsoon of 1970. Deep Sea Res. 19, 319–325.

Leetma, A., 1973. The response of the Somali Current at 2°S to the southwest monsoon of 1971. Deep Sea Res. 20, 397–400.

Legeckis, R., 1987. Satellite observations of a western boundary current in the Bay of Bengal. J. Geophys. Res. 92, 12,974–12,978.

Lin, S. J., 2004. A "Vertically Lagrangian" Finite-Volume Dynamical Core for Global Models. Mon. Weather Rev. 132, 2293–2307.

Luyten, J. R., Roemmich, D. H., 1982. Equatorial currents at semiannual period in the Indian Ocean. J. Phys. Oceanogr. 37, 1825–1848.

Madden, R. A., Julian, P. R., 1971. Detection of a 40–50 day oscillation in the zonal wind of the tropical Pacific. J. Atoms. Sci. 28, 702–708.

Madden, R. A., Julian, P. R., 1972. Description of global-scale circulation cells in the tropics with a 40–50 day period.. J. Atoms. Sci. 29, 1109–1123.

Madden, R. A., Julian, P. R., 1993. Observations of the 40-50 Day Tropical Oscillation-A Review. Mon. Wea. Rev. 122, 814–837.

Mariano, A. J., Ryan, E. H., Perkin, B. D., and, S. S., 1995. The Mariano Global Surface Velocity Analysis. U.S Coast Guard, Washington. 1.0, Rep. CG-D-34-95, 55 pp.

Marshall, J., Adcroft, A., Hill, C., Perelman, L., Heisey, C., 1997. A finite-volume, incompressible Navier-Stokes model for studies of the ocean on parallel computers. J. Geophys. Res. 102 (C3), 5753 @ S5766.

Masumoto, Y., Hase, H., Kuroda, Y., Matsuura, H., 2005. Instraseasonal variability in the upper layer currents observed in the eastern equatorial Indian Ocean. Geophys. Res. Lett. 32 (L02607).

McCreary, J. P., 1976. Eastern tropical ocean response to changing wind systems: with application to El Niño. J. Phys. Oceanogr. 6, 632–645.

McCreary, J. P., 1980. Modeling wind driven ocean circulation. Tech. rep., Hawaii Inst. of Geophys., Honolulu.

McCreary, J. P., 1981. A linear stratified ocean model of the coastal undercurrent. Philos. Trans. R. Soc. London A 302, 385–413.

McCreary, J. P., 1984. Equatorial Beams. J. Mar. Res. 42, 395–430.

McCreary, J. P., Han, W., Shankar, D., Shetye, S. R., 1996. Dynamics of the East India Coastal Current 2. Numerical solutions. J. Geophys. Res. 101, 13,993–14,010.

McCreary, J. P., Kundu, P. K., Molinari, R. L., 1993. A numerical investigation of dynamics, thermodynamics and mixed-layer processes in the Indian Ocean. Prog. Oceanog. 31, 181–244.

McCreary, J. P., Picaut, J., Moore, D. W., 1984. Effects of remote annual forcing in the eastern tropical Atlantic Ocean. J. Mar. Res. 42, 45–81.

McPhaden, M. J., Meyers, G., Ando, K., Masumoto, Y., Murty, V. S. N., Ravichandran, M., Syamsudin, F., Vialard, J., Yu, L., Yu, W., 2009. RAMA The Research Moored Array for African-Asian-Australian Monsoon Analysis and Prediction a new moored buoy array in the historically data-sparse Indian Ocean provides measurements to advance monsoon research and forecasting. Bull. Am. Meteorol. Soc. 90, 459–480.

McPhaden, M. J., Wang, Y., Ravichandran, M., 2015. Volume transport of the Wyrtki jets and their relationship to the Indian Ocean dipole. J. Geophys. Res. 120, 5302–5317.

Menemenlis, D., Hill, C., Adcroft, A., Campin, J., Cheng, B., Ciotti, B., Fukumori, I., Koehl, A., Heimbach, P., Henze, C., Lee, T., Stammer, D., Taft, J., Zhang, J., 2005. NASA supercomputer improves prospects for ocean climate research. EOS Transactions AGU 86 (9), 86–89.

Meyers, G., McIntosh, P., Pigot, L., Pook, M., 2007. The years of El Niño, La Niña, and interactions with the tropical Indian Ocean. J. Climate. 20, 2872–2880.

Mishra, P., Patra, S. K., Ramanamurthy, M. V., Mohanty, P. K., Panda, U. S., 2011. Interaction of monsoonal wave, current and tide near gopalpur, east coast of india, and their impact on beach profile: a case study. Nat. Hazards. 59, 1145–1159.

Miyama, T., McCreary, J. P., Jensen, T. G., Loschnigg, J., Godfrey, S., Ishida, A., 2003. Structure and dynamics of the Indian-Ocean cross-equatorial cell. Deep–Sea Res. Part I,50, 2023–2047.

Mohapatra, M., Mohanty, U. C., 2004. Some characteristics of low pressure systems and summer monsoon rainfall over Orissa. Current Science 87, 1245–1255.

Montegut, C. D. B., Madee, G., Fischer, A. S., Lazar, A., Iudicone, D., 2004. Mixed layer depth over the global ocean: An examination of profile data and a profile based climatology. J. Geophys. Res. 109, C12003, doi:10.1029/2004JC002378.

Mooley, D. A., Shukla, J., 1989. Main features of the westward moving low pressure systems which form over Indian region during the summer monsoon season and their relation to monsoon rainfall. Mausam 40, 137–152.

Moore, D. W., 1968. Planetary-gravity waves in an Equatorial Ocean. Ph.D. thesis, Harvard Univeristy.

Moore, D. W., McCreary, J. P., 1990. Excitation of intermediate frequency equatorial waves at a western ocean boundary: with application to observations from the Indian Ocean . J. Geophys. Res. 95, 5219–5231.

Morel, A., Antoine, D., 1994. Heating rate within the upper ocean in relation to its bio–optical state. J. Phys. Oceanogr. 24 (7), 1652–1665.

Morel, A., Maritorena, S., 2001. Bio–optical properties of oceanic waters: A reappraisal. J. Geophys. Res. 106 (C4), 7163–7180.

Mori, K., Matsuno, T., Senjyu, T., 2005. Seasonal/spatial variations of the near-inertial oscillations in the deep water of the Japan sea. Journal of Oceanography 61, 761–773.

Mukherjee, A., Shankar, D., Aparna, S. G., Amol, P., Fernando, V., Fernandes, R., Khalap, S., Narayan, S., Agarvadekar, Y., Gaonkar, M., Tari, P., Kankonkar, A., Vernekar, S., 2013. Near-inertial currents off the east coast of india. Cont. Shelf Res. 55, 29–39.

Murty, T. S., Henry, R. F., 1983. Tides in the Bay of Bengal. J. Geophys. Res. 2012.

Murty, V. S. N., Suryanarayana, A., Rao, D. P., 1993. Current structure and volume transport across 12°N in the Bay of Bengal. Indian J. Mar. Sci. 22, 12–16.

Nethery, D., Shankar, D., 2007. Vertical propagation of baroclinic Kelvin waves along the west coast of India. J. Earth Syst. Sci. 116, No-4, 331–339.

Nuncio, M., Kumar, S. P., 2012. Life cycle of eddies along the western boundary of the Bay of Bengal and their implications. J. Marine. Syst. 94, 9–17.

O'Brien, J. J., Adamec, D., Moore, D. W., 1978. A simple model of upwelling in the Gulf of Guinea. Geophys. Res. Lett. 5 (8), 641–644.

ONeill, K., 1984. Equatorial velocity profiles, part I, Meridional components. J. Phys. Oceanogr. I4, 1829–1841.

Pacanowski, R. C., Griffies, S. M., 1998. MOM 3.0 Manual. NOAA/Geophysical Fluid Dynamics Laboratory, Princeton, USA 08542.

Pandey, V. K., Singh, S. K., 2010. Comparison of ECCO2 and NCEP reanalysis using TRITON and RAMA data at the Indian Ocean Mooring Buoy point. Earth Science India 3 (IV), 226–241.

Paul, C. L., Miller, S. G., 1996. Wavelet transform and ocean current data analysis. Journal of Atmospheric and Ocean Technology. 13, 1090–1099.

Philander, S. G. H., 1983. El Niño Southern Oscillation phenomena. Nature. 302, 295–301.

Picaut, J., 1983. Propagation of seasonal coastal upwelling in the eastern equatorial Atlantic. J. Phys. Oceanogr. 13 (1), 18–37.

Pollard, R. T., 1970. On the generation by winds of inertial waves in the ocean. Deep Sea Research 17, 795–812.

Pollard, R. T., Millard, R. C., 1970. Comparision between observed and simulated wind generation inertial oscillations. Deep Sea Research 17, 813–821.

Potemra, J. T., Luther, M. E., O'Brien, J. J., 1991. The seasonal circulation of the upper ocean in the Bay of Bengal. J. Geophys. Res. 96, 12,667–12,683, doi:10.1029/91JC01045.

Prerna, S., Chatterjee, A., Murthududde, R., Mukherjee, A., Ravichandran, M., Shenoi, S. S. S., 2017. Forcing mechanism of Wyrkti Jet. Manuscript submitted to the journal.

Rao, R. R., Kumar, K., B.Mathew., 1996. Observed variability in the current field during summer monsoon experiments: Arabian Sea. Mausam 47, 355–368.

Rao, R. R., Kumar, M. S. G., Ravichandran, M., Rao, A. R., Gopalakrishna, V. V., Thadathil, P., 2009. Interannual variability of Kelvin wave propagation in the wave guides of the equatorial Indian Ocean, the coastal Bay of Bengal and the southeastern Arabian Sea during 1993–2006. Deep-Sea Res., Part-I. 57, 1–13.

Rao, R. R., Molinari, R. L., Festa, J. F., 1991. Surface meteorological and near surface oceanographic atlas of the tropical Indian Ocean. NOAA-Tech. Memo. ERL. AOML-69.

Rao, S., Behera, S. K., Masumoto, Y., Yamagata, T., 2002. Inter-annual subsurface variability in the tropical Indian Ocean with a special emphasis on the Indian Ocean Dipole. Deep-Sea Res.,Part-II 49, 1549–1572.

Rao, S. A., Dhakate, A. R., Saha, S. K., Mahapatra, S., Chaudhari, H. S., Pokhrel, S., Sahu, S. K., 2012. Why is Indian Ocean warming consistently. Climate Change. 110, 709–719, doi:10.1007/s10584–011–0121–x.

Rao, T. V. N., 2002. Spation distribution of upwelling off the central east coast of India. Estuar. Coast. Shelf Sci. 54, 141–156.

Rao, T. V. N., 2004. Flow field in the inner shelf along the central east coast of india during the southwest monsoon season. J Coastal Res. 20, issue:3, 814–827.

Rao, Y. P., 1976. Southwest Monsoon. Synoptic Meteorology, Meteorological Monographs, India Meteorological Department, New Delhi, India.

Ratnam, J. V., Giorgi, F., Kaginalkar, A., Cozzini, S., 2009. Simulation of the Indian monsoon using RegCM3-ROMS regional coupled model. Clim. Dyn. 33, 119–139, doi:10.1007/s00382–008–0433–3.

Ravichandran, M., Behringer, D., Sivareddy, S., Girishkumar, M. S., Chacko, N., Harikumar, H., 2013. Evaluation of the Global Ocean Data Assimilation System at INCOIS: The Tropical Indian Ocean. Ocean Model. 69, 123–135.

Redi, M. H., 1982. Oceanic isopycnal mixing by coordinate rotation. J. Phys. Oceanogr. 12, 1154–1158.

Reppin, J., Schott, F. A., Fischer, J., Quadfasel, D., 1998. Equatorial currents and transports in the upper central Indian Ocean: Annual cycle and interannual variability. J. Geophys. Res. 104, 15495–15514.

Rochford, D. J., 1964. Salinity maxima in the upper 1000 metres of the north Indian Ocean . Australian Journal of Marine Freshwater Research 15, 1–24.

Romea, R. D., Allen, J. S., 1983. On vertically propagating coastal Kelvin waves at low latitudes. J. Phys. Oceanogr. 13, 1241–1254.

Saji, N. H., Goswami, B. N., Vinayachandran, P. N., Yamagata, T., 1999. A dipole mode in the tropical Indian Ocean. Nature. 401, 360–363.

Saji, P. K., Shenoi, S. C., Almeida, A., Rao., G., 2000. Inertial currents in the Indian Ocean derived from satellite tracked surface drifters. Oceanol. Acta. 23, 635–640.

Sanilkumar, K. V., Kuruvilla, T. V., Jogendranath, D., Rao, R. R., 1997. Observations of the Western Boundary Current of the Bay of Bengal from a hydrographic survey during March 1993. Deep–Sea Res. Part I,44, 135–145, doi:10.1016/S0967–0637(96)00036–2.

Sanilkumar, V., Kumar, K. A., Pednekar, P., 2008. Observation on oceanographic parameters of nearshore waters off Yanam, during the cyclonic storm. Curr. Sci. 94, 530–536.

Sarma, M. S. S., Rao, L. G., 1986. Currents and temperature structure off Godavari (east coast of India) during September 1980. Indian J. Mar. Sci. 15, 88–91.

Sarma, M. S. S., Rao, L. G., 1989. Spectra of currents and temperature off Godavari (east coast of India). Mahasagar 22, 29–36.

Schott, F., Reppin, J., Fischer, J., 1994. Currents and transports of the Monsoon Current south of Sri Lanka. J. Geophys. Res. 99, 25127–25141.

Schott, F. A., McCreary, J. P., 2001. Currents and transports of the Monsoon Current south of Sri Lanka. Prog. Oceanogr. 51, 1–120.

Schott, F. A., Swallow, J. C., Fieux, M., 1990. The Somali current at the equator: Annual cycle of currents and transports in the upper 1000 m and connecting to the neighboring latitudes . Deep. Sea. Res., Part A 37, 1825–1848.

Schott, F. A., Xie, S.-P., McCreary, J. P., 2009. Indian Ocean circulation and climate variability . Rev. Geophys. 47, RG1002.

Sengupta, D., Senan, R., Murty, V., Fernando, V., 2004. A biweekly mode in the equatorial Indian Ocean. J. Geophy. Res. 109 (C10003).

Shankar, D., 1998. Low-frequency variability of sea level along the coast of India. Ph.D. thesis, Goa Univ., India.

Shankar, D., 2000. Seasonal cycle of sea level and currents along the coast of India. Curr. Sci 78, 279–288.

Shankar, D., Aparna, S. G., Mccreary, J. P., Suresh, I., Neetu, S., Durand, F., Shenoi, S. S. C., Saafani, M. A. A., 2010. Minima of interannual sea-level variability in the Indian Ocean. Prog. Oceanogr. 84, 225–241.

Shankar, D., McCreary, J. P., Han, W., Shetye, S. R., 1996. Dynamics of the East India Coastal Current 1. Analytic solutions forced by interior Ekman pumping and local alongshore winds. J. Geophys. Res. 101, 13,975–13,991.

Shankar, D., Shetye, S. R., 1997. On the dynamics of the Lakshadweep high and low in southeastern Arabian Sea. J. Geophys. Res. 102, 12551–12562.

Shankar, D., Shetye, S. R., 1999. Are interdecadal sea level changes along the Indian coast influenced by variability of monsoon rainfall? J. Geophys. Res. 104, NO.C11, 26,031–26,042.

Shankar, D., Shetye, S. R., 2001. Why is mean sea level along the coast of India higher in the Bay of Bengal than in the Arabian sea. Geophys. Res. Lett. 28, 563–565, doi:10.1029/2000GL012001.

Shankar, D., Vinayachandran, P. N., Unnikrishnan, A. S., 2002. The monsoon currents in the north Indian Ocean. Prog. Oceanog. 52, 63–120.

Shcherbinin, A. D., Arsenyev, V. S., Yu, A., 1979. The western boundary current of the Bay of Bengal. Dokl.Acad.Sci.USSR, Earth Sci. Sect. 244, 167–168.

Shearman, R. K., 2005. Observations of near-inertial current variability on the New England shelf. J. Geophys. Res. 110, doi:10.1029/2004JC002341.

Shenoi, S. S. C. ., Antony, M. K., 1991. Current measurements over the western continental shelf of India. Continental Shelf Research 11, 81–93.

Shenoi, S. S. C., Saji, P. K., Almeida, A. M., 1999. Near-surface circulation and kinetic energy in the tropical Indian Ocean derived from Lagrangian drifters. J. Mar. Res. 57, 885–907.

Shetye, S., Michael, G., 1988. Satellite -tracked drifting buoy observations in the south equatorial current in the Indian ocean. Proc. Indian Academy of Sciences. (Earth Planet. Sci.) 97, 149–157.

Shetye, S., Shenoi, S. S. C., Gooveia, A. D., Sundar, D., Nampoothiri, G., Michael, G., 1991a. Wind-driven coastal upwelling along the western boundary of the Bay of Bengal during the southwest monsoon. Continental Shelf Research 11, 1397–1408.

Shetye, S. R., 1993. The movement and implications of the Ganges-Brahmaputra runoff on entering the Bay of Bengal. Current Science 64, 32–38.

Shetye, S. R., 1998. West India Coastal Current and Lakshadweep high/low. Sadhana 23, 637–651.

Shetye, S. R., Gouveia, A. D., 1998. Coastal circulation in the North Indian Ocean. Coastal segment (14, S-W). The Sea 11, 523–556.

Shetye, S. R., Gouveia, A. D., Shankar, D., Shenoi, S. S. C., Vinayachandran, P. N., Sundar, D., Michael, G. S., Nampoothiri, G., 1996. Hydrography and circulation in the western Bay of Bengal during the northeast monsoon. J. Geophys. Res. 101, 14,011–14,025.

Shetye, S. R., Gouveia, A. D., Shenoi, S. S. C., Michael, G. S., Sundar, D., Almeida, A. M., Santanam, K., 1991b. The coastal current off western India during the northeast monsoon. Deep Sea Res., Part I 38, 1517–1529.

Shetye, S. R., Gouveia, A. D., Shenoi, S. S. C., Sundar, D., Michael, G. S., Almeida, A. M., Santanam, K., 1990. Hydrography and circulation off the west coast of India during the southwest monsoon 1987. J. Mar. Res. 48, 359–378.

Shetye, S. R., Gouveia, A. D., Shenoi, S. S. C., Sundar, D., Michael, G. S., Nampoothiri, G., 1993. The western boundary current of the seasonal subtropical gyre in the Bay of Bengal. J. Geophys. Res. 98, 945–954.

Shetye, S. R., Shenoi, S. S. C., 1988. Seasonal cycle of surface circulation in the coastal North Indian Ocean. Proc. Ind. Acad. Sci (Earth Planet. Sci.). 97, No-1, 53–62.

Shetye, S. R., Shenoi, S. S. C., Gouveia, A. D., Michael, G. S., Sundar, D., Nampoothiri, G., 1991c. Wind-driven coastal upwelling along the western boundary of Bay of Bengal during southwest monsoon. Cont. Shelf. Res. 11, 1397–1408.

Sikhakolli, R., Sharma, R., Basu, S., Gohil, B. S., Sarkar, A., Prasad, K. V. S. R., 2013. Evaluation of OSCAR ocean surface current product in the tropical Indian Ocean using in-situ data. J. Earth Syst. Sci. 122, 187–199.

Simmons, H. L., Jayne, S. R., Laurent, L. C. S., Weaver., A. J., 2004. Tidally driven mixing in a numerical model of the ocean general circulation. Ocean Modelling 6, 245–263.

Sindhu, B., Suresh, I., Unnikrishnan, A., Bhatkar, N., Neetu, Michael, G., 2007. Improved bathymetric datasets for the shallow water regions in the Indian Ocean. J. Earth Syst. Sci. 116, 261–274.

Sindhu, M., 2012. Numerical Modeling of Tides and Storm Surges in the Bay of Bengal. Ph.D thesis, Goa University.

Somayajulu, Y., Murthy, V., Sarma, Y., 2003. Seasonal and inter-annual variability of surface circulation in the Bay of Bengal from TOPEX/Poseidon altimetry. Deep-Sea Research. Part-II, 50, 867–880.

Sprintall, J., Tomczak, M., 1992. Evidence of barrierl layer in the surface layer of the tropics. J. Geophys. Res. 97, 7305–7316.

Sreenivas, P., Gnanaseelan, C., Prasad, K. V. S. R., 2012. Influence of El Nino and Indian Ocean Dipole on sea level variability in the Bay of Bengal. Global and Planetary Change. 80-81, 215–225, doi:10.1016/j.gloplacha.2011.11.001.

Srinivas, K., Kumar, P. K. D., Revichandran, C., 2005. ENSO signature in the sea level along the coastline of the Indian subcontinent. Indian J. Mar. Sci. 34, 225–236.

Stammer, D., Wunsch, C., Fukumori, I., Marshall, J., 2002a. State estimation in modern oceanographic research. EOS Trans. AGU 83 (27), 289,294–295.

Stammer, D., Wunsch, C., Giering, R., Eckert, C., Heimbach, P., Marotzke, J., Adcroft, A., Hill, C. N., Marshall, J., 2002b. The global ocean circulation during 1992–1997, estimated from ocean observations and a general circulation model. J. Geophys. Res. 107 (C9), 3118.

Stommel, H., 1948. The westward intensification of wind-driven ocean currents. Transactions, American Geophysical Union 29 (2), 202–206.

Sun, L., Zheng, Q., Wang, D., Hu, J., Tai, C., Sun, Z., 2011. A case study of near-inertial oscillation in the South China Sea using mooring observations and satellite altimeter data. Journal of Oceanography 2011.

Suresh, I., Vialard, J., Lengaigne, M., Han, W., McCreary, J., Durand, F., Muraleedharan, P. M., 2013. Origins of wind-driven intraseasonal sea level variations in the north indian ocean coastal waveguide. Geophys. Res. Lett. 40, 5740–5744.

Sverdrup, H. U., 1947. Wind-driven currents in a baroclinic ocean: with application to the equatorial currents of the eastern Pacific. Proceedings of the National Academy of Sciences 33 (11), 318–326.

Vandenbrouck, F., Berthier, Gheusi, F., 2000. Coriolis force in Geophysics: an elementary introduction and examples. European Journal of Physics 21, 359–366.

Vialard, J., Shenoi, S. S. C., McCreary, J. P., Shankar, D., Durand, F., Fernando, V., Shetye, S. R., 2009. Intraseasonal response of the northern Indian Ocean coastal waveguide to the Madden-Julian Oscillation. Geophys Res. Let., L14606, doi:10.1029/2009GL038450.

Vinayachandran, P., Neema, C. P., Mathew, S., Remya, R., 2012. Mechanisms of summer intraseasonal sea surface temperature oscillations in the Bay of Bengal. J. Geophys. Res. 117, C01005, doi:10.1029/2011JC007433.

Vinayachandran, P. N., Kurian, J., 2007. Hydrographic observations and model simulation of the Bay of Bengal freshwater plume. Deep-Sea Res., Part-I. 54, 471–486.

Vinayachandran, P. N., Kurian, J., Neema, C. P., 2007. Indian Ocean response to anomalous condition during 2006. Geophy. Res. Lett. 34.

Vinayachandran, P. N., Masumoto, Y., Mikawa, T., Yamagata, T., 1999. Intrusion of South-west monsoon current into the Bay of Bengal. J. Geophys. Res. 104, 11,077–11,085.

Vinayachandran, P. N., Murty, V. S. N., Babu, V. R., 2002. Observations of barrier layer formation in the Bay of Bengal during summer monsoon. J. Geophys. Res. 107, C12, 8018, doi:10.1029/2001JC000831.

Vinayachandran, P. N., Shetye, S. R., Sengupta, D., Gadgil, S., 1996. Forcing mechanisms of the Bay of Bengal circulation. Curr. Sci. 71, 753–763.

Vinayachandran, P. N., Yamagata, T., 1998. Monsoon Response of the Sea around Sri Lanka: Generation of Thermal Domes and Anticyclonic Vortices. J. Phys. Oceanogr. 28, 1946–1960.

Warren, B. A., Stommel, H., Swallow, J. C., 1966. Water masses and patterns of flow in the Somali basin during the southwest monsoon of 1964. Deep Sea Res. 13, 1398–1415.

Webster, F., 1968. Observations of inertial-period motions in the deep sea. Reviews of Geophysics 6, 473–490.

Webster, P. J., Moore, A. M., Loschnigg, J. P., Leben, R. R., 1999. Coupled ocean-atmosphere dynamics in the Indian Ocean during 1997-98. Nature. 401, 356–360.

WMO, 2010. Tropical cyclone operational plan for the Bay of Bengal and Arabian sea:. Tech. Rep. TCP21, World Meteorological Organization, Geneva, Switzerland.

Wu, G., Guan, Y., Liu, Y., Yan, J., Mao, J., 2012. Air-sea interaction and formation of the Asian summer monsoon onset vortex over the Bay of Bengal. Clim Dyn. 38, 261–279, doi:10.1007/s00382–010–0978–9.

Wu, L., Wang, F., Yuan, D., Cui, M., 2007. Evolution of freshwater plumes and salinity fronts in the northern Bay of Bengal. J. Geophys. Res. 112, C08017, doi:10.1029/2005JC003308.

Wyrtki, K., 1971. Oceanographic Atlas of the International Indian Ocean Expedition. Natl. Sci. Found., Washington, D. C.., 531pp.

Wyrtki, K., 1973. An equatorial jet in the Indian Ocean. Science 181, 262–264.

Wyrtki, K., 1975. El Niño—the dynamic response of the equatorial Pacific Ocean to atmospheric forcing. J. Phys. Oceanogr. 5, 572–584.

Xie, X., Shang, X., Chen, G., Sun, L., 2009. Variations of diurnal and inertial spectral peaks near the bi-diurnal critical latitude. Geophys. Res. Lett. 36.

Xie, X., Shang, X., Haren, H., Chen, G., Zhang, Y., 2011. Observations of parametric subharmonic instability-induced near-inertial waves equatored of the critical diurnal latitudes. Geophys. Res. Lett. 2011.

Yu, L., O'Brien, J. J., Yang, J., 1991. On the remote forcing of the circulation in the Bay of Bengal. J. Geophys. Res. 96, 20,449–20,454, doi:10:1029/91JC02424.

Zhai, X., Greatbatch, R. J., Zhao, J., 2005. Enhanced vertical propagation of storm-induced near-inertial energy in an eddying ocean channel model. Geophys. Res. Lett. 32.

T-811